DESIGN APPROACH WITH WIND TUNNEL TEST DATA ON AN RPV LABORATORY FOR IN-FLIGHT AEROFOIL TESTING

by

Mauro Darida

A thesis submitted in fulfillment of the requirements for the degree of

Master in Aeronautical Engineering

University of Glasgow

Department of Aerospace Engineering

September 1998

Approved by _____
Chairperson of Supervisory Committee

_____

_____

_____

Date _____

Dedicated to Iriowen
and Her Loving Kisses

TABLE OF CONTENTS

University of Glasgow

Abstract

DESIGN APPROACH WITH WIND TUNNEL TEST DATA ON AN RPV LABORATORY FOR IN-FLIGHT AEROFOIL TESTING

by Mauro Darida

Chairperson of the Supervisory Committee: _____

Department of Aerospace Engineering

Presently wind tunnels are deployed to collect the majority of the experimental data on aerofoils and on boundary layer investigations, but they have their own disadvantages. Flight testing, especially at higher Reynolds numbers, gives a practical solution to these disadvantages, but has a critical influence on the direct cost of experiments. A design study was carried out to modify an RPV, named "Condor", to demonstrate the potential use of an RPV system for in-flight laminar aerofoil research at a fraction of the cost on a manned aircraft. A wing glove, namely an outsized and removable aerofoil section attached to the wing of the RPV, was designed and built. A wind tunnel/numerical investigation was conducted to evaluate the resulting RPV wing/glove combination. Numerical modelling proved it to be capable of providing flowfield details that pointed out the need for endplates in order to acquire infinite wing aerofoil data over the glove surface. Wind tunnel testing included pressure measurements and surface flow visualization and was most beneficial in the endplates design and in validating the pressure sensing system for future flight testing. The investigation included an effort to measure the pressure distribution produced by simulated ice formations on the glove leading edge. General observations deducted from these results are presented.

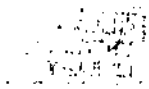

ABBREVIATIONS

ACJ	Advisory Circular - Joint
ADC	Analog to Digital Converter
AoA	Angle of Attack
BSL	Best Straight Line
CAA	Civil Aviation Authority
CMRR	Common-Mode Rejection Range
CG	Center of Gravity
CFD	Computational Fluid Dynamics
DAS	Data Acquisition System
DAQ	Data Acquisition
FSP	Full Standard Pressure
FIFO	First In First Out
IR	Infra-Red
MAC	Mean Aerodynamic Chord
PCM	Pulse Code Modulation
PCMCIA	Personal Computer Memory Card International Association
RTD	Resistance Temperature Detector
RPV	Remotely Piloted Vehicle
SSR	Solid State Resistor
UAV	Unmanned Aerial Vehicle
VAC	Volt Alternate Current
VDC	Volt Direct Current
VLA	Very Light Aeroplane

1. INTRODUCTION

1.1 HISTORICAL BACKGROUND

This section will examine past in-flight experiments which used a "wing glove" arrangement in subsonic laminar flow research. Notably such an arrangement is an excellent test bed for designing new aerofoils with improved laminar flow characteristics and hence significant drag reduction. In fact such an approach requires the minimum of modification to the test aircraft whilst permitting a number of different aerofoil sections to be tested.

Although such a research has also been conducted in wind tunnels, with valuable results, flight testing has often permitted higher Reynolds numbers to be attained. In addition, research has shown surface disturbances to be the principal cause of limited natural laminar flow (NLF), and the severity of the surface disturbances to be exarcebated by increased unit Reynolds number, which is lower during in-flight testing (Ref.1).

The earliest known attempts to attain extensive regions of laminar flow in flight were made in the late 1930's and early 1940's. The B-18 flight test by the NACA in 1939 (Fig.1.1) is a good example of such early attempts in the development of NLF.

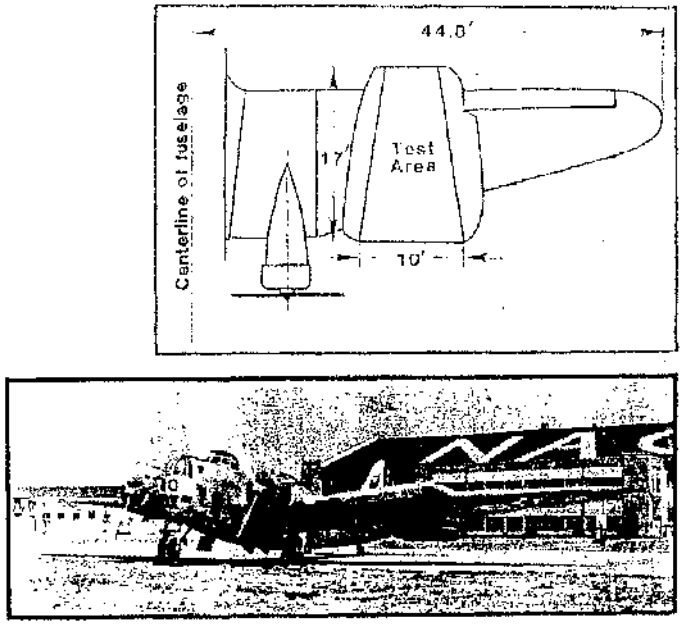

Fig. 1.1 The B-18 Glove Flight Test (Ref.1).

A wooden 17-foot chord, 10-foot span glove on the wing of the test aircraft was used, incorporating a NACA 35-215 aerofoil, and surface quality effects were evaluated. This flight test clearly displayed the importance of surface discontinuites and finish. As a result of these experiments, during the second World War several military aircraft were designed with promising NACA 6-series laminar aerofoils - perhaps the most famous being the P-51 Mustang. It is questionable that much laminar flow was achieved on the wings of these aircraft, as they flew in a harsh environment which heavily affected surface quality, not to mention the far from mature level of surface finish technology available at the time.

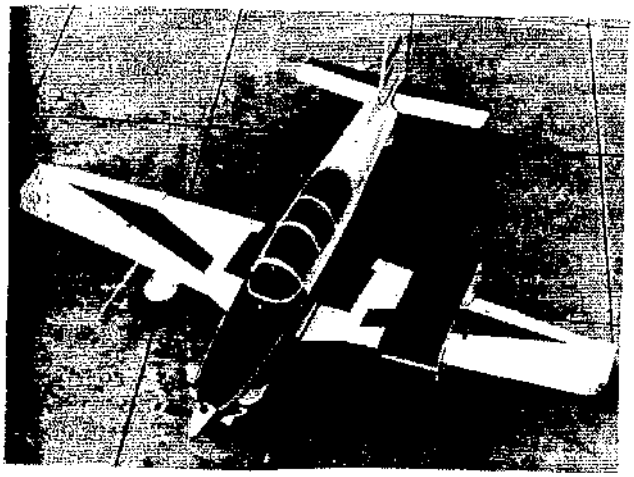

Fig.1.2 The T-34C Glove Flight Test (Ref.4).

Another significant flight test, which the author found in literature, took place during the 1960's in Lithuania. In this case the ESAG Institute used an L-13 Blanik glider (Ref.2) and several experiments, including a wake survey, were performed. A "twin" glove arrangement, where one glove acted as a "dummy", was adopted, presumably because of expected or experienced directional control problems. Unfortunately, it was impossible to trace the reference source (Ref.3).

T.U. Delft University used a similar approach during the same period approximately, according to Ref.2, which in turn points back to the same untraceable source (Ref.3).

Anyway, for almost ten years, research in NLF was dormant until the 1970's, when the energy crisis resumed flight testing and interest in the technology (Ref.5,6). Indeed, dramatically increased manufacturing capabilities - notably modern

composite materials - have made suitable surface quality attainable, while advances in miniature electronics have reduced cost and size of data acquisition equipment only dreamed of in the past, thus allowing a new breed of experiments and test beds to be conceived.

A good example in this direction is the NASA T-34C simple-turboprop aeroplane (Fig.1.2) with 92-inch chord, 3-feet span glove incorporating an NLF(1)-0215F aerofoil section. The glove skin was sheet aluminum covered with fibreglass and aluminum endplates were attached to both edges of the glove. Infrared flow visualization technique was used to spot the boundary layer transition, thus evaluating the laminar flow aerofoil performance.

Today, the prospects for a practical technology are brighter than ever, and the project which is the basis of this thesis could be an example of what may appear in future.

1.2 AIM OF THE PROJECT

The project work was initiated in October 1995 under a University of Glasgow - Faculty of Engineering - scholarship. The initial scope of the project was to adapt an RPV (Remotely Piloted Vehicle) into an airborne platform for laminar aerofoil research under subsonic regime, allowing investigations in real flight environments and conditions. Since evidence was required to show that the Department would be capable of operating the vehicle, it was decided to fly the modified RPV, named "Condor", with a wooden wing glove incorporating a standard NACA 0012 aerofoil. Success would prove that the RPV/glove combination is capable of catering for laminar aerofoil research. The so called "wing glove" is an outsized and removable aerofoil section attached to the RPV wing, which would be the key feature that should permit many different types of aerofoil sections to be tested in flight. The existing RPV airframe had to be modified in the following areas :

- provision of undercarriage;
- provision of wing extension;
- provision of dual rudder;
- provision of flight control system;
- provision of research instrumentation;
- provision of a wing glove.

At the date of the resignation of the author, several modifications had not been implemented yet : as a result, the date of the maiden flight is still uncertain, although initial wind tunnel testing of the RPV wing/glove combination has been completed.

2. CONDOR TECHNICAL DESCRIPTION

Lack of technical reference in the English language is a serious problem with the Condor, whose airframe modification was made together with the Glasgow University. The purpose of this section is to provide with a minimum of information in the English language to safely modify and operate the aircraft. The author takes here the opportunity to thank his flatmate Pavel Mistrik who helped him in translating some of the Czech technical references (Ref.7,8,9,10,11) on which this section is based. Appendix C is a gathering of English-translated information from various sources, including faxes and oral discussions.

2.1 CONSTRUCTION

The wing strength/weight ratio was optimised given the constraints that the all up weight was not to exceed 145 kg and that the level flight speed was not to exceed 180 km/h. Tailbooms are of conical shape and made of carbon fibre. The other composite parts have a core of polystyrene Ciba-Geigy Herex C 70.75 laminated with epoxy resin Ciba LY5138 (hardener HY5138, mixing ratio 100:23) and glassfibre Cs-Interglas. Epoxy resin was hot cured at 60°.

Dynamic and flutter tests were not performed on any part of the structure, which was designed with a safety factor of 1.2.

2.2 FUSELAGE

Condor fuselage is shown in Fig.2.1. The landing skid should be removed to install an undercarriage for conventional take-off and landing (see 3.4). Note the four bolts (items no.5,6) securing the wing to the fuselage. The fuselage is a semi-monocoque structure designed so that the top half may be removed along its whole length to provide full access to the interior, which is separated into three compartments. Front

compartment is devoted to video equipment or air data sensors allocation. The second compartment is a payload bay for avionics or other equipment, while the third one contains fuel tank and engine mount.

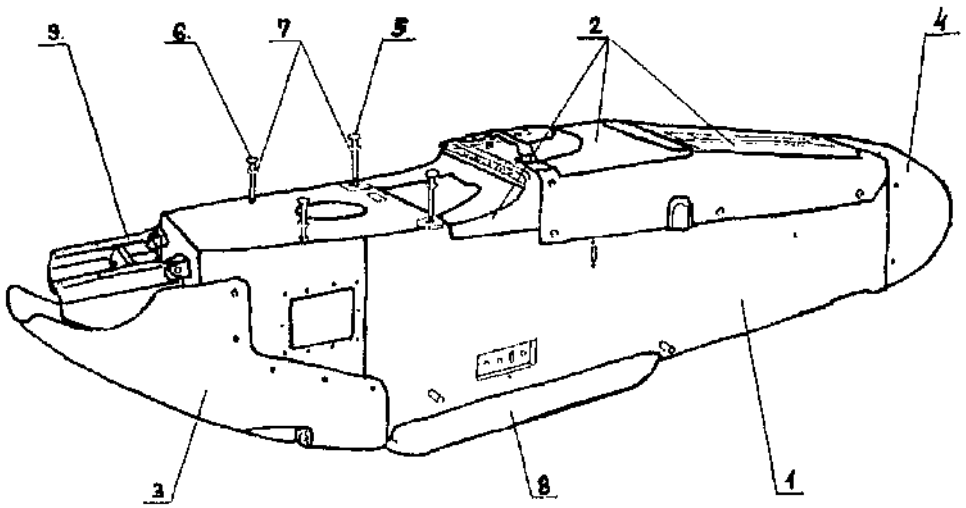

NO.	ITEM	Q.TY
1	Fuselage	1
2	Upper Cover Fairing	1
3	Engine Fairing	1
4	Front Cover Fairing	1
5	Front Wing/Fuselage Bolt M8X120	2
6	Rear Wing/Fuselage Bolt M8X90	2
7	Washer 8,4	4
8	Landing Skid	1
9	Engine Mount	1

Fig.2.1 Condor Fuselage.

2.3 FUEL TANK

The fuel tank is located at the rear fuselage and it is shown in Fig.2.2. Tube no.4 is vented; at the bottom of the tank there is a little chamber with two other tubes. Tube

no.2 feeds the engine, while tube no.3 is fitted with a cap that may be pulled out to empty the tank.

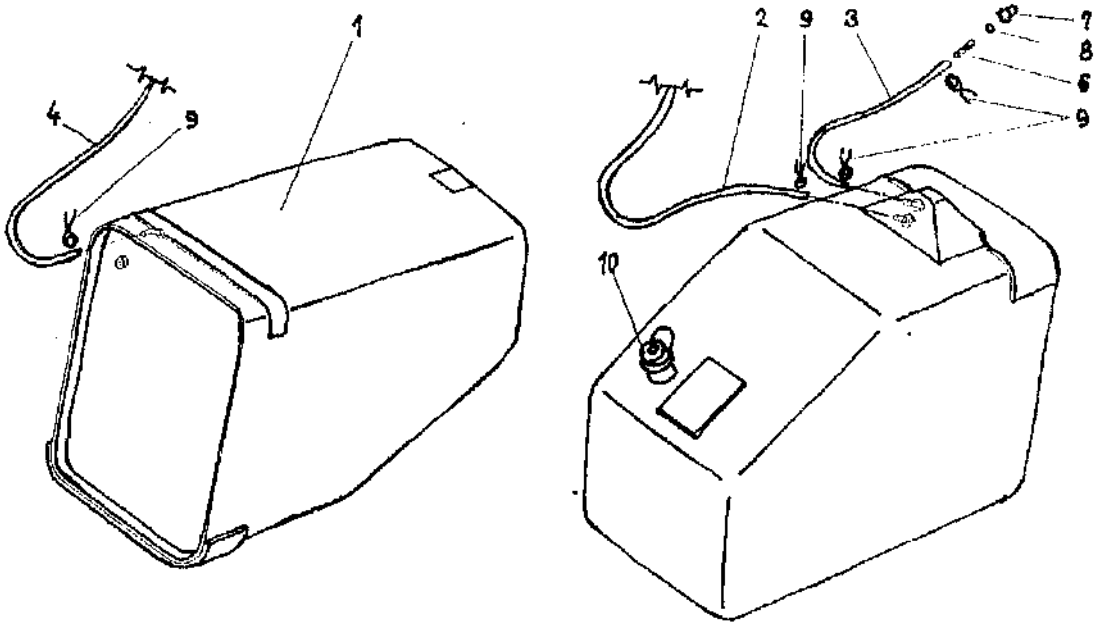

NO.	ITEM	Q.TY
1	Fuel Tank	1
2	PVC Suction Tube Φ5/1.5	1
3	PVC Purge Tube Φ5/1.5	1
4	Air Vent Φ4/1	1
6	Purge Tube Ending Body	1
7	Purge Cap	1
8	Rubber Padding	1
9	Safety Wire	4
10	Fuel Cap	1

Fig.2.2 Fuel Tank.

Refuelling is accomplished by using an external fuel pump, which is housed in a metallic box in military green colour; it needs a 24 VDC power source to be operated (polarity of the power cables is not critical). The refuelling process needs an intermediate tank from which the fuel is transferred to the RPV tank by the pump, which has an input and an output tube for this purpose. The RPV tank is filled up by

removing the fuel cap (item no.10) and then connecting the fuel pump output tube nozzle.

2.4 PARACHUTE CONTAINER

The standard parachute box is shown in Fig.2.3. It is designed to accomodate the Sojka (Ref.12,13) parachute recovery system and might not be able to accomodate an alternative system (see 3.5.1). Note the pins (item no.2) used as front point load for the chute bridles, and the tube for locating the rocket.

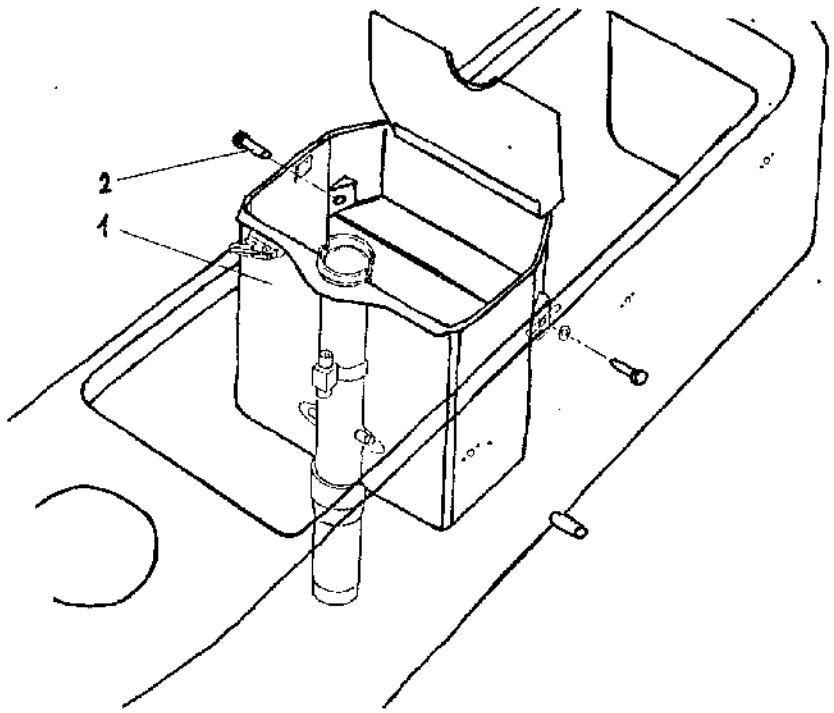

NO.	ITEM	Q.TY
1	Parachute Container	1
2	Front Parachute Pin	2

Fig.2.3 Parachute Container.

2.5 ENGINE MOUNT

The engine mount shown in Fig.2.4 is designed for supporting engine model M115V, fitted with a two-blade propeller M125R and a 28V alternator (see Appendix C for specifications). The author was told in Brno (Czech Republic) that

this model is no longer in production. Note the pins (item no.13) used as rear point load for the chute bridles.

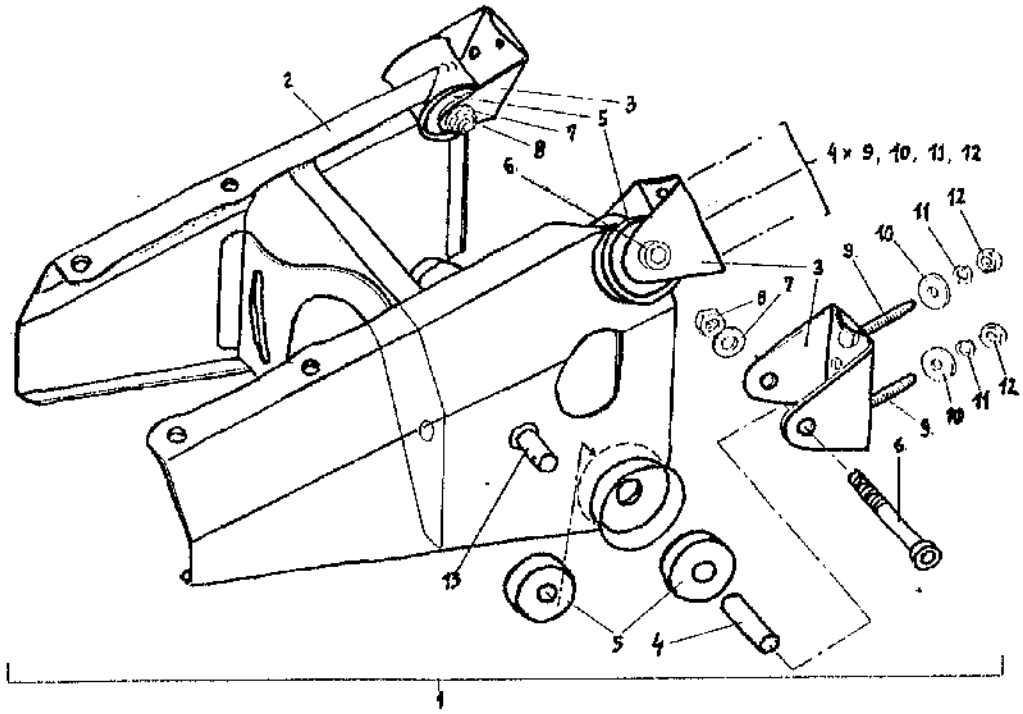

NO.	ITEM	Q.TY
1	Engine Mount	1
2	Engine Mount Body	1
3	Bracket	4
4	Spacer	4
5	Rubber Dumper	8
6	Bolt M8X60	4
7	Washer 8,4	4
8	Nut M8	4
9	Bolt M6X25	12
10	Washer 6,6	12
11	Washer 6	12
12	Nut M6	12
13	Rear Parachute Pin	2

Fig.2.4 Engine Mount.

2.6 ENGINE STARTER

The engine was delivered with a starter (Fig.2.5) to be operated manually, although it is far from being light (it weighs circa 9 kg). The starter electric motor clinched to the propeller will make it rotate when an operator presses the activation switch;

the starter is quickly withdrawn by the operator when the engine begins running. Starter operation needs an external 24 VDC source. Appendix C contains starter dimensions.

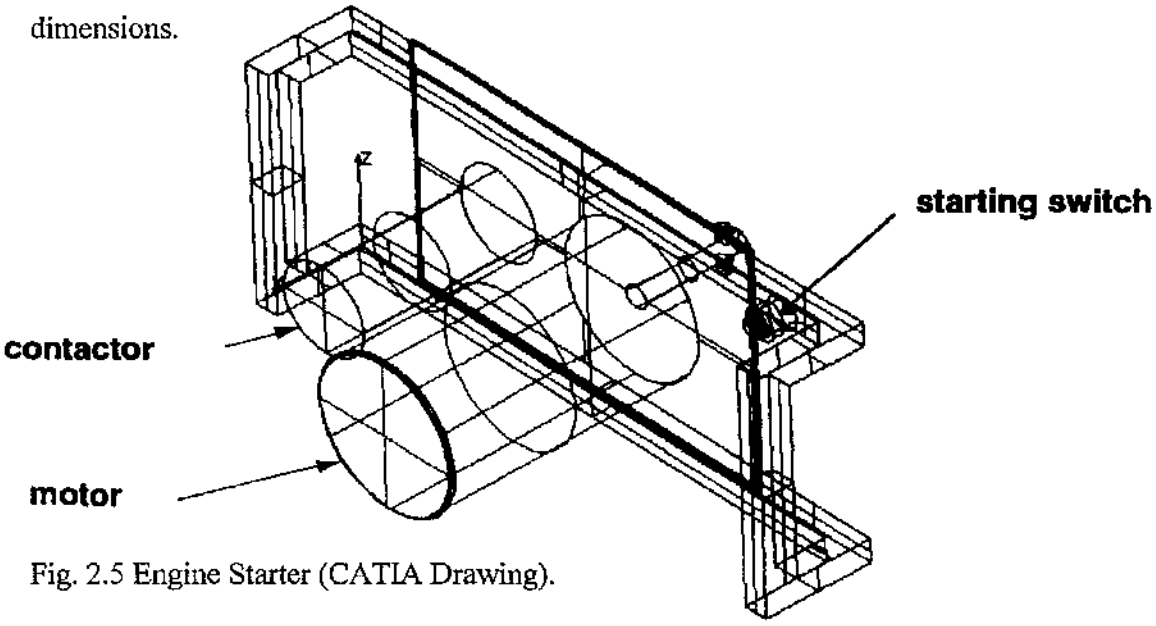

Fig. 2.5 Engine Starter (CATIA Drawing).

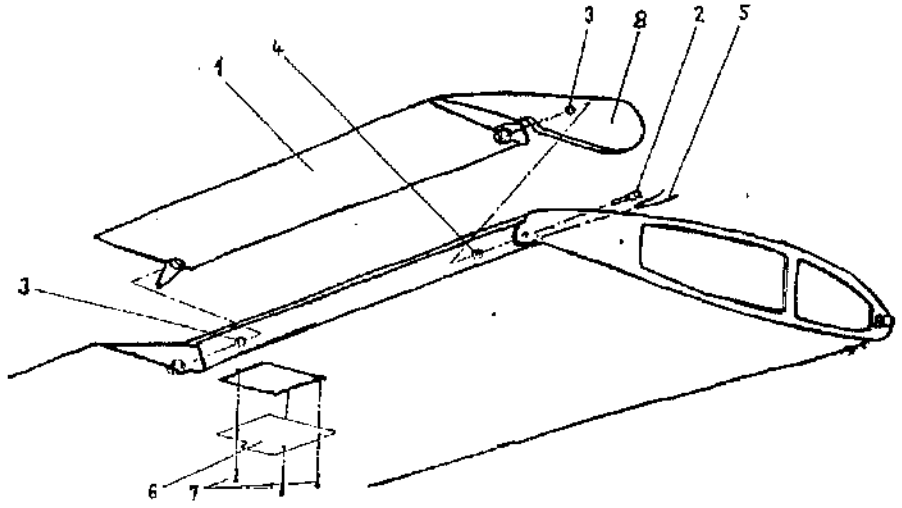

NO.	ITEM	Q.TY
1	Aileron	4
2	Bolted Pin	4
3	Ball Bearing 5	8
4	Washer 5,3	8
5	Safety Wire	4
6	Aileron Servo Cover plate (unused)	4
7	Bolt M4X12	12
8	Aileron Balance	2

Fig.2.6 Aileron Assembly.

2.7 AILERON ASSEMBLY

Aileron assembly is shown in Fig.2.6. Only inner ailerons were balanced, but they have had their aerodynamic balance (item no.8) removed because it is incompatible with the wing extension installation.

2.8 WING EXTENSION

The standard (Sojka) wing spar has three holes corresponding to three different dihedral angle settings (5-8-11 degrees). The recommended value to be first used during flight testing is 8 degrees, at the middle position.

Engineering drawings for the wing extension are not available because they were not produced at the time of fabrication. In Fig.2.7 is sketched the wing external structure as Ing.D.Lexa recollects it. The wing extension was structurally tested with a 100 lb weight (see Appendix C for details).

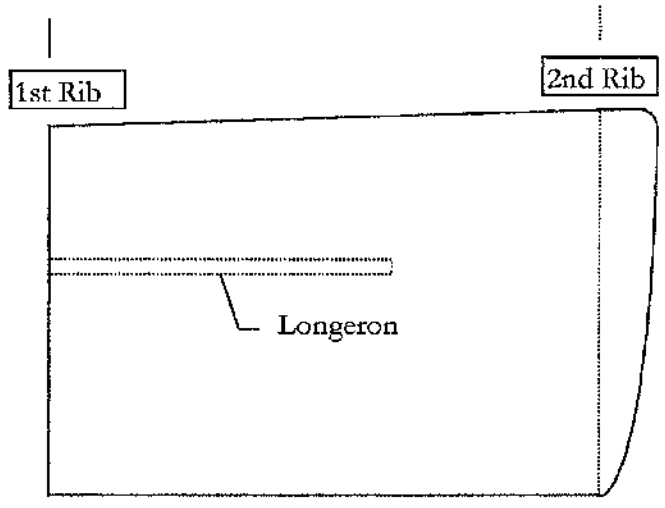

Fig. 2.7 Schematic of Wing Extension Structure Arrangement.

2.9 HORIZONTAL TAIL ASSEMBLY

The horizontal tail assembly is shown in Fig.2.8. Note the servo cover plate which is not used because of the different flight control system. The elevator is nicely balanced.

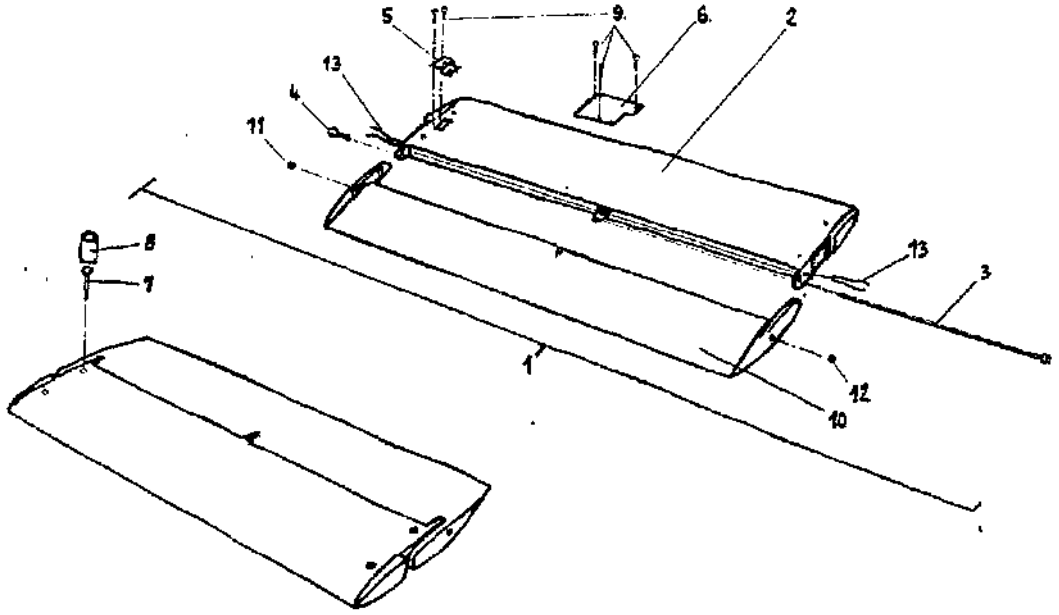

NO.	ITEM	Q.TY
1	Horizontal Tail Assembly	1
2	Stabilizator	1
3	Shank	1
4	Bolted Pin	1
5	Cable Support	1
6	Elevator Servo Cover Plate (unused)	2
7	Bolt	4
8	Spacer	4
9	Bolt M4X12	8
10	Elevator	1
11	Ball Bearing 5	1
12	Ball Bearing 6	1
13	Safety Wire	2

Fig.2.8 Horizontal Tail Assembly.

2.10 TAILBOOM

Tailboom assembly is shown in Fig.2.9. The fin will be cut in the vicinity of the fin spar in order to fit a rudder. Note that inspection door (item no.3) that should permit the rudder servo to be easily installed.

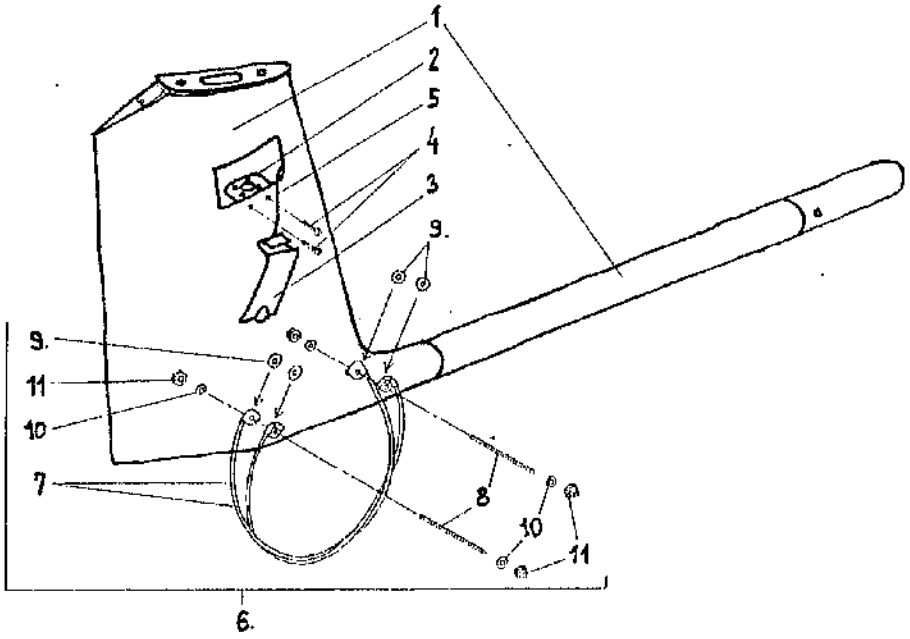

NO.	ITEM	Q.TY
1	Tailboom	2
2	Connector Support	2
3	Inspection Door	2
4	Bolt M4X12	4
5	Retainer - Silon Φ 1.4-200	2
6	Spur Assembly	2
7	Metal Wire	4
8	Threaded Rod	4
9	Washer th.1 - Φ 20	8
10	Washer 4,3	8
11	Nut M4	12

Fig.2.9 Tailboom.

2.11 CG RANGE

The recommended CG position is at 30% MAC at any take-off weight, which is the position of the rear bolts connecting the wing to the fuselage.

It is premature doing some CG calculations, as the Condor configuration is far from being frozen. A weight breakdown is presented (Tab.2.1) containing all items that will be certainly part of the Condor system in the author's opinion. Tab.2.1 is intended for future reference. CG coordinates were determined experimentally by A. Bram using the reference axes in Fig.2.10 and are given in millimeters.

ITEM	WEIGHT	C.G. COORDINATES*		
	Kg	X	Y	Z
Fuselage†	25.3	-1000	0	235
Propeller M125R	0.95			
Dry Engine M115V	19.4			
Alternator Type 443 113 516 830	4.5			
Exhaust Tube (Left)	1.3	-1400	260	145
Exhaust Tube (Right)	1.3	-1440	260	145
Standard (Sojka) Wing	12.7	-1430	0	470
Tailboom (Left)	2.7	-2415	670	380
Tailboom (Right)	2.7	-2415	-670	380
Wing Extension (Left)	3.75	-1390	2400	505
Wing Extension (Right)	3.75	-1390	-2400	505
Horizontal Tail	3.85	-3230	-70	885
Notebook Satellite 110CS	3.2			
Pressure Sensing System‡	2.49			
Controller CTLR2P/S2-S6	0.993			
Wing Glove	7.6			
Endplates 5 cm	0.681			
Autopilot P-HAL2100	0.045			
Receiver R-138DP	0.040			
Throttle Servo ps3001	0.045			
Elevator Servo ps3801	2X0.103			
Aileron/Flap Servo ps3032	4X0.103			
Main Wheel 6000 783 §	2X1.13			
Nose Wheel 0249N 3959	0.275			

Tab.2.1 Weight Breakdown.

* Fuselage coordinates refers to a weight which does include the exhaust tubes.
† Fuselage weight includes tank, parachute box, and engine mount but does not include the landing skid.
‡ Indicated weight does include two S7DC amplifiers, cabling, housing tray, two scanners 48S9GM complete of transducers, one solenoid drive SGMS5-48, two 48SM male connectors (see 3.7.3).
§ Indicated weight does not include the fork.

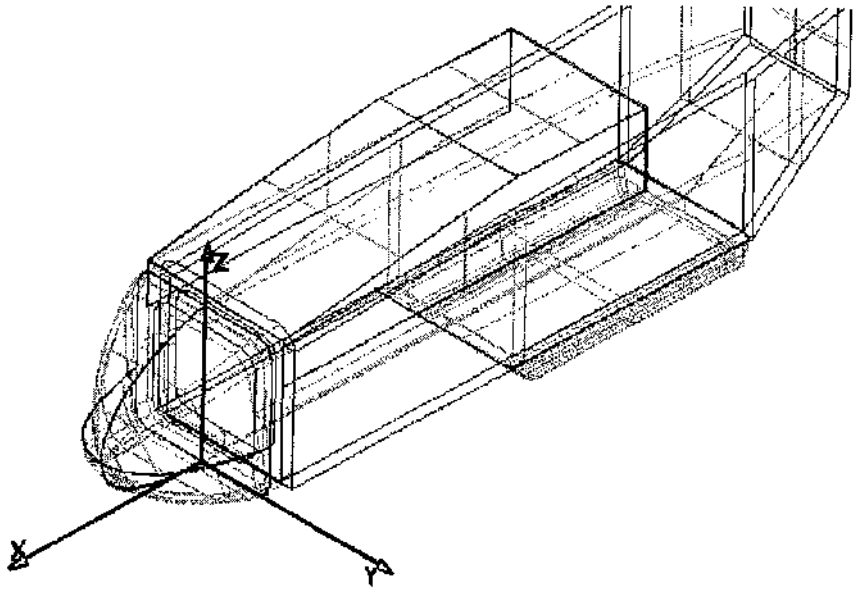

Fig.2.10 CG Reference Axes.

2.12 DRAG POLARS

The Condor is an upgrade of the Sojka model by provision of an extended wing. To date the Condor has never flown and experimental drag polars exist for the Sojka model only. T. Bauer (Ref.14) has calculated a set of drag polars for the Condor by using the previous experimental polars as a starting point. Here follows a list of all the assumptions behind Bauer's calculations which the author was able to trace back :

- wing glove effect is ignored
- drag polars are assumed to be trimmed
- flight speeds are within the subsonic regime
- angles of attack are relatively small (airflow predominantly non-separated)
- power-off conditions only are considered
- aero-elastic effects are neglected
- ground effect is ignored
- the minimum drag occurs at $C_L = 0$
- polars are approximated by a parabola
- vortex-induced drag increment due to flaps is neglected

As it was the author's intention to include results of Bauer's calculations in this thesis, they were double-checked and found mostly correct. There is a minor slip in the calculation of "R", leading suction parameter for the wing. By analizing Bauer's spreadsheet (included in Ref.14) it was clear that fig.4.7a of Ref.15 was used, while fig.4.7b would have to be used, because it is

$$R_{l_{ER}} \cot \Lambda_{LE} \sqrt{1 - M^2 \cos^2 \Lambda_{LE}} > 1.3 \cdot 10^5$$

which in turn gives a quite different value for "R". One last remark is about Bauer's calculation of the parasitic drag coefficient of the wing (Ref.14 p.48) :

$$(C_{D_o})_{wf} \cong 0.0067$$

which is formally correct, but the author found that Ref.16 gives a formula which yelds a higher, and hence more conservative, value :

$$(C_{D_o})_{wf} = R_{wf} R_{LS} C_{fw} \left[1 + L' \frac{t}{c} + 100 \left(\frac{t}{c} \right)^4 \right] \frac{S_{WET_W}}{S}$$

where, according to Ref.16 :

- $R_{LS} = 1.06$ from fig.4.2
- $C_{fw} = 0.007$ extrapolated from fig.4.3
- L' = 1.2 from fig.4.4
- t/c = 0.15 from the wing profile (NACA 2415)
- $S_{WET_W} / S = 1$ from fig.4.6

thus having eventually :

$$(C_{D_o})_{wf} \cong 0.0097$$

that is the new value implemented in Bauer's spreadsheet. Regarding drag polars with flaps deployed, it must be noted that inboard wing ailerons will be covered by the wing glove, thus leaving the outer ailerons to act as both ailerons and flaps, the so called flaperons. It is suggested to use flap angles of 15 degrees for take-off and 30 degrees for landing approach, being in the latter case some reserve deflection to mantain roll control

required. Drag polars so calculated (Fig.2.11) are also in Appendix C. The polar at 60 degrees of flap deflection was added for completeness.

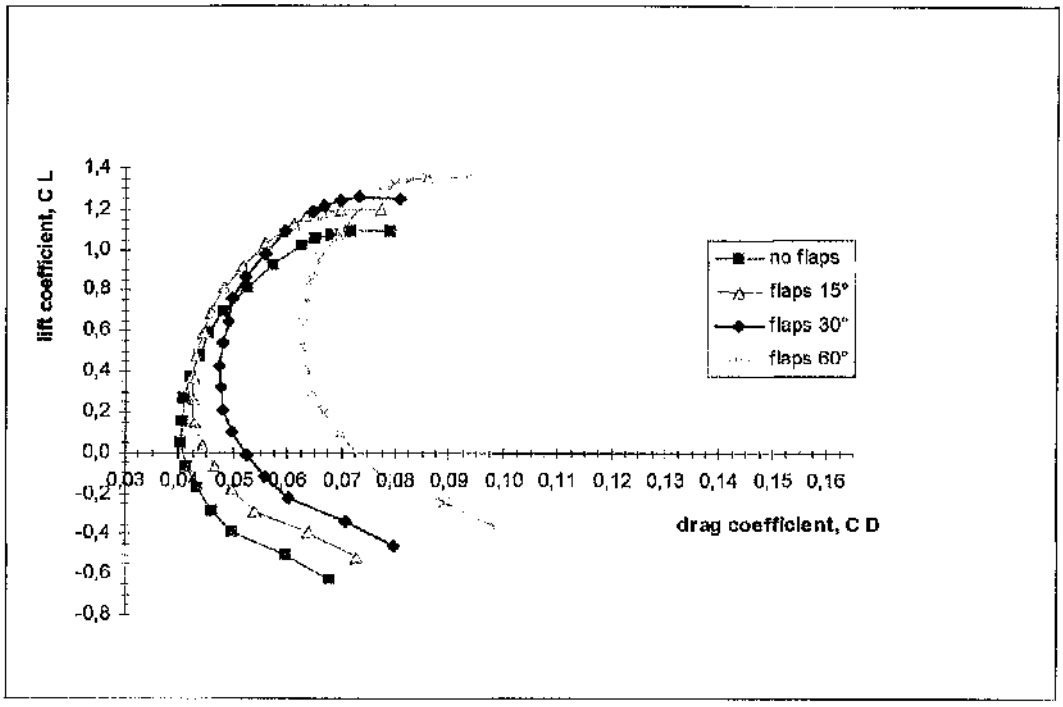

Fig.2.11 Condor Drag Polars.

3. CONDOR MODIFICATIONS DESIGN

3.1 FLIGHT CONTROL SYSTEM DESIGN STUDY

The starting point of the work was the existence of the Sojka airframe. As a first step towards the feasibility of the airframe as a flying laboratory, flight controls were designed.

Flight control system will consist of (Ref.20,21) :

- ailerons
- flaps
- elevator
- throttle
- dual rudder
- parachute recovery system
- autopilot

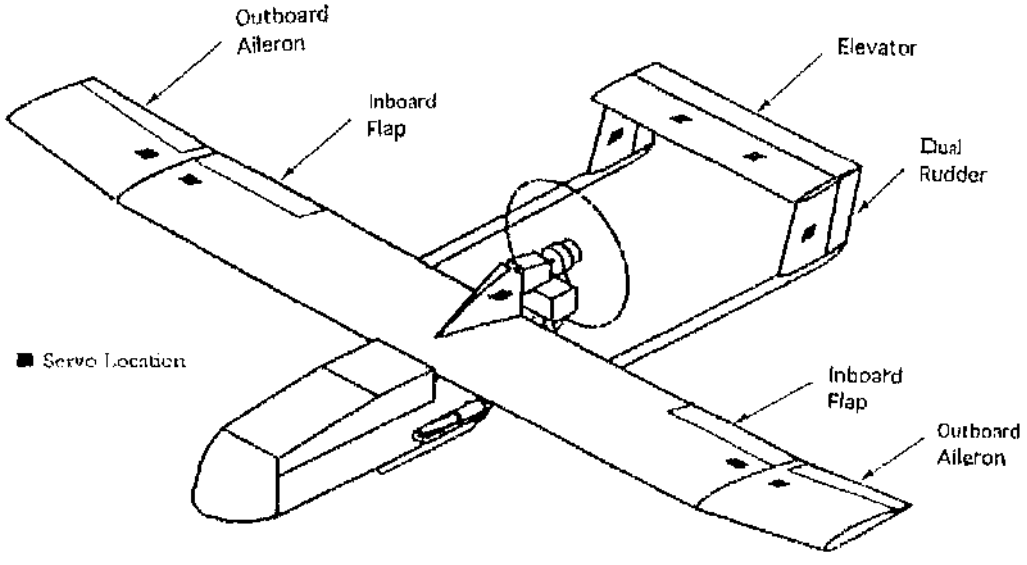

Fig. 3.1 Condor Control Surface and Servo Locations.

3.2 SERVOMOTORS

Location of the servomotors activating throttle and control surfaces is shown in Fig.3.1. Both wing and stabilizer have wells capable of receiving servos : this is a

heritage from the military version for the Czech Army. However, wing extensions are not part of the standard model, and have only pre-shaped wells : an attachment plate had to be fitted on either one to permit the servos to be fixed. Inspection doors on either fin might be used to install the dual rudder servos. In-house made brackets secure in place the wing and horizontal tail servos. Control surfaces are moved via a pushrod-horn assembly (Fig.3.2); servo-horns are secured to the servo by two small screws.

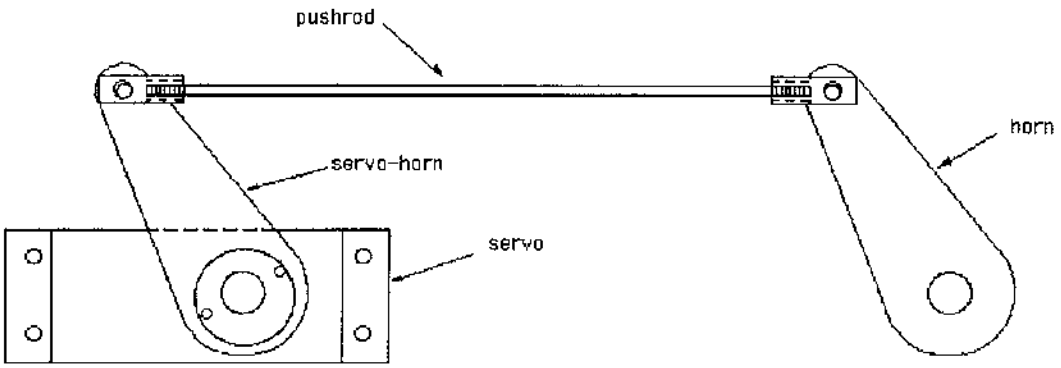

Fig. 3.2 Pushrod Mechanism.

Suitable servomotors are available in different maximum torque values. Control surfaces are moved by the torque generated by the servos, which in turn balance the control surface hingemoments. This is the reason why hingemoment calculations are fundamental in selecting the right servo for a given control surface. In fact, if a servo is underpowered, the surface will not move to full deflection; if it is too powerful, the installation will be heavy and there will be the risk of damaging the surface linkage mechanism. Servo specifications and brackets are listed in Appendix E. Hingemoments are calculated in Appendix F. The table below summarizes results of these calculations :

Control Device	Servo Model
Outboard Aileron (Flaperon)	ps3032
Inboard Aileron (Flap)	ps3032
Elevator	ps3801
Rudder	ps3032
Throttle	ps3001

3.3 RUDDER DESIGN

The current design is based on a wooden mock-up developed by A. Bram. Its dimensions has been retained in designing the rudder internal structure and hinges. The fin has a fibreglass spar at 56% of its chord, thus being the limiting factor for the rudder chord. Percentages in Fig.3.6 size the rudder section. Average clearance between fin spar and rudder should result in about 5 mm. To install the rudder a cut parallel to the fin spar has to be made, according to Fig.3.6, to remove part of the existing fin and make space for the rudder. The proposed rudder design (Fig.3.8) is described in detail in the following sections, and in two engineering drawings available at the Department. To date the rudder development has reached the stage of two moulds (Fig.3.9) which should be used for the final fibreglass rudder fabrication.

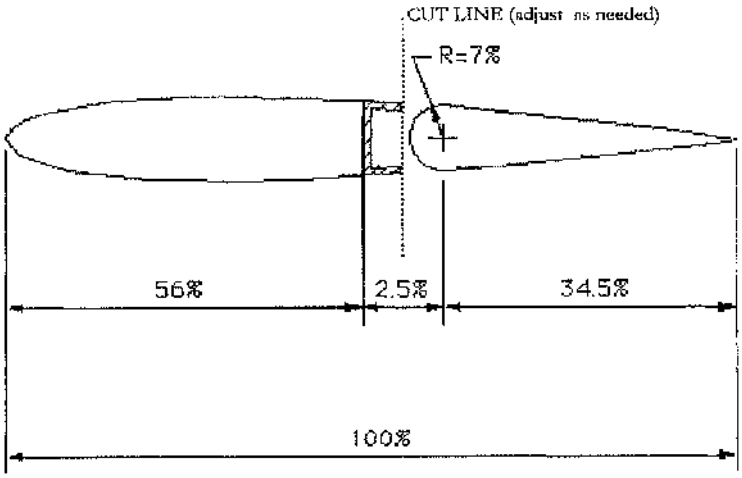

Fig.3.6 Schematic of Rudder Arrangement.

The rudder spar is conveniently located at 25% of its chord and is made from a 96 kg/ m^3 balsa block. It incorporates a rectangular section and is doubly tapered (Fig.3.7).

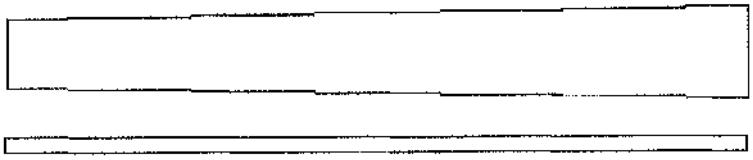

Fig. 3.7 Rudder Spar.

The rib location was dictated by the rudder servo-actuator position, which must be located at the existing inspection doors on the rudder (see 2.10). Since the servo-horn is fixed to the rib (a two piece item) and it has to be aligned with the servo-actuator, the rib location ensures that this requirement is met. Rib is made of balsa, the same type and thickness as used for the spar.

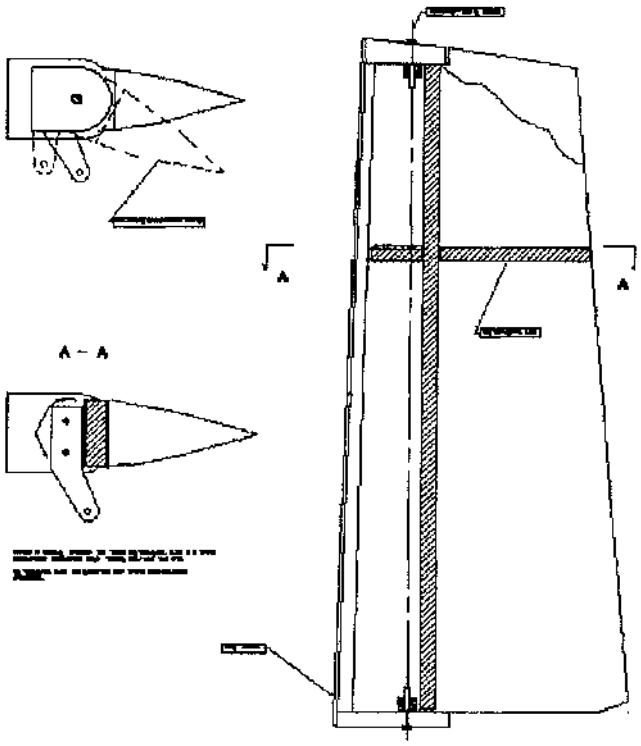

Fig. 3.8 Rudder Internal Structure.

Servo-horn shape is aft-bent in order to ensure a maximum rudder rotation of ± 25 degrees (Fig.3.10). This value seems quite reasonable if compared with values of other existing designs (Tab.3.1).

AIRCRAFT	ELEVATOR	AILERON	RUDDER
CESSNA 172	-28° +23°	-20° +15°	± 16°
CESSNA 210	-23° +17°	-25° +15°	± 24°
SKY ARROW	-24° +15°	-20° +15°	± 23°

Tab.3.1 - Control Surface Deflection Data (Ref.17, Ref.19).

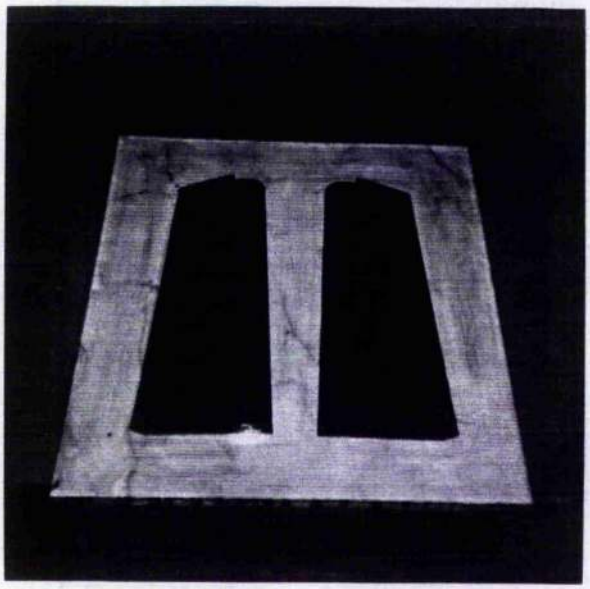

Fig. 3.9 Rudder Moulds.

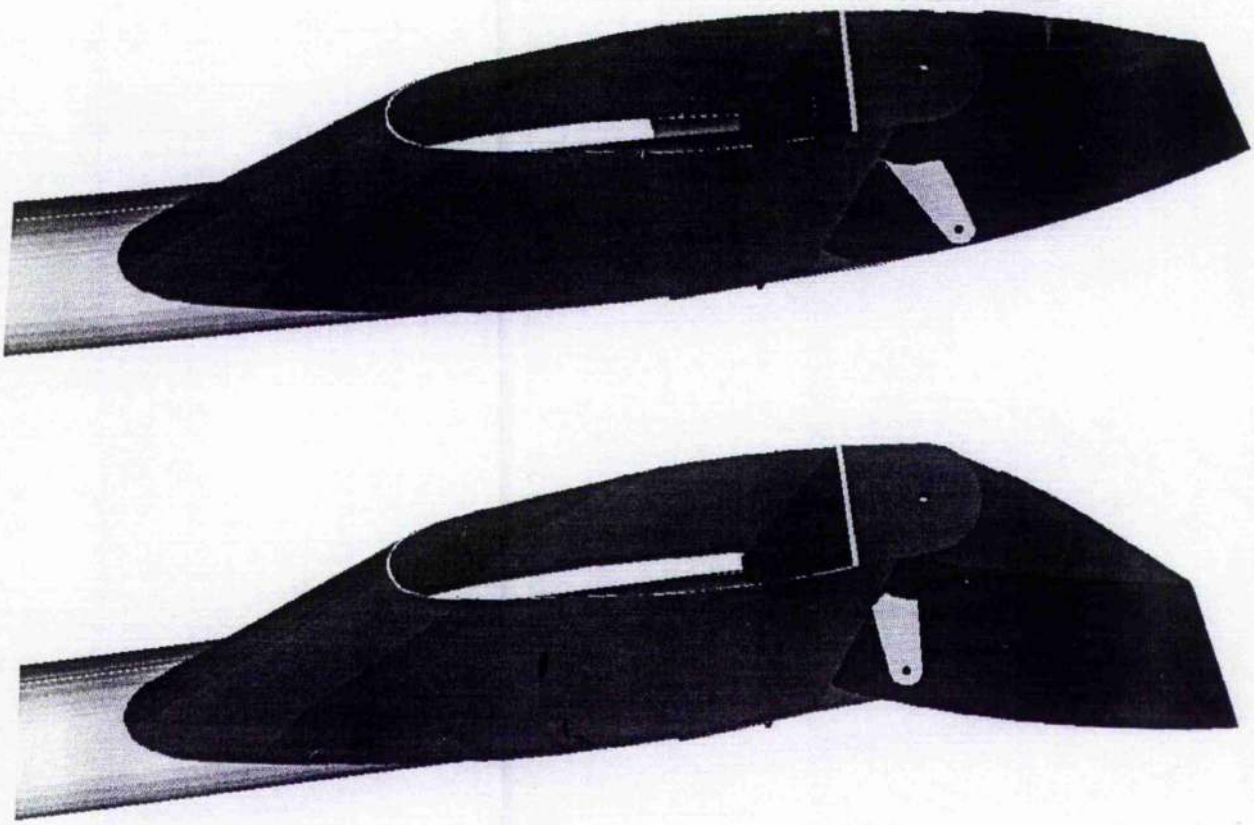

Fig. 3.10 Rudder Movement (CATIA Electronic Mock-up).

3.3.1 HINGES

The rudder shape, added to structural considerations, dictated the hinge design (Fig.3.11), made of fibreglass as the rudder skin. Each hinge has a rose bearing to facilitate both rudder removal and installation.

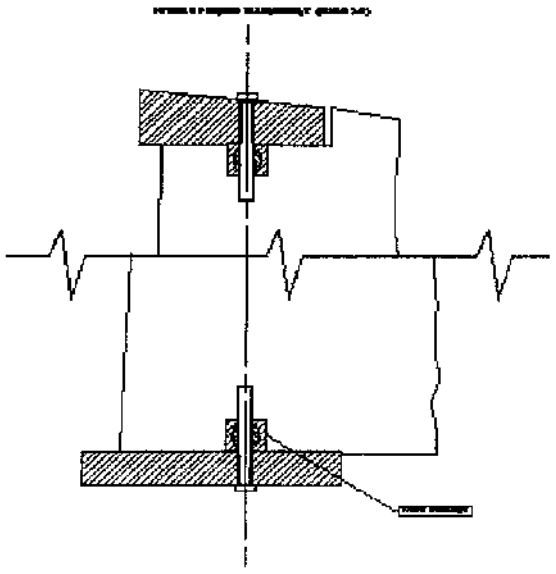

Fig.3.11 Rudder Hinge Design.

3.3.2 SERVO-ACTUATOR INSTALLATION

Servo must be placed inside existing inspection doors. Rudder movement is ensured by a pushrod-type mechanism (Fig.3.12) : the pushrod is connected to the rudder horn, which is glued and then fixed on its supporting rib.

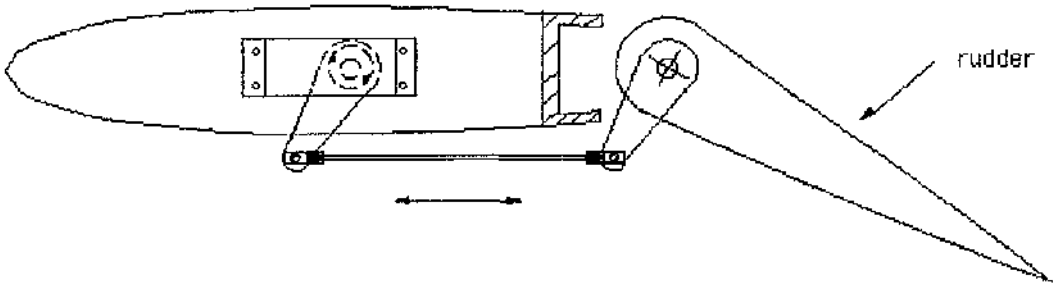

Fig. 3.12 Schematic of Rudder Servo Installation.

Rudder hingemoment calculations (see Appendix F) have shown that servo Futaba ps3032 is the one with appropriate power torque to be mounted.

3.3.3 ' SPAR STRUCTURAL ANALYSIS

Calculations follow guidelines in Ref.22. VLA 391(b) allows to use its Appendix B when mentioned. Condor main data are :

W = 145 kg $S = 4.124\ m^2$ $V_S = 21.6$ m/s

The stalling speed is calculated in Appendix F at the back of this thesis. From VLA 337(a) the limit manoeuvering factor is

$$n = 3.8$$

hence, according to VLA 335(a)(c)

$V_C = 2.4\sqrt{W/S} = 44.56$ m/s $V_A = V_S\sqrt{n} = 42.1$ m/s

3.3.3.1 LOADING

Ref.22 will be used to estimate manoeuvering and gust loads which may act on the rudder.

VLA 441(a)(1) - Manoeuvering loads

Appendix B of Ref.22 can be used to estimate limit average manoeuvering loads on the vertical tail surfaces. These loads will be multiplied by a safety factor of 1.5 according to VLA 303. VLA 423(a)(2) requires that maximum deflection is limited by the max servo torque (ps3032, 0.78 Nm). The computed hinge moments will be multiplied by 1.25 according to VLA 395(a)(b).

In this case $\beta = 0°$, that is the aircraft is at zero yaw. The program (see 3.2.2 in Appendix F) used for calculating rudder hinge moment, was modified to calculate the rudder deflection at V_A under the max torque of servo ps3032. The hinge moment coefficient was retained unchanged, as the Mach number correction would reduce it (moreover, Mach number correction is negligible at these low subsonic speeds).

According to App.B11(b)(1) we need rudder deflection δ_r at V_A with ps3032 torque. Computed hingemoments are listed in the table below

RUDDER DEFLECTION (deg)	HINGEMOMENT (Nm)
1	0.1000615
2	0.2001230
3	0.3001845
4	0.4002460
5	0.5003076
6	0.6003690
7	0.7004305
8	0.8004920
9	0.9005536
10	1.000615
11	1.100677
12	1.200738
13	1.300800
14	1.400861
15	1.500923
16	1.599797
17	1.697261
18	1.793093
19	1.889890
20	1.988616

We can see that servo max torque is reached at 8 degrees. Hence

$\delta_r = (8)1.25 = 10°$

As a result we use curve C of fig.B1 (Ref.22, App.B B11(b)(1), B11(a)(1)(i)) to estimate $\overline{w}$

$$W/S = 35.2 \text{ kg}/m^2 \Rightarrow K_{\overline{w}} = 59 \text{ kg}/m^2$$

$\Rightarrow \overline{w} = 59\frac{3.8}{4.4} = 51 \text{ kg}/m^2$ (limit average max loading)

$\overline{w}_U = 1.5(51) = 76.4 \text{ kg}/m^2$ (ultimate average manoeuvering loading)

Appendix B B11(a)(1)(v) requires to use distribution of fig.B7, reproduced in Fig.3.13 in order to calculate the limit average manoeuvering load on rudder $\overline{w}_{rud}$

area (1) $$\frac{c_r + r}{2} w = \overline{w}_{rud} c_r \Rightarrow \overline{w}_{rud} = w \frac{c_r + r}{2c_r}$$

total area $\frac{c+r}{2} w = \overline{w} c \Rightarrow w = \frac{2c}{c+r} \overline{w}$

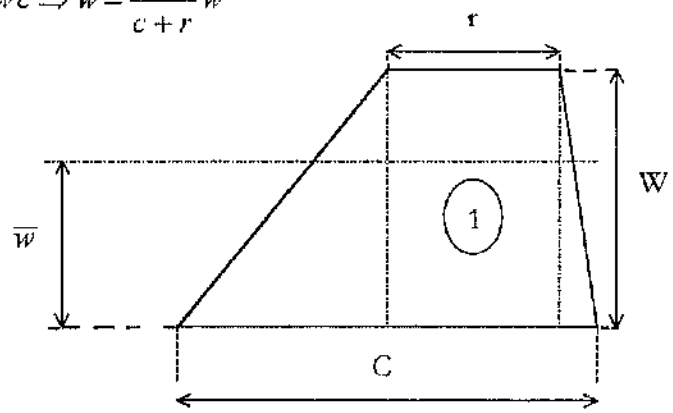

Fig.3.13 Fin Loading.

and making the substitution of w

$c_r = 157$ mm c = 380 mm r = 27 mm MAC = 160 mm

$\overline{w}_{rud} = \frac{c(c_r + r)}{c_r(c + r)} \overline{w} \Rightarrow \overline{w}_{rudU} = \frac{c(c_r + r)}{c_r(c + r)} \overline{w}_U = 83.6$ kg/ m^2

$q = MAC \cdot \overline{w}_{rudU} = 0.16(83.6) = 13.4$ kg/m = 131 N/m = 0.131 N/mm

VLA 441(a)(2) - Manoeuvering loads

In this case the yaw angle value is

$\beta = (1.3)(15) = 19.5°$

Appendix B B11(b)(2) requires to use curve C again to estimate $\overline{w}$, thus as before

$\overline{w}_U = 1.5(51) = 76.4$ kg/ m^2 (ultimate average manoeuvering loading)

but we must use distribution of fig.B6, which says at note (b) that P = 20 % of net fin load

$P = 0.20\overline{w}_U = (0.20)(76.4) = 15.28$ kg/ $m^2 \Rightarrow q = MAC \cdot P = 2.4$ kg/m = 24 N/m = 0.024 N/mm

VLA 441(a)(3) - Manoeuvering loads

This case implies $\beta = 15°$ and $\delta_r = 0°$. Distribution in fig.B8 (Appendix B) acting on the rudder is less than in case VLA 441(a)(1) and therefore this case is disregarded.

VLA 443 - Gust loads

VLA 443(c) allows to use fig.B5 (Appendix B). It is

$V_C = 44.56$ m/s = 86.6 knots $\qquad S_V = (2)(0.172) = 0.34\ m^2$

$W/S_V = 145/0.34 = 426$ kg/ $m^2 \Rightarrow \overline{w} = 99$ kg/ m^2

The curve is for an aspect ratio AR=3, thus a correction factor is applied by taking into account the Condor fin aspect ratio (AR=1.2, see Appendix C of this thesis)

$$\overline{w} = (99)\frac{5(1.2)}{3(1.2+2)} = 61.9 \text{ kg/ } m^2 \Rightarrow \overline{w}_U = (1.5)(61.9) = 92.9 \text{ kg/ } m^2$$

Distribution in fig.B8 is used for computing the total area

total area $\qquad (4w + w)\frac{c}{4}\cdot\frac{1}{2} + wc\frac{3}{4}\cdot\frac{1}{2} = \overline{w}c \Rightarrow w = \overline{w}$

while for computing the area regarding the rudder we must make a (conservative) approximation (Fig.3.14)

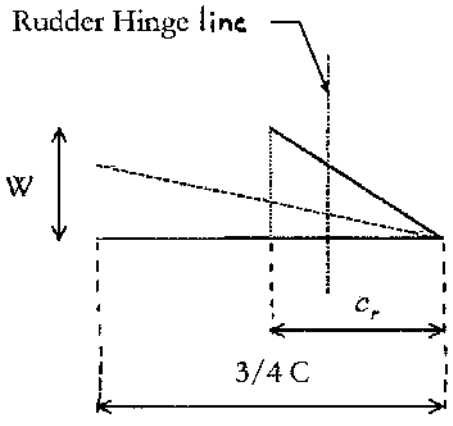

Fig. 3.14

area (1) $\qquad \overline{w}_{rud} c_r = w\frac{c_r}{2} \Rightarrow \overline{w}_{rud} = \frac{w}{2}$

and making the substitution of w :

$$\overline{w}_{rud} = \frac{\overline{w}}{2} \Rightarrow \overline{w}_{rudU} = \frac{\overline{w}_U}{2} = 46.45 \text{ kg/ } m^2$$

$\Rightarrow q = MAC \cdot \overline{w}_{rudU} = 7.43$ kg/m = 0.073 N/mm

3.3.3.2 ANALYSIS

The most stressful case is VLA 441(a)(1) using distribution in fig.B7 of Appendix B, which gives the following uniform distributed load :

$$q = 0.131 \text{ N/mm}$$

This is the average fin loading per unit length, because it was calculated using the fin MAC (see 3.3.3.1). Therefore we make certainly a conservative assumption by considering this load acting on the rudder only; in other words, on the rudder spar it will act a load which is higher than the effective one, as the fin loading is transferred to both the stabilizer spar and the rudder spar in reality.

Spar dimensions are shown in Fig.3.15. The spar is made of light balsa whose mechanical properties are listed in Tab.3.2.

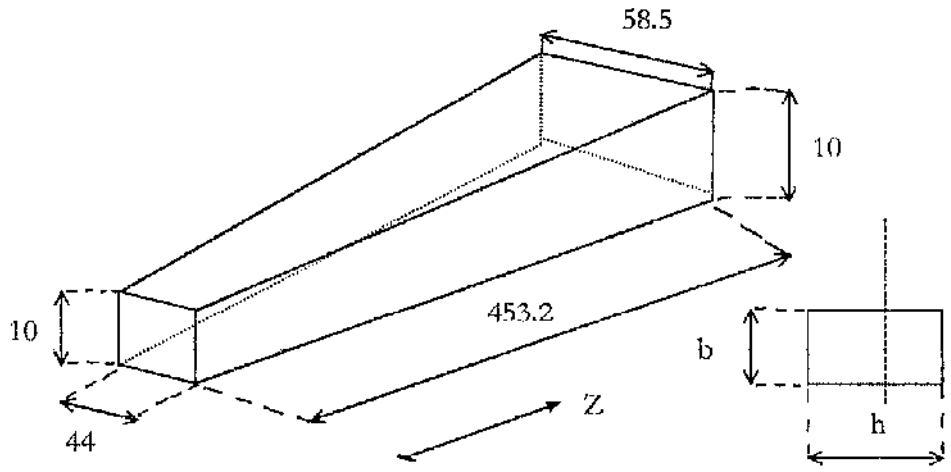

Fig.3.15 Rudder Spar Dimensions.

MATERIAL : BALSA 96 kg/ m^3	
G = 106 N/ mm^2	E = 2100 N/ mm^2
Fcu = 3.2 N/ mm^2	Ftu = 8.1 N/ mm^2
Fsu = 1.2 N/ mm^2	

Tab.3.2 Balsa Mechanical Properties (Ref.59).

Balsa grain direction must be at 45 degrees in reference to the rudder spanwise direction : this ensures that both horizontal and vertical bending shear stresses are absorbed. The spar will be bonded to the composite rudder skin, hence loads will be transferred in and out through the skin.

The reactangular-section spar is doubly tapered, hence thickness t will vary linearly, whilst cross section area A and moment of inertia I will vary non-linearly :

$b(z) = b_1 + mz$ $\qquad$ $A(z) = b(z)h(z)$

$h(z) = h_1 + m'z$ $\qquad$ $I(z) = \dfrac{b(z)h^3(z)}{12}$

In order to simplify calculations, if we make the non-conservative assumption that cross section area A and moment of inertia I vary linearly, we have :

$$I = \frac{bh^3}{12} \Rightarrow I(0) = \frac{10(44)^3}{12} = 7.1 \cdot 10^4 \ mm^4$$

$$I(L) = \frac{10(58.5)^3}{12} = 1.67 \cdot 10^5 \ mm^4$$

$$I(z) = I(0) + \frac{I(L) - I(0)}{L} z = 7.1 \cdot 10^4 + (211.4)z$$

$t(0) = 44$ mm $\qquad$ $t(L) = 58.5$ mm $\Rightarrow t(z) = t(0) + \dfrac{t(L) - t(0)}{L} z = 44 + (0.032)z$

$A(0) = 440 \ mm^4$ $\qquad$ $A(L) = 585 \ mm^4$

$$A(z) = A(0) + \frac{A(L) - A(0)}{L} z = 440 + (0.32)z$$

The spar can be regarded as a simply supported beam (Fig.3.16). In this case (Ref.23) is :

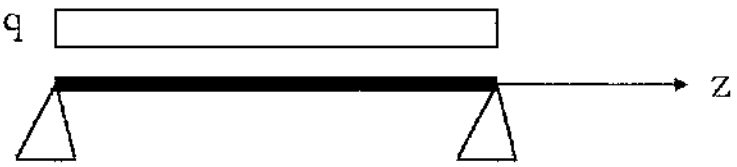

Fig.3.16 Simply Supported Beam.

$T(z) = -\dfrac{q}{2}(L - 2z)$ ---) Shear $\qquad$ $M(z) = -\dfrac{q}{2}(z^2 - Lz)$ ---) Bending

hence bending and shear stress are, respectively

$$\sigma(z) = \frac{M(z)}{I(z)} \cdot \frac{t(z)}{2} \qquad \tau(z) = \frac{T(z)}{A(z)}$$

Results of these calculations are shown in the following diagrams, where stresses are largely below the maximum allowable ones. If we simply calculate the maximum bending stress in the worst case scenario, that is maximum M(z)=M(z=L/2), minimum I(z)=I(0), and maximum t(z)=58.5 mm, we get :

$$\sigma = \frac{3360}{7.1 \cdot 10^4} 29 = 1.4 N/mm^2$$

which is still less than half the maximum allowable compression stress. This scenario will never take place, because when M(z) is maximum, I(z) cannot be minimum and t(z) cannot be maximum, hence maximum bending stress will be somewhat lower than above calculated. This and the conservative assumption made at the outset enables us to state that the rudder spar dimensions are adequate to cater for the expected loads.

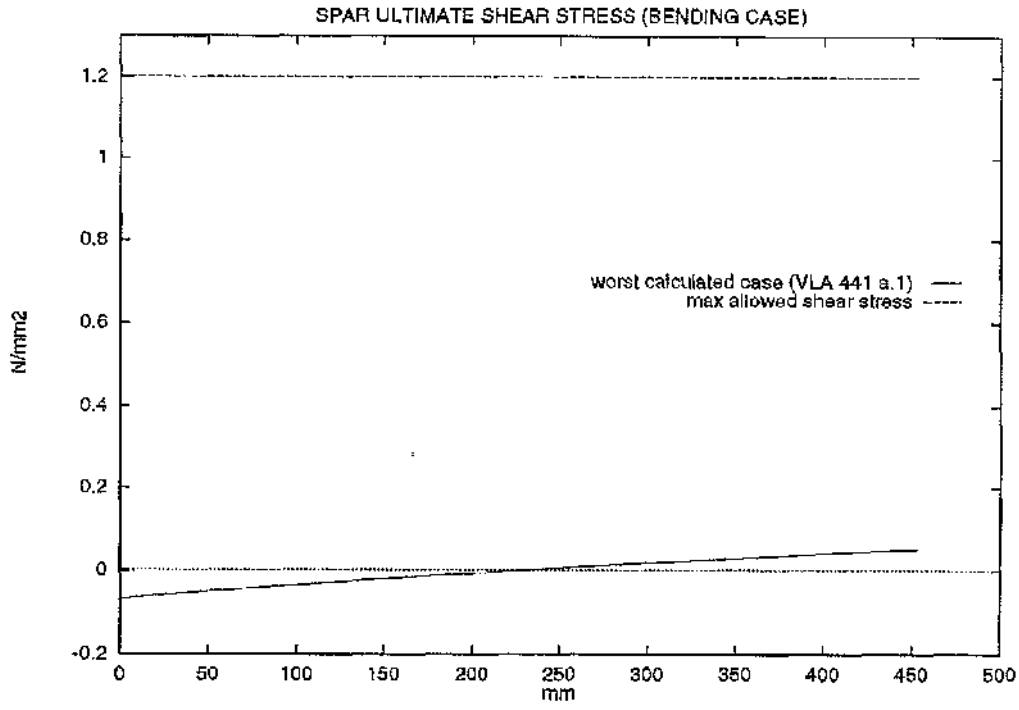

Rudder Spar Shear Stress Along the Beam Z-axis.

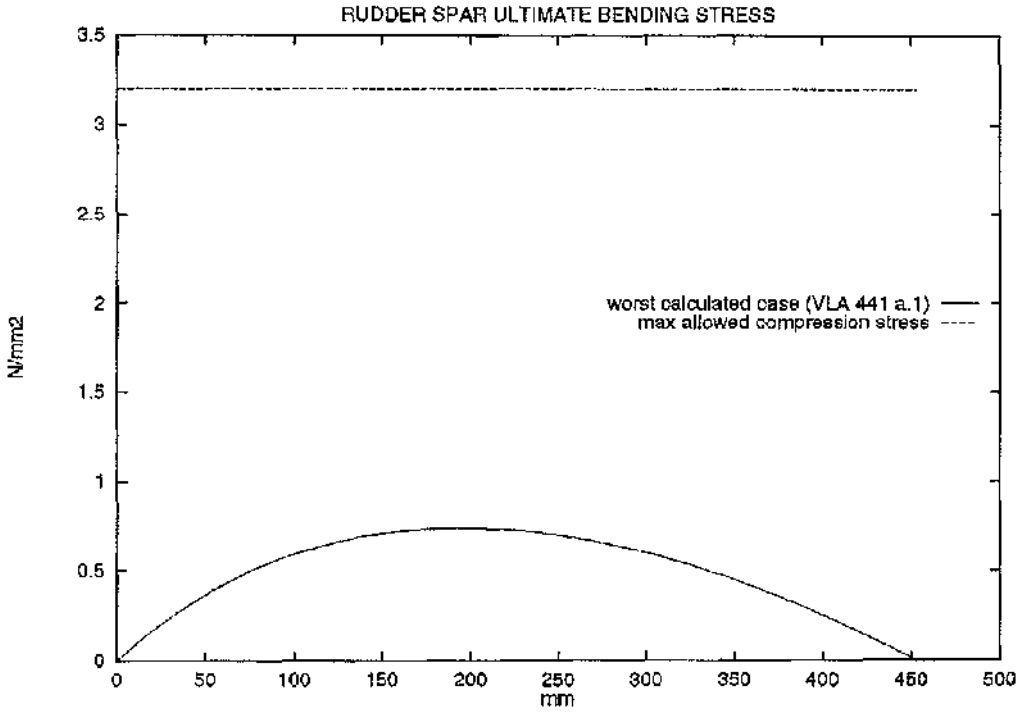

Rudder Spar Bending Stress Along the Beam Z-axis.

3.4 LANDING GEAR ARRANGEMENT

The landing gear design analyzed in the following pages meets the layout requirements of Ref.24. In particular, the CG pitch angle was set at 11.5° (Fig.3.17).

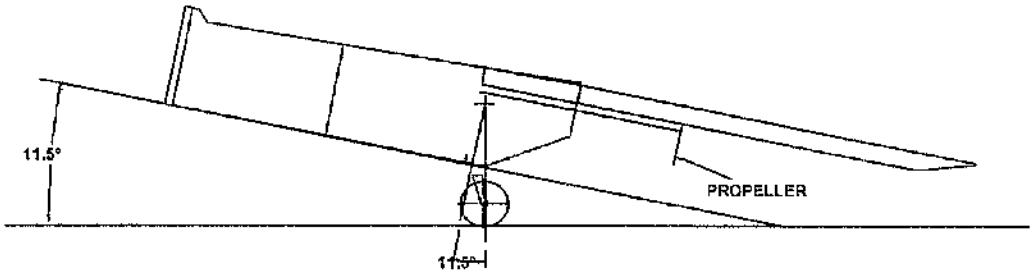

Fig.3.17 CG Pitch Angle Setting.

The purpose of this clearance angle is to prevent the CG to pitch aft of the main gear when an aircraft lands at its maximum lift coefficient with flaps up. This angle of attack is about 11° for the Sojka wing (Ref.7); the actual value is likely to be lower as the Condor has an extended wing. Moreover, being appropriate the ground clearance for the propeller (Fig.3.17), this angle value is certainly adequate as it is set at 11.5°. Front gear leg design was not performed.

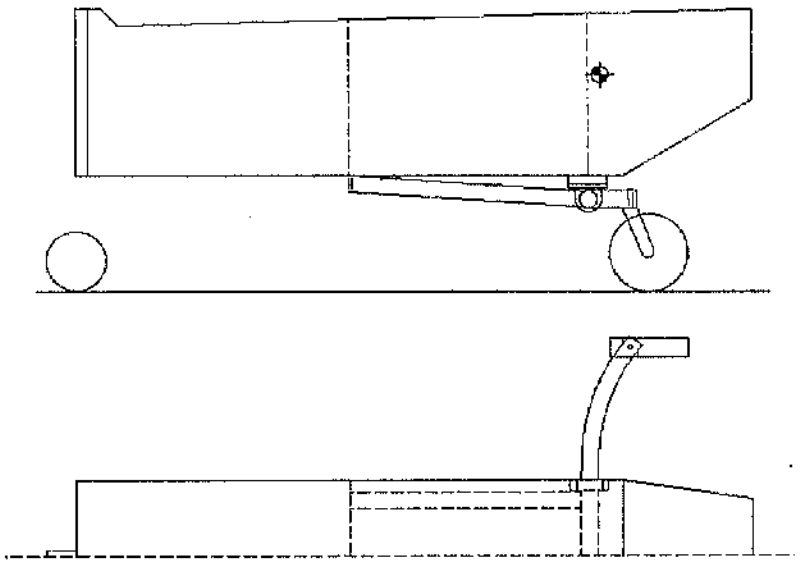

Fig.3.18 Main Landing Gear Assembly.

The proposed main gear design (Fig.3.18) consists of a torque tube supporting the wheels and connected to the aft fuselage bulkhead via the former skid attachments. Two drag stay beams are symmetrically welded to the torque tube and connected to the forward fuselage bulkhead via hinges. Invacare assembly part no. 6000 783 (fork plus wheel) has been incorporated in the design, which is illustrated in detail by one engineering drawing available at the Department. In the following the main gear is analyzed structurally. Since this design is a compromise involving several interacting factors, calculations are shown in detail for a starting configuration which was used to set up an Excel worksheet; the starting configuration was then manipulated and modified several times to optimize the design. Final design values are shown by presenting the Excel worksheet results.

3.4.4 TORQUE TUBE SIZING

The chosen material for designing the torque tube is alloy steel AISI 4340 (Ref.29), heat-treated to obtain the following ultimate tensile stress and ultimate shear stress, respectively

$$Ftu = 1241\ N/mm^2 \qquad Fsu = 751\ N/mm^2$$

The torque tube is 1.09 m long to meet the positioning requirements of Ref.22 (see also 3.4) and it has to be heat-treated at the welded joints with the two drag-stays (see 3.4); density of the chosen alloy steel is 7806 kg/m^3, hence for the following calculations we will be using

$$L = 1.09\ m \qquad \rho = 7806\ Kg/m^3 \qquad G = 75840\ N/mm^2$$

The tube will be subject to bending and torsion. A hollow tube seems to be the best solution, as a ring section deals effciently with torsion and its moment of inertia is the same about any axis ring-section plane, thus simplifying bending calculations. Bending is more critical than torsion so we consider bending first. Since the torque tube has a ring as cross section, we do not need to worry upon bending about the x or z-axis; we only need to consider the bending in maximum value, which is, from section 3.4.3 of Appendix G, pertinent to the "nose wheel clear" case

$$M_X = 737\ Nm$$

Let us take as a first try

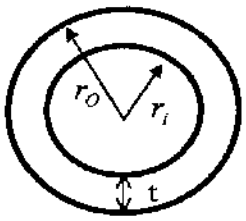

t = 1 mm
$r_O = 15$ mm $\qquad r_i = 14$ mm

it is then

$$I = \frac{\pi}{4}\left(r_O^4 - r_i^4\right) = 9588.9 mm^4 \Rightarrow \sigma = \frac{M_X}{I} y = \frac{737 \cdot 10^3}{9588.9} 15 = 1152\ N/mm^2 < Ftu$$

Since this size meets the bending requirement, we can now consider torsion, which is maximum in value again in the "nose wheel clear" case (see 3.4.3 of Appendix G)

$$T = M_y = 547 \text{ Nm}$$

hence (Ref.23)

$$J = \frac{\pi}{32}\left(d_O^4 - d_I^4\right) = 19178 mm^4 \Rightarrow \tau = \frac{T}{J} r_O = 428 \text{ N/mm}^2 < \text{Fsu}$$

Therefore these dimensions could be used for the torque tube. Total weight would be

$$Vol = \pi\left(r_O^2 - r_I^2\right)L = \pi\left(0.015^2 - 0.014^2\right)(1.09) = 9.93 \cdot 10^{-5} \ m^3$$

$$\Rightarrow mass = \rho \cdot Vol = 0.775 \text{ kg}$$

Rotation at the interface fuselage/leg is (Ref.23)

$$\theta = \frac{TL}{GJ} = 0.15 \text{ rad} = 8.6 \text{ deg}$$

These formulae were implemented in an Excel worksheet and many iterations were performed to optimize the torque tube dimensions. Eventually was considered a different alloy steel (AISI 321, Ref.29) with lower mechanical properties obtainable without heat-treatment , which was impossible to do in-house. Others parameters that varied are tube thickness and diameter; in fact, for a given ultimate stress, two solutions are possible :

1. larger diameter, smaller thickness
2. smaller diameter, larger thickness

Solution number 1 is preferable, because it is lighter, but space restrictions dictate a limit to the tube diameter. Final design values are shown in Tab.3.6.

MATERIAL :	ALLOY STEEL			SECTION GEOMETRY		Tube Lenght (mm)=	950
SPECIFICATION :	BS EN58B	(AISI 321)		TYPE :	RING		
MECHANICAL PROPERTIES				ro (mm) =	13.75		
	kpsi	N/mm2		ri (mm) =	11.25		
Ftu =	75	517.107		t (mm) =	2.5		
Fsu =	40	275.7904		Area (m2) =	0.000196		
E =	29000	199948.0					
G =	11000	75842.36					
	lb/in3	kg/m3		MAX BENDING MOMENT (Nm) =	587.4400		
Density =	0.283	7833.411		I (mm4)	f (N/mm2)		
				15493.20	521.3447		
MAX TORSION (Nm) =		466.3473					
J (mm4)	tau	theta (deg)			Volume (m3) =	0.000186	
30986.41	206.9383	4.547880			Mass (kg) =	1.461182	

Tab.3.6 Torque tube sizing.

3.4.4 DRAG-STAY SIZING

From a structural point of view the drag stay can be regarded as a beam with a fixed support (the weldment to the torque tube) under bending produced by P_2, that is the forward hinge reaction. The maximum reaction value comes from the "nose wheel clear" (see 3.4.2 of Appendix G) that is

$P_2 = 905\,\text{N}$

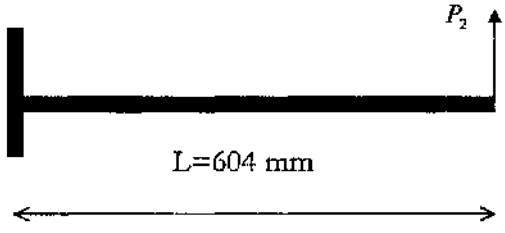

thus giving at the fixed support the following maximum bending moment

$M = P_2 \cdot L = 546620\,\text{Nmm}$

Since the drag stay is subject to bending only, an I-section should be more efficient than a ring-shaped one. Let us consider an arbitrary I-section

a = 38 mm
b = 17 mm
t = 1.5 mm
$b_1 = a - 2t = 35$ mm

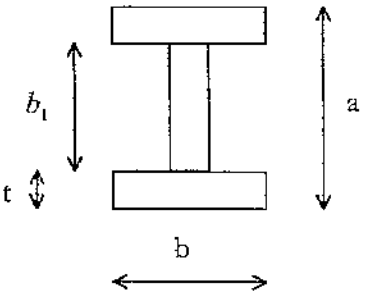

$$A = 2bt + b_1 t = 104\ mm^2 \Rightarrow I_{WW} = bt\left(a - \frac{t}{2}\right)^2 + b_1\left(t + \frac{b_1}{2}\right)^2 + bt^3 = 54393\ mm^4$$

$$I = I_{XX} = I_{WW} - A\left(t + \frac{b_1}{2}\right)^2 = 17029\ mm^4 \Rightarrow \sigma = \frac{M}{I} y = 609.9\ \mathrm{N/mm^2} < \mathrm{Ftu}$$

$$Vol = AL = 6.28 \cdot 10^{-5}\ m^3 \Rightarrow mass = \rho \cdot Vol = 0.49\ \mathrm{kg}$$

In the Excel worksheet (Tab.3.7) a ring-section has also been tried to highlight the superiority of the lighter I-section solution which was adopted.

MATERIAL :	ALLOY STEEL		SECTION1 GEOMETRY			SECTION2 GEOMETRY		
SPECIFICATION :	BS EN58B	(AISI 321)	TYPE :	RING		TYPE :	"I"	
MECHANICAL PROPERTIES			ro (mm) =	15		a (mm) =	31.5	
	kpsi	N/mm2	ri (mm) =	13.5		b (mm) =	16.5	
Ftu =	75	517.107	t (mm) =	1.5		t (mm) =	2	
Fsu =	40	275.7904	Area (m2) =	0.000134		b1 (mm) =	27.5	
E =	29000	199948.0				Area (m2) =	0.000121	
G =	11000	75842.36						
	lb/in3	kg/m3						
Density =	0,283	7833.411						
			I (mm4)	σ (N/mm2)		Iww (mm4)	I (mm4)	σ (N/mm2)
			13673.73	511.5801		44473.68	14458.12	508.0168
MAX BENDING MOMENT (Nm) =		466.3473						
Beam Lenght (mm) =	604		Volume (m3) =	8.11191		Volume (m3) =	0.000073	
			Mass (kg) =	0.635439		Mass (kg) =	0.572497	

Tab.3.7 Drag-stay Sizing.

3.4.6 BOLT ANALYSIS

Following calculations will use final design ultimate loads (Tab.3.3). The most stressful conditions are those of "nose wheel clear" case and VLA 485 side loads. Existing bolts of Invacare assembly part. no.6000783 (see 5.8) are to be checked structurally. They are the wheel axle bolt and the bolt connecting the torque tube with the Invacare assembly fork (Fig.3.26). Bolts are made of alloy steel BS EN8M, whose ultimate tensile and shear stress are respectively

$Ftu = 695\ N/mm^2$ $Fsu = 486\ N/mm^2$

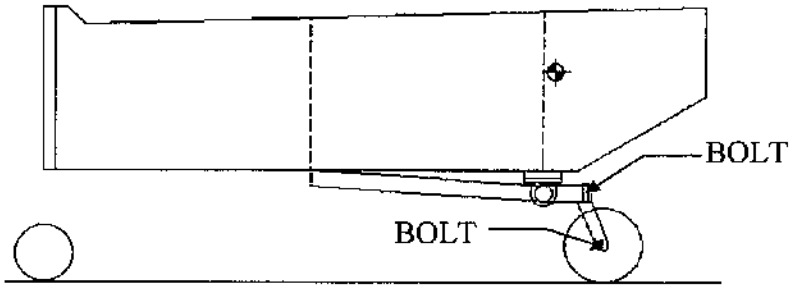

Fig.3.26 Bolt Location of Present Analysis.

AXLE BOLT

VLA 479 (a)(2)(ii) - Nose wheel clear (Fig.3.22)

The main wheel withstands V_r and D_r loads, which in turn act on the axle bolt (Fig.3.27). Since the bolt section is circular we shall consider bending from V_r only, being $V_r > D_r$. The bolt can be regarded as a simply supported beam. Bolt diameter is 8 mm. Shear stress calculation uses a fitting factor of 1.2 (Ref.24)

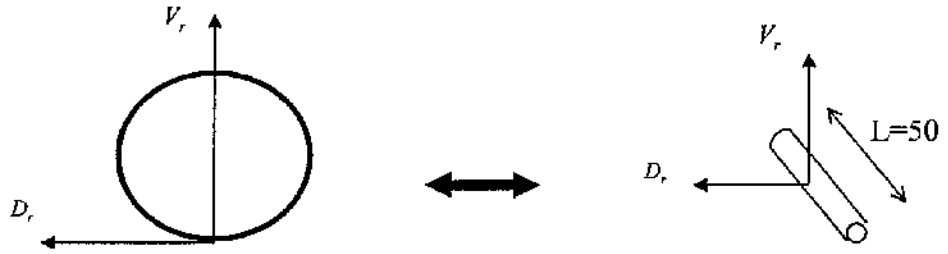

Fig.3.27 Axle Bolt Loads.

$$M = \frac{LV_r}{4} = 26700 \text{ Nmm} \qquad I = \frac{\pi R^4}{4} = 201 \ mm^4$$

$$\sigma = \frac{M}{I} R = 531 \text{ N/}mm^2 < \text{Ftu} \quad \tau = \frac{V_r}{2\pi R^2} 1.2 = 25.5 \text{ N/}mm^2 < \text{Fsu}$$

VLA 485 - Side loads (Fig.3.25)

Under side loads the main wheel, and in turn its axle bolt, may withstand S'_r or S''_r, but only S'_r needs to be considered, being $S'_r > S''_r$. The bolt can be regarded as a simply supported beam again and it can be seen that is subject to an axial load only. As a conclusion the standard axle bolt can be retained.

BOLT AT THE INTERFACE FORK/TORQUE TUBE

VLA 479 (a)(2)(ii) - Nose wheel clear (Fig.3.22)

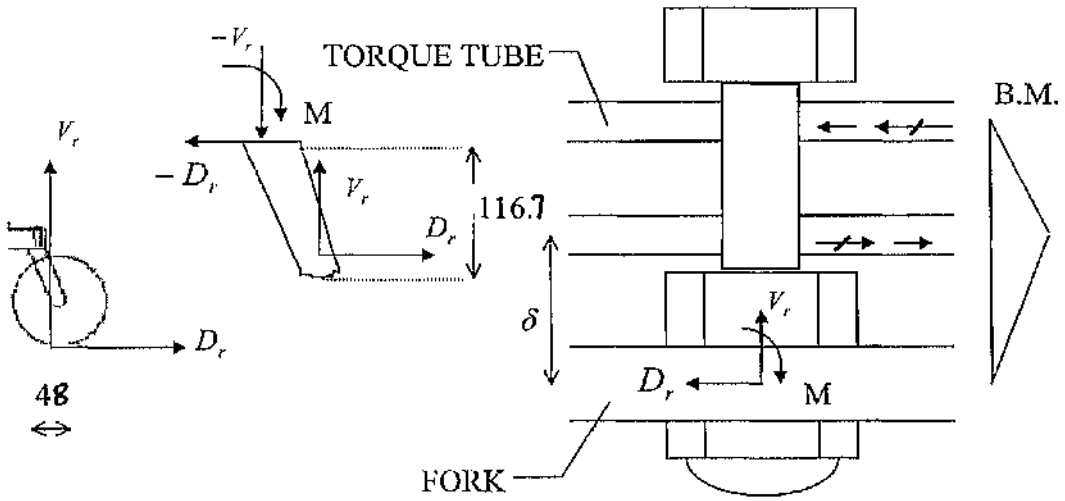

Fig.3.28 Torque Tube Bolt Loads.

The main wheel withstands V_r and D_r loads, which in turn cause the bolt to be subject to a bending stress (Fig.3.28). Since the distance "δ" is very small it can be disregarded, hence maximum bending moment acting on the bolt station shown in figure is assumed as the following

$$M = V_r(48) + D_r(116.7) = 185618 \text{ Nmm}$$

hence maximum bending stress can be calculated ($\Phi = 11$ mm, bolt diameter)

$$I = \frac{\pi R^4}{4} = 719 \ mm^4 \qquad \sigma = \frac{M}{I} R = 1420 \ \text{N}/mm^2 >> \text{Ftu}$$

The standard bolt diameter must be enlarged.

$$\Phi = 14 \text{ mm} \qquad I = \frac{\pi(7)^4}{4} = 1886 \ mm^4$$

$$\sigma = \frac{185618}{1886} 7 = 689 \ \text{N}/mm^2 < \text{Ftu}$$

VLA 485 - Side loads

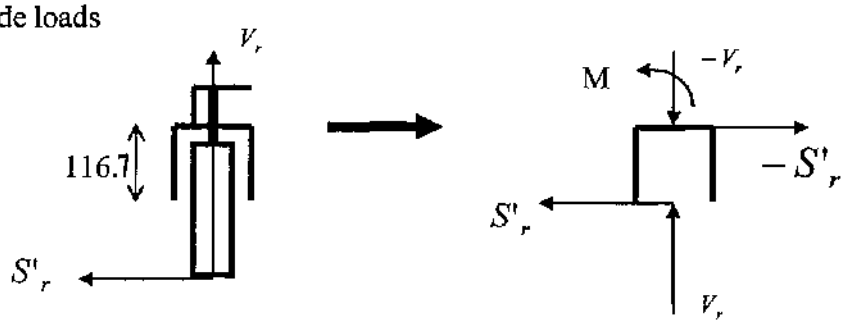

Fig.3.29 Torque Tube Bolt Side Loads.

Under side loads the main wheel, and in turn the interface bolt, may withstand S'_r or S''_r, but only S'_r needs to be considered, being $S'_r > S''_r$. On the bolt will act the following moment (Fig.3.29)

$$M = 116.7 S'_r = 124402 \text{ Nmm}$$

This bending moment is lower than the one considered in the previous case. Since shear stress is negligible, we can conclude that a 14 mm diameter bolt must replace the standard one.

3.4.7 SELECTION OF WHEEL AND TYRE

A tyre is designed to operate at a so-called maximum allowable static load, which must not be exceeded. Unfortunately minimum size tyres suitable for the RPV and available on the market had an unknown maximum allowable static load, but similar models have been used on ultralight machines for years successfully. Therefore choice of a tyre was made on the basis of other remaining criteria as follows :

1. Cost
2. Weight
3. Minimum size

It should be noted that a solid tyre was not considered from the outset, because current landing gear design has no shock absorber hence a tyre and tube is required to participate significantly in the process of shock absorption following a touchdown. If the landing gear should result in being too stiff, then rubber shock absorbers might be added under the fuselage attachments; in this case the main gear reaction load would not be transferred directly into the rubber shock absorbers because the reaction load would not be "in line" with the shock absorbers.

Selected tyres (see Appendix C) are relatively cheap and light, compared to other designs, and are in a small size suitable for use on the RPV. In addition, they were readily available at a local shop. Once a tyre is selected, it usually comes with its proper wheel.

3.5 PARACHUTE RECOVERY SYSTEM STUDY

Original Sojka recovery system is shown in Fig.3.30. It consists of a parachute rocket-launched module and an airbag. The Condor will not use an airbag, since it will be fitted with an undercarriage (see 3.4) but it still needs a parachute module (see 5.6). The main reason which precludes the use of the former Sojka parachute module is its deployment philosophy; in fact, the Sojka chute must be packed into the parachute box by expert personnel, and the rocket must be filled with propellant. This is allright for a military force, but it is not affordable by an academic department, which has no such expert staff and no permission to handle inflammable and hazardous materials such propellants. Moreover, this deployment philosophy certainly fits well the former Sojka, which is not equipped with a landing gear and must use the recovery system every flight to land safely, thus needing a quickly reusable parachute module.

Conversely, the Condor recovery system would be a safety measure required by the CAA (see 5.6) to be deployed in the event an in-flight emergency should occur. It has then been decided to purchase a commercially available parachute softpack, which could be stuffed into the existing parachute box. Alternatively, a pressure packed canopy, which provides a longer service life, could replace the existing parachute box, but in this case the fuselage might need to be modified. A commercial off-the-shelf packed canopy would solve the problems mentioned earlier, as no expert personnel would be required and the ballistic device would be ready to be fired.

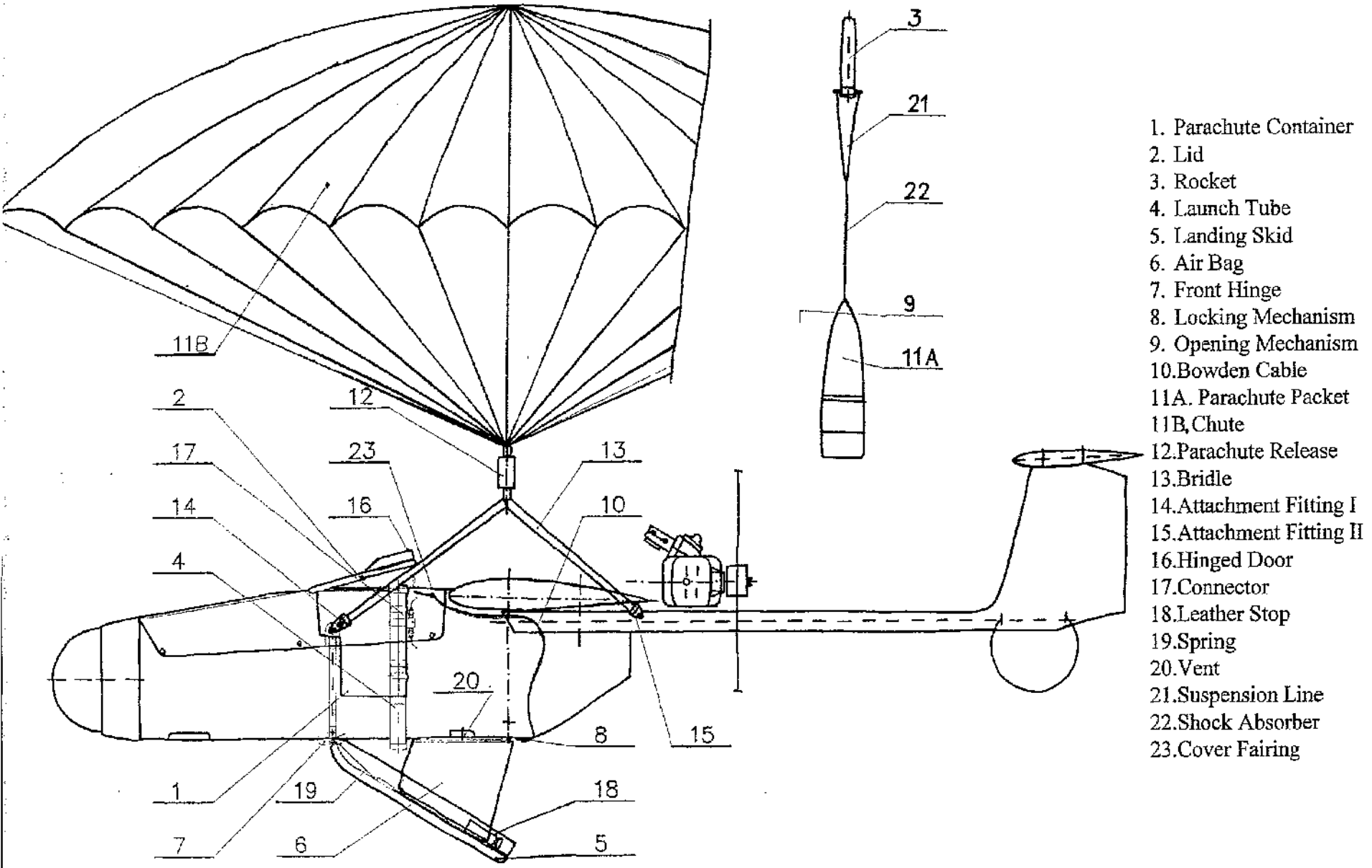

1. Parachute Container
2. Lid
3. Rocket
4. Launch Tube
5. Landing Skid
6. Air Bag
7. Front Hinge
8. Locking Mechanism
9. Opening Mechanism
10. Bowden Cable
11A. Parachute Packet
11B, Chute
12. Parachute Release
13. Bridle
14. Attachment Fitting I
15. Attachment Fitting II
16. Hinged Door
17. Connector
18. Leather Stop
19. Spring
20. Vent
21. Suspension Line
22. Shock Absorber
23. Cover Fairing

Fig.3.30 Sojka Parachute Recovery System.

3.5.1 MATCHING FORMER SOJKA CHUTE

In order to achieve a good integration of the commercial parachute recovery system with the existing airframe and fittings, it is of paramount importance to select a chute as much similar to the former one as possible in terms of installation, weight, size, and performance. This also makes it reasonable to assume chute loading will not be bigger.

The purchased chute must use the existing four airframe connections : two in the fuselage, the other two at the engine mount (see 2.5). The use of former connections ensures no airframe overloading and descent in a flight-level attitude, which is best. The two points load in the fuselage are above and in front of the RPV's center of gravity; this means the nose will pitch up sharply on deployment, thus reducing opening loads to both parachute and airframe.

Size of the canopy is basically determined by two factors :

- gross weight
- maximum speed

Gross weight is usually the maximum take-off weight (145 kg for the Condor) and determines the size of the canopy to get a certain descent rate. Maximum speed assures the canopy seams are strong enough to accept the opening loads when flight speeds are faster. A larger canopy provides slower descent rates and reduces the opening force transmitted back to the airframe, but since it is heavier may adversely affect aircraft center of gravity and may not fit into available fuselage space. The table below shows characteristics of both former Sojka and proposed parachute recovery system (it costs 1800 USD). The author researched the market and found model BRS-750 a suitable candidate (BRS also offers a "custom installation guide"). The chosen model has a max deployment speed of 160 km/h which is the Condor estimated max cruising speed, and a descent rate of 7 m/s at 340 kg. Condor lower max weight of 145 kg at take-off should result in a significant lower descent rate close to Sojka's value of 4.5 m/s. In addition, the total weight of the system is almost identical, while canopy square area is smaller.

SOJKA		BRS-750	
SYSTEM		SYSTEM	
Max Capacity	145 kg	Max Capacity	340 kg
Max Deployment	180 km/h	Max Deployment	160 km/h
Overall Weight	8.3 kg	Overall Weight	8.5 kg
Test Descent rate	4.5 m/s	Test Descent Rate	7 m/s
Deployment Height	100 - 2000 m		
Operating Temperature	-25 +40 °C		
CANOPY		CANOPY	
Type	Circular	Type	Circular
Square Area	90 sq m	Square Area	55 sq m
Softpack Size	16 lt	Softpack Size	9 lt
Texture Density	100 g/sq m		
		Softpack Repack	2 years if internal
BALLISTIC DEVICE		BALLISTIC DEVICE	
Type	N/A	Type	Solid Fuel Rocket
Thrust	620 N	Thrust	294 N
Burn Time	0.8 sec	Burn Time	1.2 sec
		Inspection Interval	9 years

Tab.3.8 Comparison between Sojka and BRS parachute recovery system.

Irvin Aerospace Limited manufactures an RPV parachute recovery system, too. The company would have the advantage of being British (BRS is American), but no system data are available to the author at the time of writing. Both companies are listed in Appendix B.

3.6 CONTROLS INSTALLATION AND RADIO SYSTEM

It was decided to fit dual rudders to enhance directional control during take-off and landing phases. Dual rudder design is discussed in section 3.3.

Ailerons and flaps will be used only in the RPV "clean" configuration, with no glove attached. This configuration in the following is called Condor "A". Inner control surfaces, former Sojka ailerons, act as flaps while the ailerons of the wing extensions are employed as flaperons. It is hoped that flaps and flaperons, along with the reduced wing loading of the Condor compared to the Sojka, will allow it to get airborne with the original powerplant while using a conventional undercarriage. In fact, the original engine might prove itself to be underpowered in reference to a conventional take-off, the Sojka having been designed to be blasted off the back of a ramp (Ref.12). Condor "B", whose name in the following will designate the flying laboratory configuration with the glove attached, cannot use flaps (the inner wing control surfaces) because in its position the glove covers the left inner aileron, hence both inner ailerons must be disabled. Condor B will then use flaperons only.

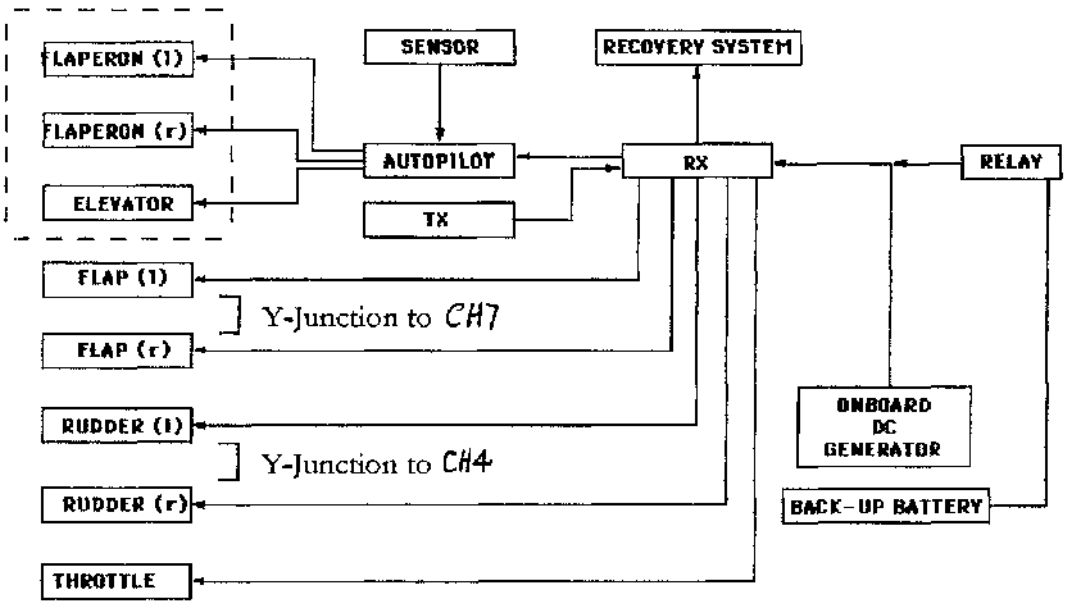

Fig.3.31 Block Diagram of Flight Control System.

The layout of the proposed radio control system is shown in Fig.3.31. The core of the system is the computer radio (TX)/FP-R138DP receiver (RX) combination. The chosen eight channel Futaba FP-T8UA computer radio (Ref.25) is fully programmable allowing flaperons electronically. It can be seen that all eight channels should end up engaged. Each outer aileron has got its own channel to have the flapcron function; the first idea was to enable both aileron differential and flaperon function, but this proved it to be incompatible with the radio programming. The inner ailerons used as flaps take another channel via a Y-junction between their servos.

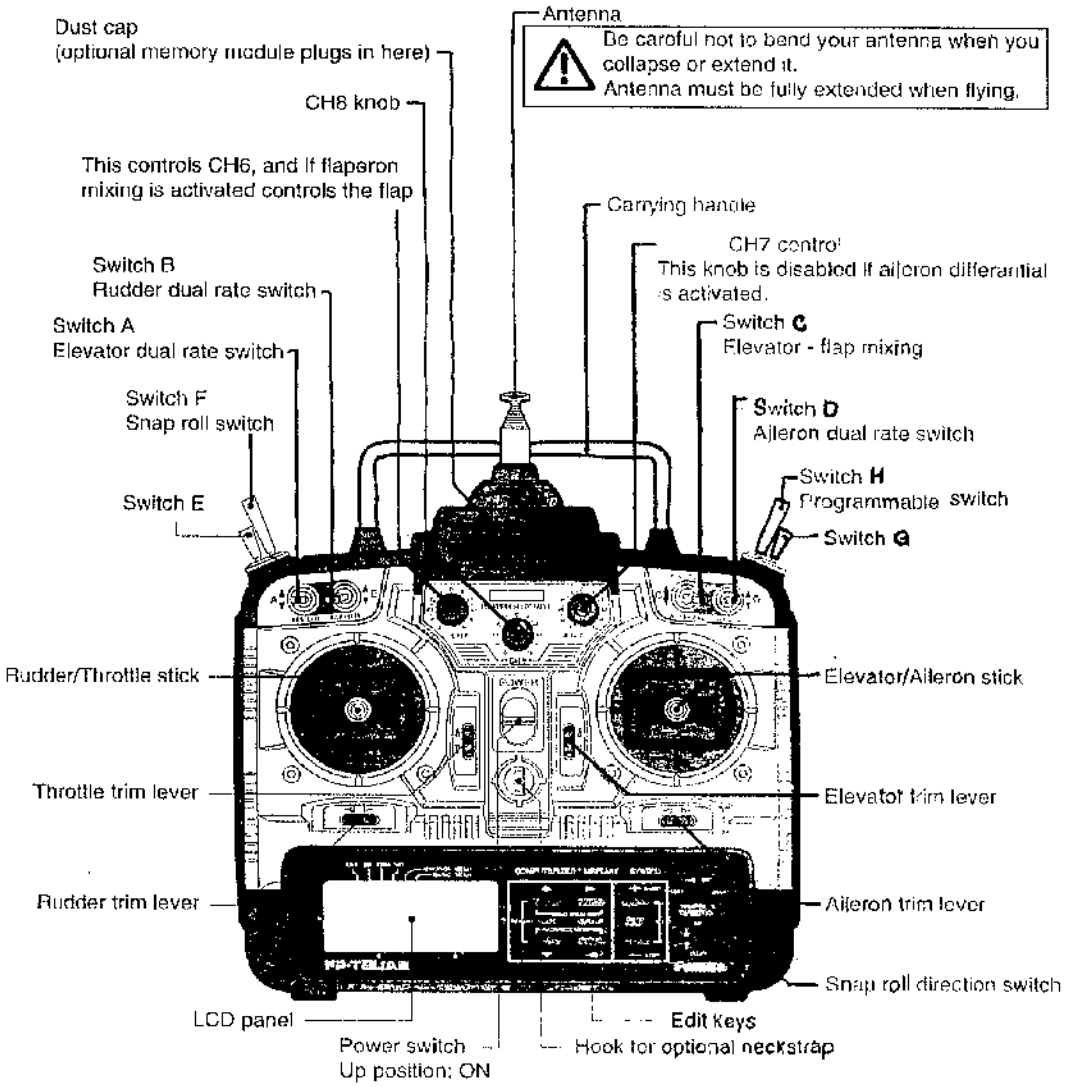

Fig.3.32 Computer Radio.

Only two channels for the four wing control surfaces could have used the flaperon function globally (two Y junctions needed), but this solution would have precluded the employment of the RPV with the glove mounted, as it would be sited in a position that blocks the inner ailerons. Conversely, assigning a separate channel to the inner ailerons and exploiting them as flaps ensures that we can make them inoperative easily while retaining the outer ailerons as fully operational when the wing glove is mounted.

The parachute release mechanism takes another channel; it would be remotely activated by the switch G (Fig.3.32) on the computer radio. The parachute recovery system is discussed in section 3.5.

The autopilot HAL2100 controls the elevator and aileron radio functions (Fig.3.31) and is capable of recovering the aircraft to a straight and level flight from any attitude automatically. It is sited on the RPV fuselage floor as far away from the receiver as possible (Fig.3.33) to avoid radio interference owing to a slight frequency emission from the microprocessor's motherboard. The Pulse Code Modulation (PCM) technology, in conjunction with a PCM receiver, permits access to a a failsafe function that, in the event radio interference is received, moves each servo to a predetermined position.

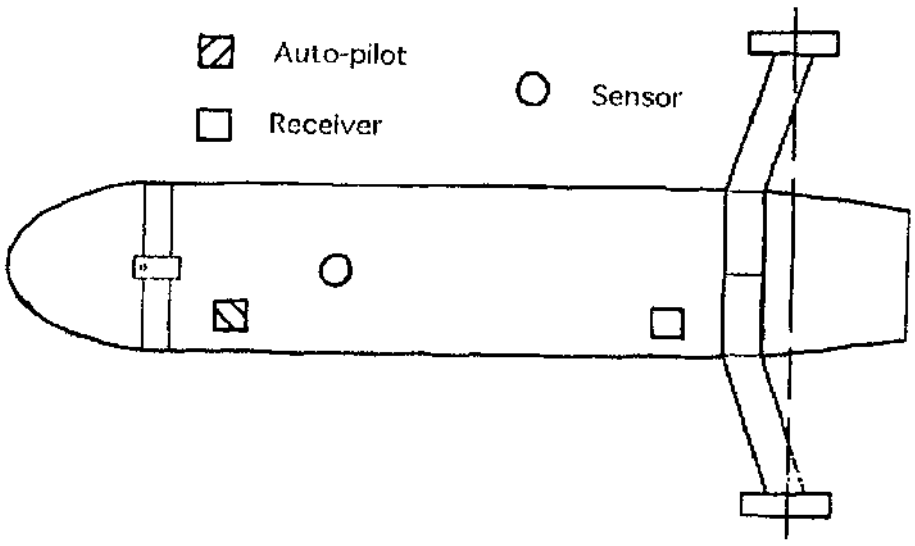

Fig.3.33 Location of Autopilot, Receiver, and Sensor.

Then some left rudder could be programmed in order to achieve a turning flight path, while the throttle could be programmed to be closed. If the receiver goes into failsafe mode, the autopilot's microprocessor sends commands to servos to return the air vehicle to level flight. As a result we would have a predictable spiral descent with the minimum of damage to the air vehicle and to third party. HAL2100 operates in conjunction with a sensor whose installation is somewhat critical. Installation was performed in accordance with guidelines of Ref.26, underneath the RPV fuselage.

On the underneath of the sensor case there are two small arrows (Fig.3.34) : one of these arrows should point forwards, depending on which configuration "+" or "x" is used. As it is of uppermost importance that the sensor four light entry holes are not obstructed by anything, the "x" position was adopted. This ensures that the sensor's view will not be blocked by the front undercarriage leg.

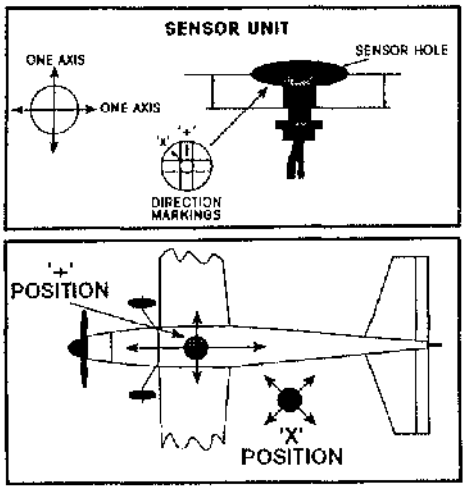

Fig.3.34 Sensor Positioning.

3.6.1 POWER SUPPLY SIZING

The proposed power supply configuration for the flight control system is shown in Fig.3.31 and uses one battery only. Previously a two battery solution was considered (Ref.21), but is was abandoned in favour of the lighter circuit in Fig.3.35 which should illustrate the concept clearly. There is a relay that is closed onto position A under normal operation, which is with the alternator functioning. In this situation the receiver and the other loads (not depicted but connected in parallel to the receiver) are fed by the regulator via a diode and a series of capacitors to stabilize the output tension; the battery is charged by the alternator, whose specifications are listed in Appendix C. The relay is closed onto position B under an alternator failure or when

the engine is off. In this situation the receiver and the other loads are fed by the battery, as long as battery endurance permits. This back-up power facility should ensure a source of current almost in any scenario (there will be a lack of power only in the event of both battery and alternator failure).

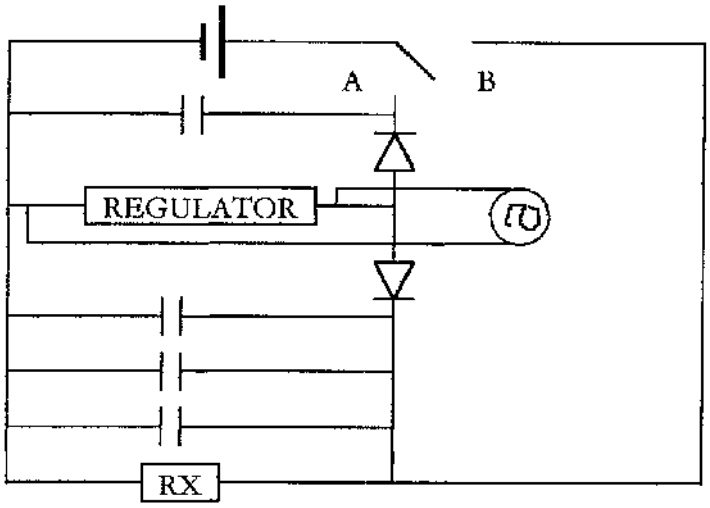

Fig.3.35 Power Supply Circuit Scheme.

Battery endurance will depend on its capacity, which can be determined knowing the maximum current drain of the circuit loads. Current drain of the most significant items, which are the powerful ps3801 and ps3032 servos, was not available in literature (Ref.27), but it was determined experimentally according to the following table :

SERVO MODEL	INPUT VOLTAGE	TORQUE	CURRENT
ps3801	4.8 V	14 kgcm	1.0 A
ps3801	6.0 V	14 kgcm	1.4 A
ps3032	4.8 V	8 kgcm	0.8 A
ps3032	6.0 V	8 kgcm	0.9 A

Servo ps3001 was not tested because of its low max torque (3 kgcm). The higher voltage input at 6V is desiderable to better cope with loss of tension problems, which will be addressed shortly. Neglecting the autopilot and receiver current drain, in the magnitude of mA, and servo ps3001 current drain, at 6 V we get the maximum output power when the two ps3801 and the remaining seven ps3032 servos are simultaneously producing the maximum torque :

$$2 \times 1.4 + 7 \times 0.9 = 9.1 \text{ Ah}$$

thus giving a battery capacity in the range 5 - 9 Ah. Parachute servo was also neglected in this calculation because still undefined (see 3.5), but the expected ps3032 servo for the nose wheel steering (see 3.4.1.1) was included. A second safety function provided by the PCM receiver regards the low battery voltage. When it drops below around 3.8V this function moves the engine to idle. The autopilot/PCM receiver/back-up power system combination will play a major role in obtaining the necessary flight permission from the CAA. Wiring cross section is an important figure to prevent loss of tension due to cable lenght. An order of magnitude for the wire cross section can be derived from the Ohm's law in the area where the loss of tension will be maximum, which is the wiring between the DC generator and the receiver, assuming that in the conductor is passing the current, 9 A, due to the total circuit load (this is a conservative approximation, since the current will be a little lower) :

$$S \cong \frac{\rho L}{\Delta V} I$$

where

L = 2 m (estimated wire lenght from receiver to battery)
ΔV = 0.5 volts (max allowed loss of tension)
I = 9 A (estimated max current load)
ρ = 0.0188 Ωmm^2/m (copper resistivity at 25 °C)

thus giving the following cross section area :

$$S = 0.7 mm^2$$

which is close to the value of a standard Futaba wire. Adopting this figure as a wiring cross section will not guarantee a loss of tension of 0.5 volts anywhere in the circuit, as there will be other losses in other parts of the circuit to be added, but certainly lower because of the lower current levels. As a result we cannot be sure that locally the tension will drop below 4.8V, which is our limit; in addition, nothing can be said about the joule effect, as the necessary data sheets are not available to the author. Neverthless, the above figure is a good starting point for more precise calculations.

3.6.2 PRELIMINARY GROUND TESTING

Ground testing of the flight control system, incomplete and with provisional items, has managed to get a somewhat advanced state. A first step was to program the computer radio to implement the channel assignment scheme in the table below, addressing the Condor A configuration :

CH1 (AIL)	RIGHT OUTER AILERON	STICK/KNOB CH6
CH6	LEFT OUTER AILERON	STICK/KNOB CH6
CH7	FLAPS (CONDOR A) HAL2100 GAIN (CONDOR B)	KNOB CH7
CH2	ELEVATOR	STICK
CH3	THROTTLE	STICK
CH4	DUAL RUDDER	STICK
CH5	RECOVERY SYSTEM	SWITCH G
CH8	HAL2100 GAIN (CONDOR A) DAS ACTIVATION (CONDOR B)	KNOB CH8 SWITCH H

The radio program was called "RPV_0A" and was developed as much as the incomplete flight system allowed. RPV_0A is loaded automatically when the computer radio is switched on; for an explanation about the settings in RPV_0A and further details on radio programming Ref.25 should be consulted. Channel 8 is devoted to the "gain control". This feature of the autopilot adjusts the servos' sensitivity via the assigned knob CH8 (Fig.3.32), thus permitting the gain setting to be varied from zero to 100 % during flight. This means that flight stability can be adjusted and manoeuvers can be smoothed on windy days. Note that channel 8 is also devoted to remote activation of the data acquisition system for the Condor B configuration. In this case the original switch H (Fig.3.32) should be replaced with a standard Futaba on/off switch.

During testing the autopilot was found faulty and replaced with a brand new one; the sensor operation was checked by shining a torch into the sensor from different positions around the RPV, according to the guidelines of Ref.26. Moreover, it was discovered that flap servos cannot be operated in the factory-set configuration, as they move unsimmetrically; to overcome the problem, one flap servo (type ps3032) was sent to the factory where it was reversed and then returned to the Department.

Because of the unavailability of expert personnel, the author himself did all the wiring using standard Futaba wires, wire extensions, female and male plugs, and a Ripmax 2.5Ah Nickel Metal Hydride rechargeable battery (see Appendix E); although this setting allowed a minimum of ground testing, it is likely that it will have to be replaced because of loss of tension problems (see 3.6.1) and, most of all, radio interference. Radio interference can be minimized by using screened cables : it will be sufficient to slide out a standard Futaba wire and replace it with a screened cable of equal lenght. The use of non-standard screened cables and battery will certainly require modifications to the autopilot, receiver, and servo fly-leads.

3.7 INSTRUMENTATION

Provision of research instrumentation is necessary in order to upgrade the air vehicle for laminar aerofoil research and hence for data acquisition in that application field. This section will consider a design specification for in-flight air data acquisition, although emphasis will be put on the instrumentation necessary for a wind tunnel test only. In-flight data measurements will be examined more in detail in another section.

3.7.1 CHOICE OF INSTRUMENTS

In general, choice of instruments for a data acquisition system is a compromise among the following factors :

- range
- desired measurement accuracy
- sensitivity to measurement
- sensitivity to disturbance
- maintanability and durability
- constancy of performance
- suitability for the environment conditions they will be subjected
- data acquisition architecture
- cost

and, in our specific application, also :

- weight
- size

This may seem complex but in practice the above factors interact with one another. For example, cost (and therefore a certain budget) will influence almost all of them, excluding a certain architecture and down-tailoring a certain accuracy measurement requirement. Often, in a semi-complete system the remaining items are almost compulsory and there is no other viable choice.

More in detail, we have also to deal with :

- computer platforms
- quantity and types of signals and sensors
- filtering requirements
- isolation requirements
- resolution requirement
- portability requirement

Since we mention "computer platforms" it is evident that we go for a PC-based system. This approach gives flexibility, versatility, fast set-up, portability on other platforms, and easy maintenance and upgrade (Ref.28). Then the first choice is between notebook and desktop computer. The latter is cheaper but unfeasible because of weight and, most of all, space restrictions. The second thing to select is the operating system, Windows or Mac OS. It has been decided for Windows merely on a value for money basis : Windows based PCs are widely available and cheaper. The other PC characteristics are directly related to the software which has to run and the ADC card to be connected (both software and card will be illustrated later). They are :

- miminum 8 MB RAM
- minimum processor 386SX (any speed, but faster is better)
- floating-point unit recommended
- minimum 800 MB hard disk capacity
- type II PCMCIA 5V capable slot

In addition the notebook must fit into the RPV fuselage, whose width is 343 mm, and with a battery life of at least one hour (estimated longest test sequence); some shock-resistant capability is desiderable (to better cope with landing loads). Selected notebook was the TOSHIBA 110CS which fulfill all the above requirements but

shock-resistant capability, which is standard; a "rugged" notebook for military purposes would meet this requirement, but it was considered too expensive for the available budget. The battery life is 2.30h in harsh conditions, more than adequate.

3.7.2 QUANTITY AND TYPES OF SIGNALS AND SENSORS

An indication of angle of attack, angle of sideslip, and outside static temperature will cover most of the expected research applications[1]. Temperature is required for calculating true airspeed. In addition, we need the value for free stream pressure and dynamic pressure. Since the glove has got 60 pressure tappings to adequately cover both lower and upper surface, we will need to measure :

- 60 pressure values over the wing glove
- one temperature value
- two angular displacements (angle of attack and sideslip)
- one free stream pressure value
- one free stream dynamic pressure value

Once the medium being measured has been identified, we still have to identify the optimum type of instruments, and take into account the factors listed previously, in selecting a particular instrument which falls into the selected type. For pressure measurements a differential transducer is universally used and it gives a differential value, which is a difference between a reference pressure and an actual pressure value. Transducers which give an absolute pressure value do exist, but are rarely used because of their cost and complexity, due to difficulty in making a perfect vacuum (Ref.30). Two suitable systems, Scanivalve ZOC22B unit and 48S9GM unit (Ref.31), were considered, and eventually the 48S9GM unit was chosen (see 3.7.5 for a discussion upon this issue). The other sensors, relevant to flight testing, will be introduced in another section.

[1] Strictly speaking, a pressure distribution in terms of Cp values under an inviscid incompressible fluid depends on the aerofoil shape and the angle of attack only.

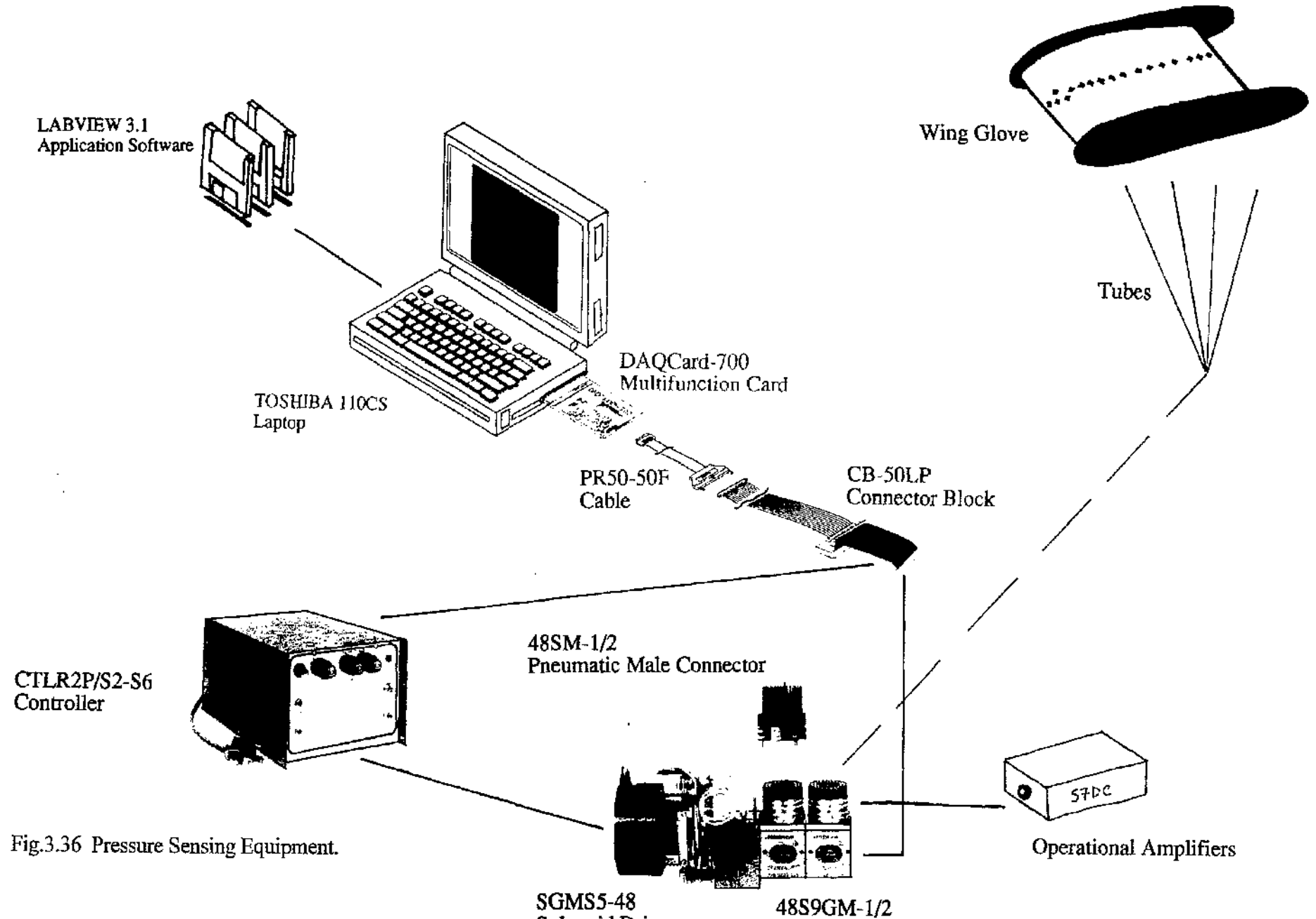

Fig.3.36 Pressure Sensing Equipment.

3.7.3 THE PRESSURE DATA ACQUISITION SYSTEM

The system consists of (Fig.3.36) :

- two 48S9GM-1/2 oiless scanners
- one SGMS5-48 solenoid drive
- two PDCR23D differential pressure transducers
- two 48SM-1/2 male connectors
- one CTLR2P/S2-S6 controller with pulser
- two S7DC strain gauge transducer amplifiers
- Labview software
- urethane tubing

In the following each item will be described.

Oiless scanner. This model S9 pressure multiplexer is driven by the solenoid drive that makes it rotating at a certain stepping rate (20 ports/sec is the maximum recommended with a Scanivalve controller and transducer). The stepping rate does include the travel volume of the transducer. Each oiless scanner contains a pressure transducer and 48 ports. The system is configured with two scanners and hence a total of 96 ports on line, but it is modular and other scanners may be added to the system (Ref.32).

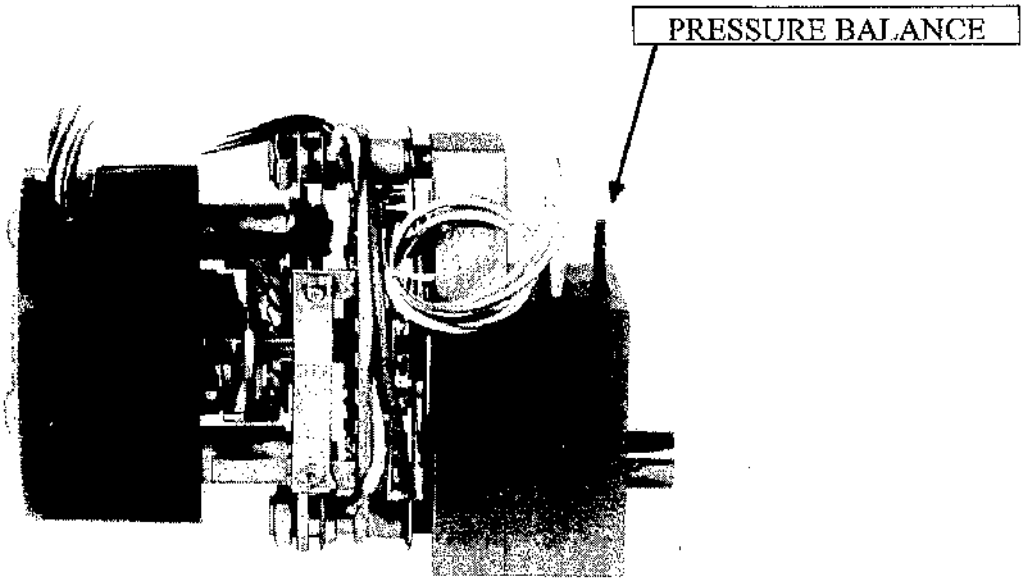

Fig.3.37 Solenoid Drive.

Solenoid drive. It is the electric motor which makes the scanner rotating (Ref.32). This model S5 has got a "balance pressure port" (see Fig.3.37) which is there for backwards compatibility only. If used in conjunction with our model S9 scanner it becomes useless and ought to be covered, although the wind tunnel test was performed with the balance pressure port uncovered.

Differential pressure transducer. The model PDCR23 (Ref.32) has a very little internal volume that allows to maximise the scanning speed, although lenght and diameter of tubes also matters. In fact, the pressure value can be regarded as a pulse, hence it needs time to settle down : a long tube with a small diameter is the worst scenario with the largest loss of pressure. The model with suffix "D" with integral cable was preferred being more practical. The Scanivalve transducer does not need temperature corrections but half an hour warm-up time is recommended. We also need to determine the transducer pressure range. What matters is the maximum expected Cp. This value depends on the aerofoil section and the angle of attack. Whilst it is difficult taking into account the infinite aerofoil sections, we can say that the angle of attack will never be large, as the aerodynamic effects which may destroy the bidimensionality of the airflow are stronger as the angle of attack increases (see 4.6.2). Assuming therefore Cp=-3 as the maximum expected, we have, by definition :

$$C_p = \frac{P - P_\infty}{q_\infty} \Rightarrow P - P_\infty = C_p q_\infty$$

and $P - P_\infty$ is indeed what the transducer measures over the wing glove surface. The formula tells us that this quantity is also larger as the dynamic pressure q_∞ increases to its maximum, which occurs at the RPV maximum estimated cruise speed at sea level (50 m/s) :

$$q_\infty = (0.5)(1.225)(50)^2 = 1531 \text{ Pa}$$

thus giving

$$P - P_\infty = (-3)(1531)Pa = -4593 \text{ Pa}$$

The first three available ranges are, starting from the smallest one :

- ± 10 in $H_2O = \pm 2490$ Pa (0.36 psi)
- ± 20 in $H_2O = \pm 4980$ Pa (0.72 psi)
- ± 1 psi $= \pm 6917$ Pa

Being the larger the range, the smaller the accuracy (see 3.7.4), ± 20 in H_2O range is preferred.

Male connector. It is a necessary accessory to connect the 48 tubes to the scanner.

Controller. It drives the solenoid electric motor (Ref.33). The model with built-in pulser has been preferred but later it was realized that the pulser is redundant since the same task can be accomplished by Tunlab, the digital interface (see Appendix A). Tunlab also supplies Home and Step control via the digital lines (during wind tunnel testing Home Pause was set to 2 sec and the Stopping Rate to 0.05 sec, see Appendix A).

S7DC amplifier. There is an amplifier per each transducer and hence a total of two. It provides all the necessary circuitry to operate the scanivalve transducer and in particular supplies 10V excitation and $\pm$ 10V output (Ref.34). Compact and reliable, it is housed in a robust die-cast aluminum enclosure suitable for harsh environments. It weighs 240 g.

Labview software. Labview Student Edition 3.1 (Ref.35) is a powerful graphical programming software enabling to fast programming the instrumentation system. It gives tools to control instruments, acquire data, analyse them, and present them. Labview is the native environment of Tunlab (see Appendix A), the system digital interface developed by the author.

Urethane tubing. The standard diameter for the SGM multiplexer is 1.02 mm (0.040 in). Four types of materials are available :

Teflon Nylon Vinyl Urethane

Urethane tubing was preferred because is resistent to weather, tearing, abrasion, and impact. It is also extremely flexible, resilient, and resist kinking, thus making it ideal for flight testing (Ref.36).

3.7.4 NOTES ON TRANSDUCER ACCURACY

Accuracy is measured in B.S.L. or in F.S.P., both given in percentage. B.S.L. stands for Best Straight Line. For instance, $\pm 0.06\%$ B.S.L. means that measurements are distant from an interpolating line (Fig.3.38) not more than the B.S.L. value, making it useful for statistical analysis. Perhaps a more useful approach is to give a percentage in F.S.P., which stands for Full Standard Pressure and the value given (in percentage) is an absolute error valid in any range. For example, if a 0-10 bar pressure gauge has a quoted accuracy of $\pm 1\%$ FSP, then the maximum error to be expected in any reading is :

$$\frac{10-X}{10}100 = 1 \Rightarrow 10 - X = 0.1$$

Therefore if an instrument is reading 1 bar, it must be :

$$1 - X = 0.1$$

thus giving a 10% error. It is then evident that the actual accuracy is lower near the bottom of the range of measurable pressures. Hence, because the accuracy in FSP is quoted as a percentage of the full scale reading of an instrument, it is an important system design rule that instruments are chosen such that their range is appropriate to the spread of values being measured, in order that the best possible accuracy is mantained in instrument reading. In short, if we were measuring pressures with expected values between 0 and 1 bar, we would not use an instrument with a 0-10 bar range.

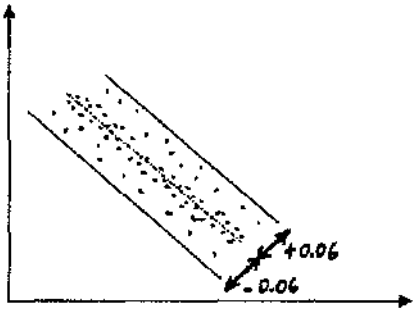

Fig.3.38 Best Straight Line (Typical).

3.7.5 ZOC22B VERSUS S9GM UNIT : PROS AND CONS

Two Scanivalve multiplexers have been considered for the pressure sensing equipment of the data acquisition system. In the following several key factors are analized which show the reason why the S9GM unit was eventually preferred. The reader should consult Ref.37 for complete ZOC22B specifications.

Cost. The ZOC unit is three times more expensive per channel.

Constancy of performance. The ZOC unit has a higher sensitivity to temperature variation. While voltage drift owing to outside temperature variation can be easily corrected mathematically (it is only a translation), a voltage drift caused by local temperature variations inside the ZOC unit can be eliminated by re-calibration only, and this is impossible to be done after the RPV has taken off.

Operational requirements. The ZOC unit is pneumatically operated, thus needing a constant pressure input in order to be in the "operate mode" or to change mode (there are four modes of operation). This implies the presence, on board of the RPV, of a somewhat cumbersome pressurized container.

Weight. Although the S9GM system weighs circa 3 kg and a ZOC unit 80 g only, the latter needs a pressurized container and a MACU unit to be operation ready. This raises the total weight significantly.

In conclusion, it seems that the ZOC unit has a faster maximum sampling rate (20 kHz versus 20Hz) only on its side, being more expensive, more complex, heavier, and more temperature sensitive. A faster sampling rate is not so paramount, as we shall be measuring low frequency signals under stationary conditions. Besides, the ZOC option would stretch the budget constraints to their extreme limits.

3.7.6 THE ADC CARD

Since it has been decided to adopt a PC-based system, an ADC is needed. In fact, most of transducers have an analog signal as output, whilst a PC requires a digital input. I/O digital lines are also required for remote de-activation of the DAQ system before landing of the RPV and for management of the Scanivalve controller. As we need to acquire more than one information (a channel is a source of information), a single multiplexed ADC, to minimize the cost, is necessary.

The selected National Instruments DAQCard-700 (Fig.3.36) is an analog input, digital I/O board for computers equipped with a Type II PCMCIA slot. The board contains a 12 bit, successive approximation ADC with 16 single ended or 8 differential analog inputs, and 8 digital I/O lines. The 8 differential analog inputs are adequate as we need to acquire :

- angle of attack
- angle of sideslip
- temperature
- values from two pressure transducers

thus making a total of five analog inputs. In Fig.3.36 it is shown the card along with the necessary connection accessories. Here are the most significant parameters of the card (Ref.38), along with their definition.

CMRR (all input ranges) : 80 dB. It is a measure to reject equal-magnitude signals on both inputs from a common-mode signal. Any induced noise will contaminate each wire equally and will be rejected by the CMRR capability.

FIFO buffer size : 512 samples. It is a queue manager using the FIFO algorithm. Collected data are stored in this buffer where they wait until the PC processor is ready to process them. It may be a critical figure in the scenario of a slow processor under a heavy workload : if the buffer is full and the processor is busy incoming data are lost.

Multiplexed ADC. Multiplexing is a technique for acquiring several signals with a single ADC. The ADC samples one channel, switches to the next, samples it, switches to the next, and so forth.

Maximum sampling rate : 100 Hz. This parameter determines how often conversions can take place. Wind tunnel testing used a sampling rate of 20Hz per channel over two channels (see 3.7.3).

Resolution : 12 bits. It is defined as the number of bits used to represent the samples (analog signals) in digital form. Currently are available ADCs with resolutions of 8, 12, or 16 bits.

Range : ± 10V, ± 5V, ± 2.5V software selectable. It refers to minimum and maximum voltage levels that the ADC can quantize. The higher the voltage, the larger the sensitivity, hence the signal resolution, for a given resolution in bits of the ADC. Therfore we will operate at ± 10V.

3.7.7 INTERFACE CONSIDERATIONS

"Scaling" is generally required within the analog-digital interface of a computer. In fact, the raw analog input signals may be too large or too small for compatibility with the range of a DAQ card and they have to be scaled upwards or downwards (apart from accuracy or noise reduction considerations). Usually the raw analog signals are scaled upwards : if inputs are below the maximum range of the DAQ card we might have a low resolution in the acquired signal. As a general rule of thumb, to avoid that, all inputs are amplified to match the maximum range of the card. Signal amplification is carried out by an operational amplifier, which is normally required to have a high input impendance so that its loading effect on the transducer output signal is minimized, and high CMRR. In data acquisition, an application requiring the amplification of low-lvel signals, so called instrumentation amplifiers are used, which are particularly good in these attributes. An instrumentation amplifier consists of a circuit containing three standard operational amplifiers. By means of amplification we increase the resolution and reduce noise of

the acquired signal. In our case we used an S7DC strain gauge transducer amplifier (Ref.34) which provided not only amplification up to the maximum range of the DAQCard-700 but also excitation for the Scanivalve pressure transducer (full scale output 17.5 mV at rated 12V excitation). Scanivalve Corporation offered a similar unit in performance (Model SCSG2 of Ref.31) but at a significant higher price, weight, and dimensions.

3.7.8 SYSTEM DESIRABLE IMPROVEMENTS

The wind tunnel experience has suggested some desirable improvements to the system, in particular to Tunlab, the digital interface, and to the tubes connections.

System testing procedures would be faster if Tunlab could address a certain scanner port directly, instead of us being forced to a manual step-counting in order to reach a given port. This could also open up some system self-testing capability development. However, it is author's opinion that such development, and others pertinent to remote operation for flight testing, are beyond the capability of the Labview Student Edition graphical "G" language used so far. In particular, the G language has shown several limits when a code becomes long and complex. Perhaps the more powerful Labview Professional Edition along with the C language-based version might be more appropriate, provided this option can be financially covered.

An intermediate connection (see accessories in Ref.36) somewhere in between the wing glove and a scanner is greatly necessary. This is because it is highly recommended to blow all tubes with clean air before each flight test sequence. In the present configuration it is very cumbersome and annoying to remove the only male connector at each scanner to have access to the tubes. Besides, this improvement would also facilitate the installation of a different acrofoil test section.

4. GLOVE DESIGN

4.1 AERODYNAMIC CONSIDERATIONS

It would be anticipated (Ref.39) that there would be two significant aerodynamic phenomena affecting the airflow over the surface of a wing glove :

1. downwash effect
2. crossflow effect

These are typically three-dimensional effects associated to a finite wing that are absent in an infinite wing producing a bi-dimensional airflow over its surface. In fact, on the RPV wing/glove combination two major sources of vorticity are likely to occur :

1. wing-tip vortex
2. vortices at the glove's edges

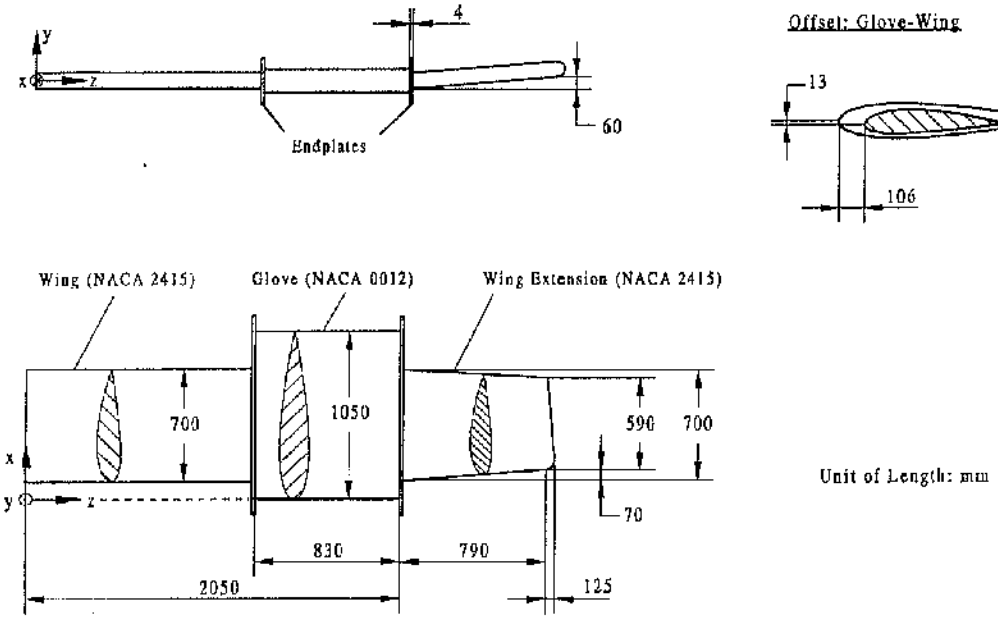

Fig.4.1 RPV Wing/Glove Geometry.

Wing-tip trailing vortices are present in any finite wing and are responsible for the downwash effect which reduces the angle of attack locally along the wing; they are also associated with spanwise velocity components ("crossflow effect") which affect the development of the boundary layer. This kind of scenario would preclude the acquisition of infinite wing aerofoil data, for which the wing glove is being primarily designed.
After these reflections it is evident that a bi-dimensional airflow at least in the glove measurement section is desirable and vital for using the wing glove for laminar aerofoil research. It is envisaged that such a task could be accomplished if investigations suggested the three-dimensional effects being of low strength or reduced significantly by means of fitting the glove with endplates.

4.2 GLOVE POSITIONING AND GEOMETRY

The glove is conveniently located in the mid-wing area approximately, in order to keep fuselage or wing-tip disturbances to a minimum (Fig.4.1). Consequently, it is sited between the two ribs available in this area of the wing. In this position its span is 0.83 m. Its planform is rectangular to meet the rectangular planform of the wing. Because in its position the glove covers the inner aileron, inner ailerons must be disabled in this RPV configuration. As the wing extensions are easily removable, it is not problematic to slide the glove over the end of the wing and to fix it to attachment fittings designed for the purpose. The minimum chord for the glove depends on the geometric characteristics of both wing and glove aerofoil test section, the finite thickness of the material the glove is made of, and the need for space for tubes of the pressure sensing system. Because of the large bulk of literature available upon it, the NACA 0012 aerofoil was chosen as the test section for design and data validation. This, and the need for space for tubes sets the minimum chord to 1.05 m (Fig.4.2). A pressure tappings strip is located near mid-glove section to minimize three-dimensional effects in the measurement plane. A total of sixty tubes connect thirty orifices on the upper surface and another thirty on the lower surface to two pressure scanners located inside the RPV wing and just underneath the glove (Fig.4.3).

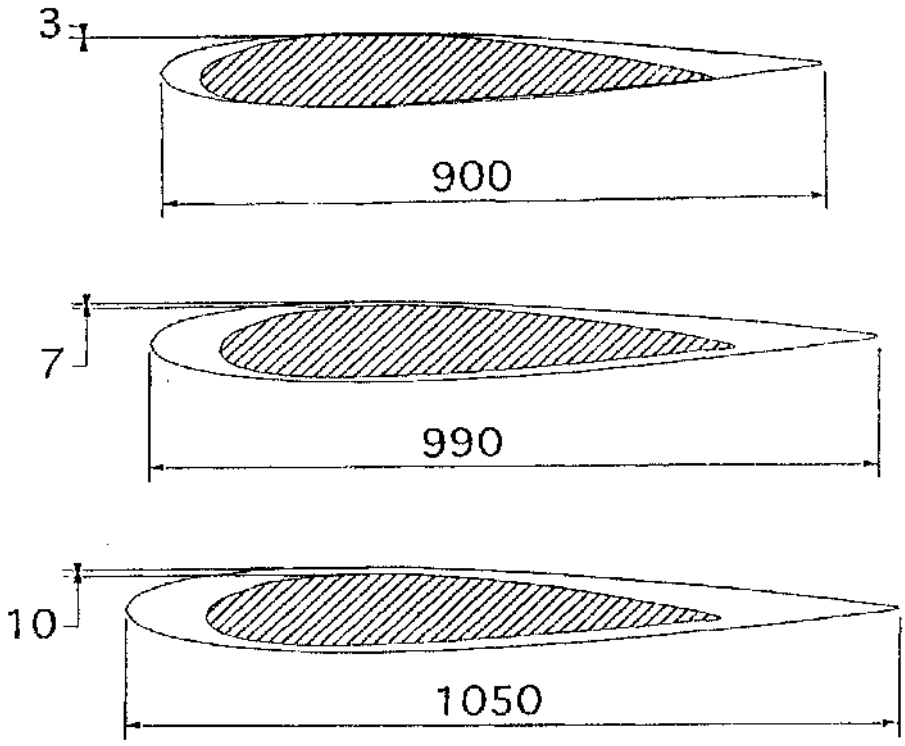

Fig.4.2 Wing Glove Chord Study.

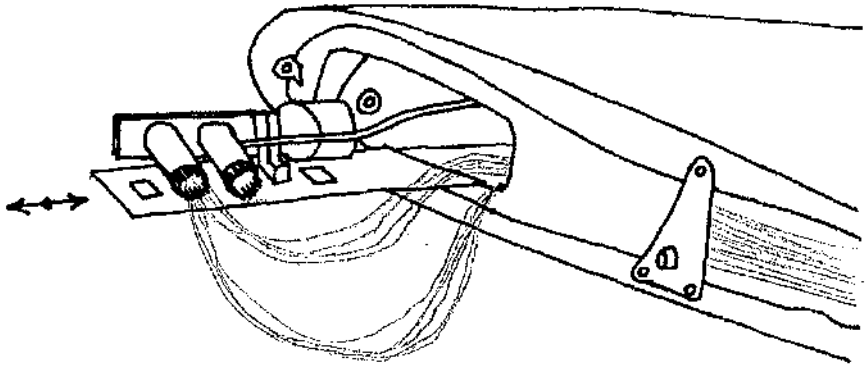

Fig.4.3 Trail-mounted Pressure Scanners.

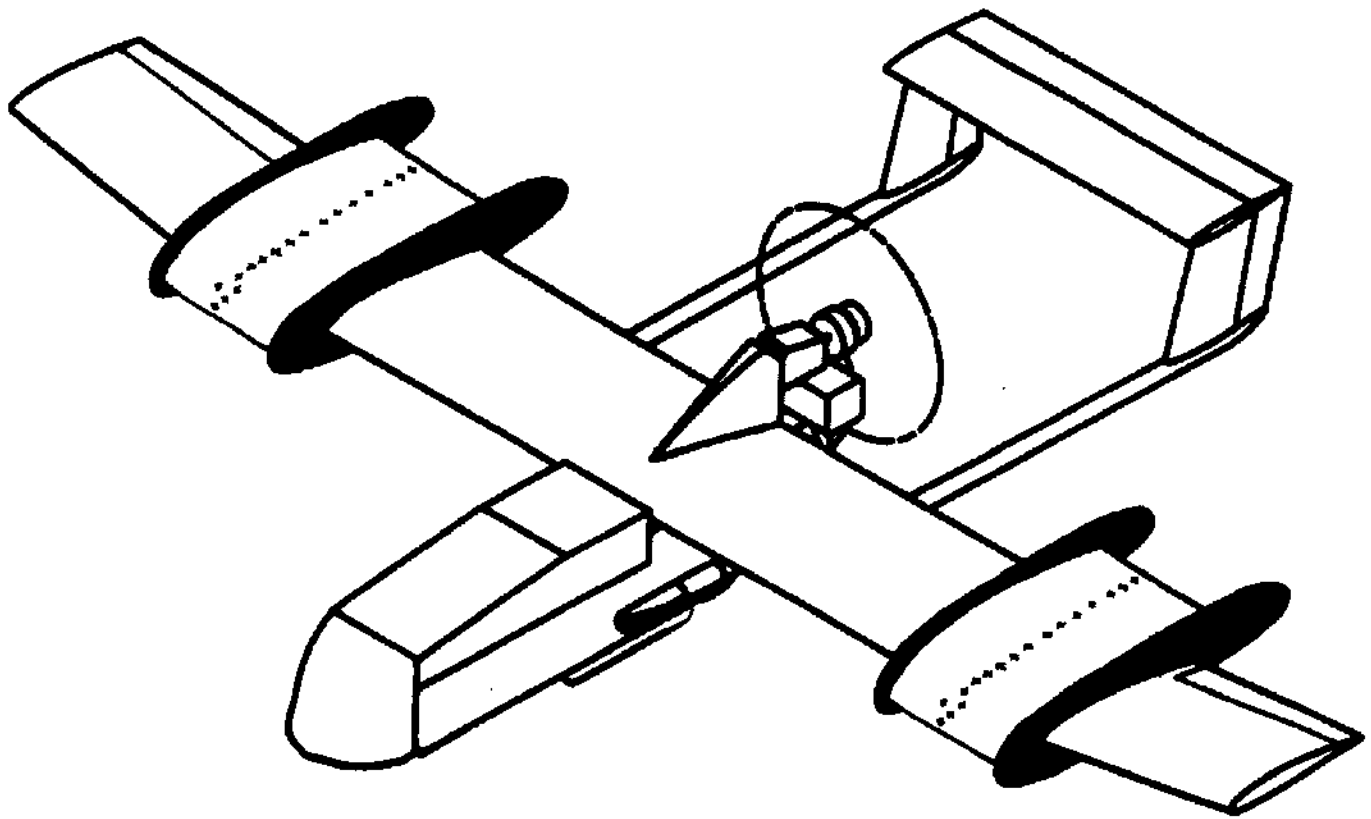

Fig.4.4 Twin Glove Configuration.

Pressure tappings coordinates are listed in Appendix D. Remarkably, the glove contains tubes only and no instrumentation, because the design philosophy was to create a removable and fully expendable glove should a new aerofoil section be tested : this ensures flexibility to test a variety of profiles by simply replacing the glove with a new one that is tubing-fitted and connected to the existing instrumentation of the Condor. The chord of the glove model is aligned with the chord of the wing and the surface is painted in matt black to facilitate flow visualization. A twin glove configuration (Fig.4.4) is likely to be employed for in-flight testing, because a single glove would induce a rolling moment about the longitudinal axis requiring a permanent aileron deflection to trim the moment out above certain speeds; this might affect test data and have an associated aeroelastic effect, namely divergence, because an aileron deflection increases the lift force causing the wing to twist.

4.3 GLOVE ARCHITECTURE

A straigthforward solution would be to adopt a classic spar-rib construction as shown in Fig.4.5; however this solution was discarded because this architecture would result in a weak structure owing to the cutouts needed by tubes to get out of the glove. This is the main reason why a more sound balsa core solution was preferred : from a central internal gap (Fig.4.6) tubes are routed through a ducting channel in the glove interior (Fig.4.7) and driven into the wing via a hole (Fig.4.8) facing the free space gained by removing the inner aileron. Current attachment fittings leave the wing almost unchanged and fully functional after removal of the glove: this enhances the flexibility concept described earlier, as it keeps to a minimum the wing modifications needed for securing the glove. The core of balsa is covered by two layers of mohogany plywood 1.5 mm thick, which make the glove's trailing edge cusped. The glove model is attached to the wing at two points located at the standard wing outboard rib (Fig.4.9) : a metal plate using the inner aileron bolt (see 2.7, item no.2), and a metal fitting using the bolt connecting the wing extension.

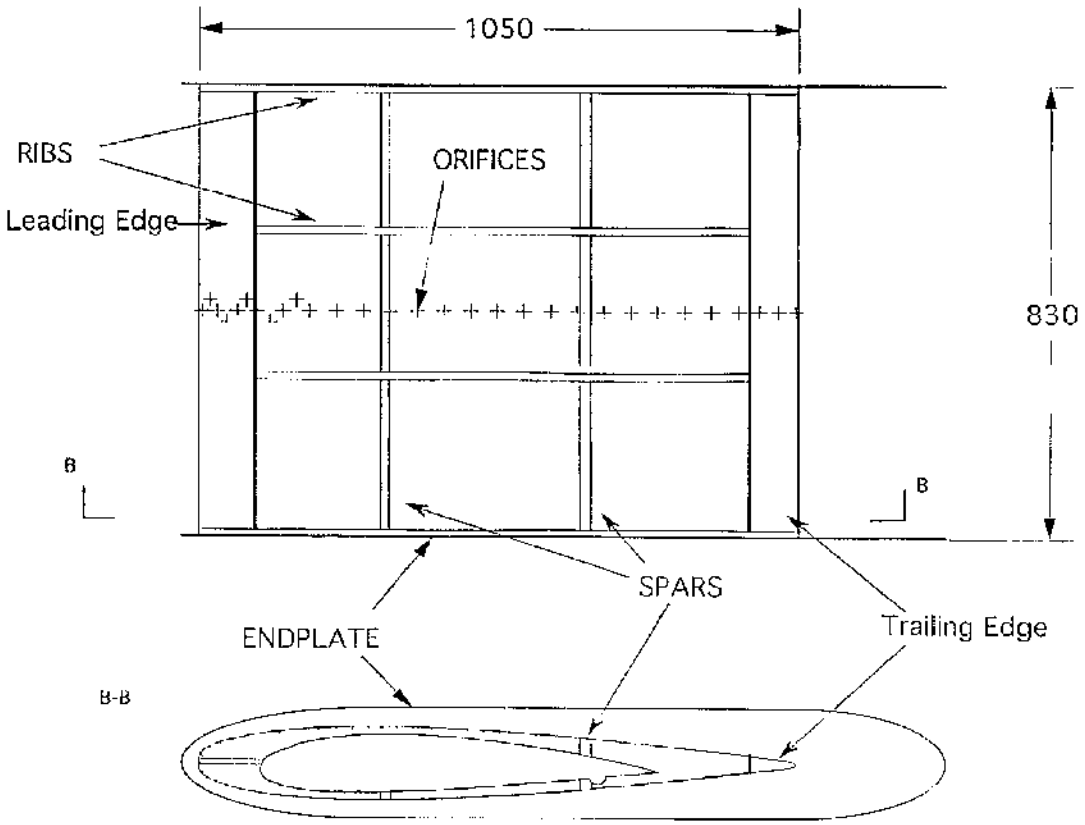

Fig.4.5 Spar-Rib Glove Architecture.

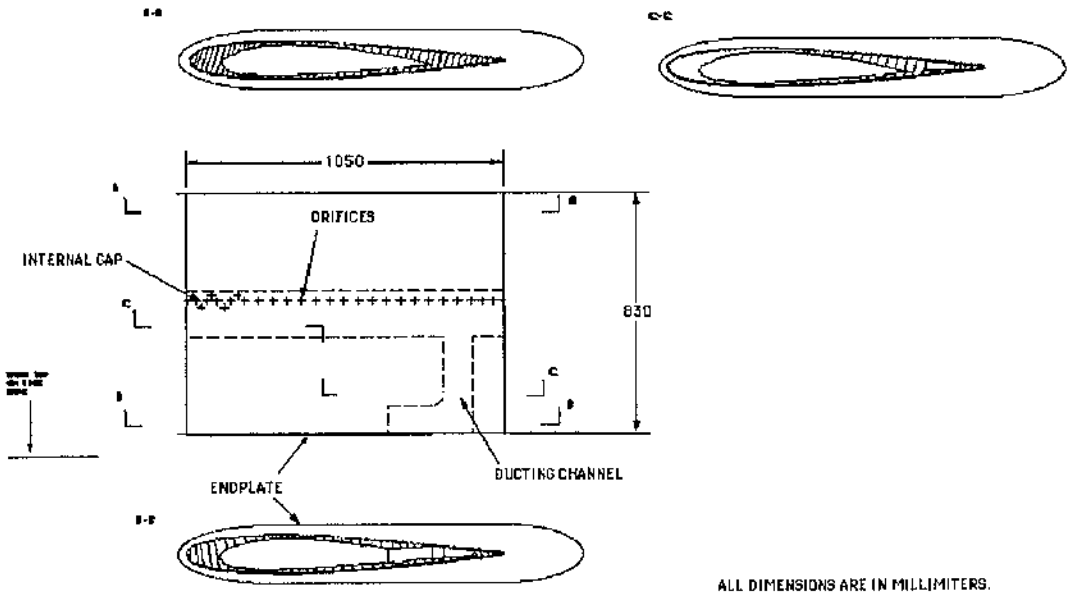

Fig.4.6 Wing Glove Architecture.

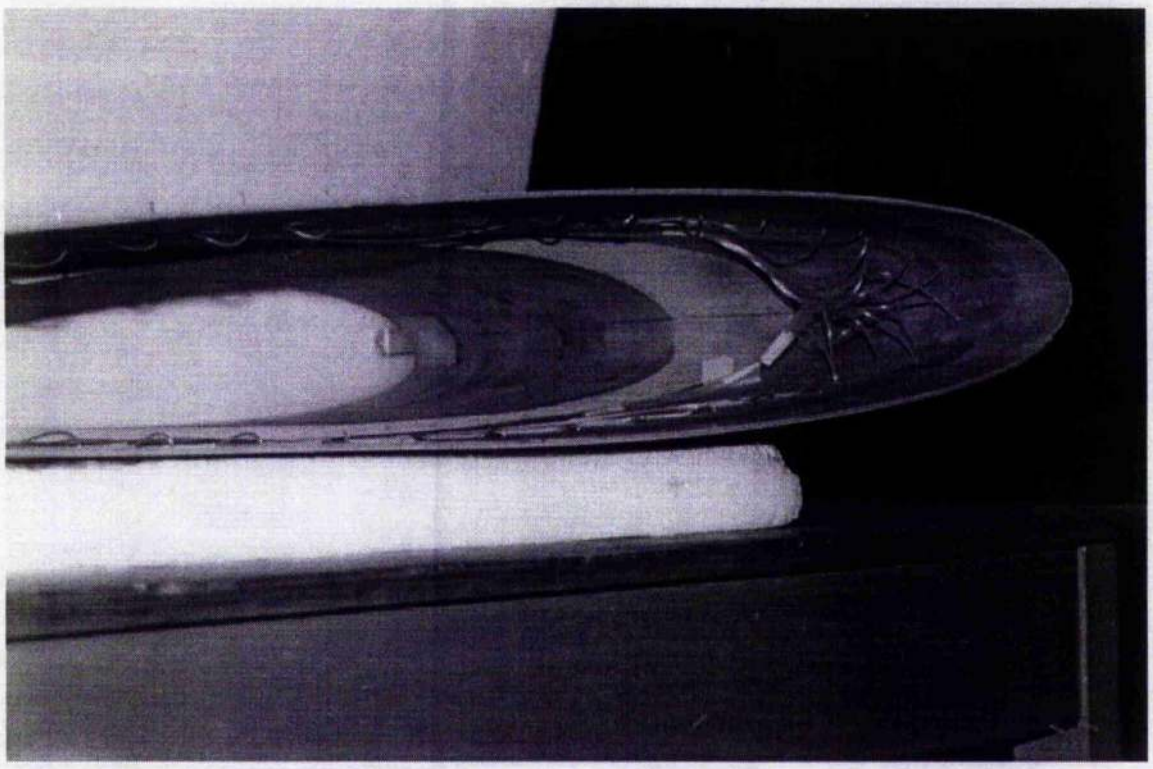

Fig.4.7 Internal Gap with Tubes.

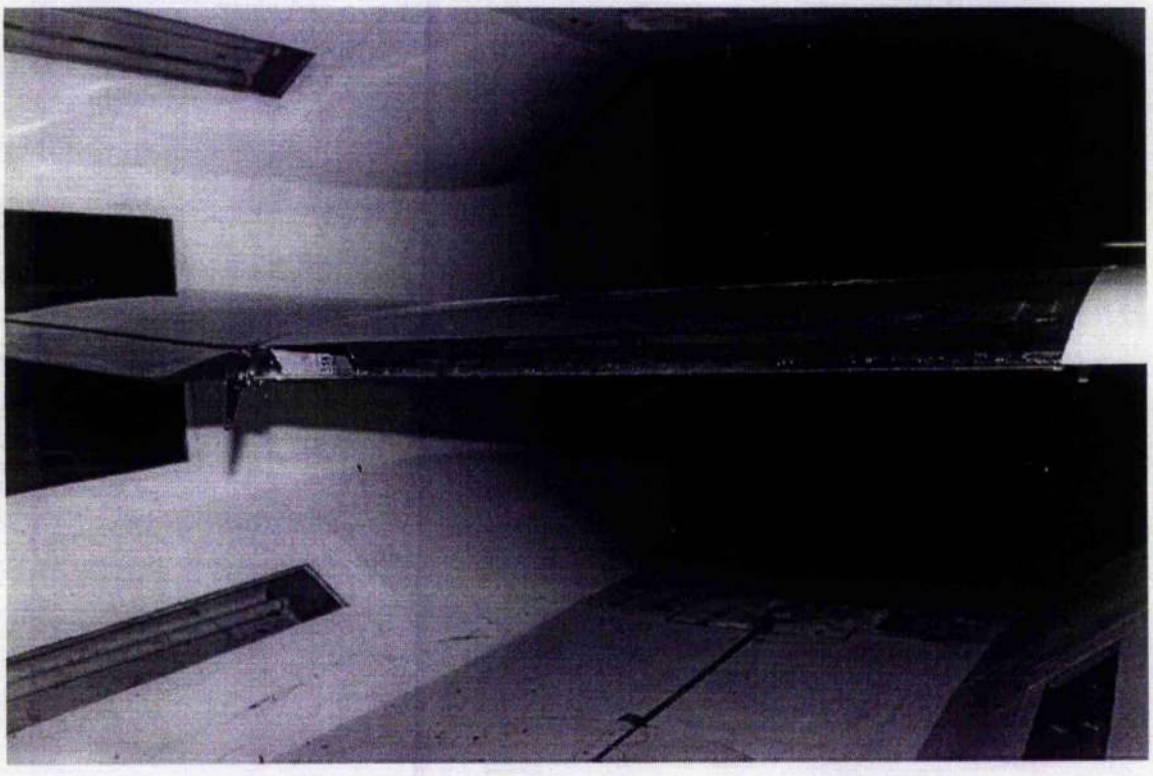

Fig.4.8 Aperture on the Wing Trailing Edge.

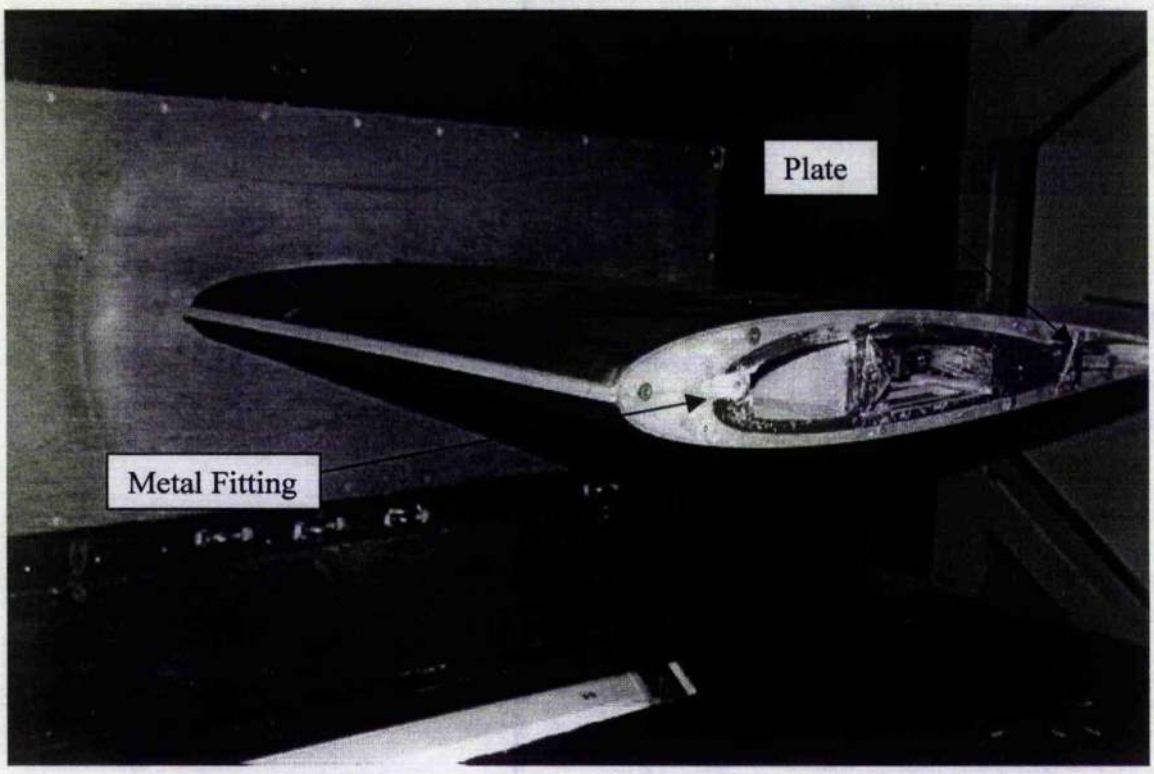

Fig.4.9 Glove Attachment Fittings.

4.4 STUDY TO LIGHTEN THE GLOVE

The wooden glove model has resulted in weighing 7.6 kg, a still acceptable but somewhat heavy weight, especially if compared with the wing extension weighing 3.75 kg, though in that case thare are no tubes which have to get out of the structure. Experience suggests that the two layer skin has a much stronger effect on weight than the core of balsa, which has already large cutouts like the central gap and the ducting channel. This is confirmed by the following calculation, which shows the saved weight obtainable by drilling a lightening 50 mm diameter hole along the leading ledge of both halves of the glove (central gap is 160 mm wide) :

$$\text{available lenght on half glove} = \frac{830}{2} - \frac{160}{2} = 335\,\text{mm}$$

$$\text{volume on half glove} = \pi(0.025)^2(0.335) = 6.57 \cdot 10^{-4}\ m^3$$

$$\text{total saved weight} = 2(6.57 \cdot 10^{-4})(96) = 126\,\text{g}$$

which is only 1.7 % of the total weight of the glove. A two layer nested skin construction seems to be mandatory to permit tubes to be installed inside the model and for getting a seamless and strong junction on the glove surface. A discussion with J.Kitching, the technician who made the current wooden glove, led to the conviction that a glove made of composite materials is technically feasible for the Department capabilities. A composite glove looks promising in an attempt to save weight because styrene sheets, for instance, are available as thin as 0.25 mm and an expanded PVC rigid foam, Divinycell grade H30, in an experiment proved it to be one third lighter than the balsa used for the core, according to the following table :

MATERIAL	THICKNESS	SHEET SIZE	WEIGHT
Divinycell H30	50 mm	2845X1295 mm	13.25 g
Balsa 96 kg/ m^3	50 mm	2845X1295 mm	39.75 g

The idea is therefore to use the current wooden glove model as a mould, thus retaining the current architecture, which is wind tunnel tested, in order to manufacture a glove with a core of Divinycell H30 and two styrene 0.25 mm thick layers for the skin. A composite glove, however, requires some care with the painting colour, in reference to its future in - flight testing.

The problem is that the finished colour can affect the glove structural strength due to solar heating of its surface; in fact, the colour of the surface determines how much solar heat it will absorb (Fig.4.10). A white surface absorbs very little of the sun's heat whilst a black surface absorbing much more (95 %) will heat up greatly. In particular, if IR surface flow visualization is planned to spot the boundary layer transition from laminar to turbulent, a black surface will give the best results (Ref.4). In this case it is advisable to cover the glove when it is on the ground to avoid high temperatures on its black surface.

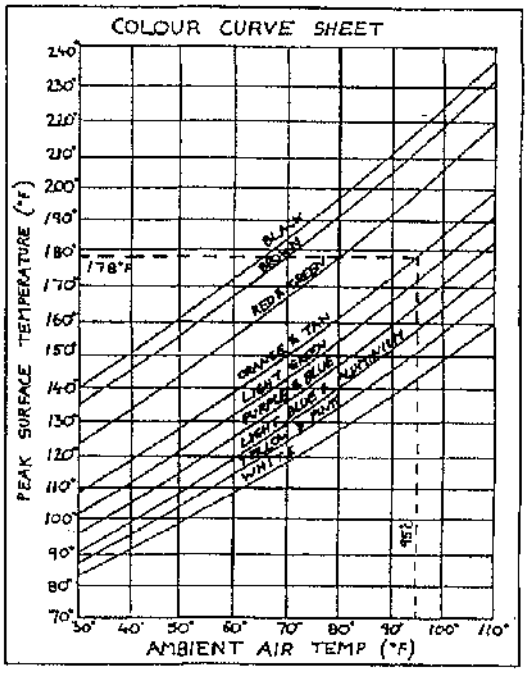

Fig.4.10 Colour-Temperature Relationship.

4.5 NUMERICAL MODELLING

To establish the quantitative effect of the endplates on the flow around the wing glove, numerical calculations were carried out considering endplates of different size. In each case the shape of an endplate follows the glove profile and the quoted height is simply the perpendicular distance from the edge of the plate to the surface of the glove. Following heights have been used :

5 cm, 10 cm, 20 cm, 50 cm, Special

The geometry of 20 cm and 50 cm endplates is shown in Fig.4.11; 5cm, 10 cm, and Special endplates geometry is shown in Appemdix D.

In order to numerically predict the effect of the endplates three software packages were used (Ref.40).

PreBFC - a CAD style geometry setup and 3D boundary mesh generator
TGrid - a 3D triangular unstructured mesh generator
Rampant - a numerical solver and postprocessor

All three packages were developed by Fluent Inc. and are therefore designed to interact with one another.

Endplates Height = 20cm	
X [mm]	Y [mm]
0	0
18.0	7.5
36.0	10.5
72.0	14.0
108.0	17.0
143.5	19.5
215.5	22.5
287.0	24.0
430.5	25.0
717.5	23.0
861.0	21.0
1004.5	18.5
1148.0	15.5
1292.0	11.5
1363.0	9.5
1406.0	7.5
1422.0	4.5
1435.0	0
chord = 1435 mm	
X_{offset} = 200 mm	

Endplates Height = 50 cm	
X [mm]	Y [mm]
0	0
25.5	168.0
51.0	228.0
102.0	308.0
152.5	377.0
203.5	423.5
305.0	495.0
407.0	528.0
610.5	550.0
1017.5	509.0
1221.0	462.0
1424.5	407.0
1628.0	341.0
1831.0	256.0
1933.0	209.0
1994.0	165.0
2017.0	99.0
2035.0	0
chord = 2035	
X_{offset} = 500 mm	

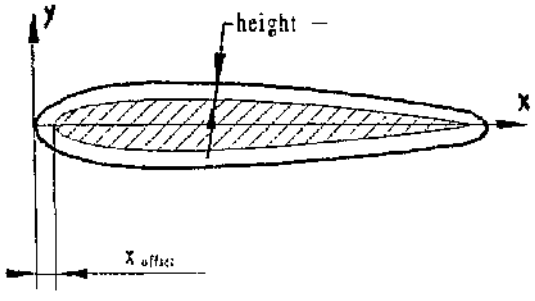

Fig.4.11 Geometry of 20 cm and 50 cm Endplates.

PreBFC provides a geometry description around which the fluid must flow (Ref.41). Calculations are performed upon the mesh which is created onto the geometry, not upon the geometry itself. In fact, a geometry description is used as a guide during the grid generation for placement of grid lines, and eventually the solver sees the grid only. It is therefore paramount to plan the geometry setup accurately, since the ability to modify the grid later or to extract a certain set of results will depend heavily on the way the geometry was defined within PreBFC. In order to illustrate this important point adequately, we will go in some detail into the process of generating the three-dimensional RPV wing/glove combination geometry. PreBFC offers the following tools to create a geometry :

- points, defined in terms of Cartesian coordinates
- curves, created from defining points
- surfaces and patches, created from defining curves.

The initial step was the input of the wing profile points (Fig.4.12). Surfaces (S1...S6) were created , each passing through two opposite curves of U1 and U2. To enhance postprocessing abilities (i.e. displaying results on the upper surface only) upper surfaces (S1,S2,S3) were given the *Zone-number* 2, lower surfaces (S4,S5,S6) the *Zone-number* 3; elements with different *Zone-numbers* can be isolated individually in TGrid and Rampant.

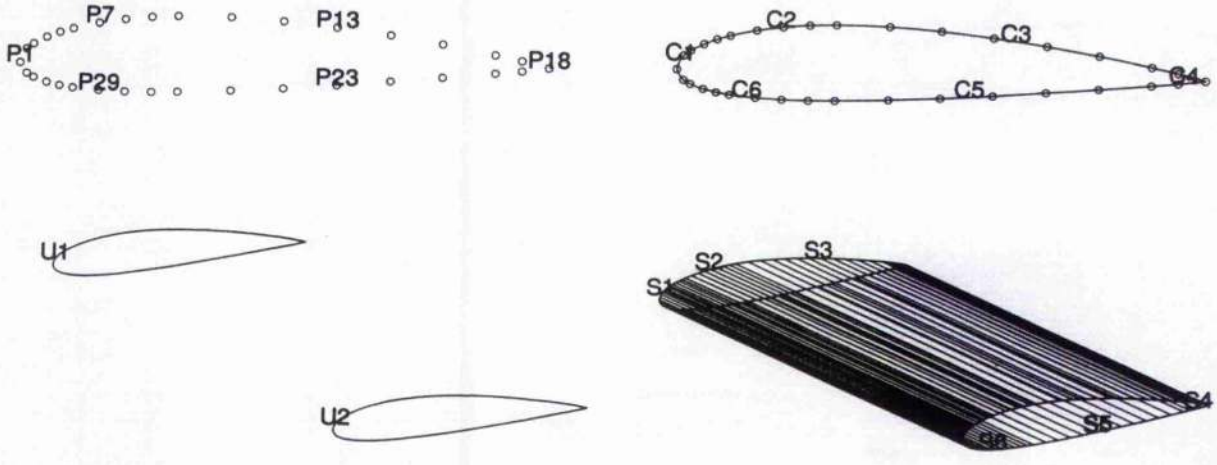

Fig.4.12 Wing Geometry Setup Steps.

The next step was the geometry input of the endplates. They had to be modelled with their finite thickness of 4 mm because Tgrid does not recognize a mesh surface that is exposed to the flow on either side. This complicates the model because now we must define either endplate side geometrically and each side is different as one is at the wing interface and one is at the glove interface. Both endplate sides, shown in Fig.4.13; had to be defined with patch surfaces (PA1...), each requiring a set of four curves to be created between the initial and end points of opposite curves (of wing and endplate profile, or of glove and endplate profile, respectively). The wing extension was set at about 5 degrees of dihedral angle and used six surfaces (S25...S30) passing through curves of U9 and U10 (Fig.4.14). The wing tip (Fig.4.15) was modelled with six patch surfaces (TI1...TI6). Boundary type is asked by PreBFC after each surface or patch creation command; as all the elements so far created belongs to the RPV wing/glove combination fitted with endplates, the boundary type for these will be *wall.* A *wall* is a solid boundary through which a fluid cannot flow. Final step is the geometry setup of the outer boundary of the computational domain. Both cylindrical-shaped and square stone-shaped outer boundaries were used with the various grids employed during the calculations. Fig.4.16 shows a square stone outer boundary. The first section (at z = 0) was set as a *symmetry* boundary type.

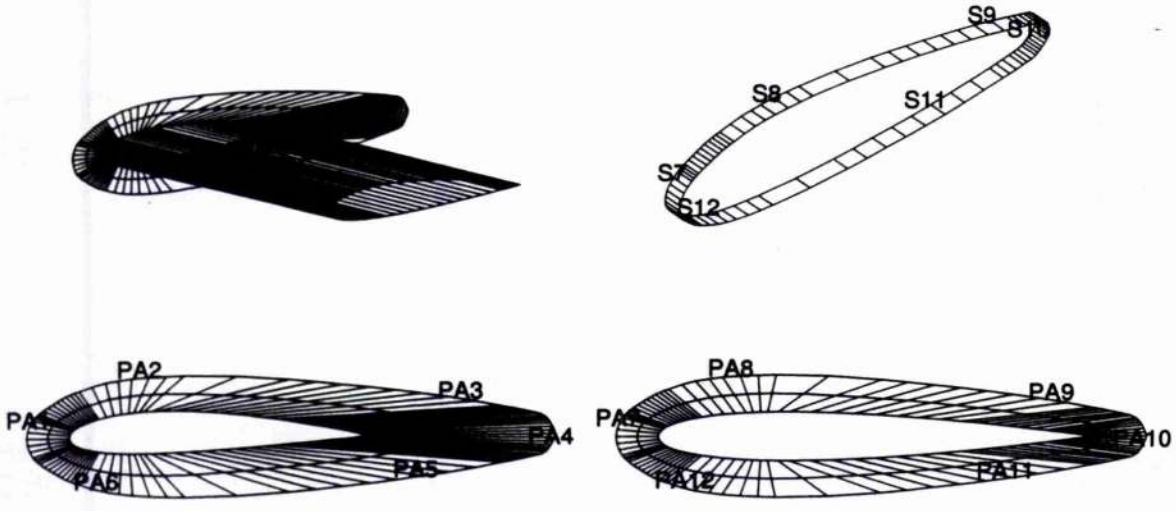

Fig.4.13 Endplates Geometry Setup.

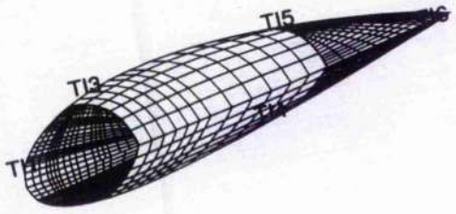

Fig.4.14 Wing Extension Geometry Setup.

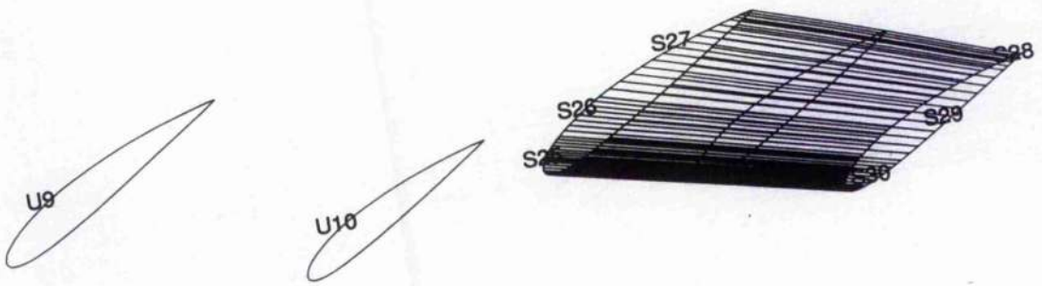

Fig.4.15 Wing Tip Geometry Setup.

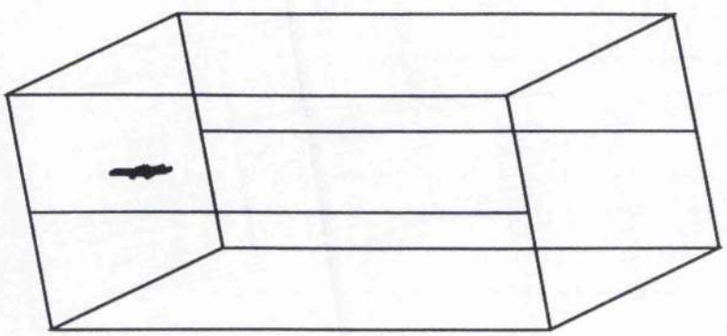

Fig.4.16 Outer Boundary.

This allowed to model only half wing, since the flow and the geometry are then considered symmetric about that surface. The model has a clearance equal to 5 times its chord radially and 8 times the wingspan longitudinally from the outer boundary. The outer boundary surfaces were set as an *inlet* boundary type, namely a boundary across which fluid enters the domain.

Starting from the boundary mesh, the tetrahedal unstructured grid was generated with TGrid (Ref.42,43). It is then necessary to examine the created boundary mesh for topological problems such as duplicate (free) nodes and unused nodes. Duplicate nodes are two or more nodes placed at the same location, which may occur where curves of different surfaces meet one another. *The boundary mesh cannot be generated if duplicate and unused nodes are present.* This was a major problem, because, although TGrid provides commands for merging and eliminating nodes, there were always duplicate nodes after merging the nodes. One can try to reduce the tolerance and try to merge again. Nodes are considered coincident when their coordinates differ less than the specified tolerance. Needless to say, there were still duplicate nodes after reducing the tolerance to the smallest acceptable value.

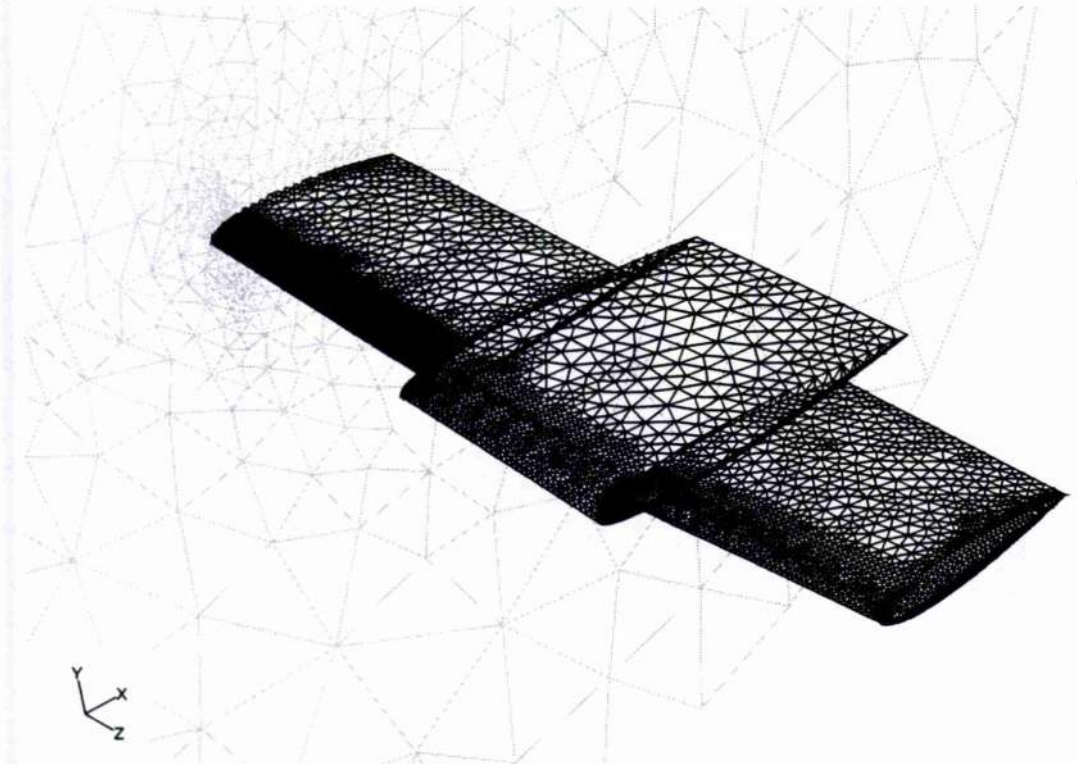

Fig.4.17 RPV Wing/Glove Boundary Grid.

Initially, changing the node distribution led to a boundary mesh, but at the cost of many time-consuming trials and errors. The author cannot explain why this empirical solution worked, but it was the only way to get a volume mesh, and hence a numerical solution, using TGrid release 2. Actually this remedy worked with the RPV wing/glove model without endplates (Fig.4.17) and with the wing model alone (Fig.4.18), but not with the complete model. Only after the release of Tgrid 2.4 it was possible to generate a boundary mesh for the complete model (Fig.4.19). Endplates were added by S. Artmann who used a new feature available in Tgrid 2.4 : duplicate nodes are displayed and then merged manually. The merge command is in the *Modify Boundary Panel*. Once the boundary mesh was created and improved in quality, the volume grid had to be initialized. In some cases Tgrid could not mesh all nodes at the first attempt. The problem was solved by reducing the *Node Tolerance* in the *Init/Mesh Controls Panel*. This tolerance is valid for the mesh initialization only and has nothing to do with the merging process of duplicate nodes. Note the finer mesh over the leading edge of the RPV wing/glove model, where higher velocity gradients are expected.

The volume mesh was then imported into the solver Rampant for calculation (Ref.44,45). The inviscid incompressible model was used, as downwash and crossflow effects are accounted by Prandtl lifting-line method within the potential flow theory. This means that in the mid area of the numerical glove model, which is expected to be the less disturbed by three-dimensional effects, the resulting numerical prediction must agree with a corresponding bidimensional experimental pressure distribution (this would indicate that the downwash effect is negligible) and that spanwise velocity components must be near to zero (this would indicate that the flow is really bidimensional) should a bidimensional flow be present in the numerical simulation.
Accordingly, following free-stream conditions of a bidimensional experiment (Ref.46) were used :

Mach = 0.3	Re = $1.86 \cdot 10^6$
$\alpha = 3.59°$ (angle of attack)	V = 98.44 m/s
Static Temperature = 268.17 °K	Air density = 0.305 kg/m^3

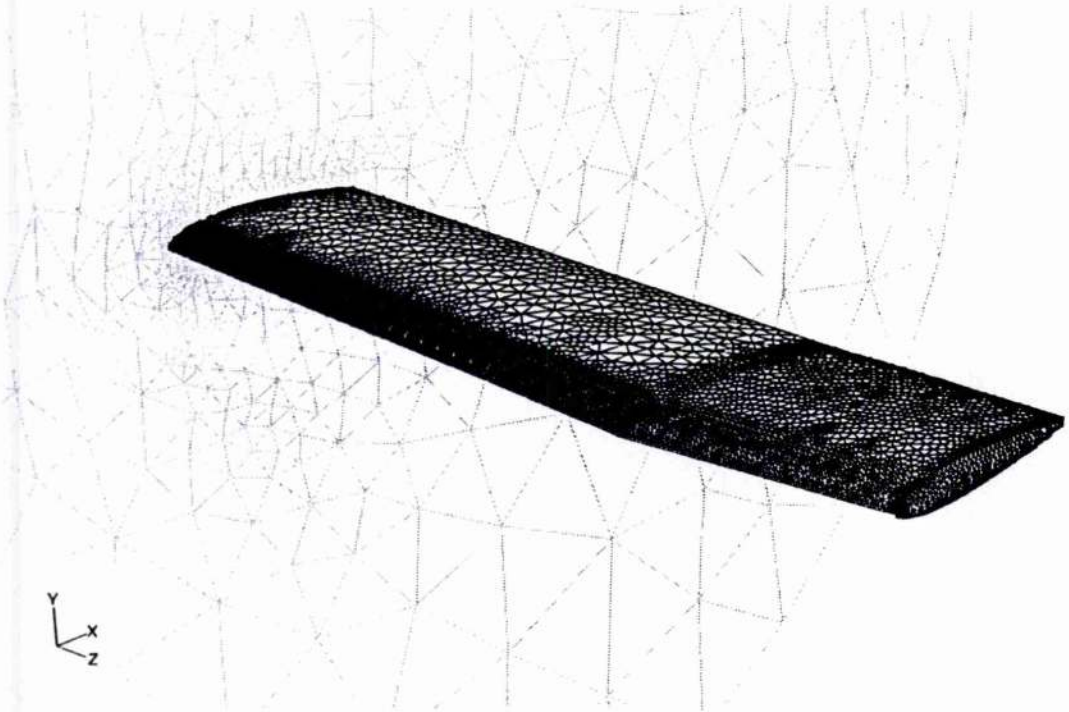

Fig.4.18 RPV Wing Boundary Grid.

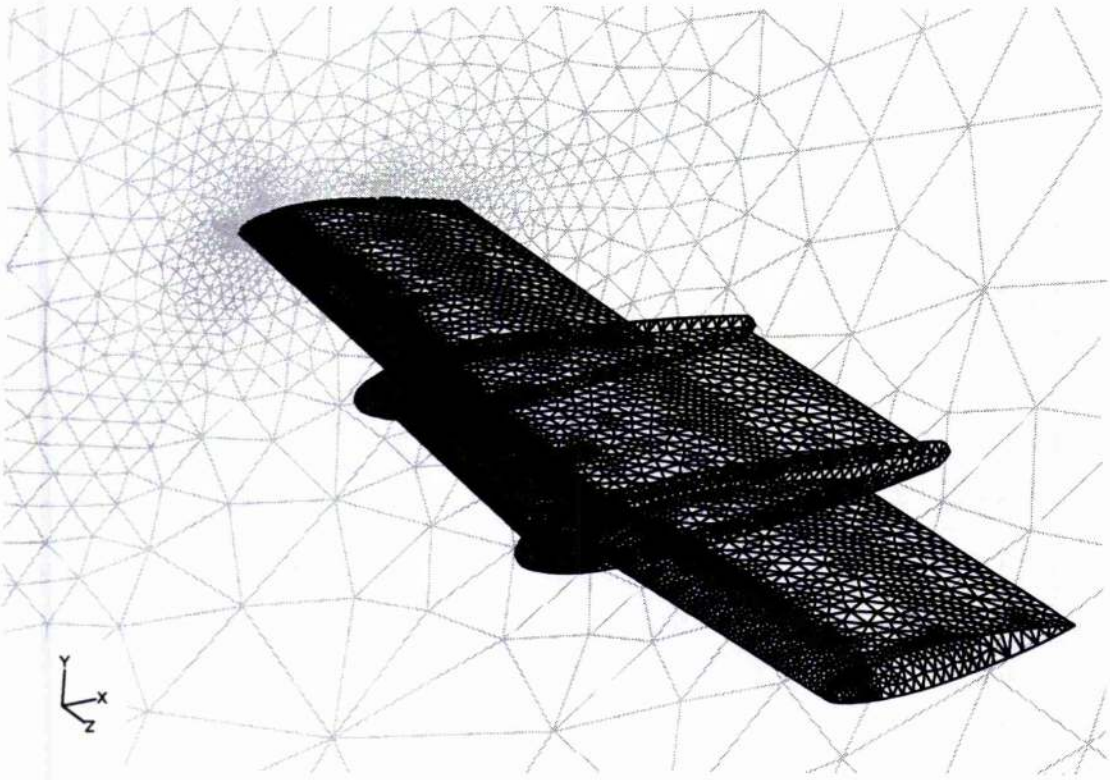

Fig.4.19 RPV Wing/Glove/Endplates (5 cm) Boundary Grid.

An average of around 130 iterations were needed to achieve a converged numerical prediction. A numerical solution was regarded as "converged" after a residual reduction of $1 \cdot 10^{-3}$. All calculations were performed on a Silicon Graphics "Indy" machine.

4.5.1 NUMERICAL RESULTS

Scope of the numerical simulation was to investigate the quantitative aspects of the flowfield around the RPV wing/glove combination fitted with endplates of different shape and size. To begin with, Fig.4.20 and Fig.4.21 show that even very large endplates have very little influence over the pressure distribution in the glove mid-section, as the leading edge peak of pressure, lowered by the downwash effect which reduces the local angle of attack, does not change significanly. This suggests that the endplates cannot reduce significantly the downwash effect mainly due to the wing-tip vortex, hence indicating the presence of a three-dimensional flow over the glove even fitted with large impractical endplates. Despite this, the flow may be two-dimensional nominally, if there are no significant spanwise velocity components. In this case, in fact, the flow can be simply regarded as two-dimensional at the effective angle of attack, which is the angle of attack reduced by the downwash effect.

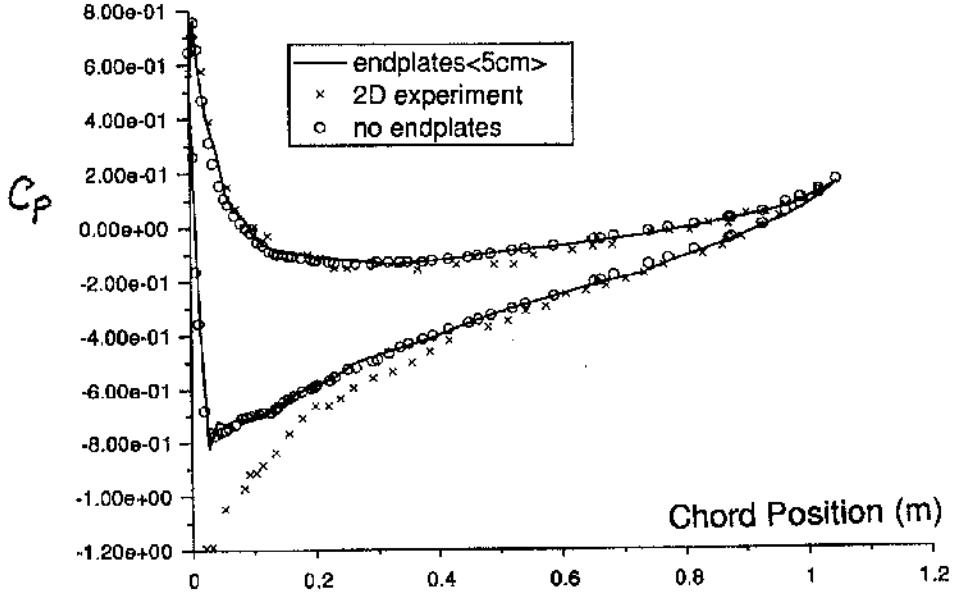

Fig.4.20 Pressure Distribution - Endplates (5 cm).

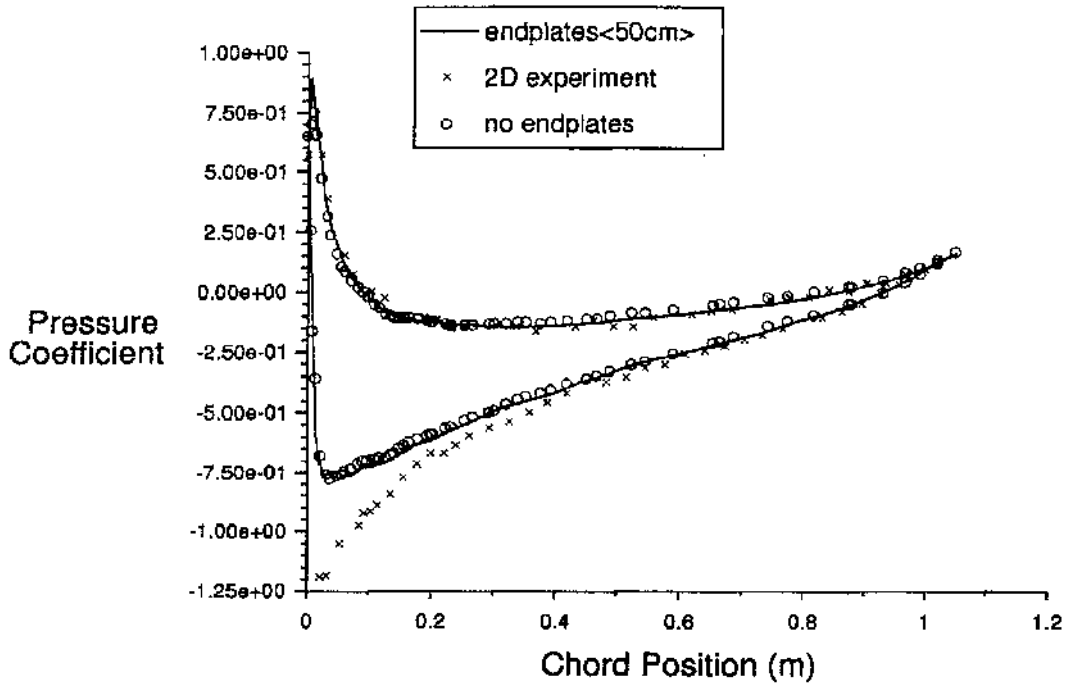

Fig.4.21 Pressure Distribution - Endplates (50 cm).

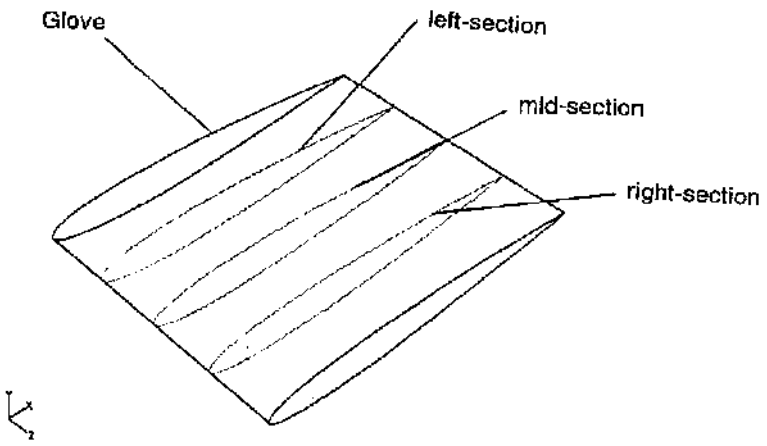

Fig.4.22 Glove Stations for Displaying Spanwise Velocity Components.

Figures 4.23-4.27 show the chordwise distribution of spanwise velocity components (Z-Velocity) at three different locations (Fig.4.22) on the glove calculated for different endplates. These figures show that endplates generally reduce the crossflow down to about less than 2 % of the free-stream velocity in reference to the glove mid-section. These results suggest that endplates can make it possible to minimize the crossflow to a level which should not have significant effect on the development of the boundary layer, hence in-flight testing could acquire infinite wing data at least in the glove mid-section. This is especially relevant to the pressure measurement, which would be performed in the glove mid-section to minimize the downwash effect. The 50 cm endplates performed best (Fig.4.26) but they are impractical for flight testing because of their size, as large areas before the aircraft centre of gravity would reduce its directional stability by producing a destabilizing moment. The smallest 5cm endplates could be employed for test-flying on the RPV, as they are associated with negligible crossflow comparable with the other configurations (excluding the 50 cm plates), and are small and light.

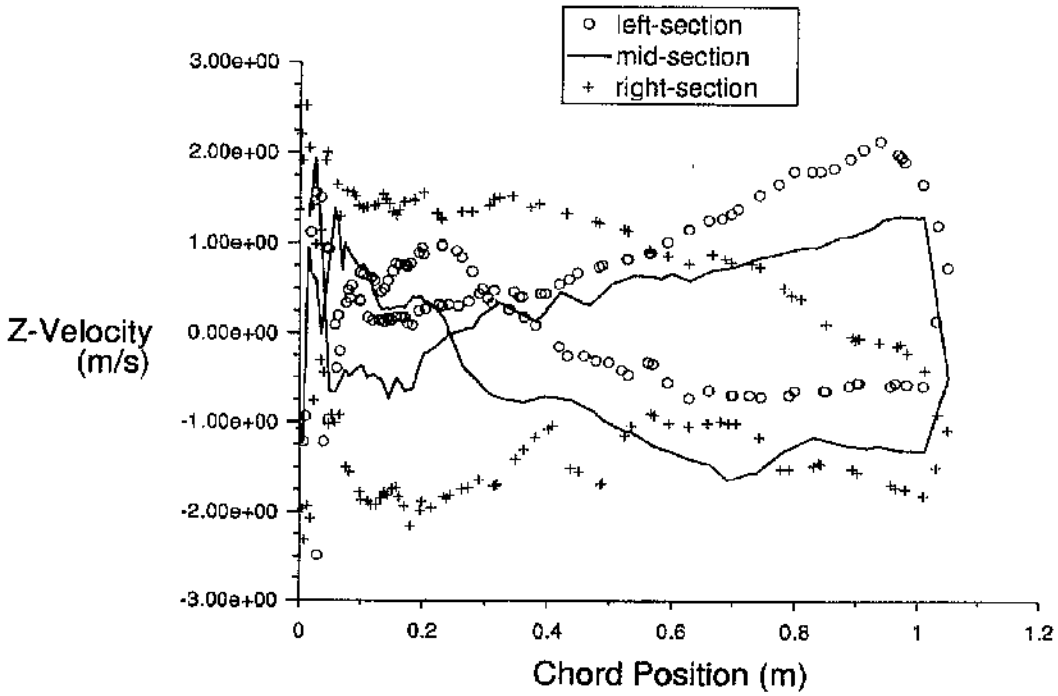

Fig.4.23 Spanwise Velocity Component - Endplates (5 cm)

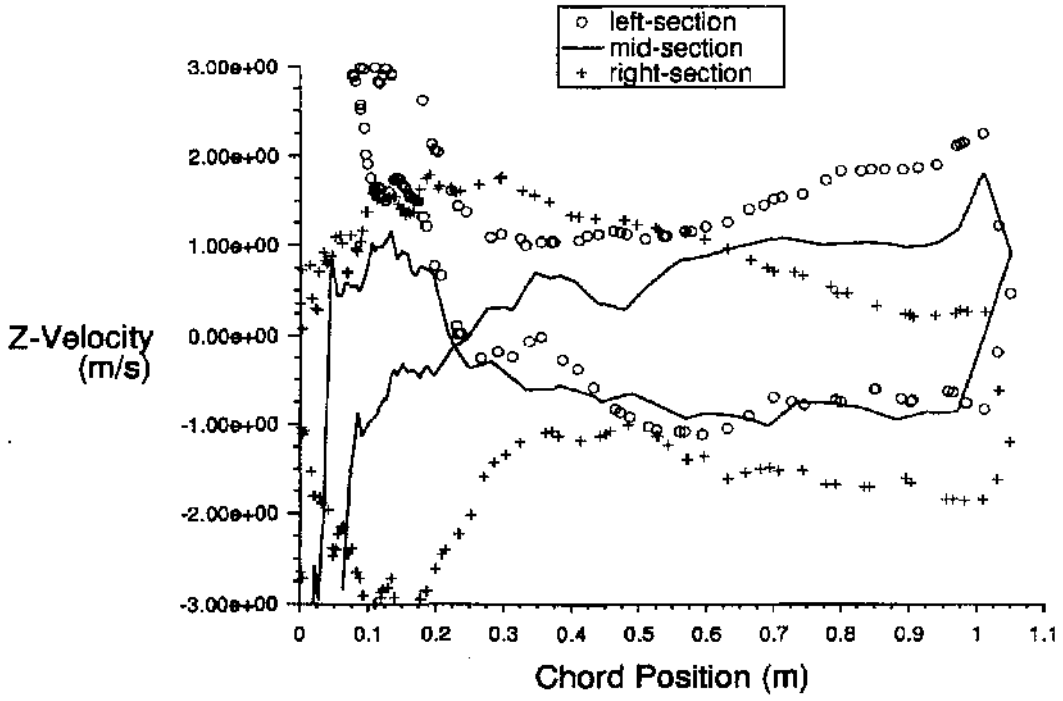

Fig.4.24 Spanwise Velocity Component - Endplates (10 cm).

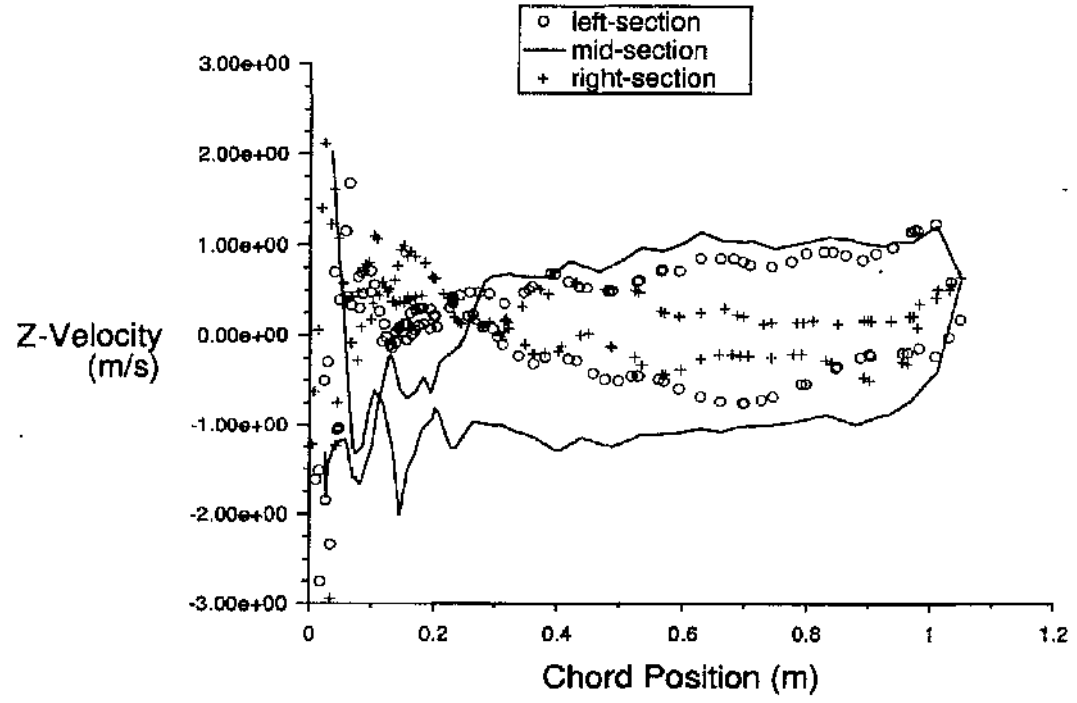

Fig.4.25 Spanwise Velocity Component - Endplates (20 cm)

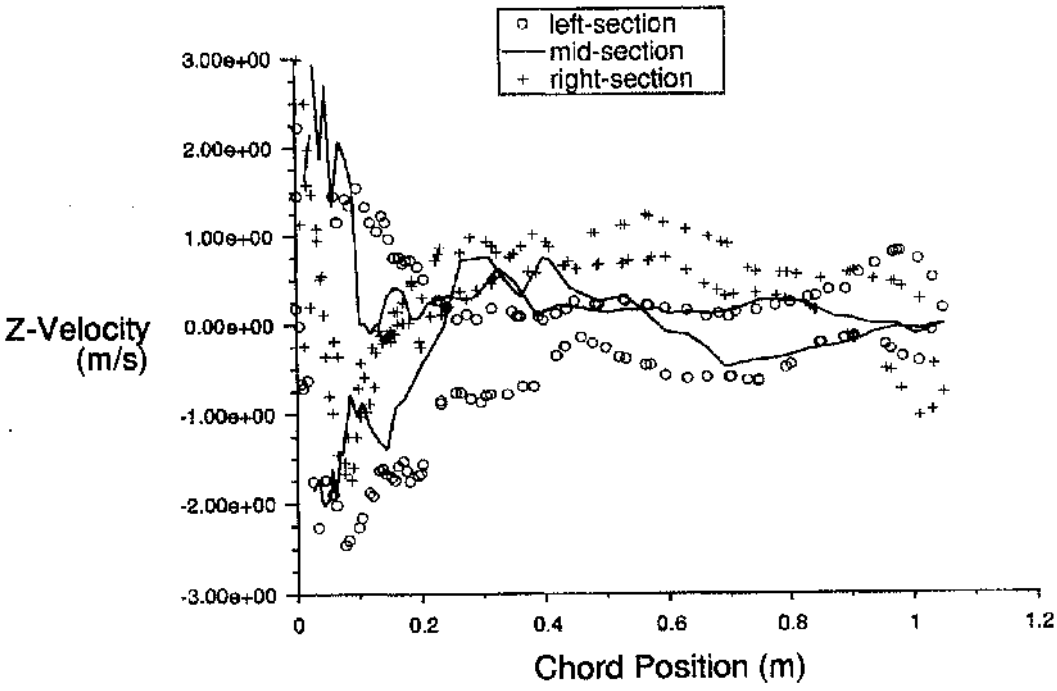

Fig.4.26 Spanwise Velocity Component - Endplates (50 cm).

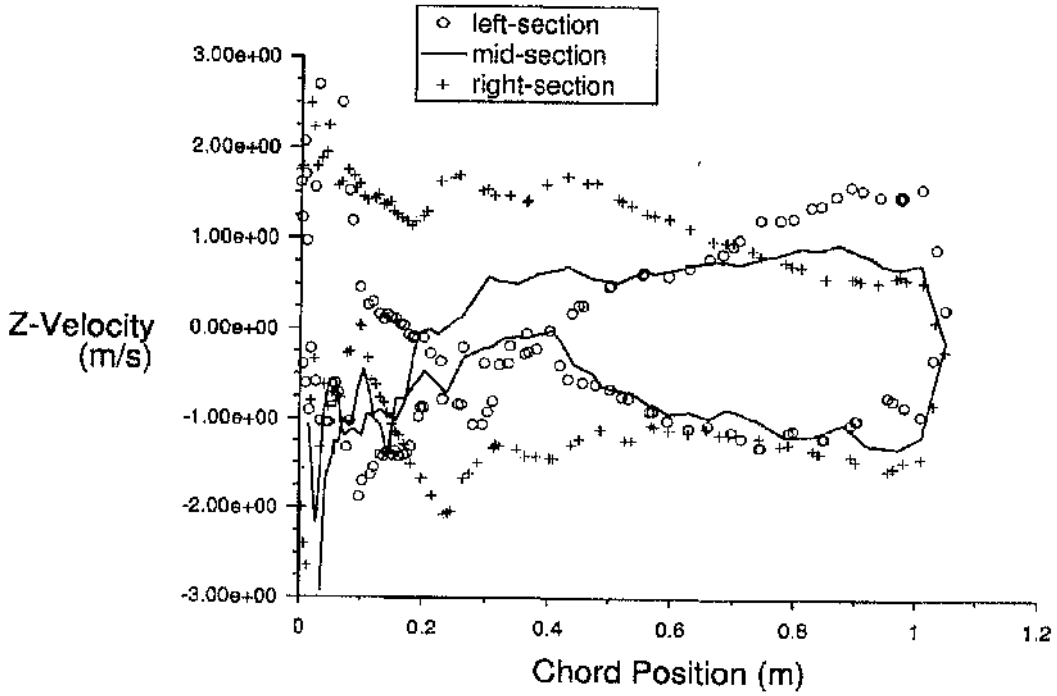

Fig.4.27 Spanwise Velocity Component - Endplates (Special).

We now turn our attention to the whole picture of the flow over the upper surface of the glove, which is the more affected by 3D effects. Figures 4.28-4.31 are contour diagrams of the spanwise velocity component (Z-velocity) over the upper surface of the glove. Non coloured parts of diagrams indicate a Z-velocity that goes beyond the selected range (-3 m/s to +3 m/s). In these diagrams one can see that the largest area of less disturbed flow is given by the 20 cm endplates (Fig.4.30). However, as they would affect aircraft directional stability, it is not advisable to use them in flight. The Special endplates (Fig.4.31) rank as the second best choice, as they have large areas purposedly concentrated behind the aircraft center of gravity, and therefore they might be considered if a large area of less disturbed flow is desired; this is indeed desirable when flow visualization is conducted.

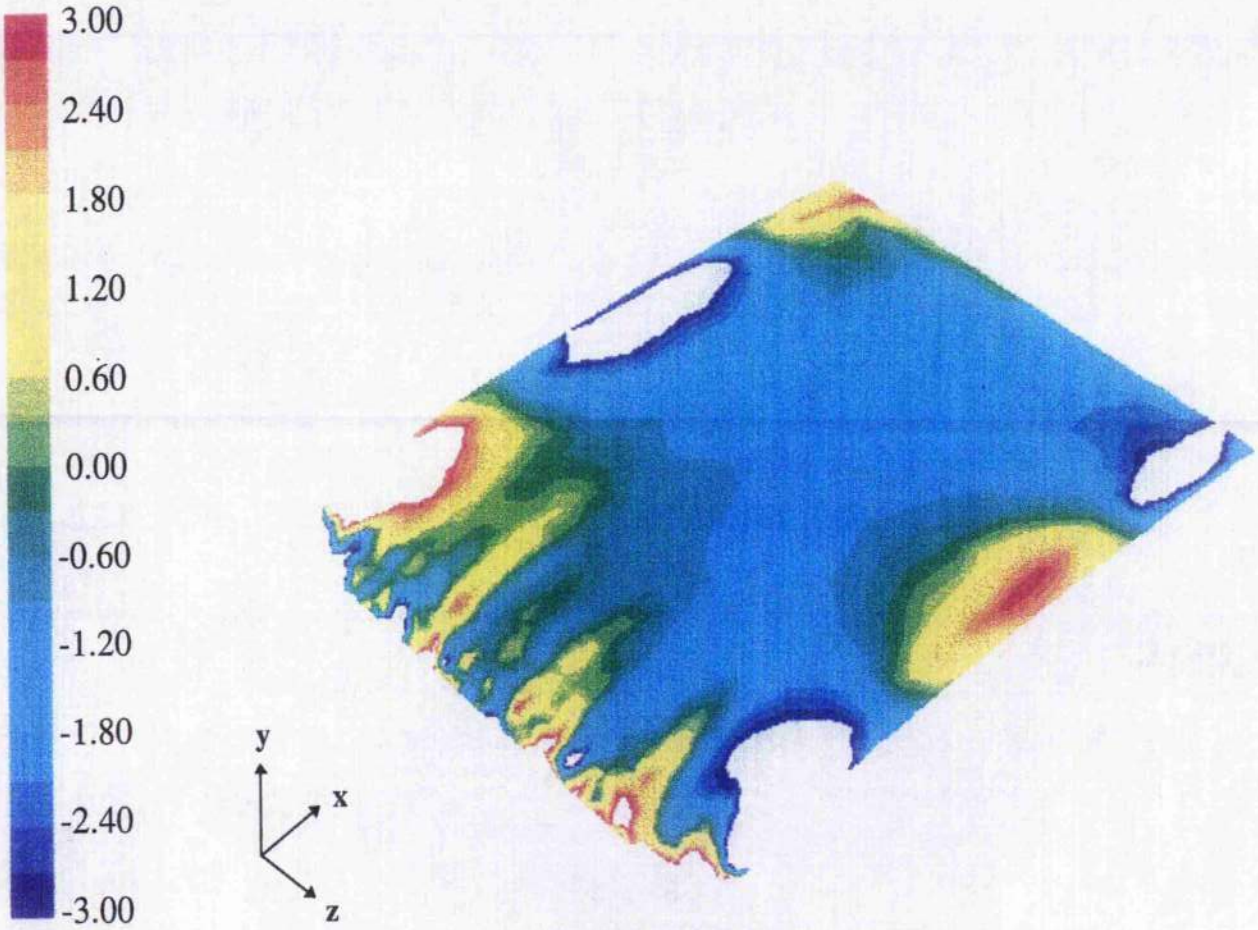

*Figure 4.28 : Contours of Z-Velocity [m/s] on Upper Glovesurface - **No Endplates***

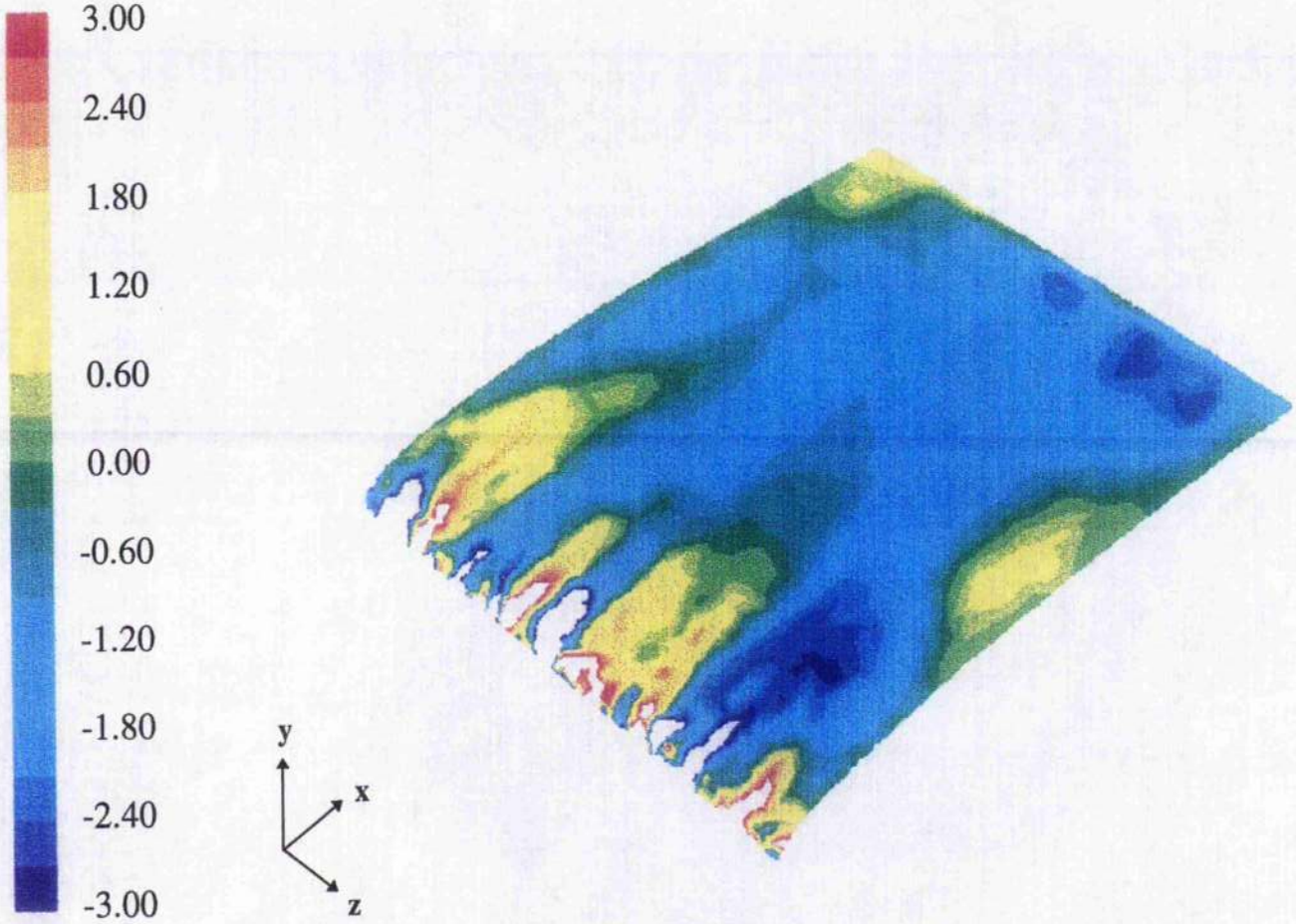

Figure 4.29 : Contours of Z-Velocity [m/s] on Upper Glovesurface - ***Endplates (5 cm)***

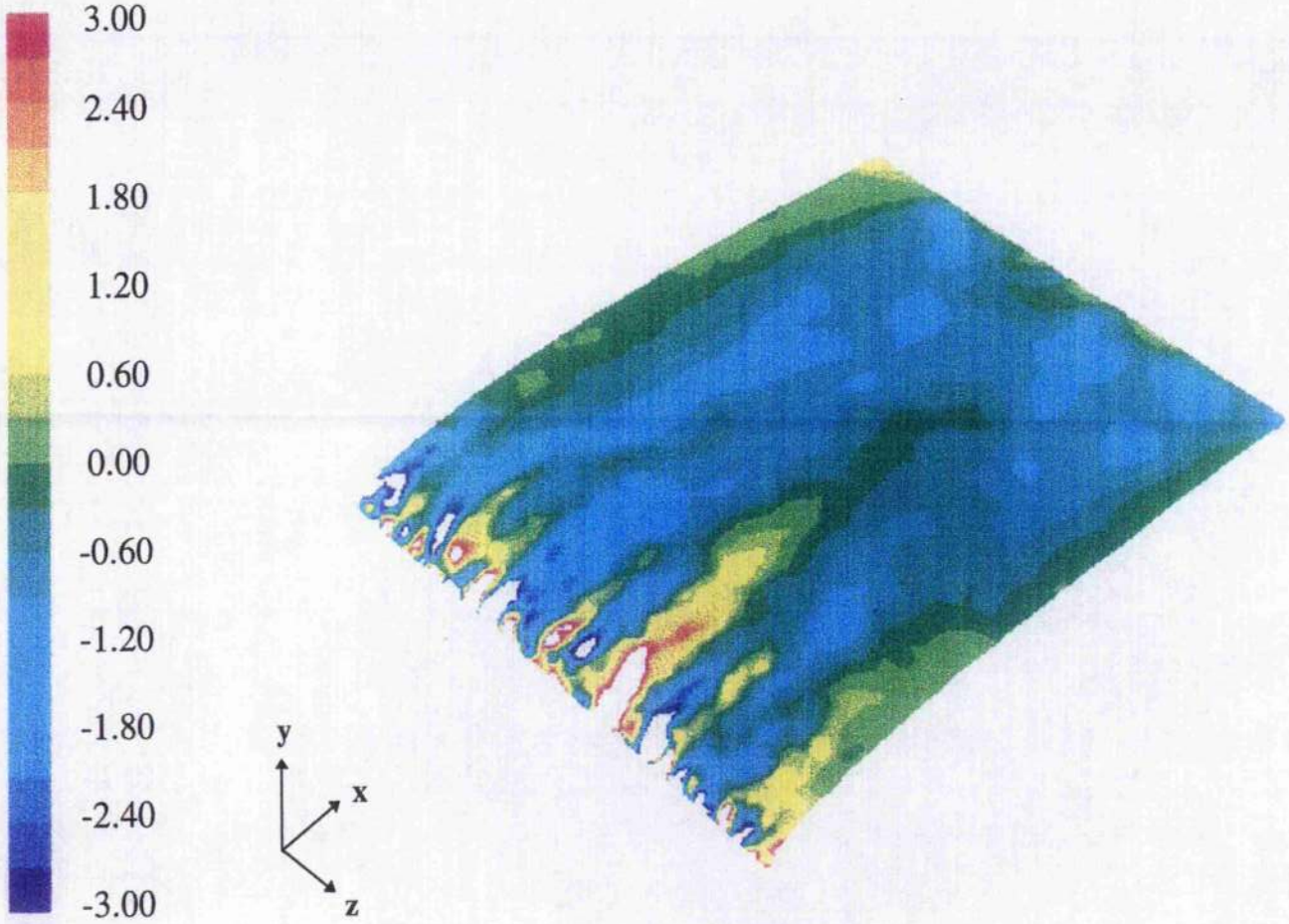

Figure **4.30** *: Contours of Z-Velocity [m/s] on Upper Glovesurface -* ***Endplates (20 cm)***

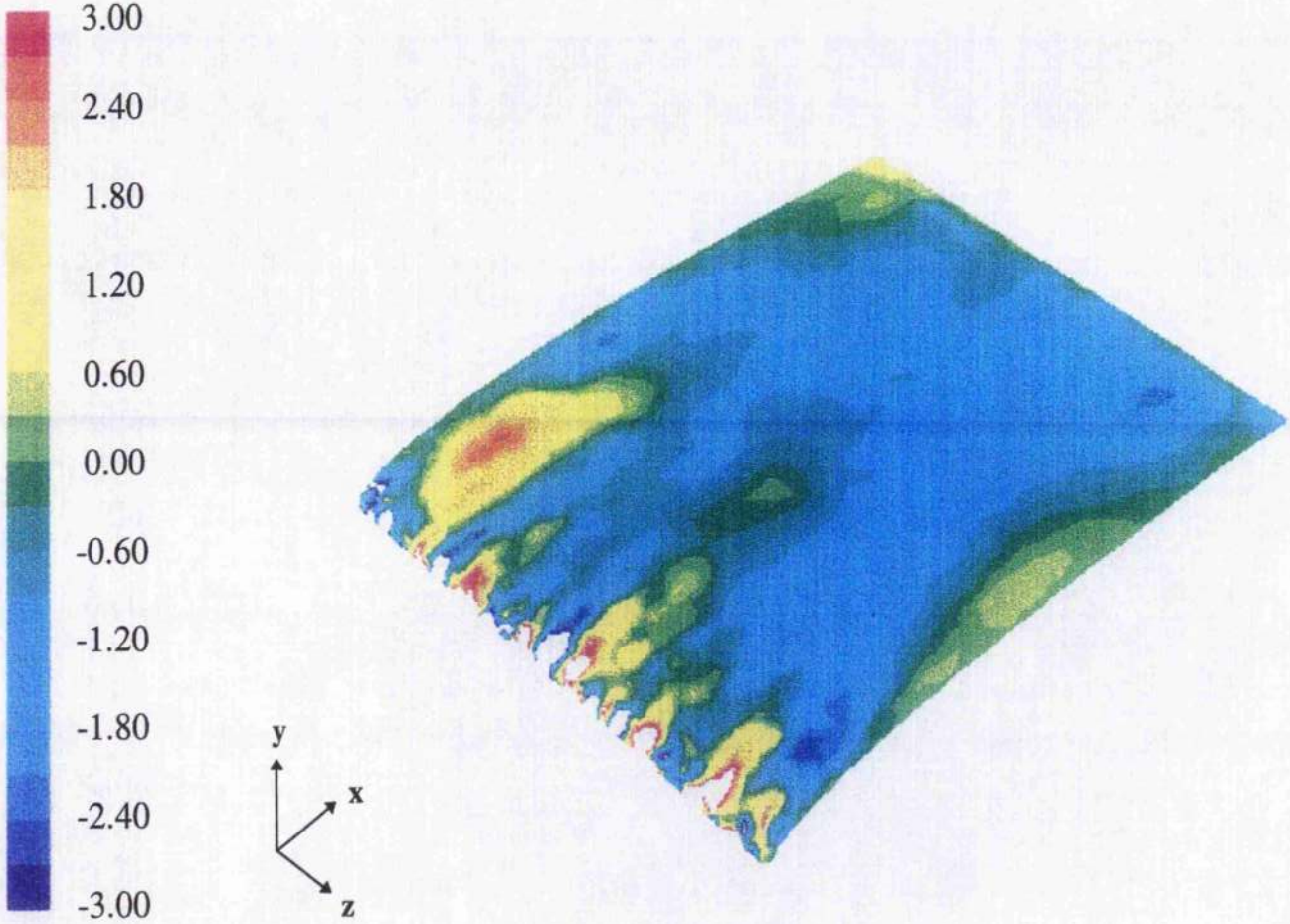

Figure 4.31 *: Contours of Z-Velocity [m/s] on Upper Glovesurface* - ***Specially Designed Endplates***

4.6 WIND TUNNEL TESTING

A wind tunnel investigation was conducted, in addition to the CFD analysis, to evaluate the three-dimensional effects of the flow around a full-scale RPV wing/glove combination and to build confidence in its pressure data acquisition system (Ref.54). Tests were carried out in the Glasgow University "Handley Page" low-speed closed-return wind tunnel. The RPV wing/glove combination was supported by a rig which held the wing in place at the tunnel (Fig.4.32) and located horizontally in its 2.13X1.61 metre octagonal working section (Fig.4.33). Variation of the angle of attack of the wing between 0 and 6 degrees was produced by manually moving a saddle at the top of the rig (Fig.4.34). The saddle rotation was calibrated in degrees by means of an inclinometer. An aperture closer (Fig.4.35) closes tha gap between the wing and the wind tunnel wall. There are two sections :

1. the moving section attaches to the upper and lower surface of the wing and slides through the fixed section when the wing is tilted
2. the fixed section attaches to the wind tunnel.

The two sections overlap somewhat to effect a seal. Experiments were conducted at a speed of 30 m/s. The Reynolds number was $2.3 \cdot 10^6$.

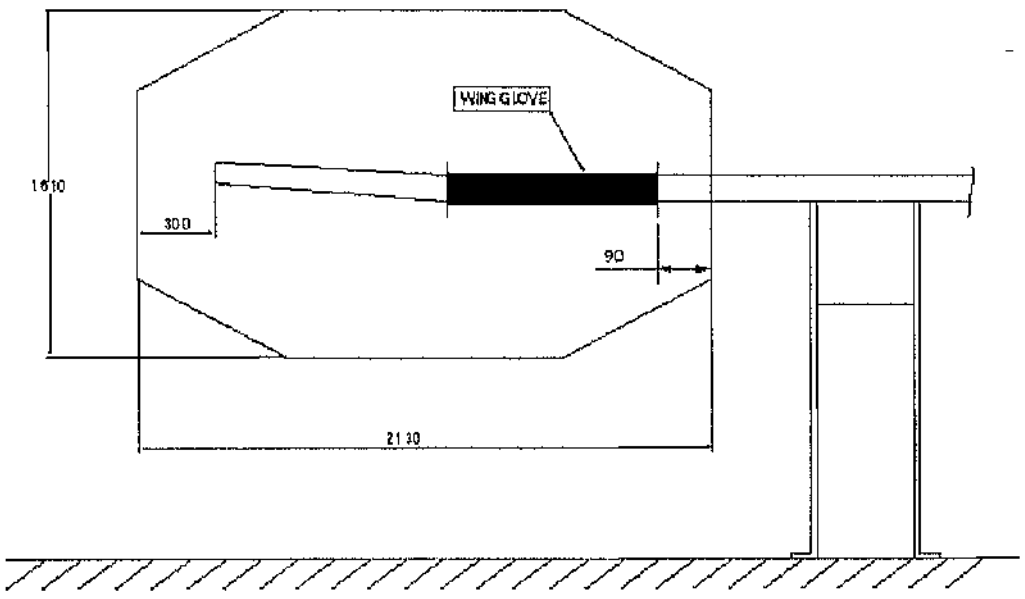

Fig.4.32 Schematic of the Wind Tunnel Test Rig.

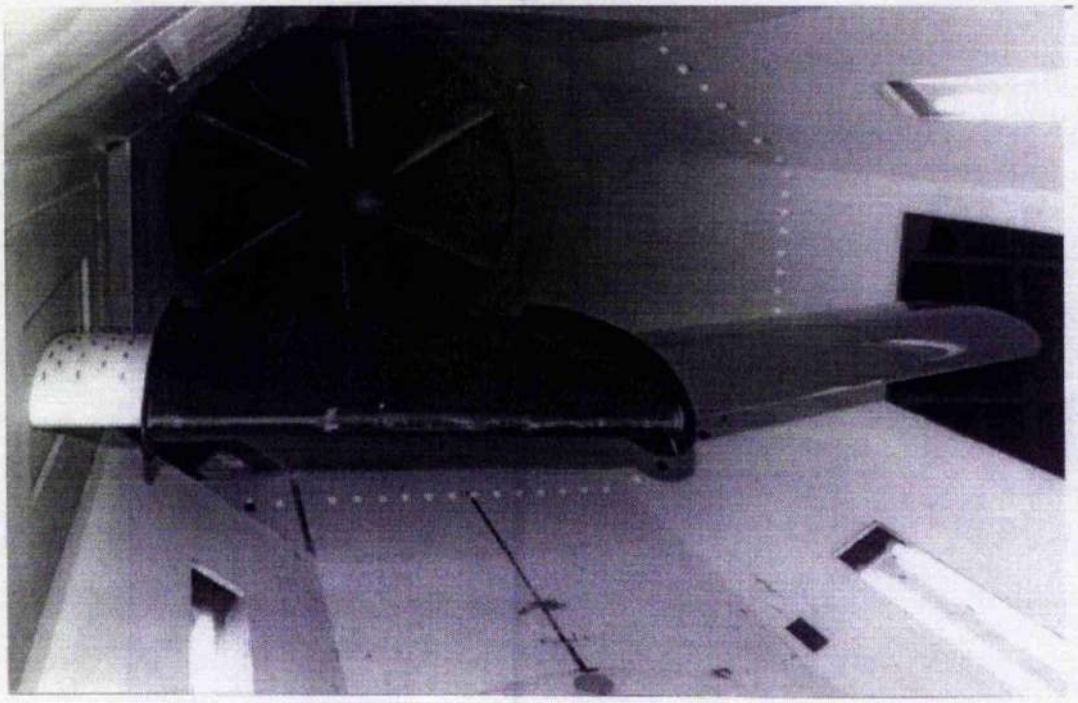

Fig.4.33 The RPV/Wing Glove Combination in the Octagonal Working Section.

Fig.4.34 The Wind Tunnel Test Rig.

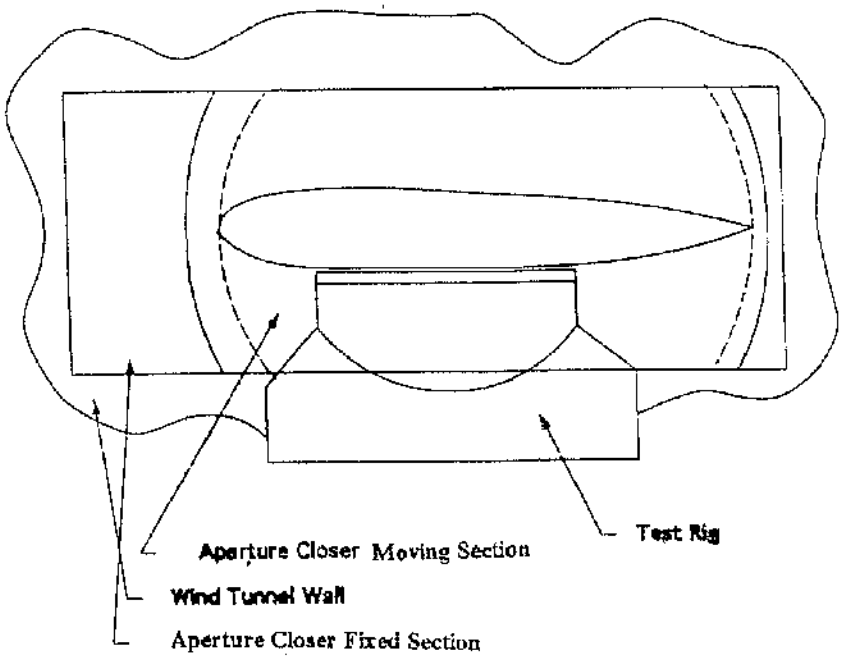

Fig.4.35 Aperture Closer.

Transducers were calibrated when mounted on the glove model prior to commencing tests by using a water gauge. The Scanivalves tube arrangement is depicted in Fig.4.36. During testing port 8 was not functioning, consequently the tube of port 8 was disconnected from the valve (the corresponding pressure tapping is at X = 0.7608 mm, see orifices coordinates in Appendix D). During initial testing the author forgot to apply a correction factor to the free-stream velocity read on the tunnel instrument; this velocity correction affects the Cp values as follows :

$$Cp = \frac{Cp_{STORED}}{\sqrt{K}}$$

where K = 1.1392 (Tunnel Constant). The above formula must be applied on the Cp stored values relevant to the following configurations :

1. No plates and wing extension installed, AoA = 0-6 degrees
5 cm plates and wing extension installed, AoA = 0-6 degrees.

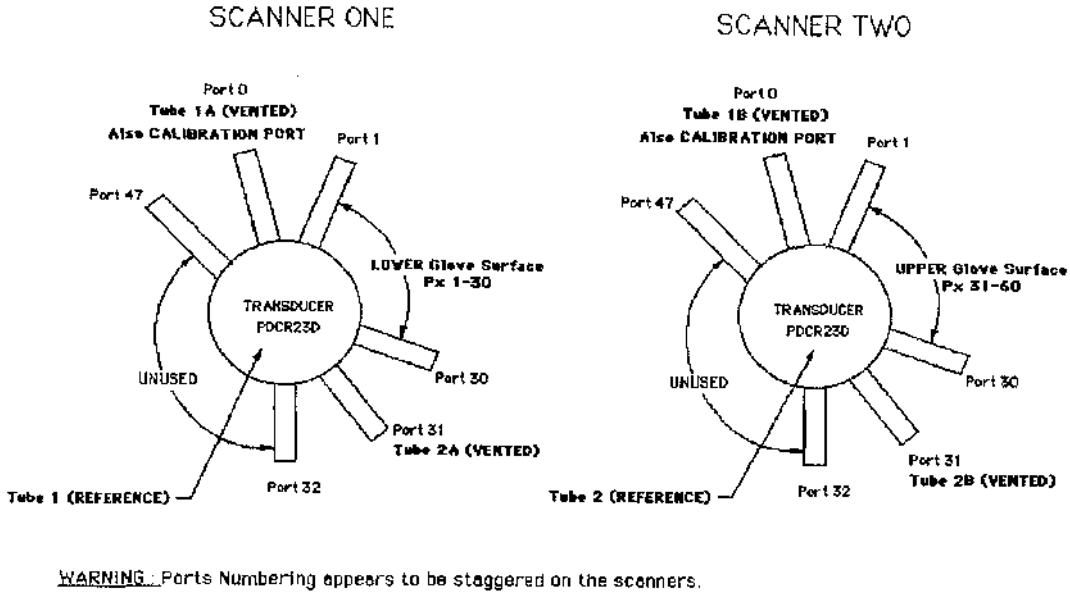

Fig.4.36 Pressure Valves Arrangement.

The author included this velocity correction in the Fortran program written for postprocessing display. Wind tunnel boundary corrections were not applied on the acquired data, because their evaluation is uncertain and dubious; they tend to increase the measured pressure values (Ref.47).

4.6.1 TEST SERIES

Four configurations were tested, with the baseline being the RPV wing/glove combination without endplates and with the wing extension in place. The other configurations were produced by mounting different types of endplates (see Appendix D). Further tests were made to verify that the tip-vortex effect was stronger without wing extension in place and to better evaluate the magnitude of this effect on the configuration being tested.

4.6.2 PRESSURE MEASUREMENTS

Accuracy of measured pressure values depends on the accuracy of the transducers employed (Ref.32) and on the wind tunnel boundary effects (see 4.6). Figures from 4.37 to 4.43 show pressure distributions at the measurement station near the mid glove. Each figure contains six individual pressure distribution readings taken at the same angle of attack and configuration : they differ slightly and this is due to the oscillation of the wing/glove model in the wind tunnel working section. In these figures experimental pressure coefficients are compared against a two-dimensional inviscid incompressible numerical solution at the same (measured) angle of attack. It can be noted that a good agreement between measured and calculated distribution of pressure is attained at an angle of attack (measured AoA) of five degrees, and that agreement is relevant to a calculated AoA = 4 degrees (Fig.4.41); and at a measured and calculated AoA of zero degrees (Fig.4.37). After examining the remaining figures one can conclude that this difference between measured and calculated pressure distribution seems almost absent at zero degrees of angle of attack (the little difference might be due to an error in measuring and setting the wing at zero degrees in the wind tunnel working section) and becomes stronger and stronger as the angle of attack increases. When measured AoA=5 degrees, this difference gets one degree. When measured AoA = 6 degrees, this difference gets larger than one degree (Fig.4.43). In the author's opinion the fact that such a difference gets larger and larger as the angle of attack increases excludes that this is simply due to a mis-measurement of the angle of attack which the wing glove is set at, and it strongly suggests that is mainly owing to the downwash from the tip-vortex. Indeed, the downwash effect is clearly visible in Figures 4.44-4.46, and in Fig.4.46 in particular, where the peak of pressure at the glove leading edge decreases dramatically when both wing extension and plates are removed. Then it can be said as a conclusion, in accordance with the CFD analysis, that the downwash effect cannot be reduced significantly in the current wing/glove combination, even in the event of employment of endplates, although the 5 cm plates seem to behave slightly better in this respect (Fig.4.46). The pressure sensing equipment performed flawlessly and no problems were experienced during testing, thus qualifying the system and its software code for flight testing in the future.

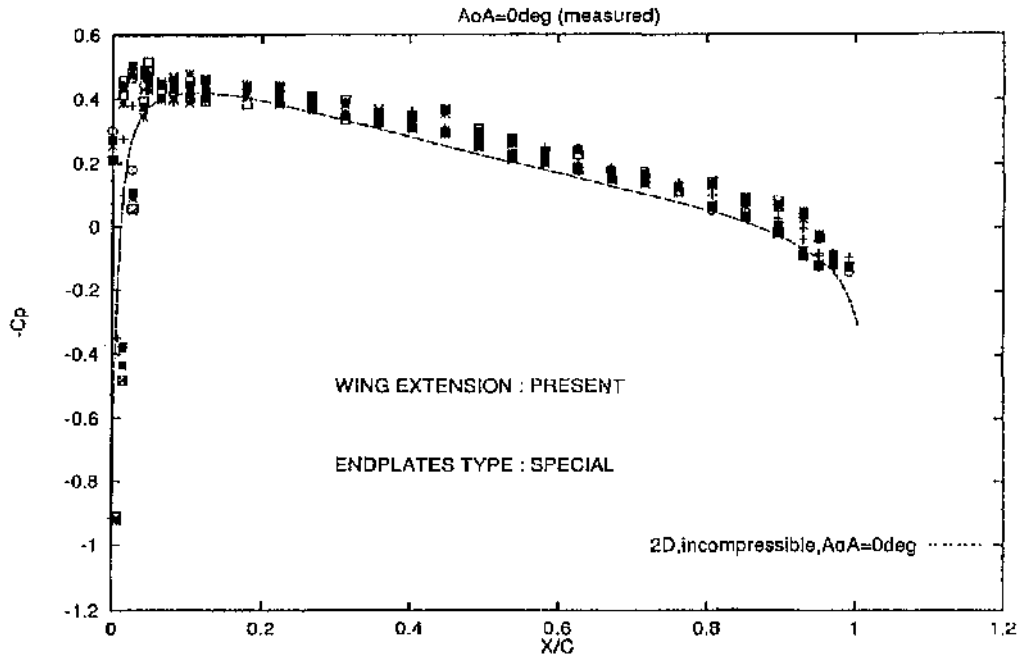

Fig.4.37 Mid Upper Glove Surface Pressure Distribution (AoA=0 deg).

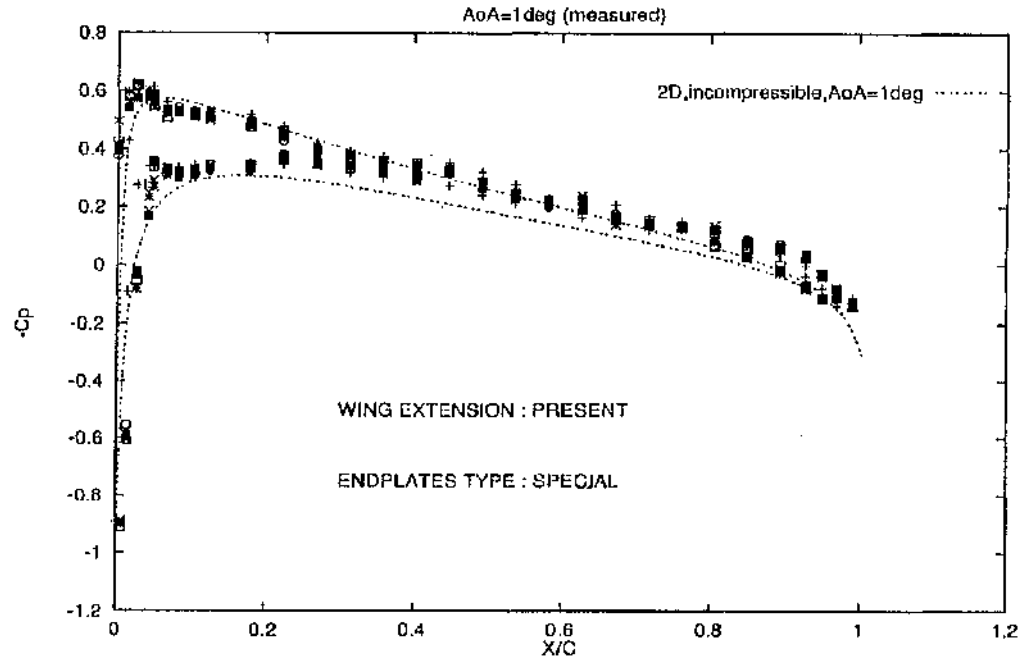

Fig.4.38 Mid Upper Glove Surface Pressure Distribution (AoA=1 deg).

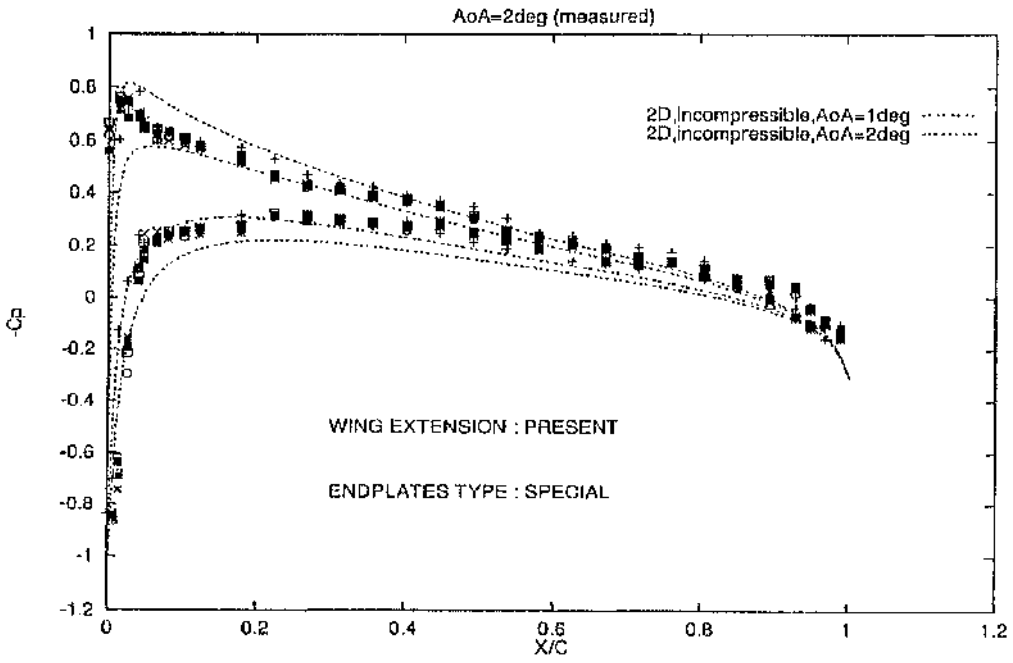

Fig.4.39 Mid Upper Glove Surface Pressure Distribution (AoA=2 deg).

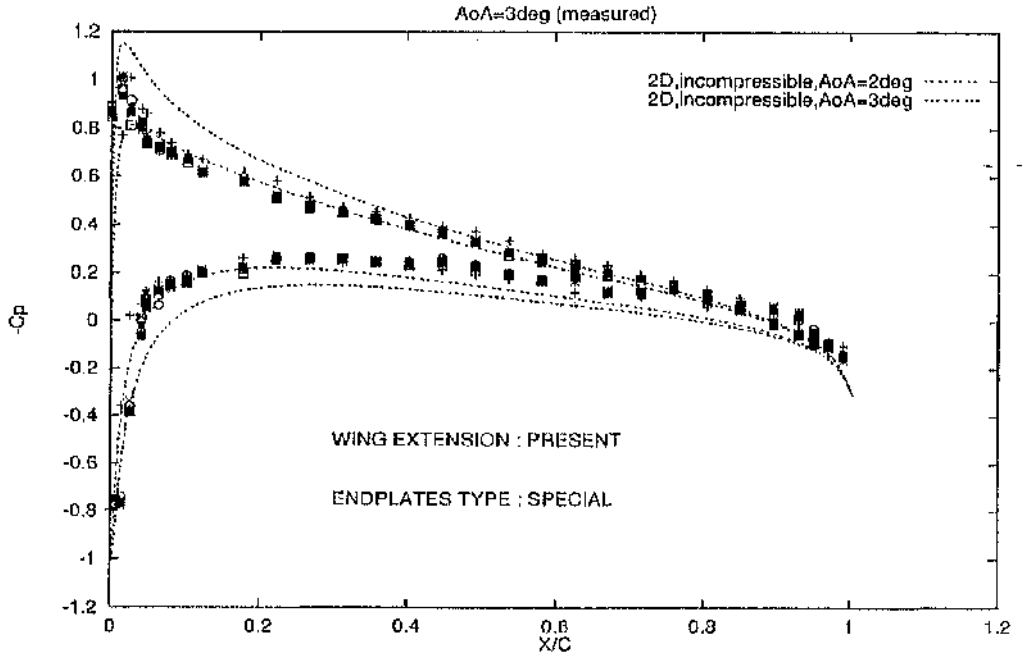

Fig.4.40 Mid Upper Glove Surface Pressure Distribution (AoA=3 deg).

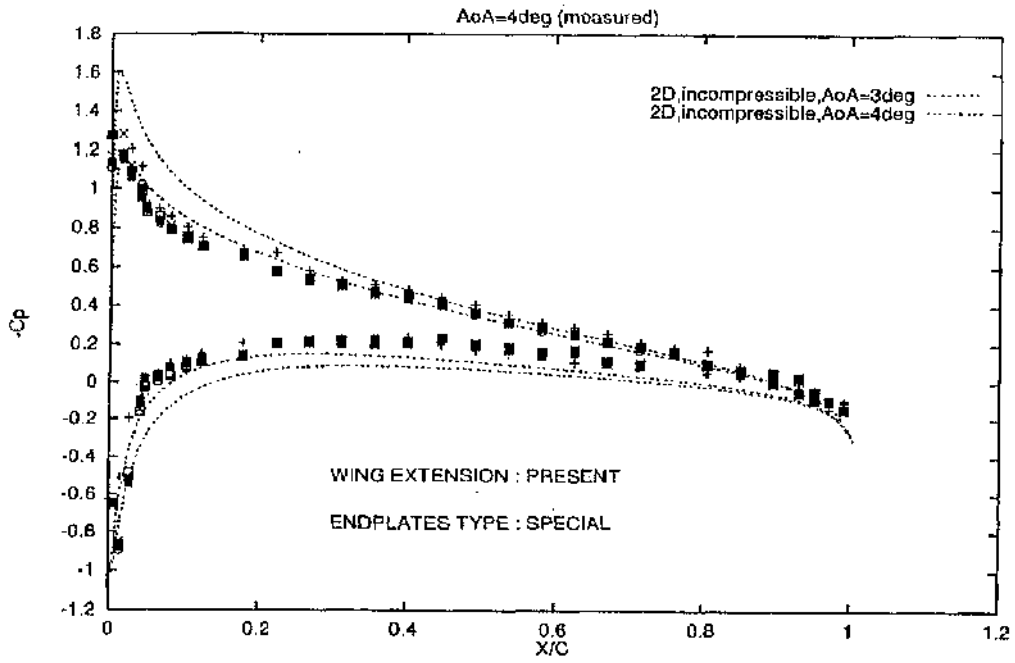

Fig.4.41 Mid Upper Glove Surface Pressure Distribution (AoA=4 deg).

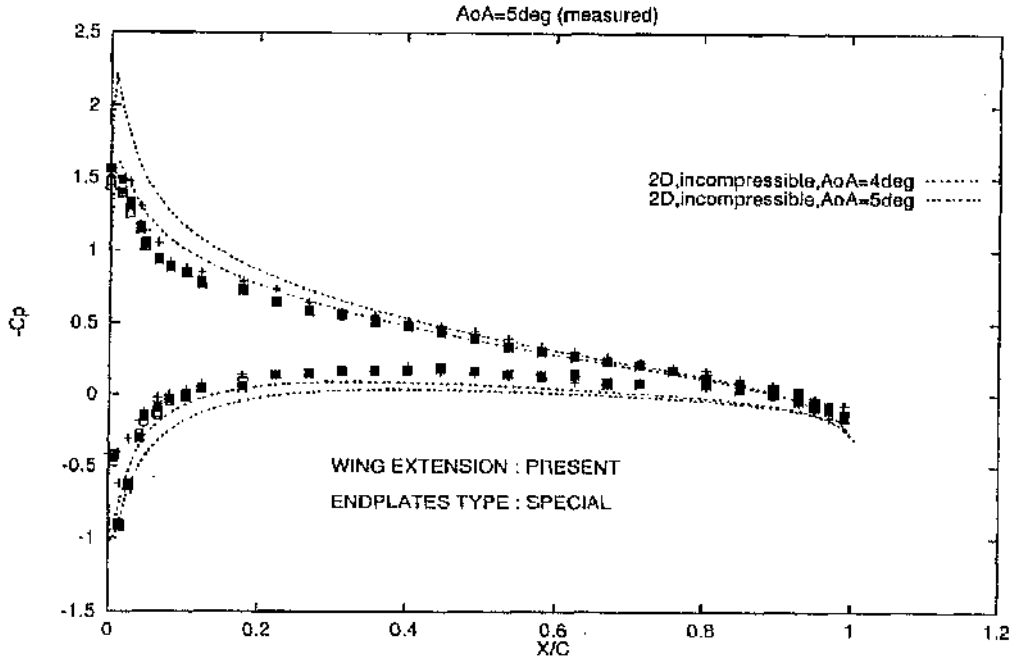

Fig.4.42 Mid Upper Glove Surface Pressure Distribution (AoA=5 deg).

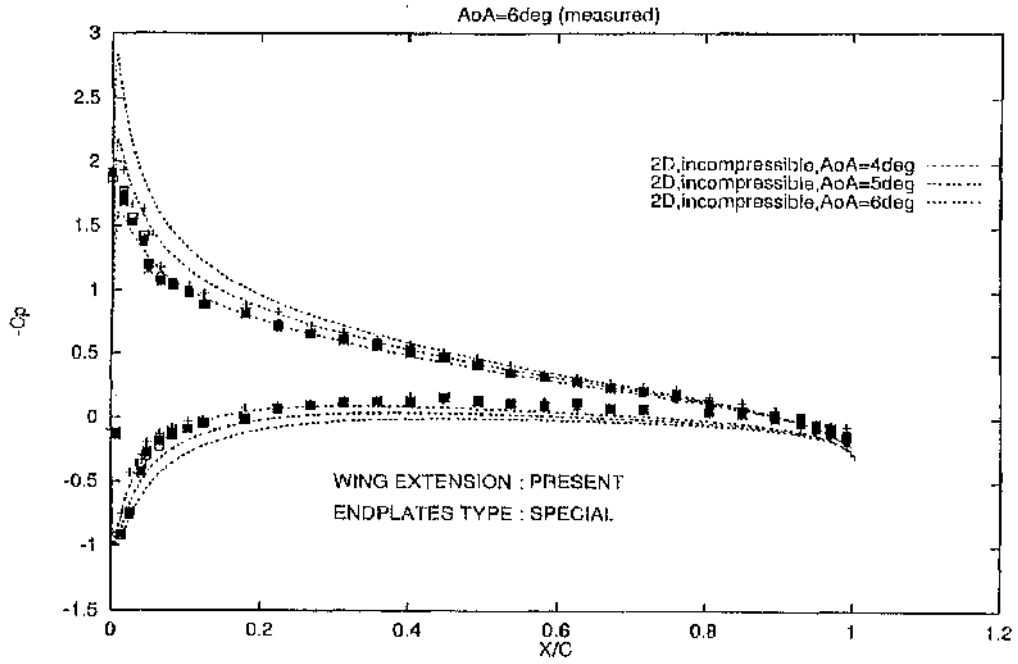

Fig.4.43 Mid Upper Glove Surface Pressure Distribution (AoA=6 deg).

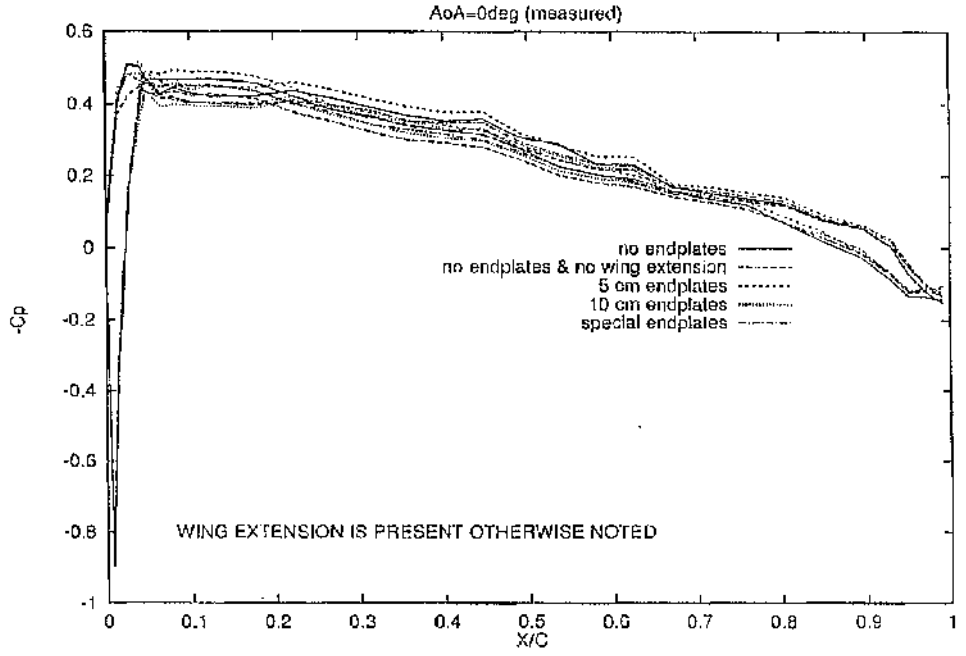

Fig.4.44 Comparison of Pressure Distributions for Different Configurations (0 deg).

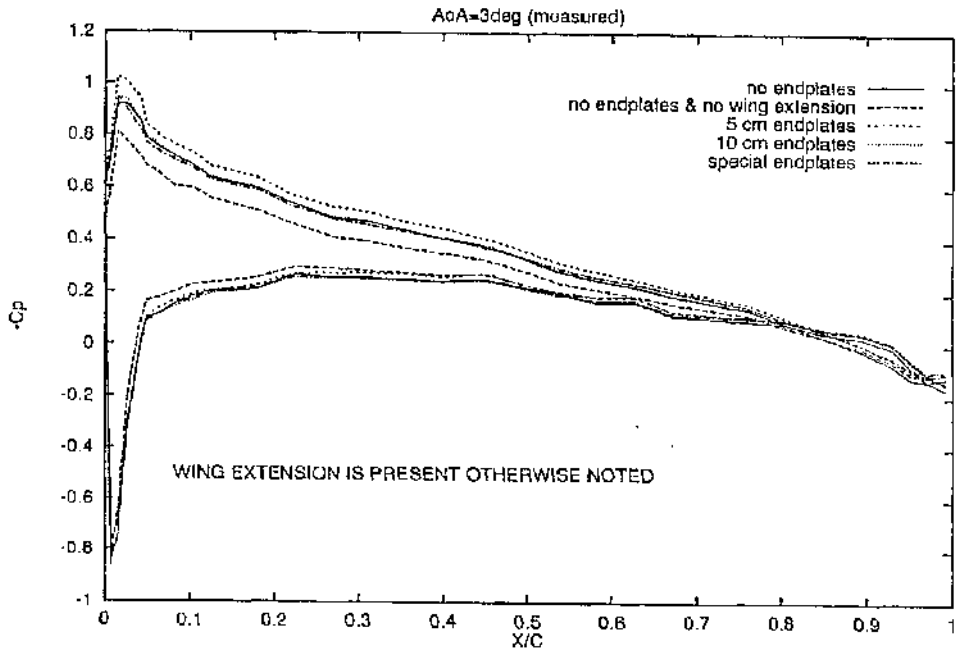

Fig.4.45 Comparison of Pressure Distributions for Different Configurations (3 deg).

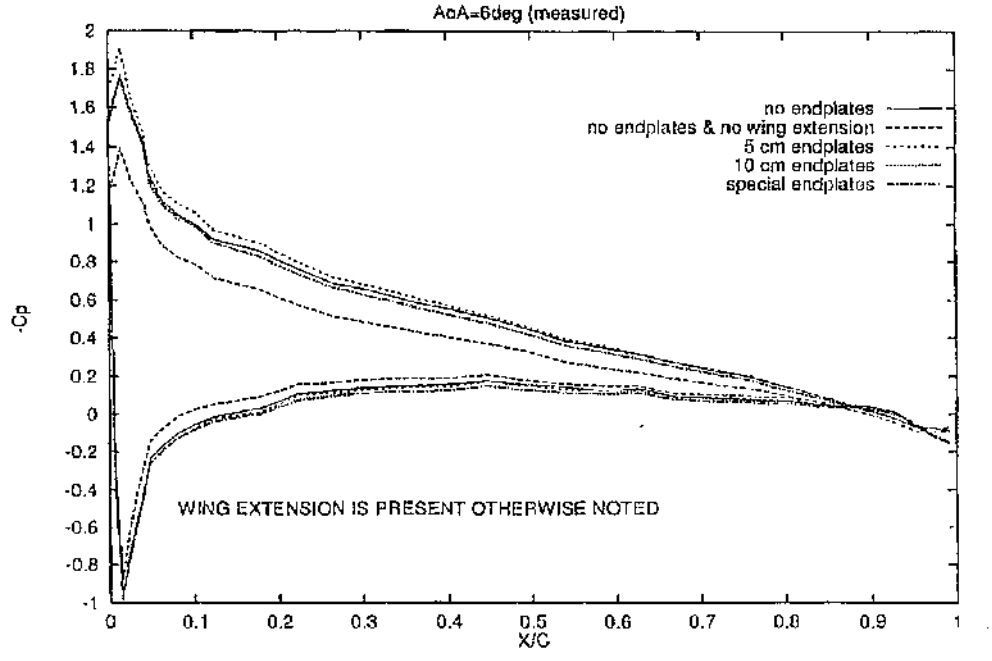

Fig.4.46 Comparison of Pressure Distributions for Different Configurations (6 deg).

4.6.3 SURFACE FLOW VISUALIZATION

Surface flow visualization tests were conducted on the RPV wing/glove combination in order to study the crossflow effect over the glove surface, which could disturb the development of the boundary layer and consequently destroy the bidimensionality of the flow. Surface flow visualization was performed by applying to the glove upper surface odina-oil as the moving medium treated with Saturn Yellow "Dayglo" fluorescent powder as the indicative dye. The viscosity of the mixture was adjusted by trial and error. Despite the name, odina-oil looked like a sort of poly glycol and experience has shown that this material has a low viscosity, making it difficult to use (Ref.47); neverthless, preliminary testing with other liquids available at the Department laboratory facility proved them even more disappointing. Odina-oil was cleaned up with soap and water. Fluorescent lighting permitted black and white photographs to be taken with the tunnel off. Shutter speed and time exposure for the camera settings were again determined by trial and error. Photographs were retouched digitally to reduce an annoying reflex (still visible) and to enhance the image quality. Retouching was done by varying the level of brightness of different areas of the image. Both retouched images and original photographs are proposed here.

4.6.3.1 RESULTING PATTERNS

Different types (in size and shape) of endplates were fitted and tested at an angle of attack of four degrees, whilst the baseline configuration was tested at angles of attack between 0 and 4 degrees. Photographs (see Figures 4.47-4.54) show that endplates and the wing extension can substantially reduce the crossflow on the upper surface of the wing glove. Increasing the height of the endplates reduces the crossflow as it may be expected : compare Fig.4.53, which depicts the glove with endplates 10 cm high, to Fig.4.52 with the glove fitted with endplates 5 cm high (note that 20 cm plates performed superbly in the CFD study, although they were not wind tunnel tested because of their size). "Special" endplates (Fig.4.54) performed best among the types tested. As it may be expected the crossflow effect gets larger as the angle of attack increases (compare Fig.4.47 to Fig.4.50). The crossflow effect can be clearly seen in Fig.4.51, where there are no endplates installed and the wing extension has been removed; however, this is a case

of academic interest only, as the RPV cannot fly without the wing extension (the glove blocks the inner ailerons). It is concluded that, since the crossflow from the photographs appears to be negligible in the configurations of practical interest (the previous CFD study showed it to be less than 2% of the free-stream velocity at AoA = 3.59 degrees), the flow can be regarded as nominally two-dimensional at least at the measurement station of the glove. Glove fitted with Special endplates gave the largest area of less disturbed flow.

4.7 FINAL REMARKS

After the CFD and the wind tunnel study a conclusion can be drawn on what type of endplates should be employed for flight testing on the RPV. It has been highlighted that there is no debate upon the downwash issue, since this effect was strongly present in every configuration analysed. Despite this, it does make sense the use of endplates, as they are capable of significantly reducing the crossflow effect, which was negligible more or less in every configuration with endplates and quantified by the CFD analysis in about less than 2 % of the free-stream velocity at the measurement station. Large endplates performed best, but their size make them impractical for flight testing on the RPV. Having said that, for pressure measurement the best compromise are the 5 cm plates, which are small and light. If surface flow visualization is planned, it is convenient to have as large an area of less disturbed flow as possible, hence the Special plates would be the best second choice. In-flight surface flow visualization is not as remote as it would seem, since the IR technique (Ref.4) would be quite suitable : it requires no surface coating, uses remote sensing, and the same setting is used for all flight conditions.

Fig.4.47 Surface Flow Visualization of the Baseline RPV Wing/Glove Configuration at AoA = 0 deg (corresponding photograph is shown below).

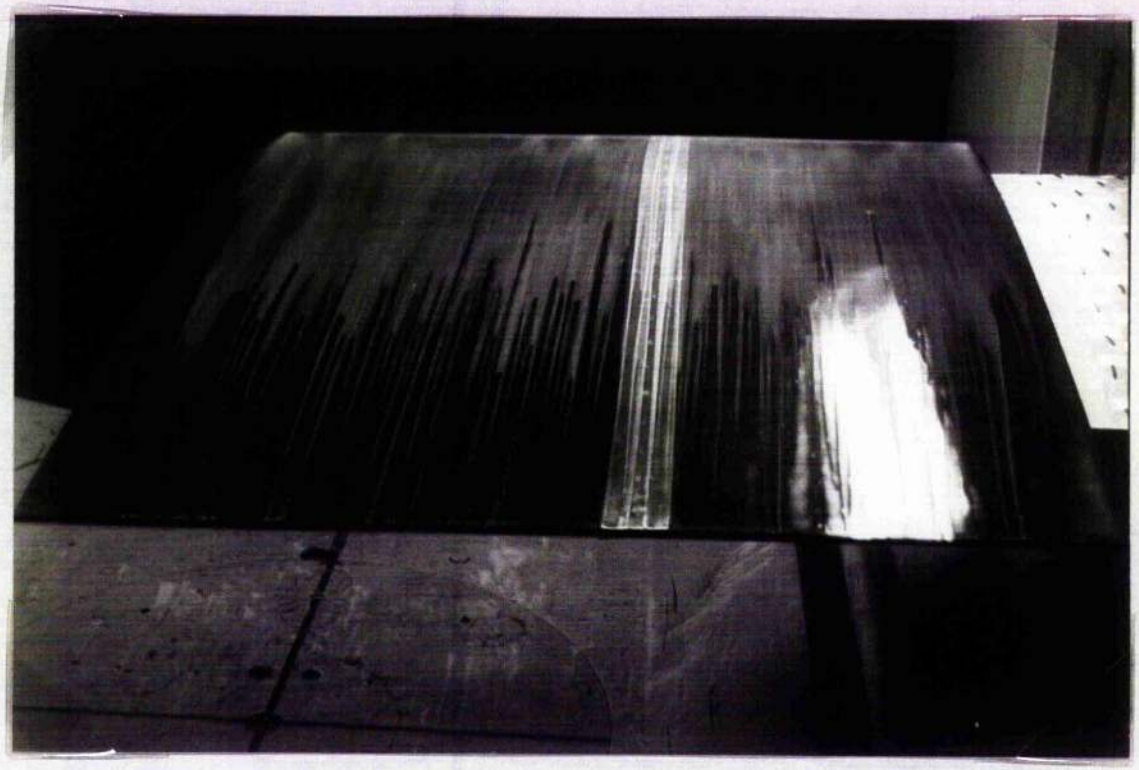

Fig.4.48 Surface Flow Visualization of the Baseline RPV Wing/Glove Configuration at AoA = 1 deg (corresponding photograph is shown below).

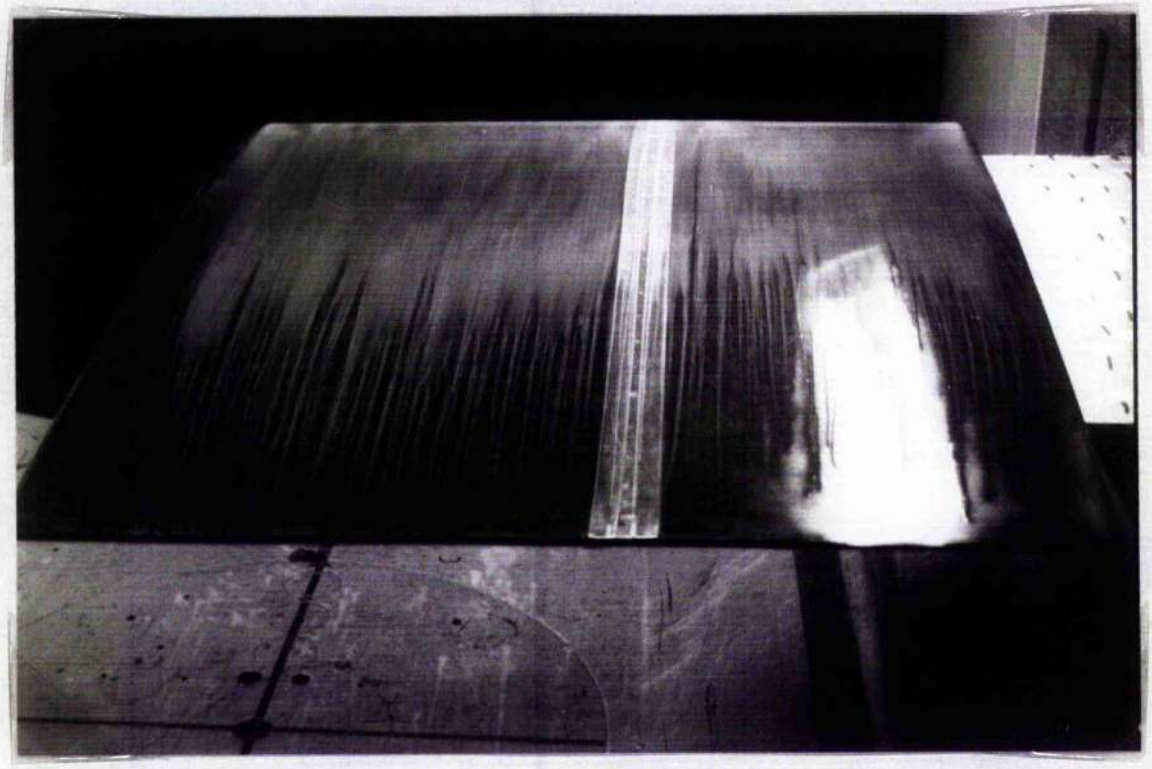

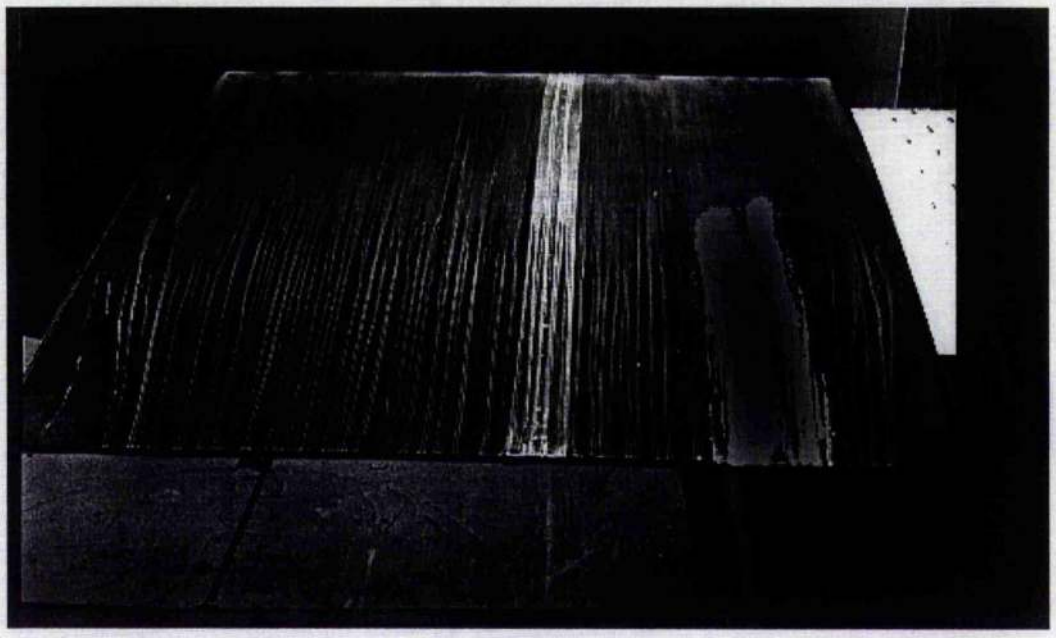

Fig.4.49 Surface Flow Visualization of the Baseline RPV Wing/Glove Configuration at AoA = 3 deg (corresponding photograph is shown below).

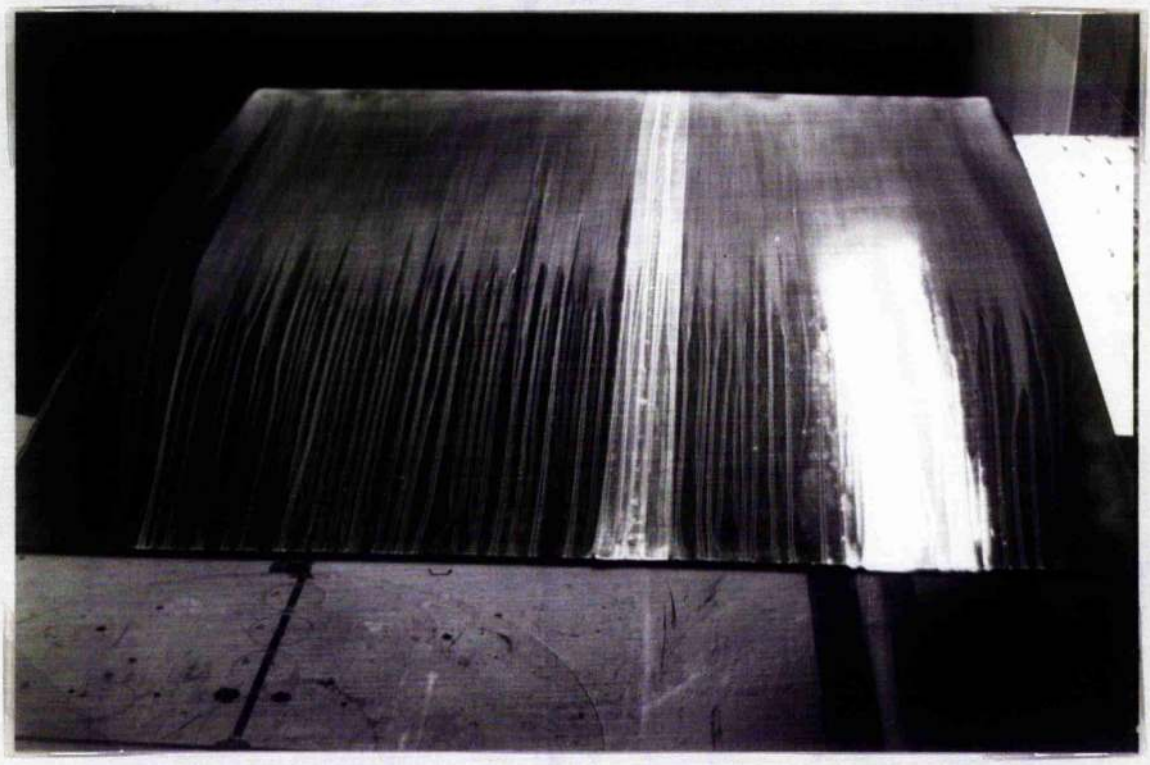

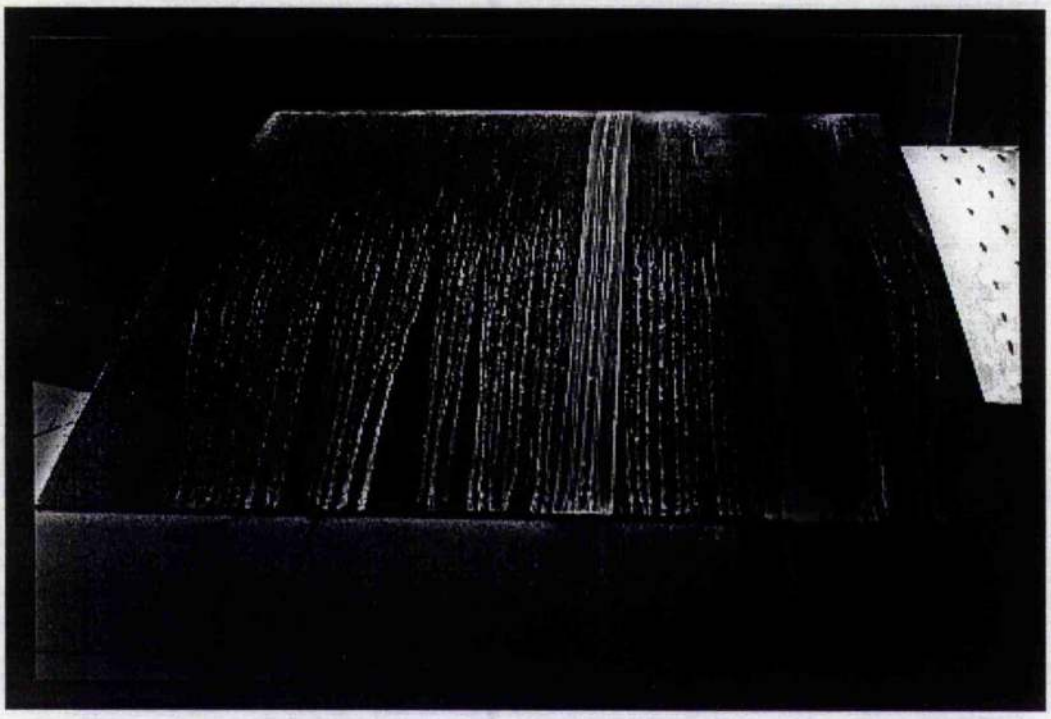

Fig.4.50 Surface Flow Visualization of the Baseline RPV Wing/Glove Configuration at AoA = 4 deg (corresponding photograph is shown below).

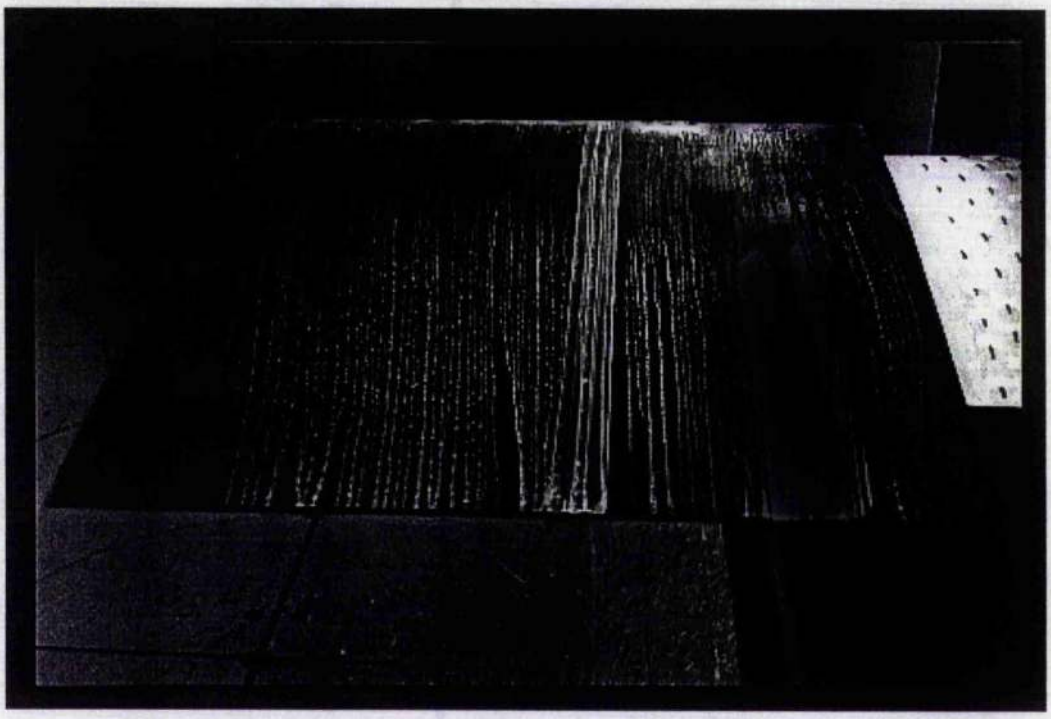

Fig.4.51 Surface Flow Visualization Without Endplates and Wing Extension at AoA= 4 deg (corresponding photograph is shown below).

Fig.4.52 Surface Flow Visualization With 5 cm Endplates and Wing Extension at AoA= 4 deg (corresponding photograph is shown below).

Fig.4.53 Surface Flow Visualization With 10 cm Endplates and Wing Extension at AoA= 4 deg (corresponding photograph is shown below).

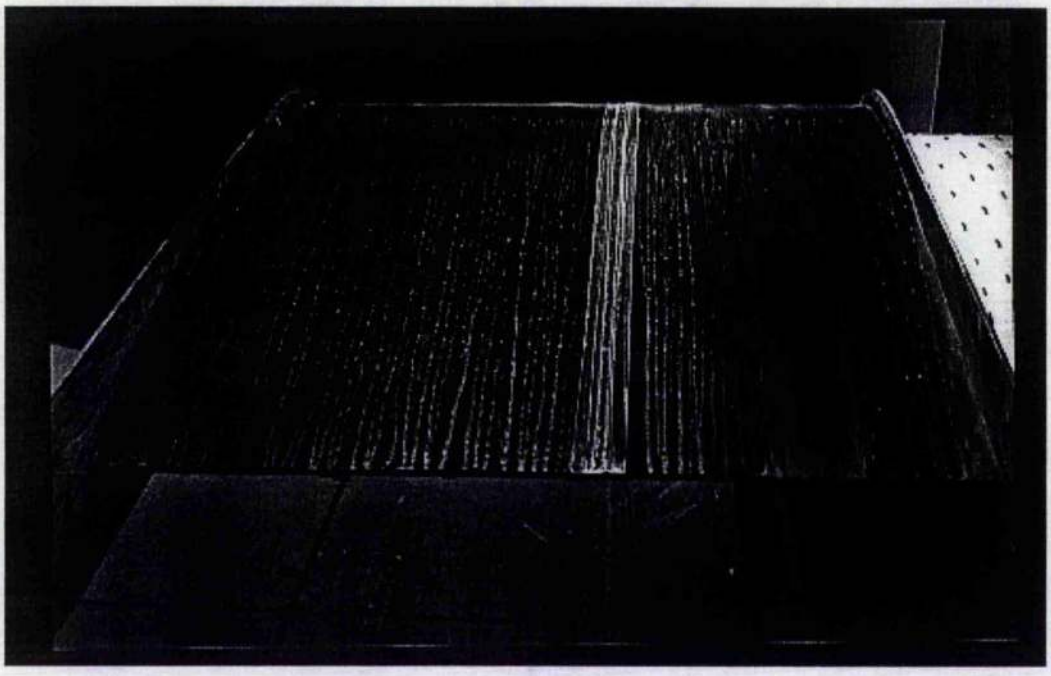

Fig.4.54 Surface Flow Visualization With Special Endplates and Wing Extension at AoA= 4 deg (corresponding photograph is shown below).

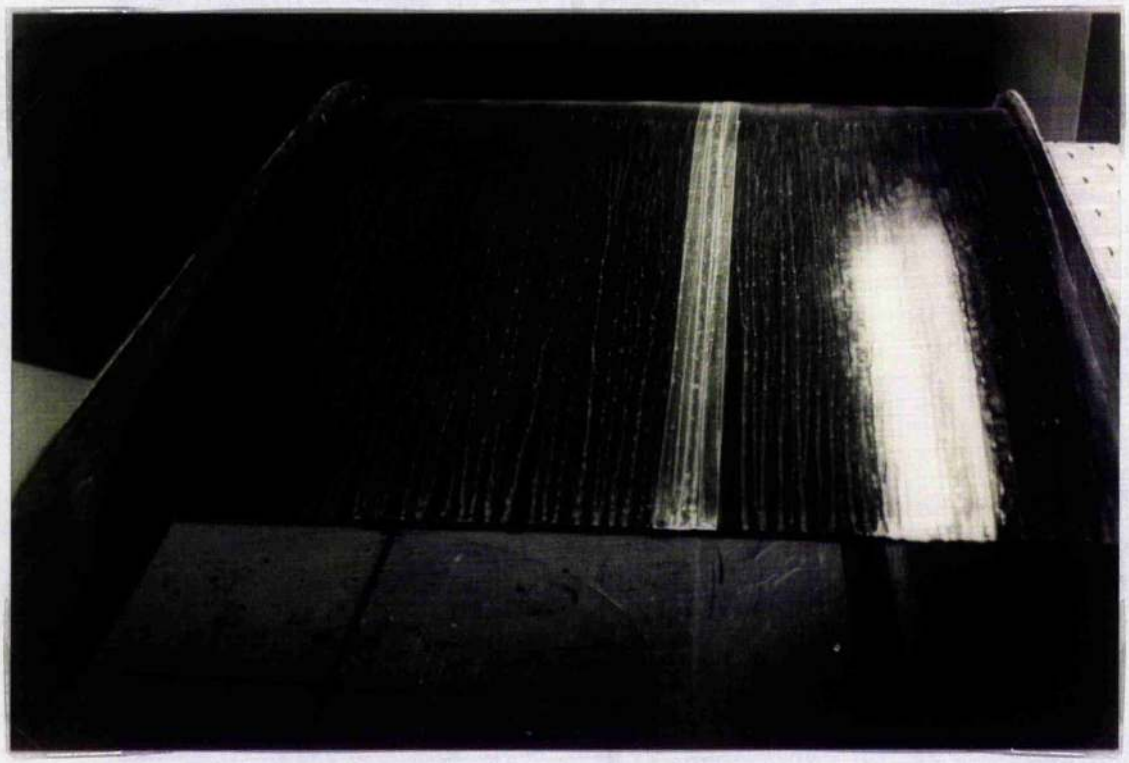

5. AIR DATA ACQUISITION

As we said earlier, scope of the RPV flying laboratory will be to perform laminar acrofoil research by means of in-flight measurements, such as monitoring the pressure distribution over the test profile of the wing glove. This task requires also to know the local angle of attack in vicinity of the glove, plus the air temperature. Dynamic pressure is required primarily to calculate Cp values which use impact pressure as reference (see 3.7.3). Combining the temperature and dynamic pressure data can generate true airspeed (see also equations in Ref.48). Temperature data also generate altitude and static pressure. Similar combinations are employed to provide the full spectrum of air data information, but all of that information has its basis in the temperature and pressure measurements made by the sensors (Fig.5.1). Pressure or temperature measurements of the air through which an aircraft is flying requires a sensing element be exposed to the ambient air. All sensing elements may be heated to prevent icing that would compromise the unit's accuracy.

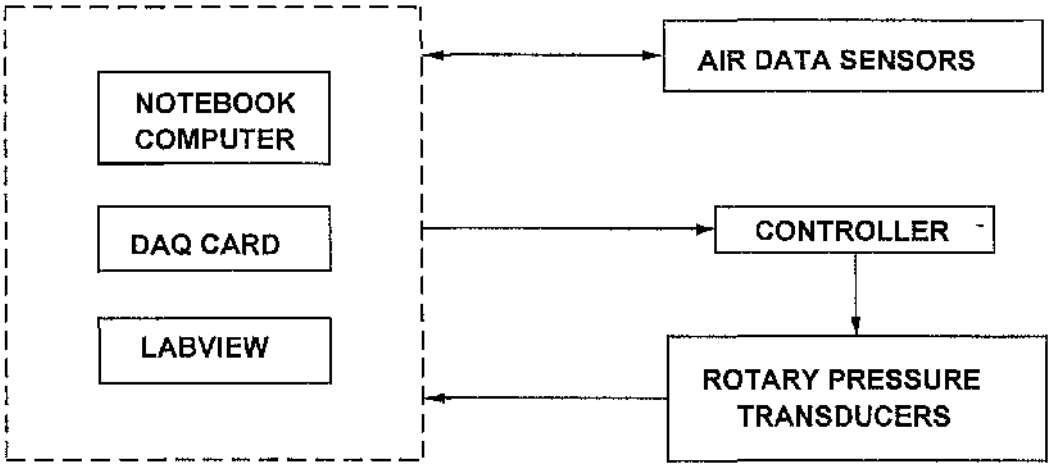

Fig.5.1 Block Diagram of Data Acquisition System.

5.1 PRESSURE SENSING

The pressure distribution in mid glove surface has been measured by the S9GM pressure multiplexer described in section 3.7.3, which is wind tunnel tested. Dynamic pressure can be measured by the same S9GM using a pitot-static system

connected to the Scanivalve transducers : the reference value will be again the free stream static pressure, while an actual Scanivalve port will measure the total pressure, thus giving the dynamic pressure as the differential pressure transducer output. Let us check out whether the transducer selected range (see 3.7.3) is still appropriate. Maximum estimated dynamic pressure was :

$$q_\infty = 1531 \text{ Pa} = 0.22 \text{ psi}$$

which is what the Scanivalve transducer will measure, being by definition :

$$q_\infty = P_t - P_\infty$$

that is pitot pressure minus static pressure. The selected transducer range was ± 0.72 psi, perfectly adequate.

For pressure measurements, flush ports, pitot-static probes or pitot probes provide access to the air for free stream static and/or total pressures (Ref.49). Impact pressure results from force of the moving airstream against the aircraft as it flies. The force of the moving air against the back of the closed tube (called a pitot probe) facing into the airstream creates impact pressure. More challenging than the pitot measurement is obtaining accurate static pressure, that is because the aircraft influences and disturb the atmosphere through which it flies. The disturbed atmosphere in turn affects the ability to get an accurate static pressure measurement. One common way to measure free stream static pressure involves the use of flush static ports on the sides of the fuselage, but this solution requires finding locations on the aircraft fuselage undisturbed by moving air, by performing an extensive study of the aircraft pressure distribution. For this reason the author prefers placing the free stream static pressure measurement location off the fuselage, on the head of a pitot-static probe. By moving the static pressure measurement away from the surface of the aircraft the errors and repeteability problems caused by the fuselage are largely eliminated. Fig.5.2 shows a miniature pitot-static probe with static and total head pressure pickups, specifically designed for RPVs; vanes for angular displacement measurements (see 5.3) are also visible.

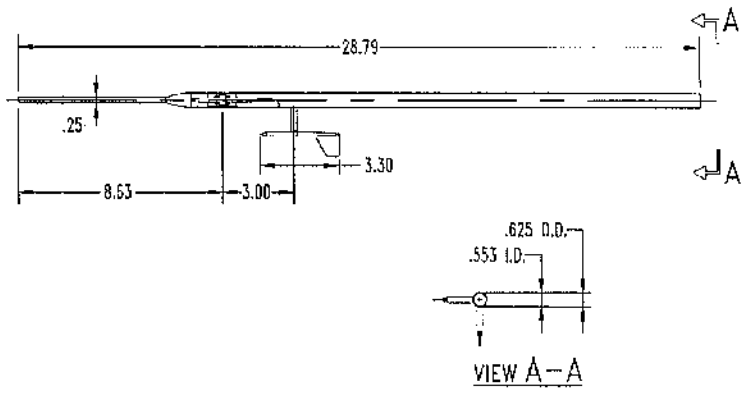

Fig.5.2 100400 Mini Air Data Boom (Courtesy of Endevco UK Ltd).

5.2 TEMPERATURE MEASUREMENT

Air temperature measurement devices can be easily incorporated in a pitot-static probe. Four types of sensors are available, being based on the same principle, that is an element which changes its electrical resistance with any air temperature changes :

- resistance temperature detector (RTD)
- thermistor
- thermocouple
- solid state resistor (SSR)

RTDs and thermistors are a relatively common class of devices used for measuring temperature. RTDs are used in the temperature range of -270 °C to 1100 °C to give a measurement accuracy of ± 0.5 % full scale. They have a linear response, but a big disadvantage is the extra care required in the connection wiring, which can alter the total resistance of the RTD and affect the measurement. Thermistors are much smaller and cheaper but since they use semiconductors, their response is definitely non-linear, although they give a fast output response to temperature changes; on the

other side, they have a lower measurement sensitivity than RTDs, because their small size makes the self-heating effect greater. Thermocouples have high accuracy ($\pm$ 0.2 %) but their response is not quite linear. In addition, they require a "reference junction" to be mantained at 0 °C, thus making them impractical. In conclusion, an SSR seems the best solution, and indeed is very much the norm on air data booms. An SSR has a linear response with a VDC output (VDC output is more desiderable than a VAC one because the latter requires a more complex pickup installation involving a bridge), and wiring will not affect the measurement. It is a device available in different Ohms values : being the voltage the same, the higher the resistance, the lower the current, but higher the noise; it is advisable to choose a middle value. Temperature range also varies; -5 - +30 °C range should be sufficient for flying at 1000 ft during summer. LM135H (Ref.50, p.1-1165) shown in Fig.5.3 is a possible candidate; it has a rather uncommon output proportional to °K. An SSR is relatively expensive compared with other sensors (LM135H costs circa nine pounds).

5.3 ANGULAR DISPLACEMENT MEASUREMENT

We need to measure two angular displacements :

- angle of attack
- angle of sideslip

which both are a measure of absolute angular positions. Rotational displacements can be measured by four types of devices :

- encoder
- resolver
- syncro
- potentiometer

Encoders are out of consideration because they measure a relative angular displacement only. The other two are expensive and have a VAC output. This leaves the servo potentiometer as the remaining choice, which is universally used in our application.

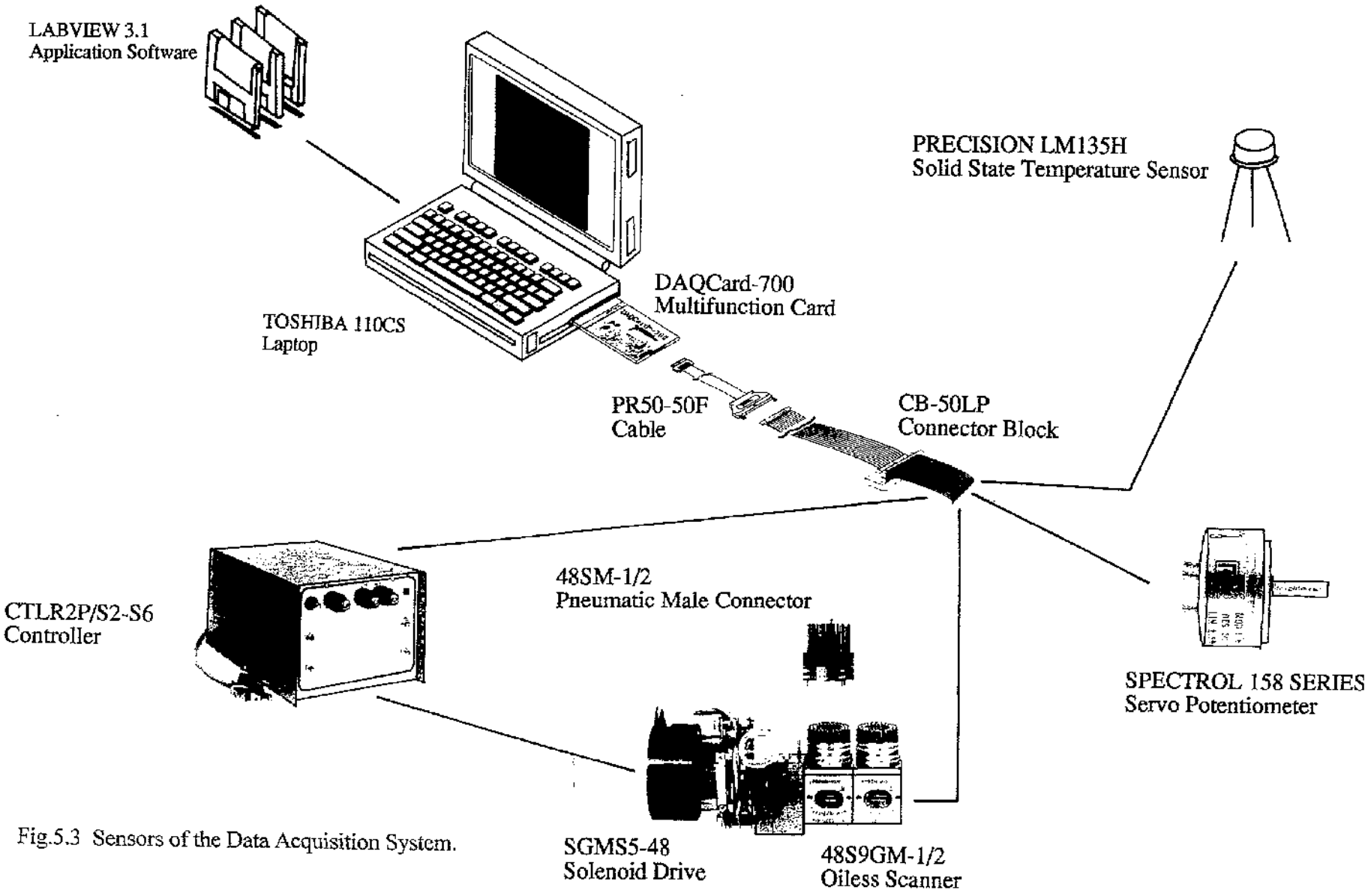

Fig.5.3 Sensors of the Data Acquisition System.

Inside a servo potentiometer there is a wiper that rotating changes instantly the lenght of the resistor in contact with, thus yelding a linear voltage response. Note that the electrical rotation of a potentiometer may be larger than the mechanical one : the latter cannot be exceeded because of mechanical failure. Fig.5.3 shows a possible candidate, the SPECTROL 158 Series continous rotation servo potentiometer (Ref.50, p.1-732), with a resonable price. Usually a vane is mechanically coupled to a potentiometer pickup which provides an output signal proportional to vane travel, thus measuring angles of attack and sideslip. Vanes are are commercially available either as stand-alone elements or as flow angle sensors incorporated in pitot-static probes (Ref.51).

5.4 LOCATION OF AIR DATA SENSORS

On the market are available so called multifunction probes, which have incorporated vanes for flow angle measurements in addition to the already present pitot-static system (Fig.5.2). Others, more sophisticated models, provide pitot and static pressure measurements in addition to pressures used to calculate angle of attack and angle of sideslip (Ref.52), thus reducing external sensors in number and reducing mounting locations. This contributes to aircraft weight savings; however, a single multifunction probe positioned off the RPV nose would not measure the "local" angle of attack in the vicinity of the glove, that is an angle of attack affected by the fuselage interference and three dimensional aerodynamic effects (see 4.1). Hence, in the author's view should be favoured a solution which involves positioning a stand-alone wing-mounted flow angle sensor (Fig.5.4) near the glove for measuring the local angle of attack, and a multifunction probe off the RPV nose to measure angle of sideslip and free stream pitot-static pressure (Fig.5.5). All air data sensors must be connected to the ADC card (see Fig.5.3 and section 3.7.6) : they are subject to the same interface considerations of section 3.7.7. Basically, there are two ways to implement the above concept : an in-house solution and a commercial solution.

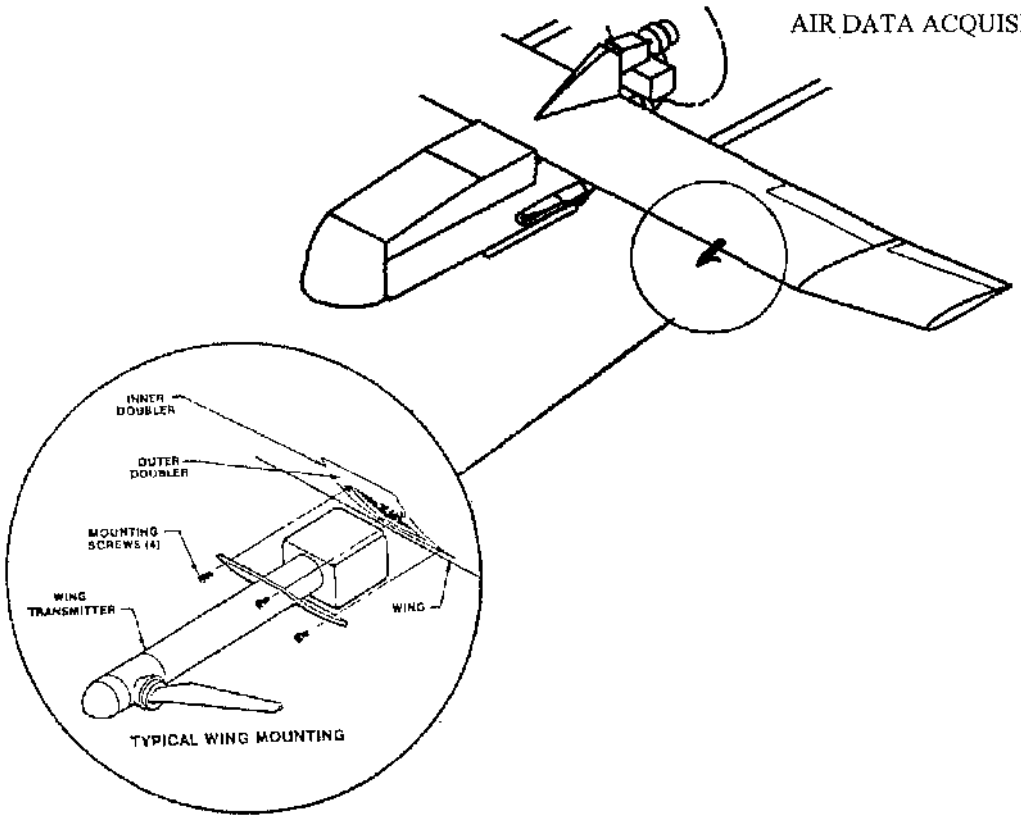

Fig.5.4 Wing-Mounted Flow Angle Sensor (Typical).

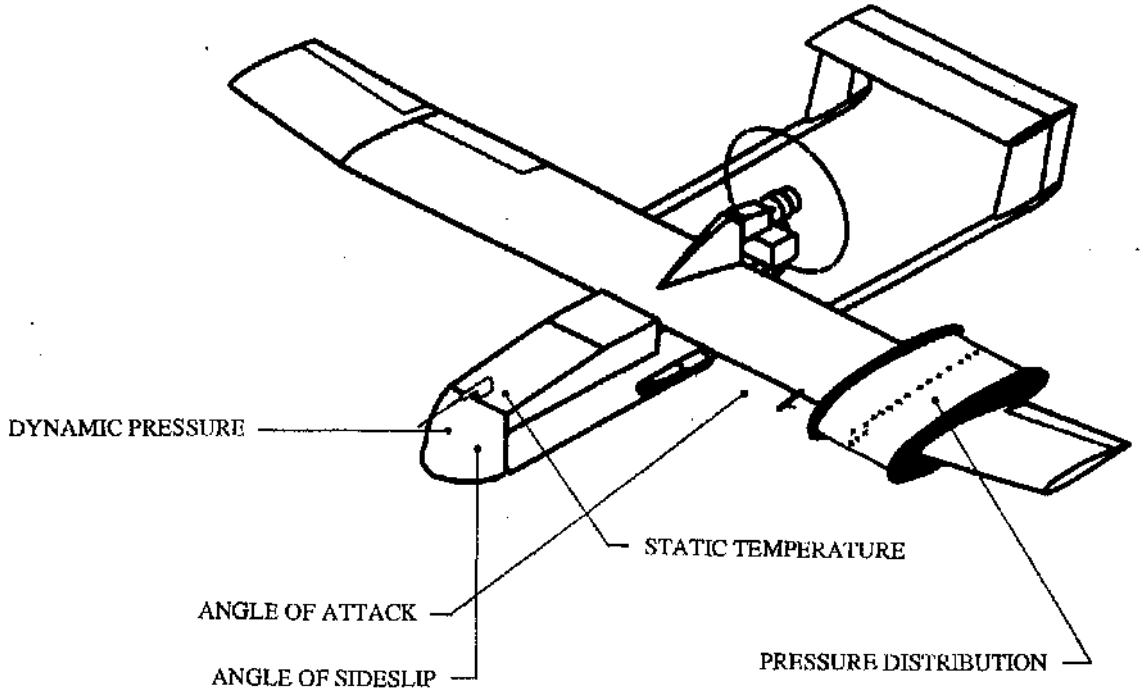

Fig.5.5 Flying Laboratory Sensors Location (Present Study).

Certainly the in-house solution is cheaper and could employ the sensors selected in the previous sections (subject to market availability), but it needs design expertise, and most of all manpower and wind tunnel time. In addition, the in-house solution must develop a swivel-head air data boom (Fig.5.6) with static and total head pressures obtained from a gimbal-mounted weathervane nose that swivels at least in two directions, in order to account for pitot error, since reliable pitot pressure sensing requires a probe constantly parallel to the airflow. Conversely, commercial straight-nose boom pitot inlet designs have been refined through years of aerodynamic research for accurately measuring pitot pressure when the local flow angle at the probe is not aligned with the probe head. There are even so-called shielded pitot probes that can provide essentially zero pitot error to ± 50 degrees flow angle and beyond.

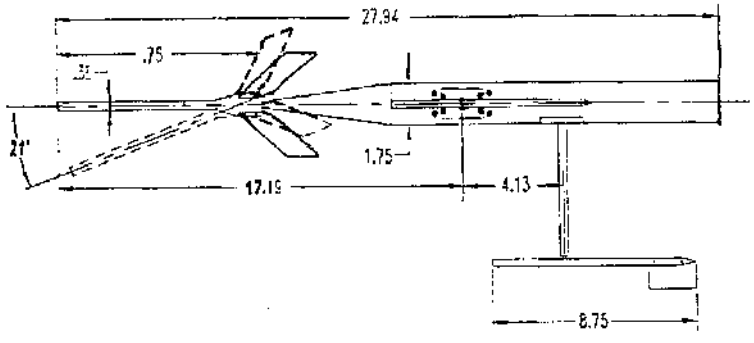

Fig.5.6 Typical Swivel-Head Air Data Boom (Courtesy of Endevco UK Ltd).

5.5 ISOLATION REQUIREMENTS

The main concern is isolation of the RPV data acquisition system from thermal noise and interference of sparks from the engine ignition system. The two-stroke engine sparks will generate spikes within the following frequency range :

- 107 Hz (max power, 6400 rpm)
- 37 Hz (idle, 2200 rpm)

Other noise sources might occur in the amplifying elements of the circuitry, owing to the random trapping and release of electrons in energy levels and other statistical phenomena (Ref.53).

An obvious and effective way to reduce the effects of external interference is to prevent its introduction into the system. The use of differential inputs to the ADC card is highly advisable (differential inputs were used during the wind tunnel test, too), along with some signal filtering. In our measurement situation the physical quantities being measured have a value which is either constant or changing slowly with time. Our maximum sampling rate will be about 20 Hz while from the above we can see that the estimated noise component frequencies are higher. In this circumstance the signal processing element required would be a 30 Hz low-pass filter.

5.6 CAA REQUIREMENTS

The Condor will be a civilian operated RPV and under such a status will come under the jurisdiction of the British Civil Aviation Authority and the rules laid down by it. The CAA was contacted and the outcome appeared to be that the RPV would need to comply with the Air Navigation Order to be treated as an aircraft with exceptions granted on the basis of limited usage. Whilst not exhaustive, the following is a list of the restrictions to comply in order to fly the Condor :

- Prohibition from flying :

1. in controlled airspace or in an aerodrome traffic zone, except with the permission of the relevant air traffic control unit ;

2. at a height exceeding 400 feet above ground level;

3. for aerial work (i.e. for hire or reward) without the Authority permission ;

- not beyond 1000 metres from the operator, or visual range if less ;

- not within 500 metres of any congested area of a city, town or settlement ;

- not within 500 metres of any person, vehicle or structure, except during take off and landing when this distance can be reduced for persons necessarily present for the safe operation of the RPV ;

- not without a serviceable mechanism that will land the RPV in the event of a failure of its control systems or radio link ;

- not without the operator of the RPV ensuring that any load carried by the RPV is properly secured.

5.7 COMPARISON BETWEEN WIND TUNNEL AND FLIGHT

When comparisons are made between tunnel and flight there are uncertanties in the data obtained by each method. It is beyond the scope of this section to address the matter in detail; only note the different Reynolds number (an increase from 2 to 3 millions is possible within the Condor flight envelope) and the fact that flight test data often is acquired while the aircraft is accelerating : this makes the maximum lift coefficient higher than the true one (Ref.47).

5.8 COSTING

Cost is the main reason behind the decision to develop an RPV flying laboratory. The selected pressure sensing apparatus costs around £ 7500 in current U.K. prices. A notebook computer complete with data acquisition card and signal conditioning modules costs around £ 3000. To this figure are to be added the cost of two RPV airframes, a flight control system, a parachute recovery system, and an air data acquisition system. The construction materials used for the manufacture of the glove are inexpensive. CFD and wind tunnel testing included, the total development cost is estimated at under £ 30000. It should be possible quite quickly to recover this initial outlay because of the RPV cheap cost per flight hour rate, that is estimated at £ 30 per hour, which is considerably less than £ 500 per hour of running cost of the University of Glasgow wind tunnel. The following page contains a table with the purchased part list (Tab.5.1).

ITEM	CODE	Q.TY	PRICE	TOT. PRICE	SUPPLIER	MANUFACTURER	NOTES
COMPUTER RADIO	FP-T8UP FF8	1	267.87	267.87	Paisley Model Centre	Futaba Corp.	8 Channels
RECEIVER	R-138DP	1	114.99	114.99	Paisley Model Centre	Futaba Corp.	PCM 1024 Standard
SERVOMOTOR	PS3001B	5	15.99	79.95	Paisley Model Centre	Futaba Corp.	Received with the Radio
SERVOMOTOR	PS3032	6	54.99	329.94	Paisley Model Centre	Futaba Corp.	8 Kg cm Torque
SERVOMOTOR	PS3801	2	64.99	129.98	Paisley Model Centre	Futaba Corp.	14 Kg cm Torque
STANDARD CHARGER		1	Not Applicable		Paisley Model Centre	Futaba Corp.	Received with the Radio
SANYO NICADS		1	Not Applicable		Paisley Model Centre	Sanyo Corp.	Received with the Radio
AUTOPILOT	P-HAL2100	1	59.99	59.99	Paisley Model Centre	Ripmax Plc.	Sensor Included
SPARE SENSOR	P-HAL2100/05	1	19.95	19.95	Paisley Model Centre	Ripmax Plc.	Autopilot Spare Sensor
BATTERY PACK	0-4N2500NMHWF	2	38.99	77.98	Paisley Model Centre	Futaba Corp.	
Y-SERVO JUNCTION	P-AL0731	4	5.99	23.96	Paisley Model Centre	Futaba Corp.	
SWITCH HARNESS	P-F1403 W/2 LED	1	24.99	24.99	Paisley Model Centre	Robbe	Red&Green LEDs
SERVO EXTENSION	Y-MA7756	3	9.99	29.97	Paisley Model Centre	Futaba Corp.	
SERVO PLUG PACK (A)	Y-MA2165	3	9.95	29.85	Paisley Model Centre	Futaba Corp.	
SERVO PLUG PACK (B)	Y-MA2242	4	9.95	39.8	Paisley Model Centre	Futaba Corp.	
MAIN WHEEL	6000 783	2	40	80	R.Kincaid & Co.	Invacare Carters Ltd	200X50 mm fork included
NOSE WHEEL	0249N 03959	1	14.97	14.97	R.Kincaid & Co.	Invacare Carters Ltd	6X1.5 in
LABVIEW 3.1		1	27	27	Prentice Hall International	National Instruments Corp.	Student Edition
DAQ-700 CARD	776985-01	1	560.48	560.48	Imex Systems Ltd.	National Instruments Corp.	
PR50-50F CABLE	182799-OR5	1	79.32	79.32	Imex Systems Ltd.	National Instruments Corp.	0.5 m long
CB-50LP I/O CON. BLK	777101-01	1	23.27	23.27	Imex Systems Ltd.	National Instruments Corp.	Connector Block for DAQ-700
S7DC AMPLIFIER		2	161	322	Imex Systems Ltd.	RDP Electronics Ltd.	Amplification & Excitation
NOTEBOOK COMPUTER	SATELLITE 110 CS	1	1149	1149	PC World Glasgow	Toshiba Corp.	
SCANNER	ScanCo 48S9 GM-1/2	2	1644	3288	Scanivalve Corp.	Scanivalve Corp.	S/N 3107/3108
SOLENOID DRIVE	ScanCo SGMS5-48	1	437	437	Scanivalve Corp.	Scanivalve Corp.	
PRESSURE TRANSDUCER	PDCR23D	2	831	1662	Scanivalve Corp.	Scanivalve Corp.	20 H2O Range
URETHANE TUBING	URTH-040	320 ft	30	30	Scanivalve Corp.	Scanivalve Corp.	
SOLENOID CONTROLLER	CTLR2P/S2-S6	1	709	709	Scanivalve Corp.	Scanivalve Corp.	
MALE CONNECTOR	48SM-1/2	2	103	206	Scanivalve Corp.	Scanivalve Corp.	Spares
TOTAL AMOUNT				**9817**			

Tab.5.1 Purchased Part List

6. POSSIBLE APPLICATIONS

UAVs, unmanned vehicles operating in the air, can do jobs too dangerous for human presence, and can carry sensors or manipulators of very low weight. In addition, their operating cost is generally cheap compared to that of a manned aircraft. After the initial pump priming phase it is envisaged that the Condor will be again modified to demonstrate the suitability of the vehicle for a variety of civil applications. Possible modifications would be to include environmental and atmospheric monitoring equipment (Ref.55), communications relay equipment (Ref.56), surface mapping equipment, video and photographic cameras, infra-red and thermal sensors, accurate position sensors, floats for amphibious craft research (Ref.14), and a radio altimeter for ground effect research. In this chapter a simple modification of the wing glove is presented: we could fly the Condor with ice shapes on, in order to study the icing of aircraft surfaces. It is an example of the many avenues that the Condor vehicle operation could open up.

6.1 ICE TEST

Icing of aircraft surfaces is a well-known phenomenon which occurs under certain meteorological conditions and is potentially dangerous. In particular, ice formations on the wing of an aircraft alter its aerodynamic profile causing a dramatic reduction in the lift force and, in severe icing conditions, even a fatal stall.

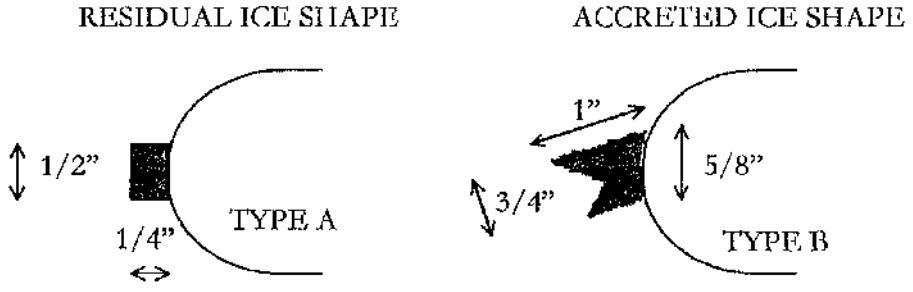

Fig.5.7 Wing Leading Edge - Typical Ice Shapes (Courtesy of British Aerospace).

The Aerodynamic Office of British Aerospace at Prestwick provided two typical ice shapes, named "A" and "B" (Fig.5.7) in the following. Ice type A is a typical residual ice shape, while ice type B is a typical accreted ice shape (critical). Wooden bars were shaped accordingly and attached on the leading edge of the glove fitted with 5 cm endplates, in order to simulate ice type A and type B formation. The same setup and tunnel conditions as described in section 4.6 were used. A selection of measured pressure distributions is shown in Figures 5.8-5.11. Examination of the above figures leads to the following general observations :

1. Lift reduction gets larger as the AoA increases
2. Ice type B causes a more marked reduction in lift compared to that caused by ice type A
3. Ice type A does not affect significantly the pressure distribution over the lower lifting surface
4. Ice type B pressure distribution over the lower lifting surface at AoA = 2 deg (Fig.5.10) is more disrupted than that at AoA = 4 deg (Fig.5.11); this is probably due to the different position of the stagnation point.

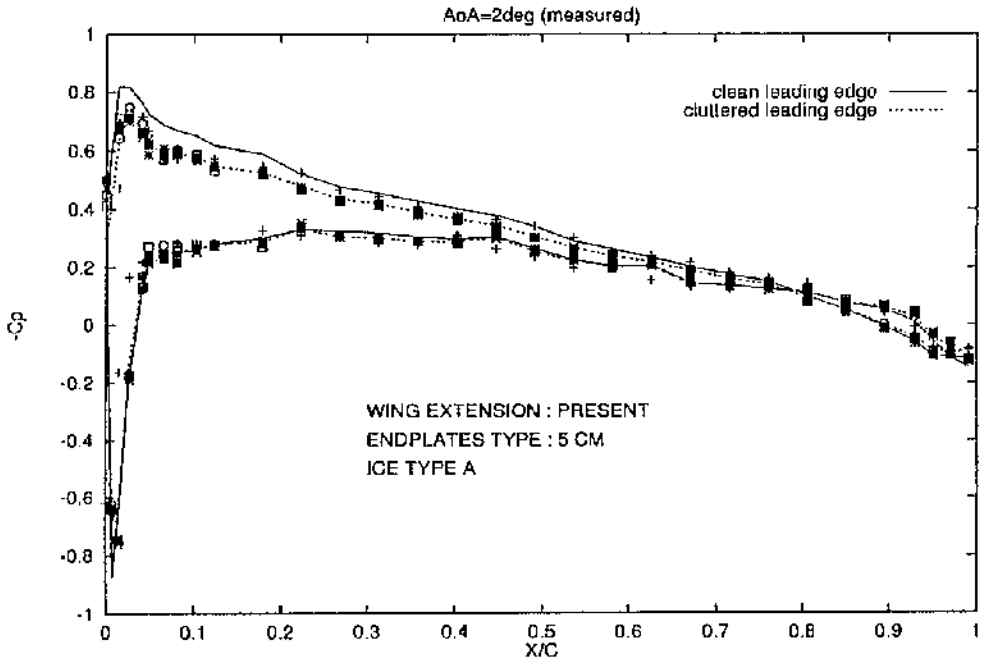

Fig.5.8 Chordwise Pressure Distribution at AoA = 2 deg (Ice Type A).

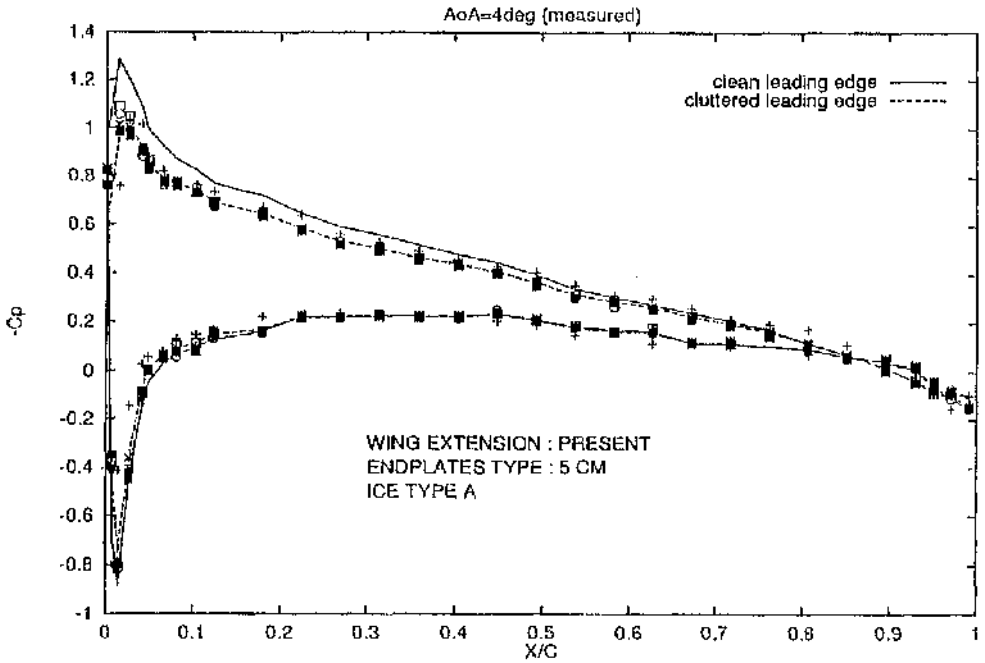

Fig.5.9 Chordwise Pressure Distribution at AoA = 4 deg (Ice Type A).

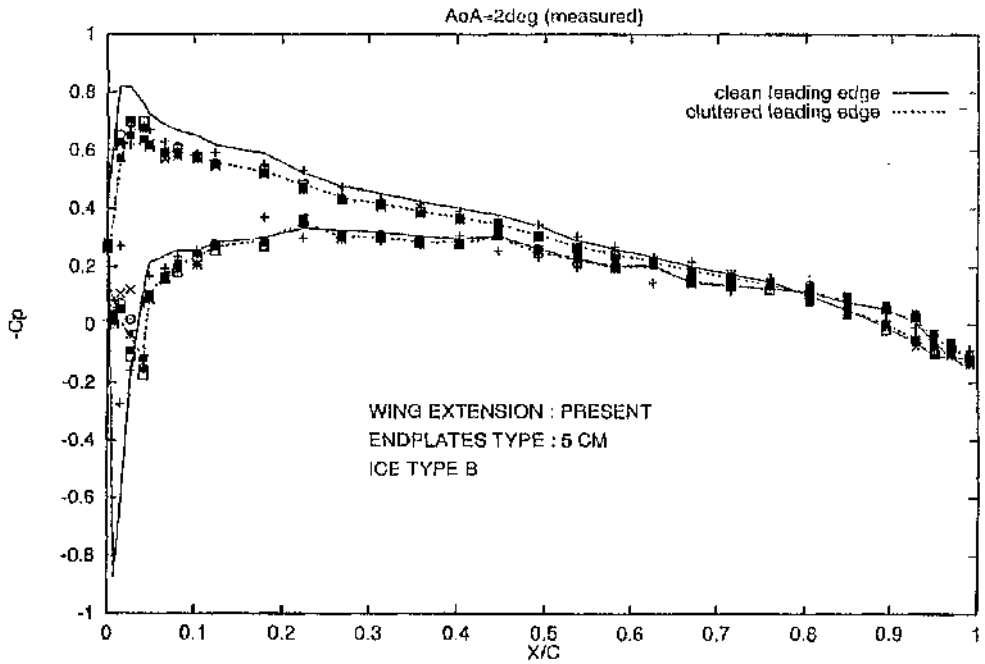

Fig.5.10 Chordwise Pressure Distribution at AoA = 2 deg (Ice Type B).

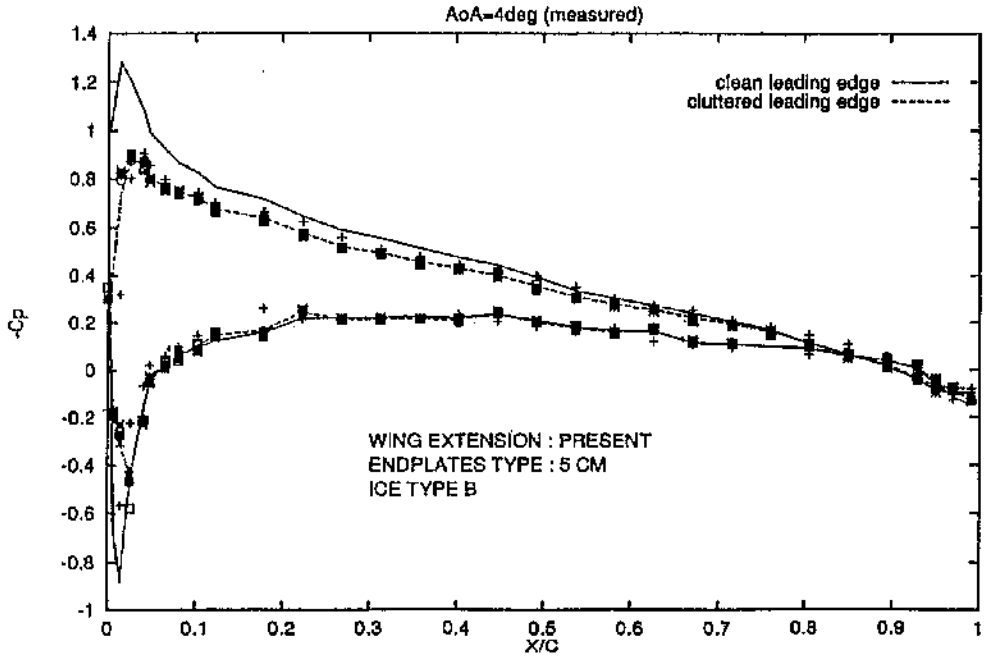

Fig.5.11 Chordwise Pressure Distribution at AoA = 4 deg (Ice Type B).

UNRESOLVED PROBLEMS

There are still problems to be solved in order to get the RPV Condor to fly. This section identifies problems which are still unresolved and tasks to be accomplished in order to complete the work.

AREA	REQUIRED TASK(S)	SECTION(S) OF INTEREST
Dual Rudder	Completion of dual rudder construction; installation, ground and flight testing.	3.3
Landing Gear	Fitting the RPV airframe with a fixed landing gear.	3.4
Parachute Recovery System	Fitting the RPV airframe with a parachute recovery system; system ground and flight testing.	3.5 5.6
Electrical System	Provision of current for the on-board instrumentation. Source of current is the on-board alternator.	Chapter 5 Appendix C
Flight Control System	Replacement of current wiring with screened cables and replacement of current battery with acid-lead batteries; modification of all fly-leads to accept these non-standard components; radio programming; system ground and flight testing.	3.6
Air Data Sensors	Provision of pitot-static probe, flow angle sensor, temperature sensor; integration of existing software digital interface with new sensors.	Chapter 5 Appendix A

ACKNOWLEDGMENTS

The project has been highly multi-disciplinary with a number of individuals who gave their contribution. The author wishes to thank the following people in particular :

Dr L.Smrcek and **Mr D.P.Coldbeck**, my supervisors, who were always available for discussions and advice.

Dr F.N.Coton, Senior Lecturer. He gave valuable advice on selection of a pressure measurement system and on aerodynamic phenomena, as well as on wind tunnel testing techniques.

Dr C.Goodchild, Senior Lecturer. He was available for useful advice and discussions on air data acquisition and data acquisition in general.

Mr R.Gilmour, Research Technologist. He impressed me with his personal commitment and his competence during the wind tunnel testing.

Mr A.McCartney, Technician. Alex sadly died prematurely. I will remember his jokes and his availability, as well as his competence in Electronics.

Mr J.Kitching, Technician. His unrivalled craftmanship and accuracy were vital. "Big John" is the one who made the wing glove.

Dr F.D.Marquez, for his friendship and stimulating discussions.

Dr Y.F.Yao, for his help and valuable discussions on CFD.

Mr W.Gray, Sales Director, Imex Systems Ltd. Walter gave me excellent technical support and was available at any time for help.

Dipl.Ing. D.Lexa, AERON spol s.r.o., Brno, for his exquisite hospitality during my technical visit to his firm.

Mr B.Gribben, Ph.D. candidate, for his friendship and support, as well as valuable discussions on CFD.

Dipl.Ing. J.Kuzdas, Air Force and Air Defence Technical Institute, Praha. During a visit to his institute he organised a video session exclusively for myself on the spot ! Thanks again.

Mr B.Grimsley, Paisley Model Centre. He gave me an insight into the unknown world of aeromodelling, as well as good technical support.

Last the author thanks the Department of Aerospace Engineering and Faculty of Engineering of the University of Glasgow for the scholarship under which the research was carried out.

REFERENCES

1. R.D.Wagner, D.V.Maddalon, D.W. Bartlett, F.S.Collier, A.L.Braslow, *Laminar Flow Flight Experiments - A Review*, NASA IAA Conference Proceedings, Issue 17, 1992

2. M.N.Taylor, L.Smrcek, *Wing Glove Test Bed Feasibility Study*, Technical Soaring, Vol.20, No.1, January 1996

3. Anon., Letectvi a Kosmonautika 16/94, Neznarne Blaniky

4. J.M.Brandon, G.S.Manuel, R.E. Wright, B.J.Holmes, *In-Flight Flow Visualization using Infrared Imaging*, Journal of Aircraft, Vol.27, No.7, July 1990

5. W.Wohlrath et alii, *Design and Flight Test Evaluation of a Laminar Wing Glove on a Commuter Aircraft*, ICAS paper 94-5.4.1

6. R.Henke, F.X.Münch, A.Quast, *A Wind Tunnel Test Campaign and Comparison With Flight Test Data*, Proceedings - 8th AIAA Applied Aerodynamics Conference, AIAA paper 90-3045-CP, August 20-22, 1990, Portland, USA

7. Anon., *Aerodynamické Charakteristiki Bezpilotnich Prostredku SOJKA V-III*, Praha, 1991

8. M.Hupak, J.Kuzdas, *Zpràva K Pevnostni Zkousce Kridla Letounu SOJKA III (Crash Test)*, VTÚl a PVO, Praha, 1991

9. M.Hupak, J.Kuzdas, *Zpràva K Pevnostni Zkousce Kridla Letounu SOJKA III (Limit Loads)*, VTÚl a PVO, Praha, 1991

10. D.Lexa, *Katalog Dilu Draku Bezpilotnìho Prostredku SOJKA III*, Aeron Brno spol s.r.o, 1997

11. D.Lexa, *Technicky Popis Draku Bp SOJKA III*, Aeron Brno spol s.r.o, 1997

12. J.Kuzdas, L.Smrcek, M.N.Taylor, *Development Of The Sojka Remote Piloted Vehicle System*, Proceedings - 11th RPV's International Conference, Bristol, UK

13. Anon., *Multi-Purpose Unmanned Vehicle System SOJKA III/TV*, VTÚl a PVO-Praha & MH HTI-Budapest

14. T.Bauer, *Adding Floats To a Radio Controlled Remotely Piloted Vehicle*, Final Year Project, Department of Aerospace Engineering, University of Glasgow, June 1997

15. E.Torenbeek, *Synthesis of Subsonic Airplane Design*, Delft University Press, 1982

16. J.Roskam, *Airplane Design : Part VI, Preliminary Calculation of Aerodynamic Thrust and Power Characteristics*, Roskam and Engineering Corporation, Ottawa, USA, 1991

17. J.Roskam, *Airplane Design : Part VII, Determination of Stability, Control and Performance Characteristics*, Roskam and Engineering Corporation, Ottawa, USA, 1991

18. I.H.Abbott, A.E. Von Doenhoff, *Theory of Wing Sections*, Dover Publications Inc., New York, 1959

19. Anon., *SKY ARROW 650TC Flight Manual*, Iniziative Industriali Italiane, Roma, Italia

20. M.Darida, D.P.Coldbeck, L.Smrcek *The Glasgow University Remote Piloted Vehicle System*, Proceedings - 1st AIA Conference & Symposia, September 19-21, 1996, Ankara, Turkey

21. M.Darida, L.Smrcek, D.P.Coldbeck *Feasibility Study on an RPV For The Utilization As A Flying Laboratory*, Proceedings - 12th RPV's International Conference, September 9-11, 1996, Bristol, UK

22. Anon., *JAR-VLA*, CAA Printing and Publication Services, 1991, UK

23. E.F.Bruhn, *Analysis and Design of Flight Vehicle Structures*, Jacobs Publishing Inc., Indianapolis, 1973

24. L.Pazmany, *Landing Gear Design For Light Aircraft*, Pazmany Aircraft Corporation, Vol.I, 1986, USA

25. Anon., *Futaba FP-8UAP Instruction Manual*, Futaba Corporation, 1996

26. Anon., *HAL2100 Instruction Manual*, Ripmax Plc.

27. Anon., *Modellers Handbook*, Ripmax Plc., 1996

28. Anon., *1996 Instrumentation Reference and Catalogue*, National Instruments Corporation

29. J.Woolman, R.A.Mottram, *The Mechanical and Physical Properties of The British Standard EN Steels*, 3 Volumes

30. A.S.Morris, *Principles of Measurement and Instrumentation*, Prentice Hall Int., Second Edition, 1993

31. Anon., *Short Form Catalog*, Scanivalve Corporation

32. Anon., *Scanivalve Model S Catalog*, Scanivalve Corporation

33. Anon., *CTLR2P/S2-S6 Solenoid Controller Instruction Manual*, Scanivalve Corporation

34. Anon., *Technical Manual for Transducer Amplifier Type S7DC*, Issue K, RDP Electronics Ltd.

35. L.K.Wells, *Labview Student Edition User's Guide Release 3.1 for Windows*, Prentice Hall Int., 1995

36. Anon., *Pressure Accessories*, Catalog No.G800, Scanivalve Corp.

37. Anon., *Zoc33/64 Electronic Pressure Scanning Module Technical Information Manual*, Scanivalve Corporation

38. Anon., *DAQ-700 Card User Manual*, May 1995 Edition, National Instrument Corporation

39. M.Darida, L.Smrcek, F.Coton, *Development Of an RPV Laboratory For In-Flight Aerofoil Testing*, Proceedings -15th AIAA Applied Aerodynamics Conference, AIAA Paper 97-2234, June 23-25, 1997, Atlanta, USA

40. Anon., *Rampant Tutorial Guide*, Release 3.1, July 1994, Fluent Inc.

41. Anon., *preBFC User's Guide*, Release 4.3, Fluent Inc., 1994

42. Anon., *TGrid User's Guide*, Release 2.2, Fluent Inc., 1994

43. Anon., *TGrid User's Guide*, Release 2.4, Fluent Inc., 1996

44. Anon., *Rampant User's Guide*, Release 3.1, Fluent Inc., 1994

45. Anon., *Rampant User's Guide*, Release 4.0, Fluent Inc., 1996

46. Anon., *Experimental Data Base For Computer Program Assessment*, AGARD Advisory Report No.138, 1979

47. W.H.Rae jr.,A.Pope,*Low-Speed Wind Tunnel Testing*, John Wiley & Sons, Inc., 1984, USA

48. Anon., *Air Data Handbook*, Rosemount Aerospace Corporation

49. Anon., *Pitot and Pitot-Static Probes*, Bulletin 1013, Rosemount Aerospace Corporation

50. Anon., *The RS Catalogue on CD-Rom* November 1996-February 1997, RS Components Ltd

51. Anon., *Angle of Attack Systems*, Brochure 1044, Rev. 4/95, Rosemount Aerospace Corporation

52. Anon., *Flow Angle Sensors*, Bulletin 1014, Rev. 2/96 Rosemount Aerospace Corporation

53. R.W.Henry, *Electronic Systems and Instrumentation*, John Wiley & Sons, USA, 1978

54. M.Darida, L.Smrcek, *RPV Wing Glove Configuration : Wind Tunnel Testing Results*, Proceedings - 16th AIAA Applied Aerodynamics Conference, June 15-18, 1998, Albuquerque, USA

55. J.Vitali, S.Tsach, H.Avni, S.Gali, V.Weissberg, *Development Approach of the Heron Medium Altitude Long Endurance UAV*, ICAS Paper 96-4.2.2, Proceedings - Vol.I, 20th ICAS Congress, Sorrento, Italia, September 8-13, 1996

56. K.Takasawa, *Feasibility Study on a Microwave-Powered Unmanned Aerial Vehicle For The Communication Relay Utilization*, Proceedings - Society of Automotive Engineers, P-246, 1991

57. Anon., *Claris CAD User's Guide*, Claris Corporation, 1988

58. Anon., *Claris CAD New Features Guide*, Claris Corporation, 1990

59. Anon., Manuale di Tecnica Aeronautica, Ed. Cremonese, 1971

Tunlab User's Manual Version 1.1

Via Ricciardi 53
81100 Caserta - Italia

1. Tunlab User Reference

1.1 WHAT IS TUNLAB

Tunlab is a program designed and configured to perform pressure measurements over the mid surface of a wing glove in a wind tunnel and along with a certain combination of hardware, which includes a National Instrument DAQ-700 card plus corresponding driver installed and a Scanivalve SGM module with two pressure scanners. Tunlab itself must run in a computer with Windows95 as the operating system and be capable of supporting Labview (version 3.1 or later), the Tunlab native software development platform.

Any other use should be regarded as inappropriate and it is likely to lead to wrong results, occasional malfunctions, incorrect data display or even to a computer crash. This warning also applies when engineering units different from those requested are entered (Tunlab uses standard SI units). However, the author estimates that the program could be easily adopted to perform other types of pressure measurement, by using the same combination of hardware and by making minimal changes to the code. In the latter case the code ought to be re-validated.

In its present state Tunlab acquires 60 pressure values, but with a small change it could acquire a maximum of 92 pressure values (this is a constraint of the Scanivalve SGM module).

Tunlab was validated by running a numerical simulation and by use in a real wind tunnel environment. The code performs some vital checks during the acquisition process (see section 2), in order to ensure that only reliable data are acquired, although it does not check everything. For instance, when Tunlab has to save a file on the hard disk, it will not check whether there is enough disk space.

Please note that if you want to install Tunlab from scratch you need to replace file named "daqdrv" of Labview Student Edition with the one dated September 22, 1997, which is in the disk enclosed to this manual. You will also need to install Labview and NI-DAQ for PC compatibles version 4.9.0f1 drivers.

Unless otherwise noted, no part of this manual requires previous Labview experience.

1.2 HOW DOES TUNLAB WORK

Tunlab is the digital interface of the data acquisition system in fig.1. Pressure values of the tubes coming from the wing glove are converted into analogue signals (voltages) by differential pressure transducers (two in the present configuration, one per scanner). The analogue signals are fed into an ADC (a DAQ-700 card) and acquired by Tunlab, which converts them into engineering units and eventually stores them in the form of non-dimensional cp values and voltages in the computer's hard disk.

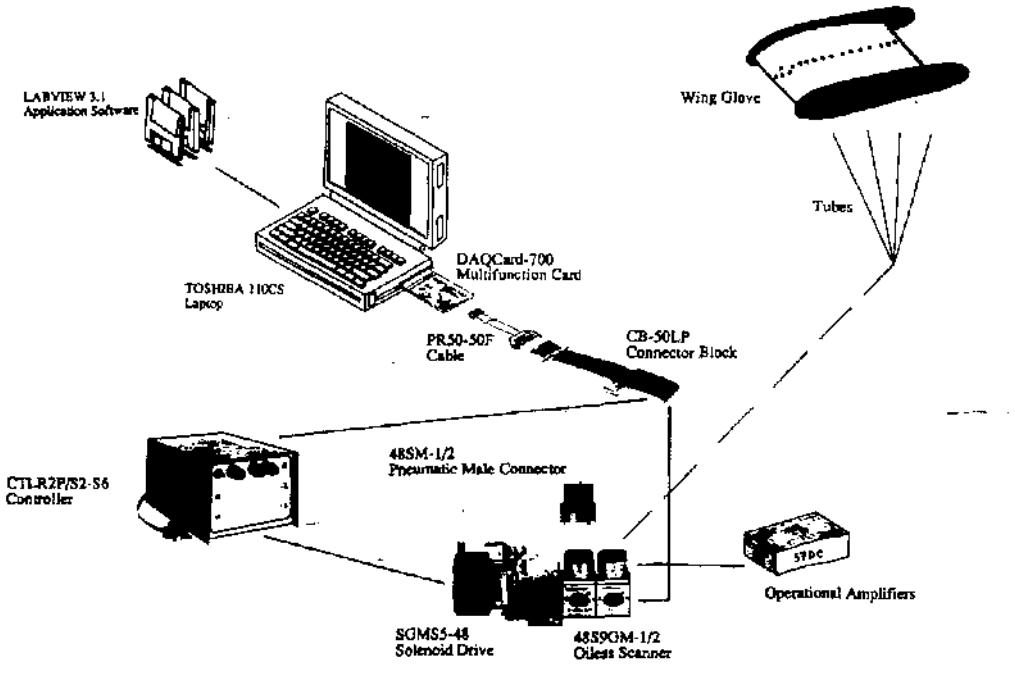

Fig.1 Wing Glove and Data Acquisition System

In order to load Tunlab, double-click the Labview icon in the Windows95 desktop. After a few moments, a blank, untitled panel window appears. You can safely ignore it. Select **Open** from the **File** menu; next, open the Tunlab folder by double-clicking on it. Finally, double-click on **tunlab.vi** to open it. After a while, the Main Front Panel appears, as shown in fig.2.

1.3 THE TUNLAB ENVIRONMENT

1.3.1 Main Front Panel

The panel in fig.2 is what should appear on the screen if Tunlab has been loaded correctly. It is the Tunlab's main panel. From here the user sets device parameters, displays the acquired data and checks that everything is taking place as planned. Any value in any "control" cell can be changed by clicking on the cell and editing a new value (the cursor gets hand-shaped when it is near a cell). However, the new values will not be saved after quitting

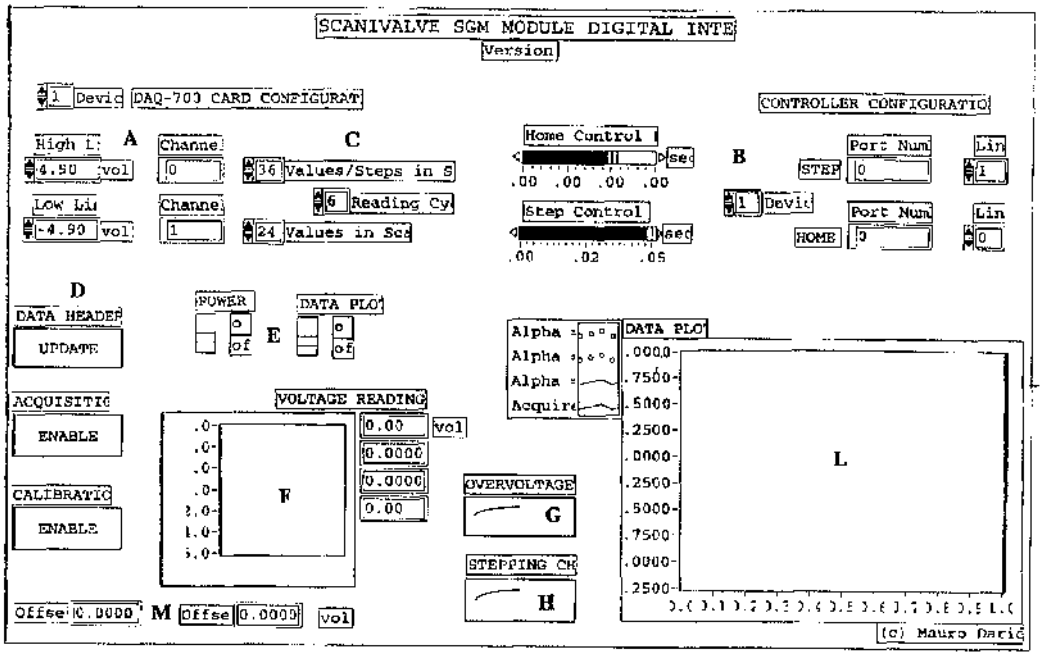

Fig.2 Main Front Panel

the program. In order to save them you need to have some knowledge of the Labview environment and read section 2 to modify the code accordingly. Please note that a value in an "indicator" cell cannot be edited from the keyboard as it is intended for displaying output data only (such as Offset1 in "M" of fig.2).

The Main Front Panel will be described starting from the top. A similar set of features has been grouped for clarity whenever possible. Refer to fig.2 if otherwise noted.

Control Parameters

The area marked as "A" contains some ADC control parameters. See fig.3 also.

High Limit

Specifies the maximum voltage the ADC card measures. The default value is 4.90 V.

Low Limit

Specifies the minimum voltage the ADC card measures. The default value is -4.90 V.

Channel1

Identifies the analogue input channel to be measured by the transducer number one. The default value is zero.

Channel2

Identifies the analogue input channel to be measured by the transducer number two. The default value is one.

Device

Is the device number assigned to the DAQ-700 card. This value is used by the operating system.

The area marked as "B" contains some control parameters for the Scanivalve CTRL2P/S2-S6 controller.

STEP Port Number

Specifies the port configured for a high logic state digital output. The default value is zero.

STEP Line

Specifies the individual line within the port to be used for sending a STEP command to the Scanivalve controller.

STEP Control

Sets the pause between two STEP commands. The default value is 0.05 seconds, which is based on the Scanivalve recommended scanning rate of 20 ports/sec.

HOME Port Number

Specifies the port configured for a high logic state digital output. It must have the same value of the STEP Port Number. The default value is zero.

HOME Line

Specifies the individual line within the port to be used for sending the HOME command to the Scanivalve controller. The default value is one.

HOME Control

Sets the pause between a HOME command and a subsequent STEP command. The default value is set to two seconds, which will work well with most of the "ports in use" configurations.

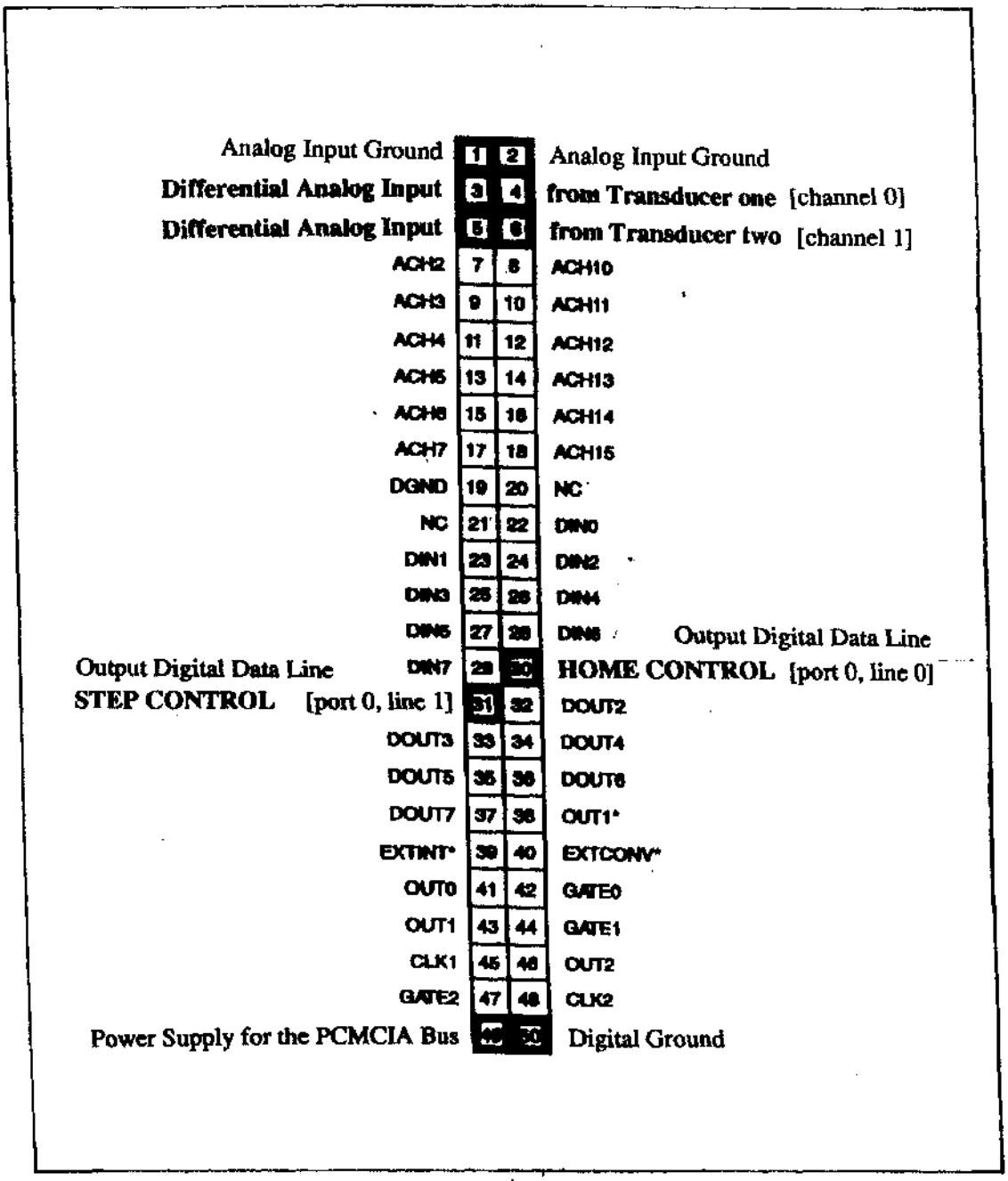

Fig.3 DAQ-700 Card I/O Connector Pin Assignments

Note: The default values in "A" and "B" will work well with the DAQ-700 I/O connector pin assignments of fig.3. If other assignments are used, the default values need to be changed.

Numerical Controls

The area marked as "C" contains numerical controls useful to set the way a data acquisition will be performed.

Reading Cycles

Specifies the number of times you want to perform a scanning session. It must be a positive number. The default value is irrelevant.

Values/Steps in Scanner1

Tunlab is designed to handle two Scanivalve scanners (model S9). The so-called scanner number one refers to channel zero of the ADC card and it is regarded as the "master" scanner, where the total number of steps of a scanning session are set. The so-called scanner number two refers to channel one of the ADC card and it is regarded as the "slave" scanner, because it will follow suit even if the total number of px tubes connected to it is lower than the total steps set in the master scanner. This arrangement allows to acquire a different number of pressure values in the slave scanner from the master scanner, despite the fact that they step simultaneously during a scanning session. Values/Steps in Scanner1 must be equal to the number of pressure values to be acquired by the master scanner and **never** less than Values in Scanner2 (see following description). It must be a positive number. The default value is irrelevant.

Values in Scanner2

Specifies the number of pressure values to be measured by the slave scanner during a scanning session. It must **not** be greater than Values/Steps in Scanner1 and it must be a positive number or zero. If it is zero the slave scanner (scanner number two) is inactive. In the latter case at least the reference tube and the two vented tubes used to read the offsets must be connected (see fig.4). *Actually Tunlab requires that tubes carrying the px values to be measured must be in between the two vented tubes measuring the offsets (fig.4 shows the recommended configuration - see also 1.4).* The default value of this parameter is irrelevant.

Switches

The area marked as "E" contains two switches.

Power Switch

Must be "ON" in order to acquire data. If Tunlab is launched and the Power Switch is in the "OFF" position, there will be a warning message and then the program will be quitted.

Data Plot Switch

Must be "ON" in order to display data in real-time in the monitor marked as "L". If the Data Switch Plot is OFF and Tunlab is launched, the program will run normally but the monitor marked as "L" will remain blank.

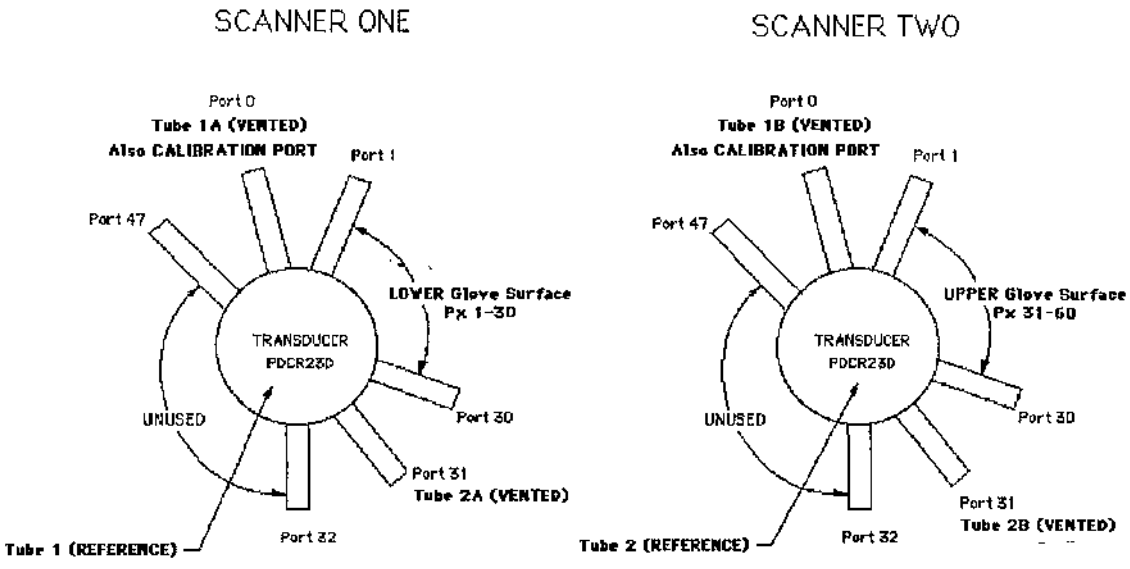

Fig.4 Scanivalve SGM module recommended arrangement

Buttons

Buttons of the Main Front Panel are located in the area marked as "D". There are three buttons whose functions are described in the following.

Data Header Button

Activates the Data Header Update Panel (see fig.5). Click on this button whenever you wish to update the data header of your files. If the header is not updated at the end of a test run (called in this manual as data acquisition session, too) *the subsequent test run uses the same header of the previous one.*

Acquisition Button

Activates a data acquisition session. Scanning sessions are performed as many as indicated by the Reading Cycle cell in "C".

Calibration Button

Activates the calibration Panel (see fig.6). Click on this button whenever you wish to calibrate the two transducers of the Scanivalve SGM module.

Indicators

There are four indicators located in the areas marked as "G", "H", and "M". They are described in the following.

Overvoltage Indicator

Turns to red when a voltage is outside the range High Limit-Low Limit in "A". In this case an error message is displayed along with a CONTINUE and a STOP button. Clicking on the STOP button will stop the program and control will be returned to Labview; by clicking on the CONTINUE button you can keep acquiring data being aware that the previous value is unreliable (the latter case is not recommended).

Stepping Check Indicator

Turns to red and display "ERROR" when the stepping check fails (see 2.1 for more details). An error message will appear along with a CONTINUE and a STOP button. Clicking on the STOP button will stop the program and control will be returned to Labview; by clicking on the CONTINUE button you can jump to the next scanning session (if any) and all the data of the current scanning session are discarded (neither displayed nor stored).

Offest1 and Offset2 Indicators

Show the offset value measured from transducer number one and two, during a scanning session. The offset values are updated at each new scanning session.

Monitors

In the Main Front Panel there are two monitors. They are described in the following.

Voltage Readings Monitor

Is allocated in the area marked as "F". It shows a set of four curves. The top and bottom red curves are the High and Low Limits in "A", respectively. The green curve shows the voltages which are being measured from the master scanner, while the cyan curve shows the voltages which are being measured from the slave scanner (number two). Sometimes only part of the cyan curve is converted in cp values and stored. This is because the slave scanner

performs as many steps as the master scanner, but only useful values from the slave scanner are displayed as cp values and saved, although they are displayed all as measured voltages.

Data Plot Monitor

Is located in the area marked as "L". It shows a set of four curves. The first three curves (starting from the top) are pertinent to different angles of attack and are experimental data on the NACA 0012 taken from the literature. The green curve is a cp distribution at 4 degrees of angle of attack, the yellow one is at two degrees, and the red one is at zero degrees. They are meant to be guidelines for a rough visual check only, since the refer to a Mach number and a Reynolds number higher than those achievable in the "Handley Page" wind tunnel of the university of Glasgow. The fourth curve (white) is the real-time cp distribution over the mid glove surface measured during a scanning session. If more than a scanning session has been set (that is, Reading Cycles is higher than one), at the end of a scanning session the monitor will be cleared and a new curve of cp values will be displayed, and so forth. The "guideline" curves stay the same, of course.

1.3.2 Data Header Update Panel

This panel is a graphical interface which allows the user to interactively input the information required for a file data header of a test run. It is vital to enter this panel (by clicking the Data Header Update Button in the Main Front Panel) after each data acquisition

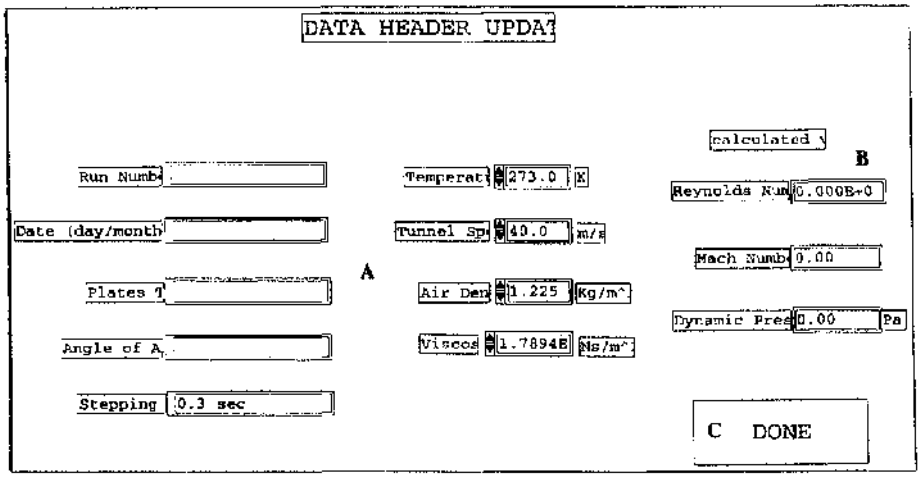

Fig.5 Data Header Update Panel

session and change the Run Number in the corresponding cell. In fact this value is used by the program to name the two files generated by Tunlab at the end of each data acquisition session (see 1.4.1). The panel is indeed quite simple and does not require much explanation. A similar set of features has been grouped for clarity whenever possible. Refer to fig.5 if otherwise noted.

Control Values

The area marked as "A" contains some "control" cells which must be filled with the information required. Some of the values must be entered in accordance with the displayed engineering units. Here is a list of them :

- temperature must be in Kelvin degrees;
- wind tunnel speed must be in m/s;
- air density must be in Kg/ m^3;
- air viscosity must be in Ns/ m^2 (or equivalent SI units).

Output Values

The area marked as "B" contains values which are a result of calculations made by the program, based on the data entered in "A". As a result, they do not require an input from the keyboard.

Buttons

There is one button only and is marked as "C" in fig.5. The DONE button should be clicked when all the requested data in "A" have been entered. When the DONE button is clicked Tunlab saves the data header and returns to the Main Front Panel.

1.3.3 Calibration Panel

This panel is accessed by clicking on the Calibration button in the Main Front Panel. The panel allows the user to calibrate the two pressure differential transducer of the Scanivalve SGM module simultaneously. The panel was conceived for a calibration which uses a water gauge. It is described in the following starting from the right side. A similar set of features has been grouped for clarity whenever possible. Refer to fig.6 if otherwise noted.

Output Values

In the area marked as "B" voltages measured from scanner number one and two are displayed at the end of the calibration. Initially they stay blank. In the area marked as "G" offsets and voltages after each reading from the water gauge are displayed.

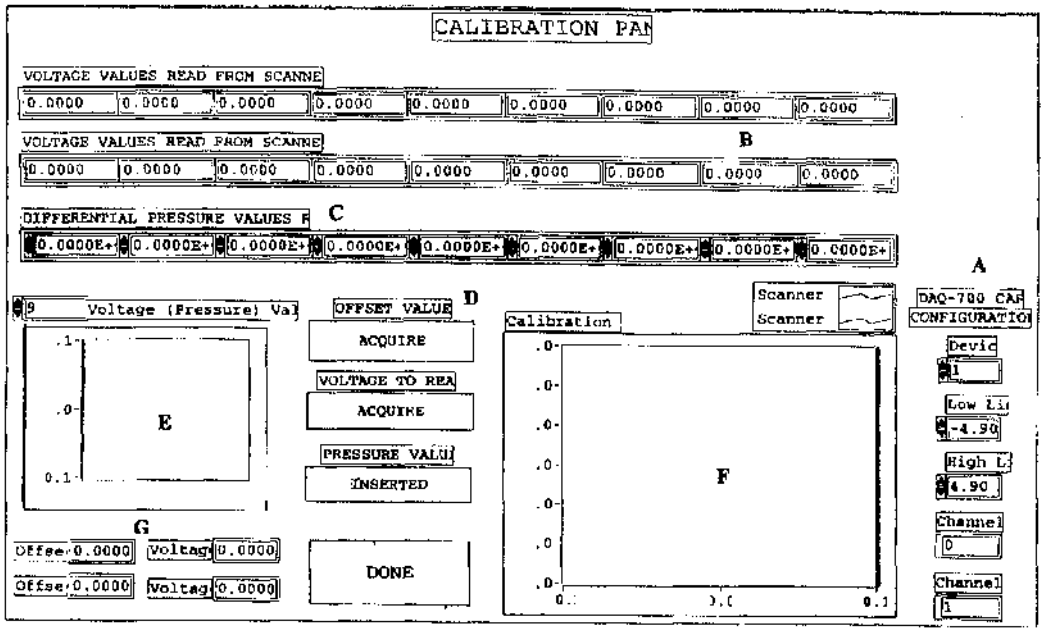

Fig.6 Calibration Panel

Control Values

In the area marked as "C" the user enters the differential pressure values read from the water gauge.

Buttons

The area marked as "D" contains four buttons. They are described in the following.

Offset Value Button (red)

By clicking on this button the user tells the program to acquire the offsets of transducer number one and two, respectively. The two acquired offsets are displayed in "G".

Voltage to Read Button (orange)

By clicking on this button the user tells the program to acquire the voltages of transducer number one and two, from the tubes connected to the water gauge. The two measured values are displayed as digits in the cells in "G" and as points in monitor "E".

Pressure Value Button (violet)

After clicking this button the program will accept the pressure value inserted in "C".

Done Button

By clicking on this button the user returns to the Main front Panel. As soon as the last pressure value is inserted in "C", the calibration curves are displayed in monitor "F" and saved.

1.4 TUNLAB AND DATA ACQUISITION

In this section two practical sessions with Tunlab are described. One is a data acquisition session, the other a calibration session. The scope is to make the user familiar upon how to manage Tunlab's controls in practice.

Warning : ASCII file x_glove.txt containing the pressure tappings' coordinates might need to be modified if a configuration different from that in fig.4 is adopted.

1.4.1 Anatomy of an Experiment

Suppose you are in front of your laptop with a wing glove in the wind tunnel ready to be tested. You may want to check that each tube works correctly before starting the measurements. Use for this purpose the **Analog I/O** option from the **Test** menu of the NIDAQ Configuration Utility, after reading pp.332-334 of "Labview Student Edition User's Guide" by Lisa Wells. Just double-click on **NIDAQ Configuration Utility** in the Labview group window under **Programs** of the Windows95 desktop.

If the check is positive, all you need to do is to load Tunlab. Follow instructions in paragraph 1.2 in order to load Tunlab successfully. Now you should be in Tunlab's Front Main Panel (refer to fig.2). Check the values in "A", "B", and "C" and change them accordingly, if necessary. In "E" click on the Power Switch to put it ON, and click on the Data Plot Switch if you want the measured cp values to be displayed in monitor "L" (this is very much the norm). Run Tunlab by clicking on the run button, which is the first icon with an arrow on the Labview menu bar, at the top right corner of the screen. If you cannot locate the run button, read p.9 of "Labview Student Edition User's Guide" by ρρLisa Wells.

Once Labview is running (you will see that the run button has changed in appearance) you are in bussiness. First, you create a data header by clicking on the Data Header Update

button (refer to fig.5). Enter the requested information in "A". If you are asked to replace a file click on the OK button that appears. Note that Run Number of this panel is an alphanumeric string of maximum **seven** characters. This is a restriction of the operating system, as the string will be used to name the files which contains the saved data. If you enter a string with more than seven characters, at a certain point the program will ask you a filename. Actually the maximum allowable length of a filename in Windows95 is eight characters, but we need one in reserve since the filename with the measured voltages is automatically generated by adding a "v" to the run number alphanumeric string. Click on the DONE button to return to the Main Front Panel.

Next, as you have got a data header, you can commence to acquire data. Click on the Acquisition Button. You should see the offset values in "M", and the measured voltages as points in monitor "F"; when the scanning session is over, the calculated cp values (the white curve) are displayed in monitor "L", along with the "guideline" curves. The indicators "G" and "H" should remain neutral in color. If you have set more than a scanning session in Reading Cycles in "C", a new scanning session will be started automatically. New offset values will appear in "M", and new points in monitor "F". At the end of this new scanning session, a new curve of cp values will be drawn in monitor "L", and so forth. At the end of the last scan, the data acquisition session is over, and data are saved automatically. For instance, if your Run Number was the string "test1", you will end up with two files named "test1" and "test1v" in c:/lvse/ containing the cp and voltage values, respectively (for a description of these files see 2.1.3). These files can be read by any text-editor. To quit Tunlab, simply select **Exit** from the **File** menu.

1.4.2 Anatomy of a Calibration

Suppose you want to calibrate the two transducers of the Scanivalve SGM module. You need a water gauge readily available and possibly a partner who will operate it. The water gauge should be equipped with a valve so that the offset of both transducers can be quickly measured before each pressure value from the water gauge is acquired. Follow instructions in paragraph 1.2 in order to load Tunlab successfully.

Now you should be in Tunlab's Front Main Panel (refer to fig.2). In "E" click on the Power Switch to put it ON, and Run Tunlab by clicking on the run button, which is the first icon

with an arrow on the Labview menu bar, at the top right corner of the screen. If you cannot locate the run button, read p.9 (exercise 1.1) of "Labview Student Edition User's Guide" by Lisa Wells. Once Tunlab is running (you should see that the run button has changed in appearance) click on the Calibration button and comply with the following mode of operation. You should now be able to see the Calibration Panel (refer to fig.6).

Step 1

Check the value in Voltage (Pressure) Values to Read at the top of monitor "E". The default value is nine and ought not to be changed.

Step 2

Decide which nine values of differential pressure will be measured by the water gauge during the calibration process. For example:

-20 -15 -10 -5 0 5 10 10 15 20 inches H_2O

is a good choice, considering the sensitivity range of the Scanivalve transducer (model PDCR23D). These values must be converted into pascals before entering them from the keyboard.

Step 3

Calibration can commence. The valve has been switched so that the tubes are disconnected from the water gauge. Click on the Offset Values button (red) in "D" to measure the offsets, which will be displayed in "G".

Step 4

The valve has been switched so that the tubes are connected to the water gauge. Following the example values of step 2, -20 inches H_2O has been set up. After a few minutes (in order to allow the water gauge to build up the requested pressure) click on the Voltage to Read button (orange) in "D" to measure the voltages coming from both transducers, which will be displayed in "G" as digits and in monitor "E" as points.

Step 5

Click on the first cell in "C" and enter the pressure value set up on the water gauge (-20 inches H_2O in our example). Next, click on the Pressure Value button (violet). The program will accept the value.

Step 6

Go back to step 3 and repeat the sequence up to step 5 until all nine pressure values are entered in "C".

As soon as the last pressure value is entered in "C" an OK button will appear. A few moments after clicking on the OK button two calibration curves (one per transducer) will be drawn in monitor "F". They are also saved in three files (see 2.4 for more details).
Click on the DONE button to return to the Main Front Panel. To quit Tunlab, simply select Exit from the **File** menu.

2. Tunlab Technical Reference

The scope of this section is to facilitate any further modification that Tunlab may require for whatever reason it may be. In the following it is assumed that the reader has a somewhat advanced knowledge of Labview along with some experience upon a programming language.

2.1 STRUCTURE OF THE CODE

All the files the code consists of are locked to prevent any modification made by accident by an inexperienced user. Files need to be unlocked prior to any change. In particular, Tunlab is meant to be the code which, with appropriate modifications, will be deployed as a subVI within the software integrating the data acquisition system on board of the CONDOR RPV. The code was written using the G language available under Labview Student Edition version 3.1 for Windows and the "top-down" programming technique developed during the 70s. This technique ensures to have a robust code which is easy to debug, to maintain, and to modify, although it usually leads to a longer code.
The main program is tun_lab.vi which displays the main menu (called the Main Front Panel in the previous section) as a user-friendly interface. The main program calls a number of subVIs which in turn call other subVIs, forming a "tree" which is the classic structure of a code developed according to the top-down technique.
The code is described fairly in detail in the subsequent paragraphs by extensive use of flow charts. Each paragraph will describe a VI with its flow chart, I/O files and subVIs (if any). The reader should consult the corresponding VI files for a more detailed picture.

2.1.1 Tunlab_vi Main Program

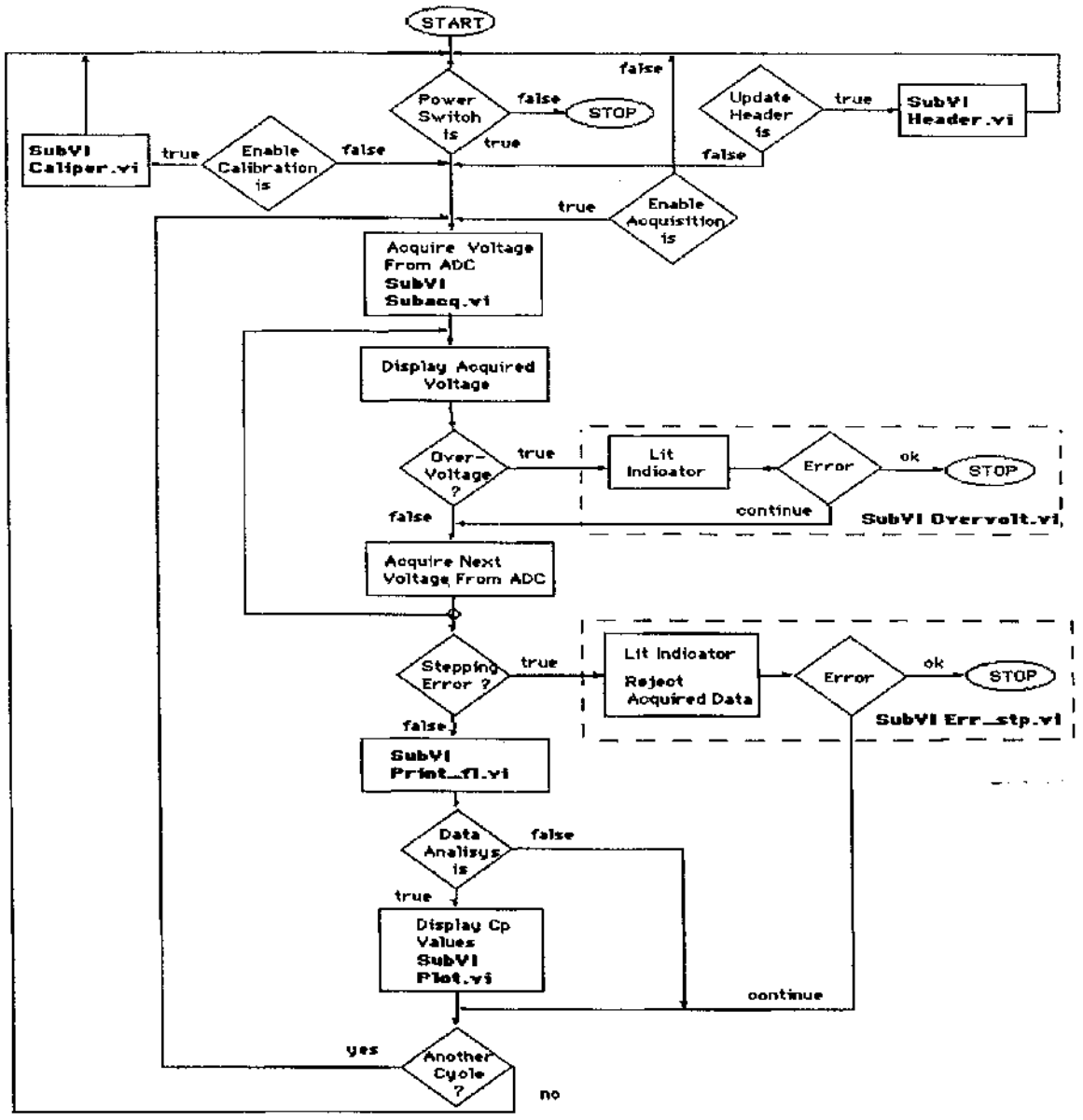

Fig.7 tunlab_vi Flow Chart

The flow chart is shown in fig.7. Refer to the tun_lab.vi file for more details.

Input Files

None

Output Files

None

Called SubVis

subacq.vi

cal_ref.vi

overvolt.vi

plot.vi

header.vi

caliper.vi

Simple Error Handler.vi

err_stp.vi

print_fl.vi

2.1.2 Header.vi SubVI

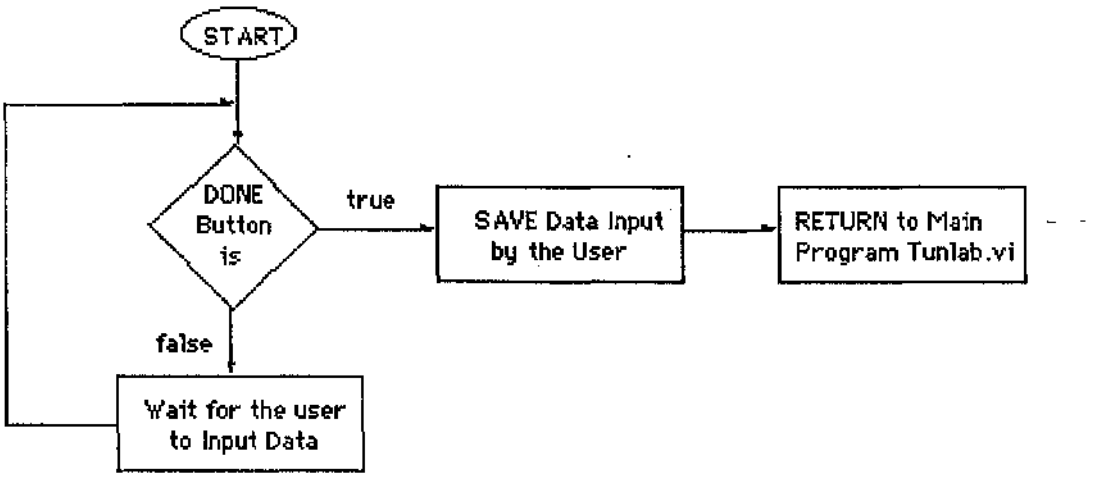

Fig.8 header.vi Flow Chart

The flow chart is shown in fig.8. Refer to the header.vi file for more details.

Input Files

None

Output Files

header.txt contains the data header.

q.txt contains the free stream pressure value.

run_no.txt contains the Run Number value. It is the alphanumeric string used by print_fl.vi to generate the two files with raw and converted data of an acquisition session.

Note : All are standard ASCII files.

Called SubVis

Write Characters to File.vi

2.1.3 Print_fl.vi SubVI

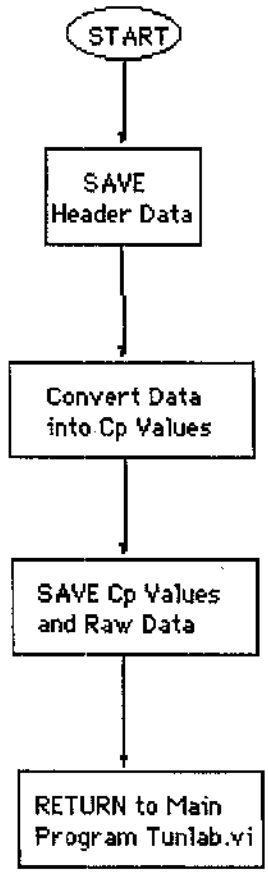

Fig.9 print_fl.vi Flow Chart

The flow chart is shown in fig.9. Refer to the print_fl.vi file for more details.

Input Files

header.txt contains the data header.

q.txt contains the free stream pressure value.

run_no.txt contains an alphanumeric string (Run Number value) entered by the user.

Output Files

<run number> contains a data header and corresponding cp values of a data acquisition session.

<run number>v contains the same data header as the <run number> file plus corresponding voltages measured during a data acquisition session. The last saved value is an offset.

Note : All are standard ASCII files.

Called SubVIs

Write Characters to File.vi

Write to Spreadsheet File.vi

Read Characters from File.vi

Read from Spreadsheet File.vi

Polynomial Interpolation.vi

2.1.4 Caliper.vi SubVi

The flow chart is shown in fig.10. Refer to the caliper.vi file for more details.

Input Files

None

Output Files

cal1x.txt contains measured voltages from transducer number one.

cal2x.txt contains measured voltages from transducer number two.

caly.txt contains measured differential pressure values from the water gauge.

Note : All are standard ASCII files.

Called SubVIs

Write to Spreadsheet File.vi

subacq.vi

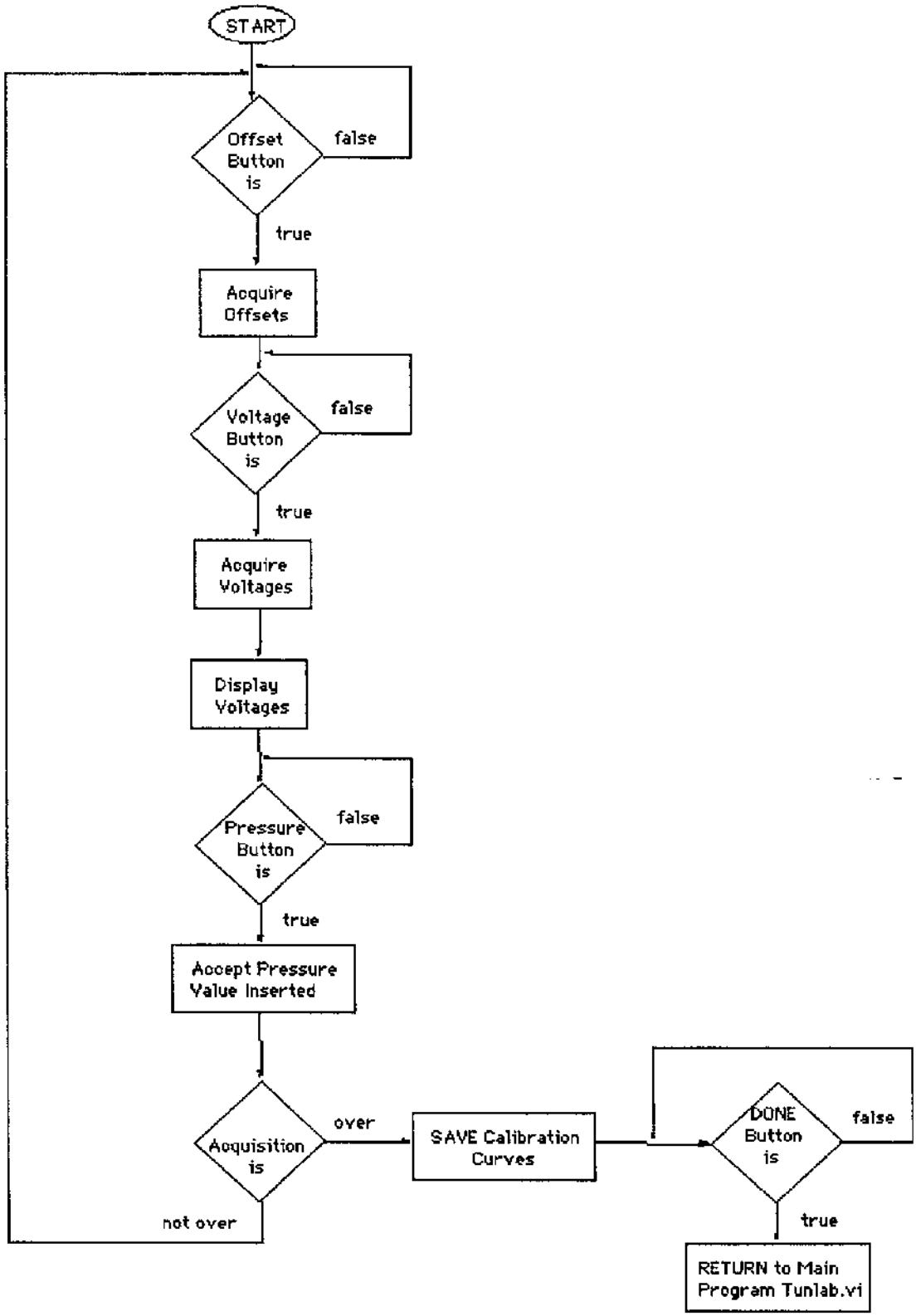

Fig.10 caliper.vi Flow Chart

Company Addresses

Item : Parachute Recovery System

Ballistic Recovery Systems, Inc.
Contact Person : Gregg Ellsworth, Domestic Sales Manager
1845 Henry Av.
South St. Paul, MN 55075-3541, USA
Fax : 612 457-8651

Irvin Aerospace Limited
Contact Person : Dr M.G.Woollard, Engineering Director
Icknield Way
Letchworth Hertfordshire SG6 1EU, UK
Tel : 01462 482000
Fax : 01462 482007

Item : Pressure Differential Transducers

Scanivalve Corporation
Contact Person : Derek Greener, European Technical Director
Avon Valley Business Park
23 St. Annes Road
Bristol BS4 4EE, UK
Tel : 0117 987 3435
Fax : 0117 987 3626

Item : Condor Airframe Manufacturer

AERON spol s.r.o.
Contact Person : Dipl.Ing. Daniel Lexa
Traubova 6
CZ 657 31 Brno, Czech Republic
Tel/Fax : 05 412 115 61

Item : Toshiba Satellite 110CS Notebook

PC World
Contact Person : Andrew McKie, Business Account Manager
30 Finnieston Street
Glasgow G3 8HB, UK
Tel : 0141 221 9044
Fax : 0141 221 7264

Item : National Instruments Hardware

IMEX Systems Ltd
Contact Person : Walter Gray, Sales Director
Coatbridge Business Park
Main Street, Coatbridge ML5 3RB, UK
Tel : 01236 440840
Fax : 01236 449392
Internet : www.imex.co.uk

Item : Air Data Booms

ENDEVCO UK Ltd
Melbourne, Royston
Hertz SG8 6AQ
Tel : 01763 261311
Fax : 01763 261120

Rosemount Aerospace, Inc.
Contact Person : Brad K.Elliott, Senior Marketing Engineer
14300 Judicial Road
Burnsville, MN 55306-4898, USA
Fax : 612 892 4948
E-mail : bradell@gw.rmtaero.bfg.com

Item : Radio Control Equipment

Paisley Model Centre
Contact Person : Bill Grimsley
80-82 Arkleston Road
Paisley PA1 3TS, UK
Tel : 0141 889 4221

Ripmax Plc
Ripmax Corner, Green Street
Enfield EN3 7SJ
Fax : 0181 804 1217

Item : RS Catalogue

Glasgow Trade Counter
38 Baird Street
Glasgow G4 0ED, UK

Fax : 0141 552 4448

Item : Condor Airframe Epoxy Resin and Foam

CIBA-GEIGY GESELLSCHAFF MBH
Contact Person : Friedrich Fitzma, Division Polymere
Postfach 319
Breitenfurterstrabe 251
A-1231 Wien, Austria
Fax : 0222 80111 421

Item : Condor Airframe Glassfibre

CS-INTERGLAS AG
Postfach 1103
D-89151 Erbach, Germany
Fax : 07305 955 513

Item : Landing Gear Wheels

Invacare Ltd
Purchasing Department
South Road, Bridgend Industrial Estate
Bridgend, Mid Glamorgan CF31 3PY, UK
Fax : 0656 766274

Item : Alternator Manufacturer

PAL-MAGNETON
Hulinska 4, 767 53 Kromeriz, Czech Republic
Fax : 0634 247 84

Item : Divinycell Expanded PVC Rigid Foam

Anglitemp Ltd.
Contact Person : D.M.McFarlane
Westmorland Road, West Chirton Middle Industrial Estate
North Shields, Tyne & Wear NE29 8TB
Fax : 0191 257 8445

Condor Data Source

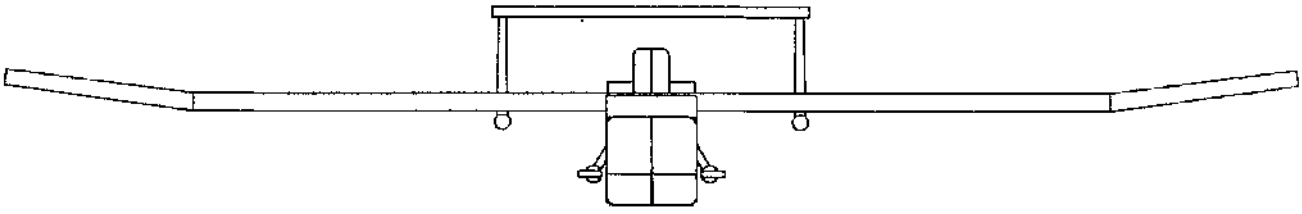

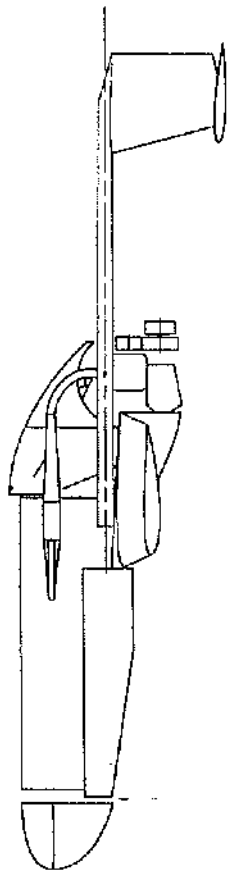

CONDOR

Remote Control Aircraft

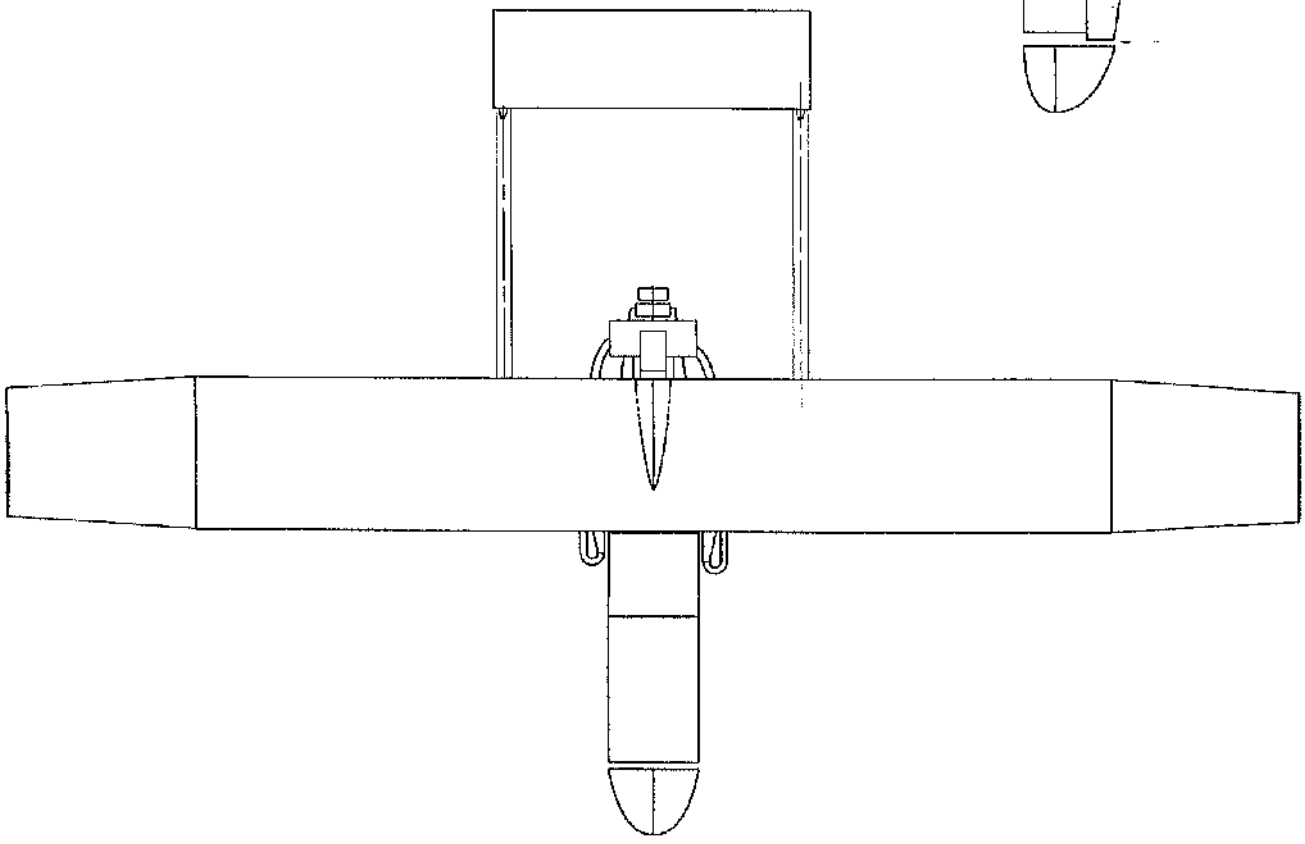

CONDOR SPECIFICATIONS

	WING	TAILPLANE	FIN
Area	4.05 sq m	0.638 sq m	0.177 sq m
Span	5.93 m	1.425 m	0.453 m
MAC	0.684 m	0.448 m	0.380 m
Aspect Ratio	8.68	3.18	1.16
Swept Angle	0 deg	0 deg	0 deg
Taper Ratio initial	1	1	1.36
extension	0.84		
Aerofoil	NACA 2415	NACA 0010	NACA 0010
Dihedral initial	0 deg	0 deg	0 deg
extension	5-8-11 deg		

Fuselage

Fuselage/Wing Incidence	1° 30' ÷ 1° 48'
Overall Lenght	4.07 m
Width	0.40 m
Height	N/A

Other Data

Maximum Take-off Weight	145 kg
Engine Power	16.5 kW
Propeller Diameter	0.85 m
CG Range	30 % MAC at any weight
Elevator Chord	0.184 m
Elevator Area	0.262 sq m
Wing/Tailplane Incidence	3° 40' ÷ 4° 40'
Limit Load Factors	-4 / +4
Fuel Capacity	19 lt
Control Surface Deflections (Aileron/Elevator)	-15° +12°

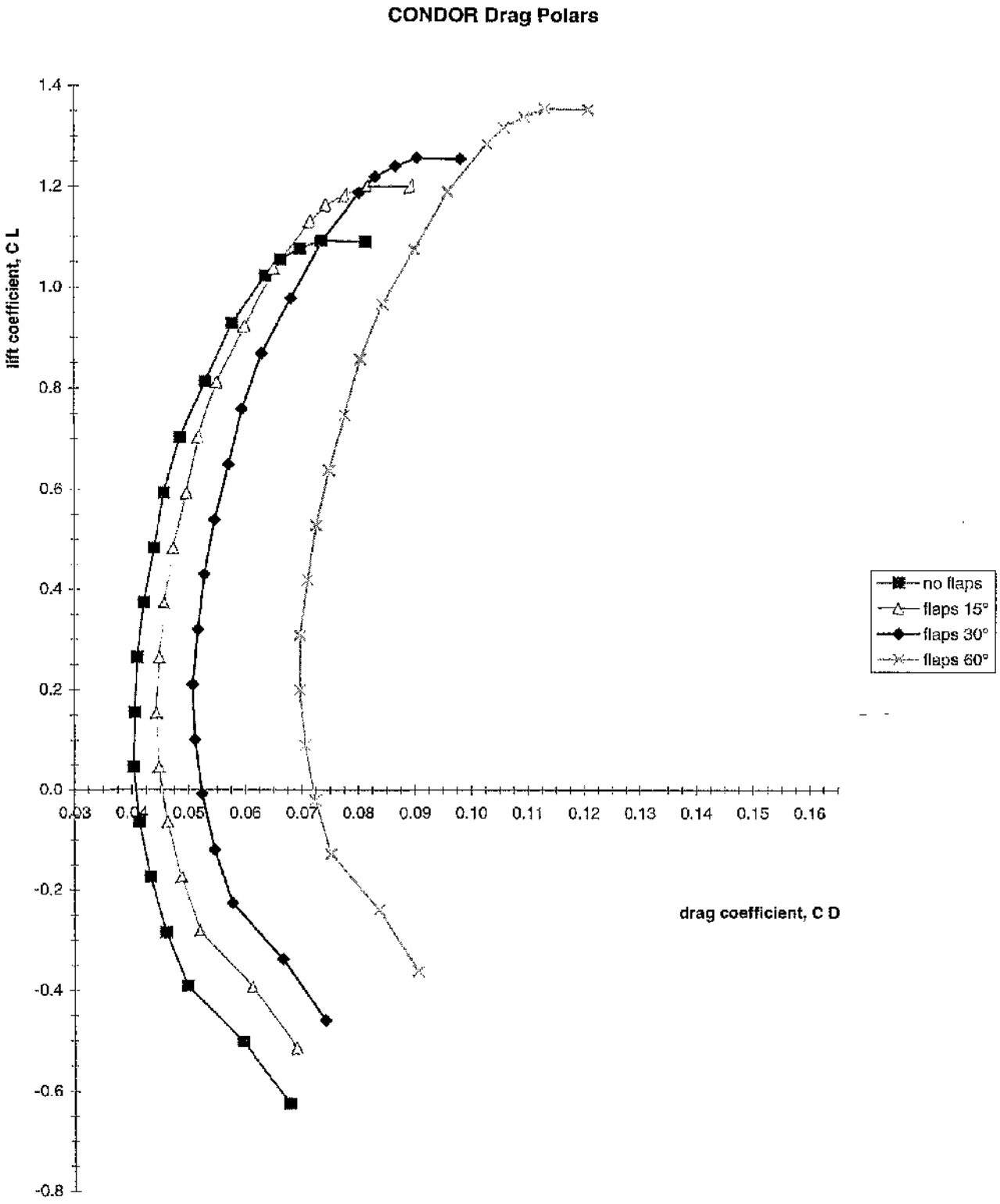
CONDOR Drag Polars
lift coefficient, C L
drag coefficient, C D
1.4
1.2
1.0
0.8
0.6
0.4
0.2
0.0
-0.2
-0.4
-0.6
-0.8
0.03
0.04
0.05
0.06
0.07
0.08
0.09
0.10
0.11
0.12
0.13
0.14
0.15
0.16
no flaps
flaps 15°
flaps 30°
flaps 60°

CONDOR Drag Polars

(Outboard) Flap Deflection Angle = zero

α	CL	CD
-9,858	-0,6236	0,06769
-8,182	-0,50124	0,05943
-6,875	-0,39022	0,04981
-5,71	-0,28356	0,04608
-4,41256	-0,17283	0,04324
-3,15628	-0,06337	0,0413
-1,9	0,04609	0,04028
-0,64372	0,15556	0,04052
0,61256	0,26502	0,0409
1,86884	0,37448	0,04198
3,12513	0,48395	0,0437
4,38141	0,59341	0,04533
5,63769	0,70287	0,0481
6,89397	0,81234	0,05248
8,324	0,92714	0,0571
9,716	1,02257	0,06275
10,483	1,05468	0,06512
11,36	1,07625	0,06818
12,213	1,09195	0,07153
13,7	1,09061	0,07889

(Outboard) Flap Deflection Angle = 15 deg

α	CL	CD
-9,858	-0,51461	0,07289
-8,182	-0,39224	0,06405
-6,875	-0,28122	0,05396
-5,71	-0,17457	0,04983
-4,41256	-0,06384	0,04653
-3,15628	0,04563	0,04415
-1,9	0,15509	0,04268
-0,64372	0,26455	0,04249
0,61256	0,37402	0,04243
1,86884	0,48348	0,04307
3,12513	0,59294	0,04434
4,38141	0,7024	0,04553
5,63769	0,81187	0,04786
6,89397	0,92133	0,0518
8,324	1,03613	0,05591
9,716	1,13154	0,06116
10,483	1,16364	0,06341
11,36	1,18519	0,06638
12,213	1,20089	0,06971
13,7	1,19959	0,07716

CONDOR Drag Polars

(Outboard) Flap Deflection Angle = 30 deg

α	CL	CD
-9,858	-0,4592	0,07978
-8,182	-0,33684	0,07064
-6,675	-0,22582	0,06032
-5,71	-0,11916	0,05598
-4,41256	-0,00843	0,05245
-3,15628	0,10103	0,04984
-1,9	0,21049	0,04816
-0,64372	0,31995	0,04773
0,61256	0,42942	0,04745
1,86884	0,53888	0,04787
3,12513	0,64834	0,04891
4,38141	0,75781	0,04988
5,63769	0,86727	0,05198
6,89397	0,97673	0,0557
8,324	1,09154	0,05956
9,716	1,18694	0,0646
10,483	1,21902	0,06678
11,36	1,24056	0,06971
12,213	1,25626	0,07304
13,7	1,25499	0,08053

(Outboard) Flap Deflection Angle = 60 deg

α	CL	CD
-9,858	-0,36107	0,09875
-8,182	-0,23871	0,08908
-6,875	-0,12769	0,07835
-5,71	-0,02103	0,07364
-4,41256	0,0897	0,0697
-3,15628	0,19916	0,06669
-1,9	0,30862	0,06461
-0,64372	0,41809	0,06379
0,61256	0,52755	0,0631
1,86884	0,63701	0,06312
3,12513	0,74648	0,06377
4,38141	0,85594	0,06435
5,63769	0,9654	0,06605
6,89397	1,07487	0,06937
8,324	1,18967	0,07278
9,716	1,28506	0,07746
10,483	1,31712	0,07952
11,36	1,33864	0,08238
12,213	1,35434	0,08569
13,7	1,35311	0,09325

WING EXTENSION STRUCTURAL TEST

Date : April 1997
Wing : Dry, Undamaged
Note : Inner aileron was removed from the wing at the time of the test.

Calculation of applied load

RPV MTOW ---) W =145 Kg
RPV Max Cruise Speed ---) v =180 Km/h (50 m/s)
RPV Wing Area ---) S = 2.8 mq
Area of Wing Extension ---) S_{ext} = 0.59 mq

$$C_L = \frac{2W}{\rho v^2 S} = \frac{2(1450)}{(1.225)(50)^2(2.8)} = 0.34$$

If we look at the Sojka RPV polars we have $\alpha = 1$ deg at $C_L = 0.34$
At this angle of attack ($\alpha = 1$ deg) the numerical solution of Rampant gave, after integration of the pressure distribution over the wing extension only, the following coefficient :

$$C_{N_{ext}} = 0.154$$

JAR-VLA 337 (a) suggests a load factor of n = 3.8
We can now estimate the total lift on the wing extension :

$$L_N = 0.5\rho v^2 S_{ext} C_{N_{ext}} = (0.5)(1.225)(50)^2(0.59) = 139N = 14Kg$$

and therefore the limit applied load :

$$L_{N_{lim}} = nL_N = (3.8)(14)Kg = 54Kg$$ (119 lb)

Performing the test

A weight of 100 lb, corresponding to n = 3.2, was applied at about 3/4 of the wing extension span, for 3 minutes.
The measured deflection at the wing extension tip was 115 mm
After removal of the weight the measured deflection was zero approximately.

VERTICAL TAIL GEOMETRY

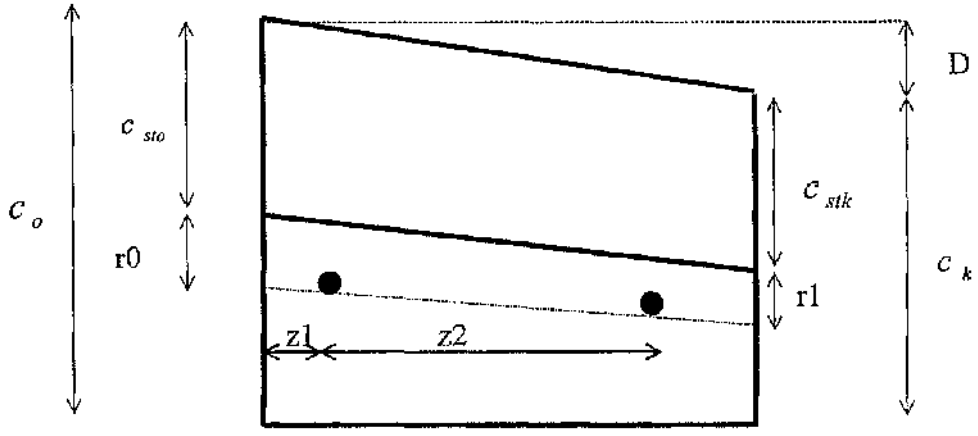

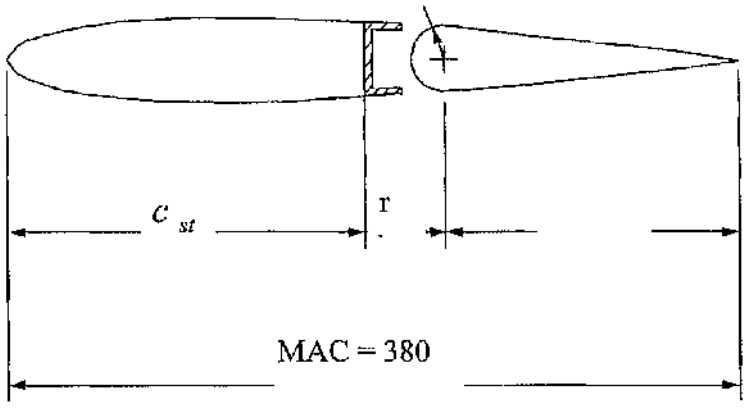

b = 453
c_o = 450
c_{sto} = 265
c_{stk} = 198
D = 116
z1 = 0

c_k = 332
r0 = 37
r1 = 24
c_{st} = 223
r = 27
z2 = 453

ALL DIMENSIONS IN MILLIMITERS (NOT TO SCALE)

OUTBOARD AILERON GEOMETRY

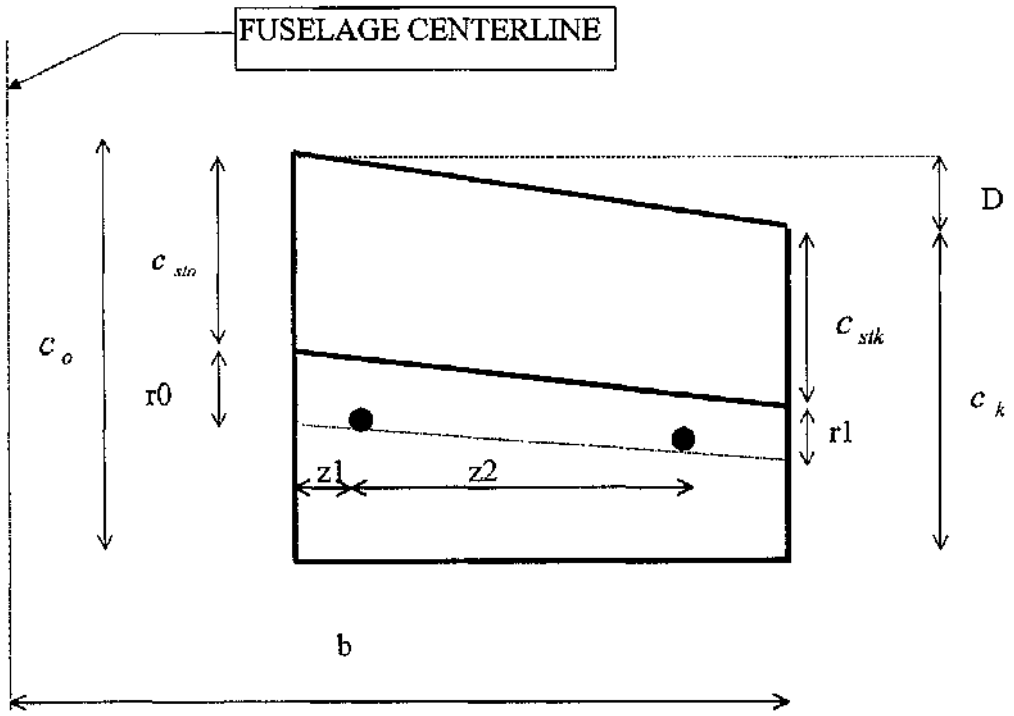

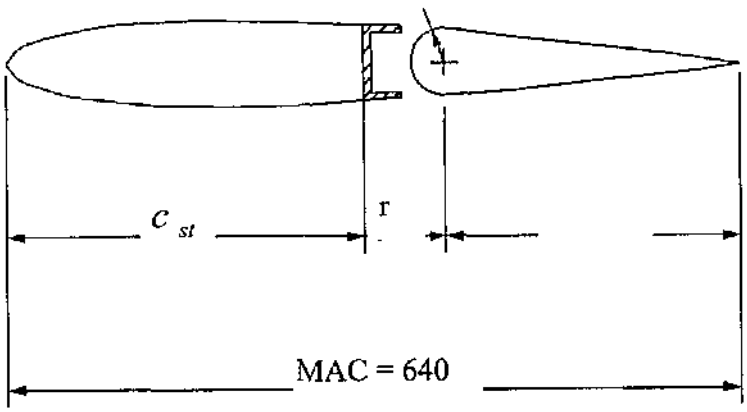

b = 2820
c_o = 700
c_{sto} = 590
c_{stk} = 490
D = 80
z1 = 0

c_k = 590
r0 = 35
r1 = 25
c_{st} = 540
r = N/A
z2 = 800

ALL DIMENSIONS IN MILLIMITERS (NOT TO SCALE)

HORIZONTAL TAIL GEOMETRY

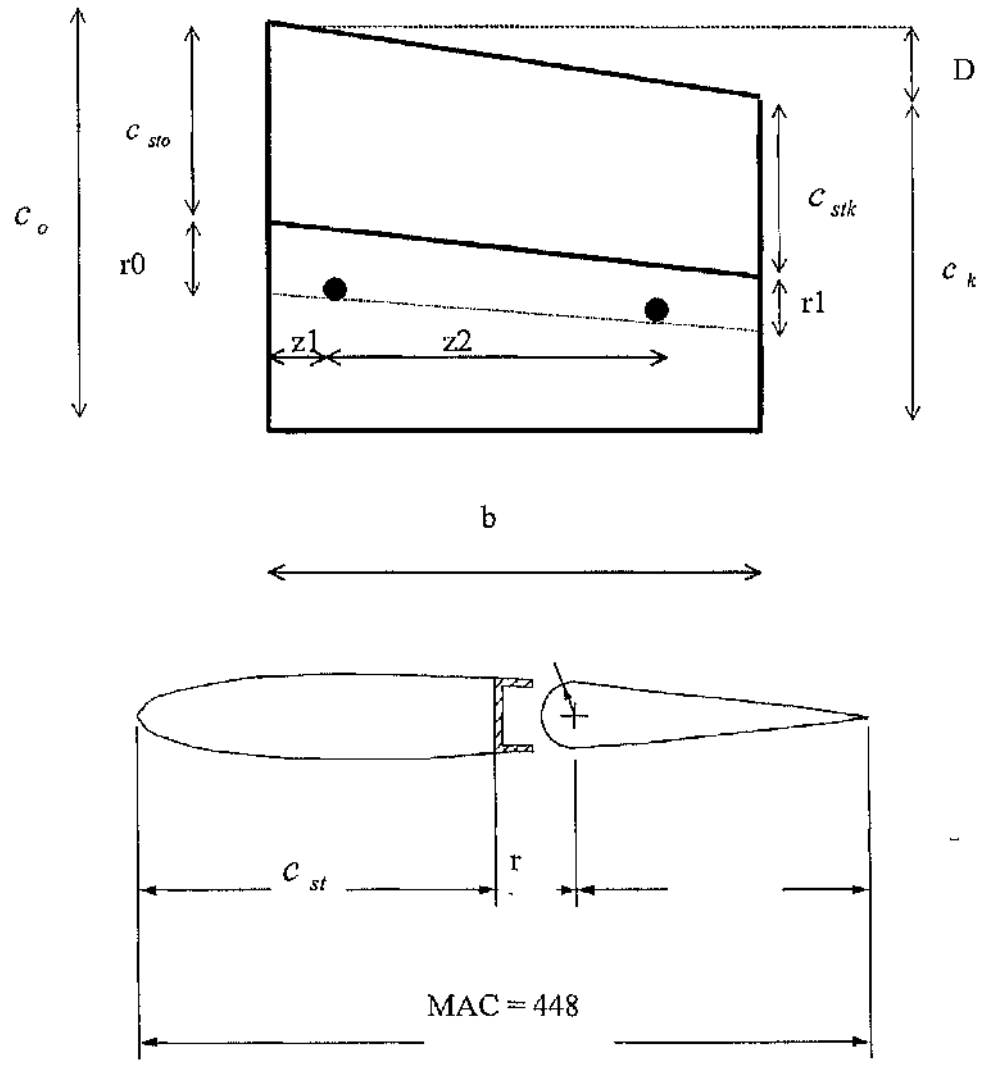

b = 1425
c_o = 448
c_{sto} = 264
c_{stk} = 264
D = 0
z1 = 220

c_k = 448
r0 = 36
r1 = 36
c_{st} = 264
r = 36
z2 = 0

ALL DIMENSIONS IN MILLIMITERS (NOT TO SCALE)

INBOARD AILERON GEOMETRY

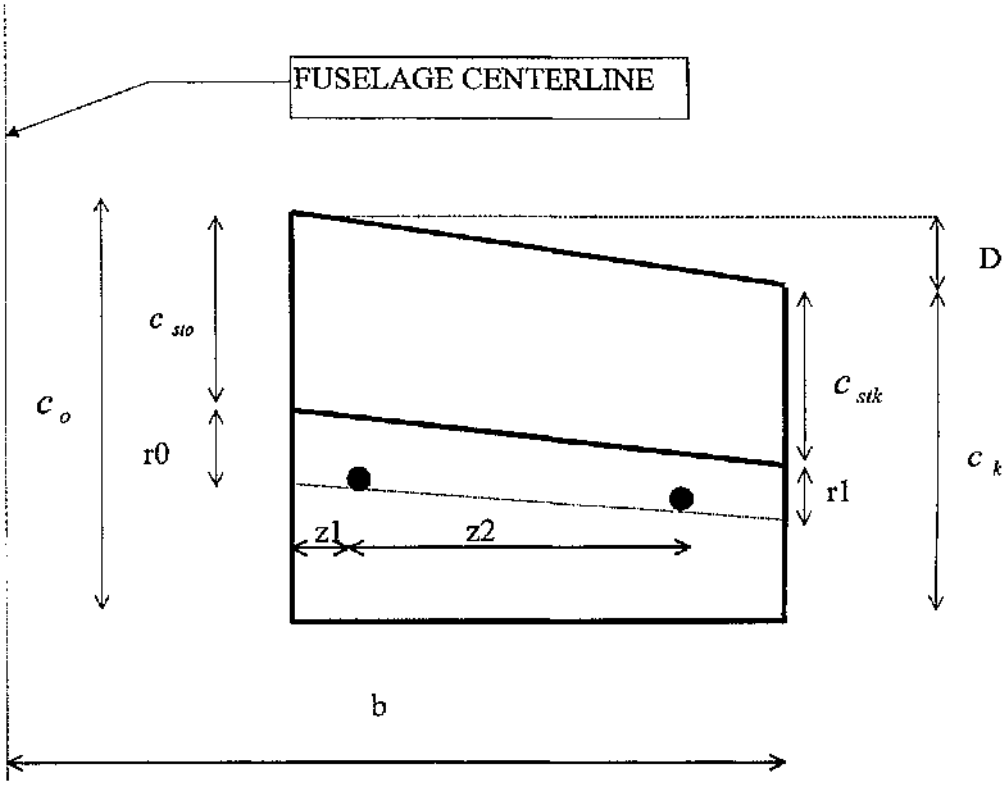

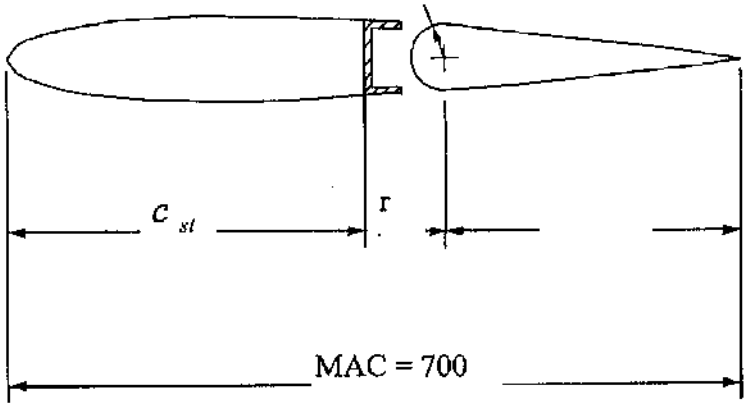

b = 2050
c_o = 700
c_{sto} = 567
c_{stk} = 567
D = 0
z1 = 0

c_k = 700
r0 = 27
r1 = 27
c_{st} = 567
r = 27
z2 = 832

ALL DIMENSIONS IN MILLIMITERS (NOT TO SCALE)

POWERPLANT DATA

Manufacturer		Ustav Pro Vyzkum Motorovych Vozidel CS 180 68 Praha 9 - Lihovararska 12
Engine Model		M115V
Engine Type		Two Stroke Flat Air Cooled
Number of Cylinders		2 - Opposed
Bore		62 mm
Stroke		52 mm
Displacement		314 cm^3
Compression Ratio		11 : 1
Reduction Gear Ratio		1.55 : 1
Carburettor		Diaphragm Type
Maximum Power		16.5 kW/6000 rpm
Maximum rpm		7500
Ignition		via 12V Battery
Alternator		PAL 28V/35A Type 443 113 516 830
Current Supply		N/A
Lubrication		Mixture of Fuel and Oil
Fuel Consumption (at 4400 rpm)		5.94 kg/hour
Minimum Fuel Grade		96 Octane
Oil		MOGUL TS (M2T - Super) CASTROL TTS - Super CASTROL TTS - Syntec
Fuel/Oil Ratio		40 : 1
External Dimensions	Lenght	360 mm
	Width	488 mm
	Height	336 mm
Dry Engine Weight		19.4 kg

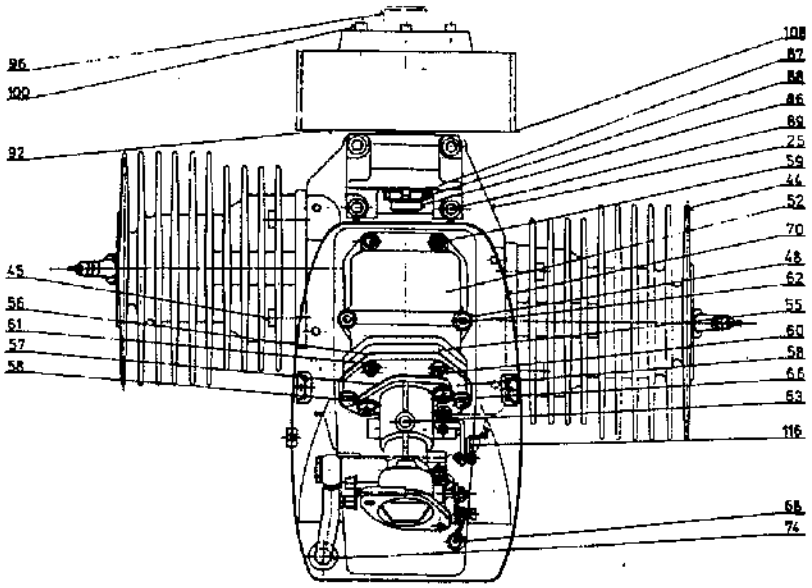

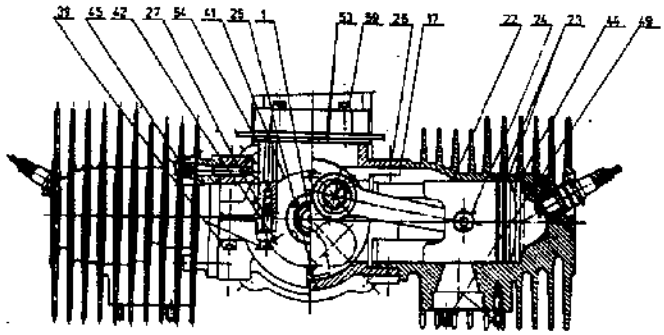

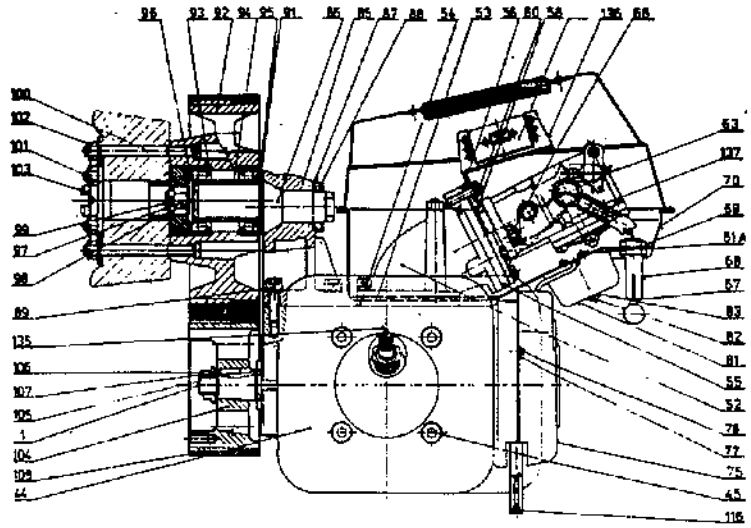

ENGINE MODEL M 115V THREEVIEW

Engine Model	M 115V	Umidity	42 %
Propeller Model	V 115.25	Ceiling	Cloudy
Temperature	24 ° C	Date	30.6.94

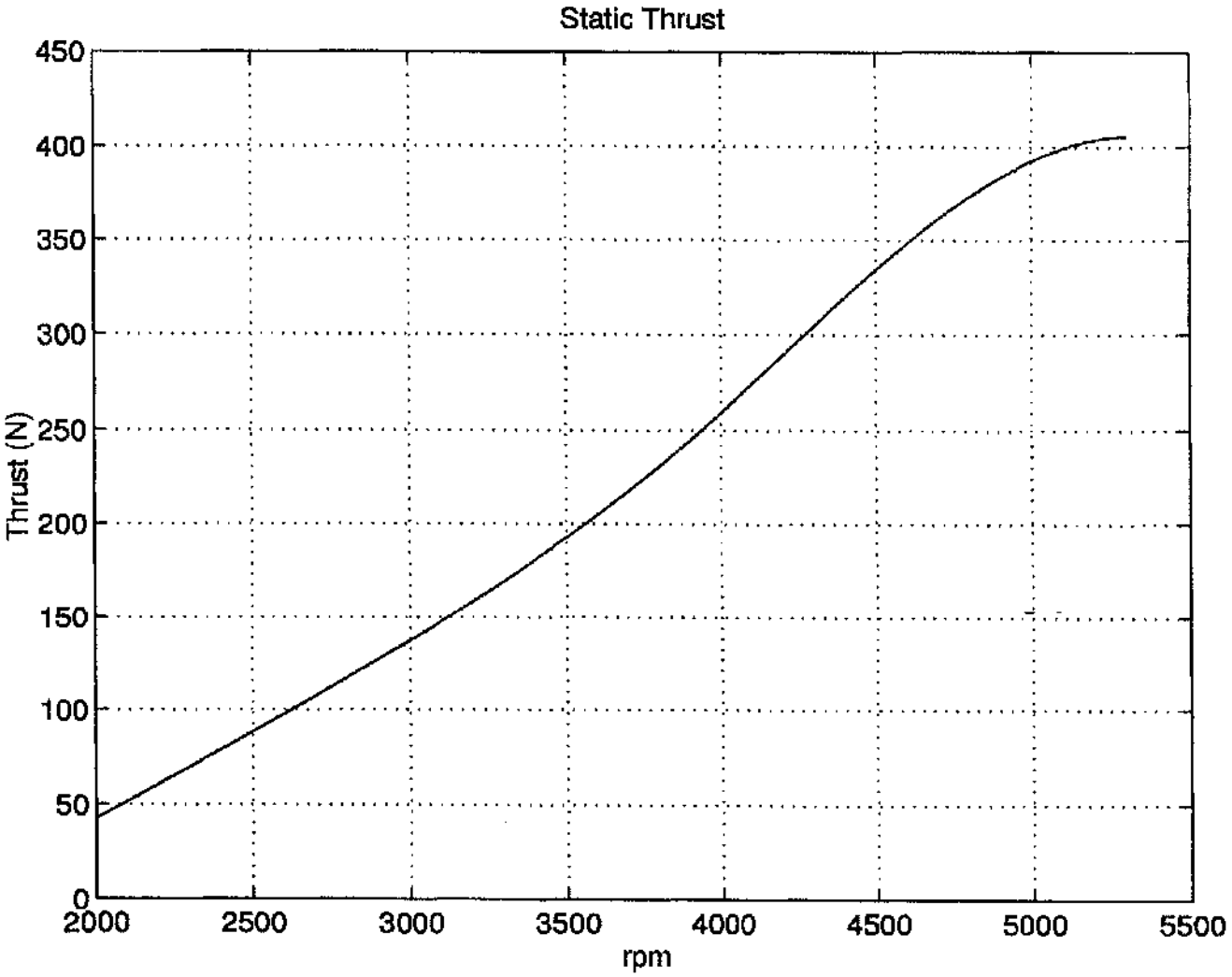

Engine Model	M 115V	Date	11.2.97
Temperature	18 °C	Barometric Pressure	98.5 hPa
Fuel	BA 96 Super	Oil	Castrol Synt.
Oil/Fuel Ratio	35 : 1	Reduction Gear Ratio	1.5 : 1
Ignition System	12V Battery	Exhaust Tubes Without Silent Blocks	

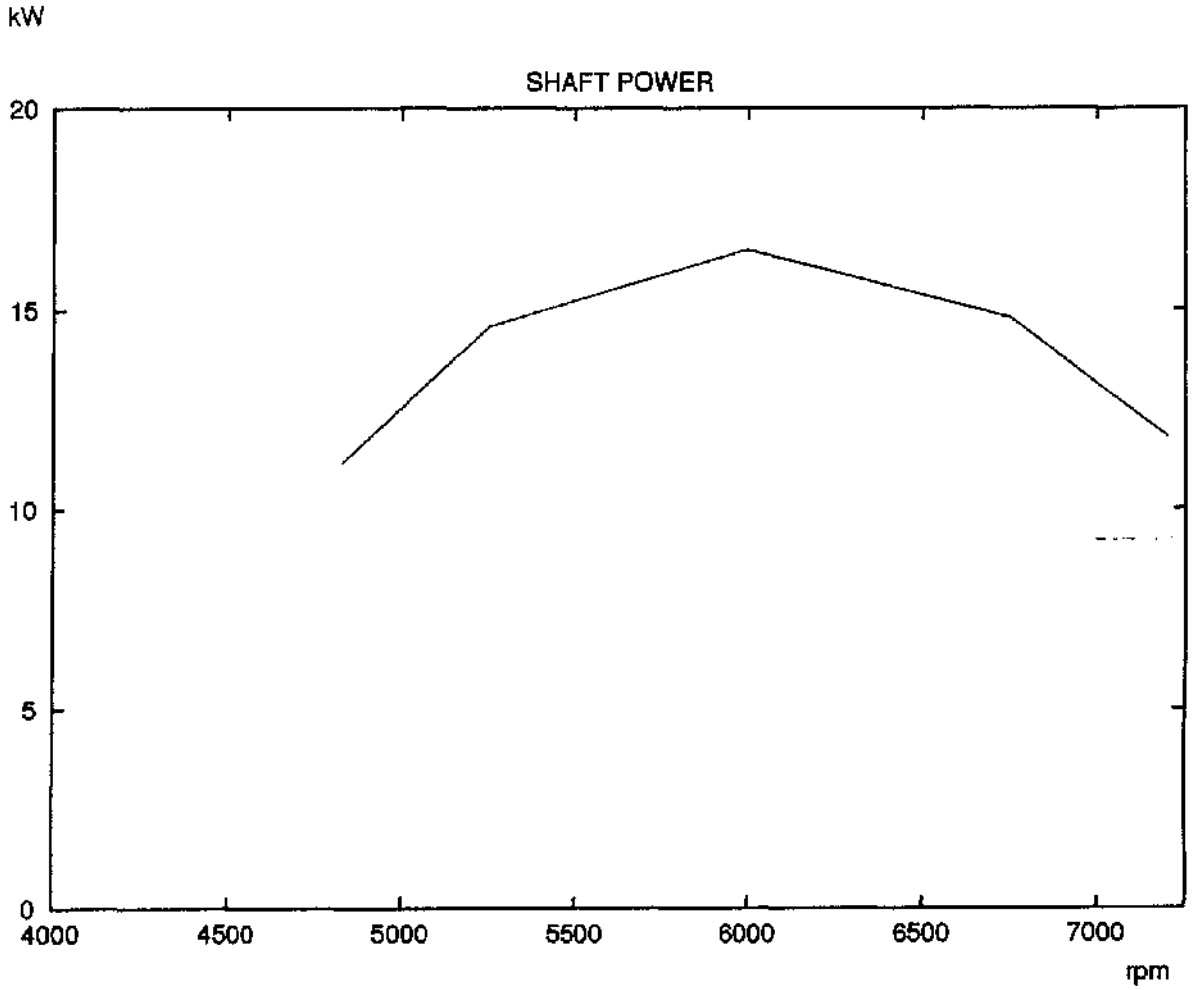

ALTERNATOR 28 V 35 A

TYPE: 443 113 516 830

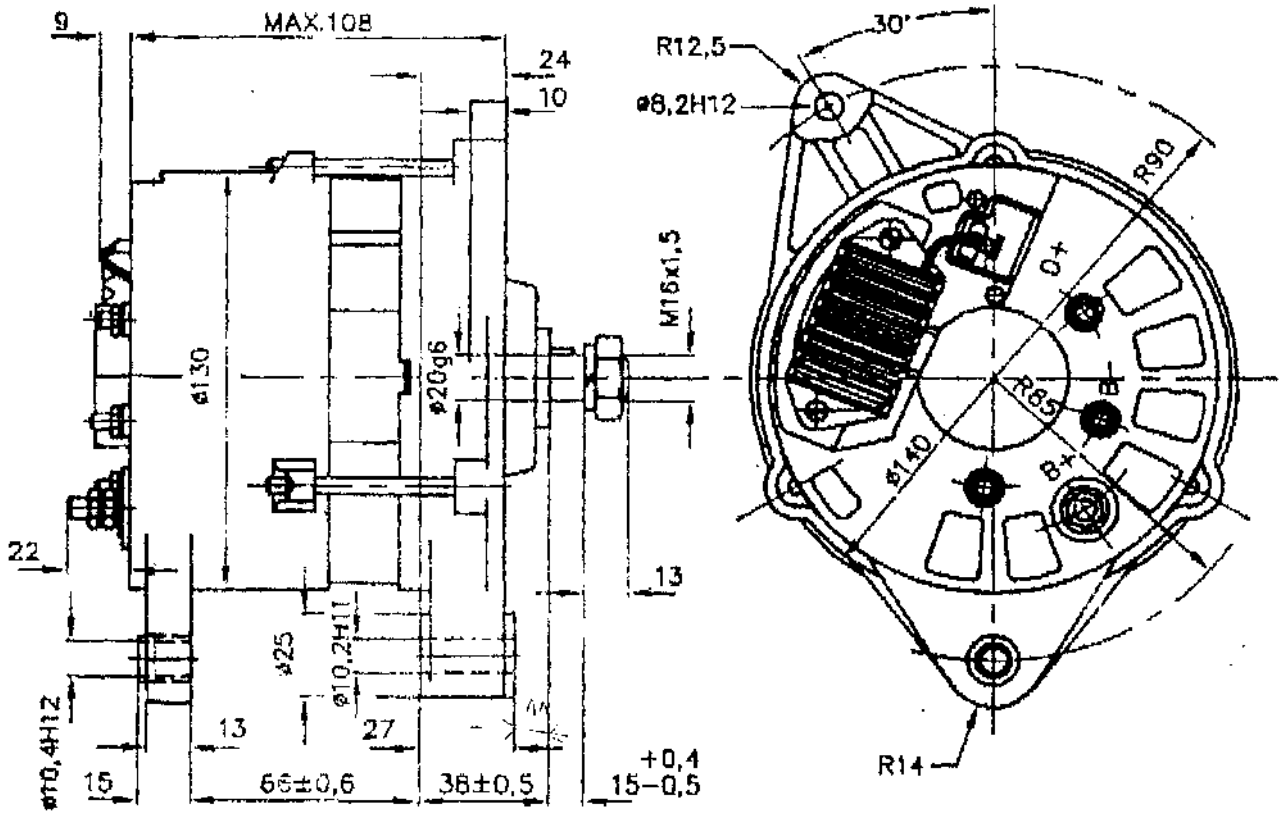

NOMINAL VOLTAGE:	28 V
NOMINAL CURRENT:	35 A
START OF CHARGING U=25V/I=0:	1 150 r. p. m.
MAX. SPEED:	8 000 r. p. m.

BULT-IN SEMICONDUCTING VOLTAGE REGULATOR

DERIVED TYPES

443 113 516 830	WITHOUT FAN AND PULLEY	4,5 kg
443 113 516 831	WITH FITTED ON RIGHT-HANDED FAN AND ONE GROOVE PULEY	5,2 kg
443 113 516 832	WITH FITTED ON RIGHT-HANDED FAN AND TWO GROOVES PULEY	5,3 kg
443 113 516 833	WITH SEPARATELY PACKED RIGHT-HANDED FAN WITHOUT PULEY	4,7 kg
443 113 516 836	WITH FITTED ON LEFT-HANDED FAN AND ONE GROOVE PULEY	5,2 kg

PAL - MAGNETON

HULÍNSKÁ 4, 767 53 KROMĚŘÍŽ
CZECHOSLOVAKIA
TEL.: 0634/44 11 11 FAX: 0634/247 84

CHARACTERISTICS

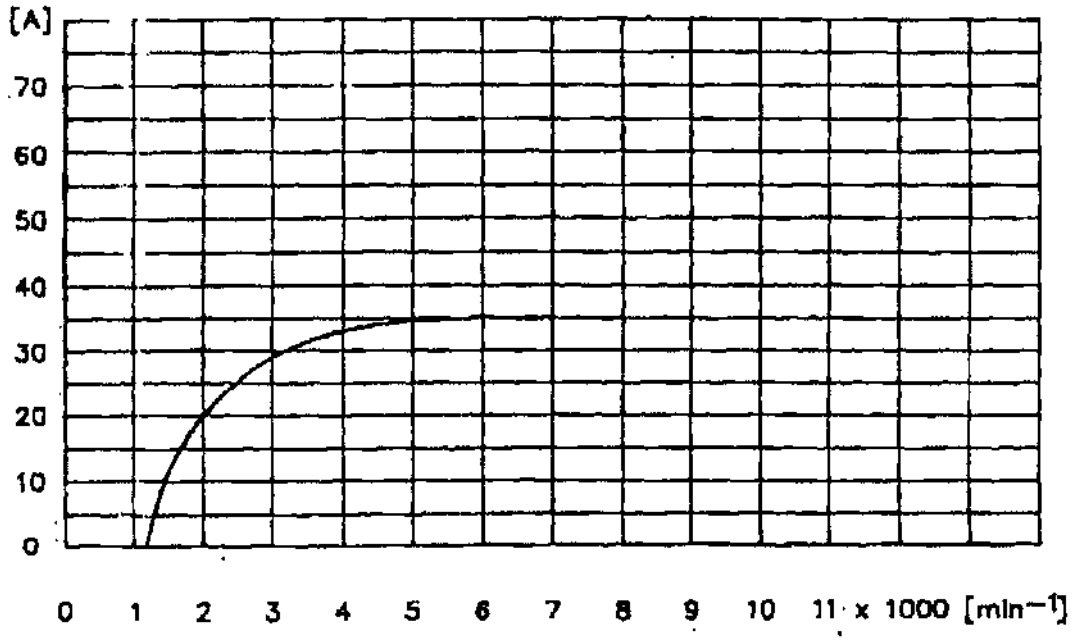

WIRING DIAGRAM

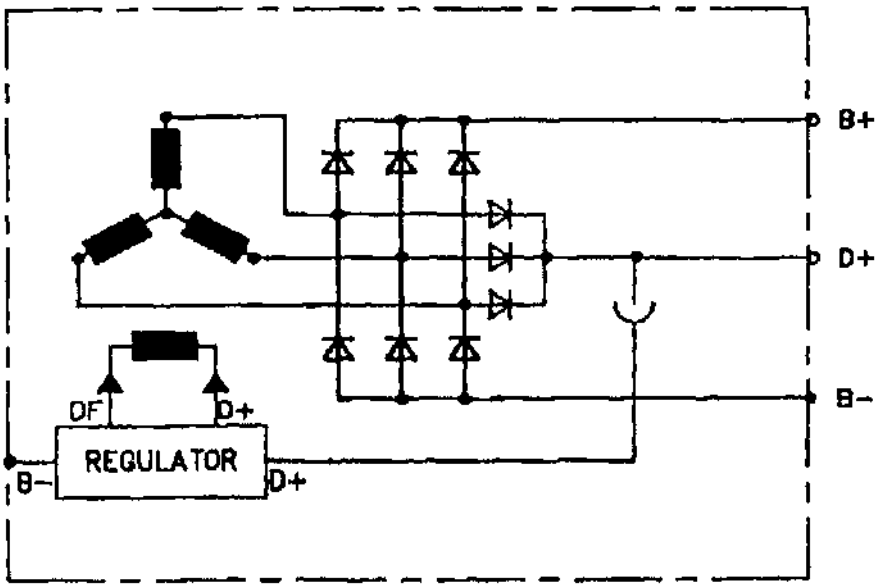

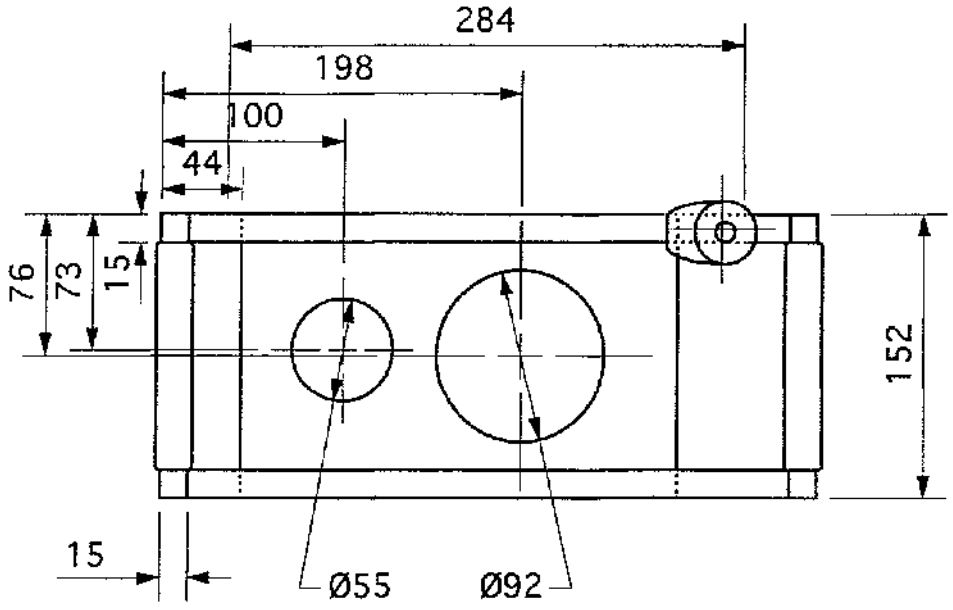

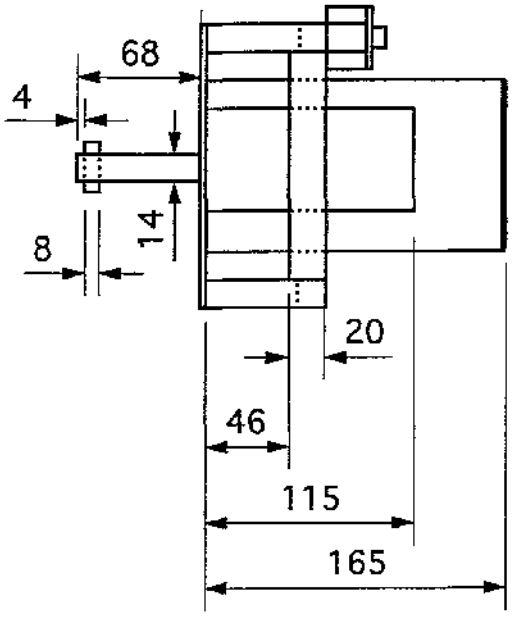

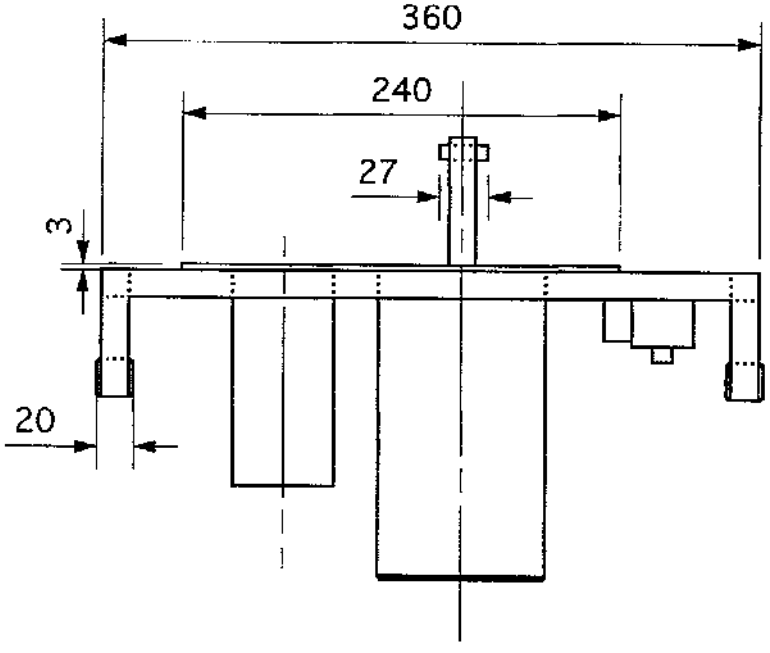

STARTER

Units : mm

PROPELLER DATA

Model	V125R
For Engine Type	M115
Propeller Characteristics	Fixed Pitch
Diameter	850 mm
Blade Material	Ash
Number of Blades	2
Angle of Blade Setting at $R_{75\%}$	20° 55'
Weight	0.95 Kg
Service Life	N/A

Engine Model	M 115V	Altitude	Sea Level (ISA)
Propeller Model	V 125B	Date	15.2.94

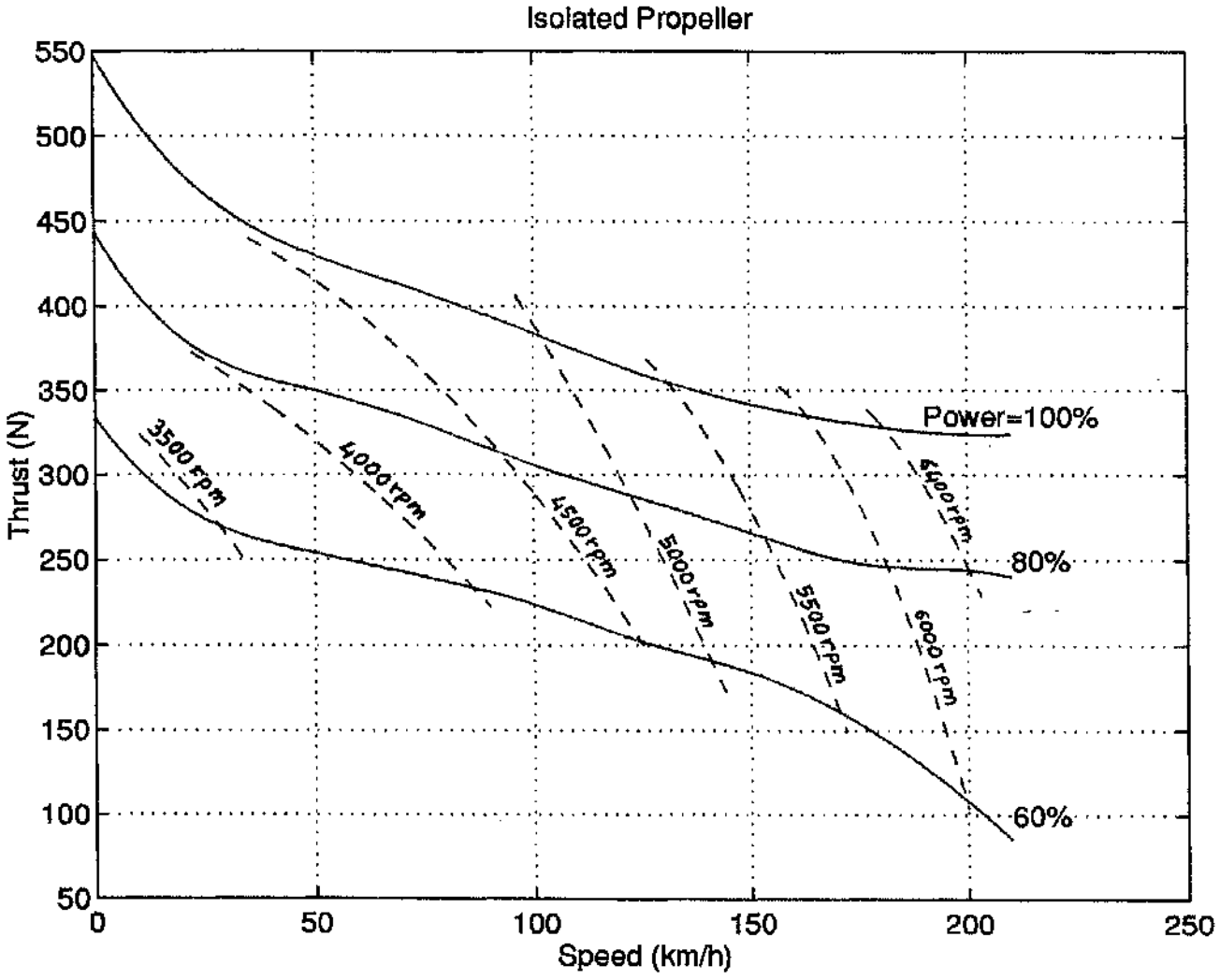

MAIN WHEEL CODE 6000 783
TYPE 200X50 mm

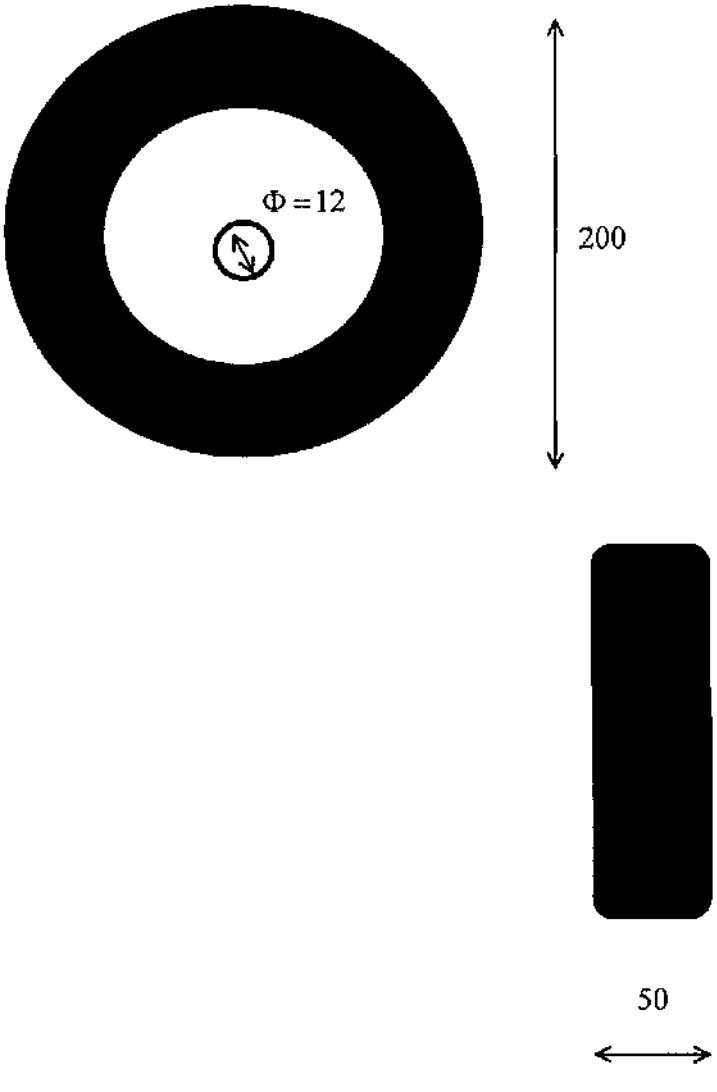

MAX INFLATION PRESSURE : 36 PSI (2.5 BAR)

WEIGHT : 1.13 Kg

ALL DIMENSIONS IN MILLIMETERS (NOT TO SCALE)

NOSE WHEEL CODE 0249N 3959
TYPE 152X28 mm

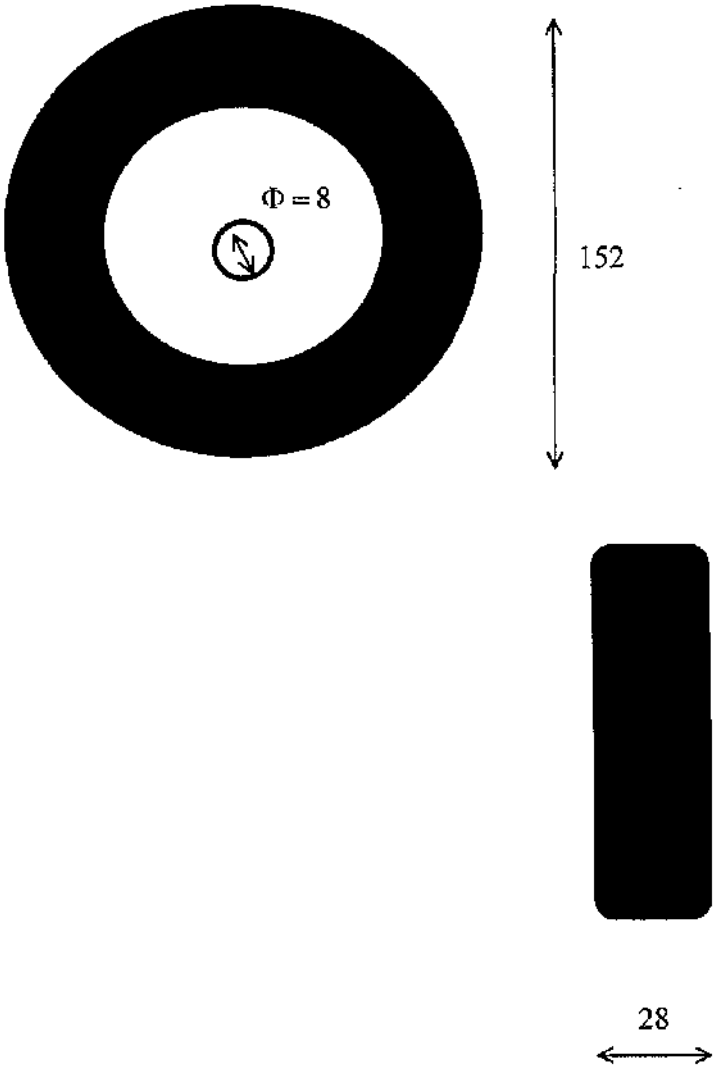

MAX INFLATION PRESSURE : 36 PSI (2.5 BAR)

WEIGHT : 0.275 Kg

ALL DIMENSIONS IN MILLIMETERS (NOT TO SCALE)

Appendix

D

Wing Glove Data

GLOVE DATA

Chord :	1.05 m
Span :	0.83 m
Aspect Ratio :	0.79
Aerofoil :	NACA 0012
Offset of Glove/Wing Chord :	zero
No. of Pressure Tappings :	30 + 30
Max Reynolds Testing Number :	$3.2 \cdot 10^6$
Weight :	**6.92 kg** (15.25 lb) without plates, paint, glue, tubes, attachment fittings; **7.60 kg** (16.75 lb) including paint, glue, tubes, attachment fittings, without endplates
Materials :	Balsa 96 kg/ m^3 for the core; Marine Mohogany Plywood for two layer skin; Mohogany for the endplates (4 mm thick); Aluminum BS 1470/NS4 for the fittings
Painting :	Herberts STANDOX, Grey 405 0360 as undercoat; Anti-Bloom as thinner; Matt Black Hycote Acrylic Paint
Glue for tubes :	LOCTITE 454
Endplates Weight :	681 g (Type 5 cm) 1.38 kg (Type 10 cm) 1.23 kg (Type Special)

Px No.	31		32	33	34	35	36	37	38	39	40	41	42	43
Px No.		30	29	28	27	26	25	24	23	22	21	20	19	18
X/C	0	0.0073	0.0145	0.0264	0.0414	0.0482	0.0655	0.0810	0.1030	0.1234	0.1789	0.2236	0.2684	0.3132

Px No.	44	45	46	47	48	49	50	51	52	53	54	55	56	57
Px No.	17	16	15	14	13	12	11	10	9	8	7	6	5	4
X/C	0.3580	0.4027	0.4474	0.4922	0.5370	0.5817	0.6265	0.6712	0.7160	0.7608	0.8055	0.8503	0.8951	0.9296

Px No.	58	59	60											
Px No.	3	2	1											
X/C	0.9507	0.9703	0.9911											

COORDINATES OF PRESSURE TAPPINGS

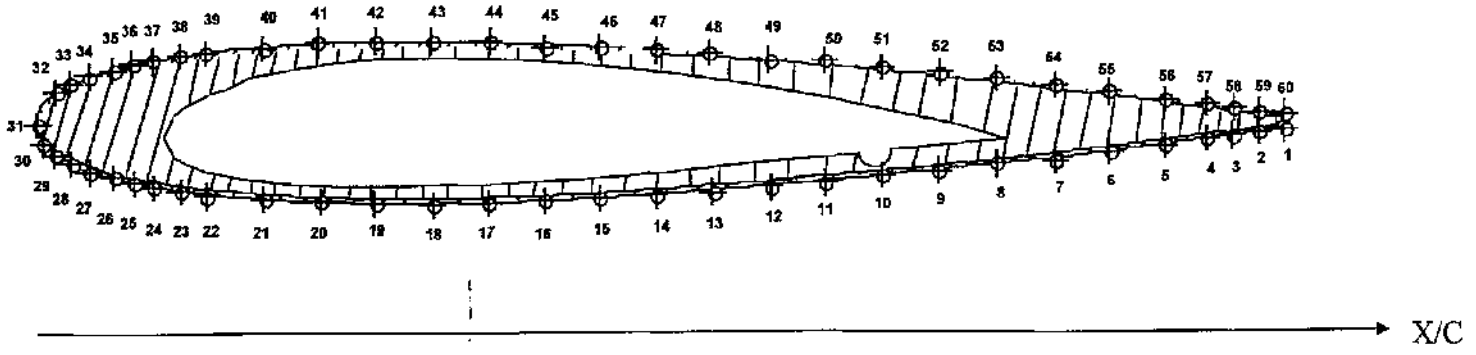

Geometry Data Of Endplates With Constant Height

Endplates Height = 5cm	
x [mm]	y [mm]
0	0
14.0	30.5
57.0	56.0
85.0	68.5
113.5	77.0
170.5	90.0
227.0	96.0
283.5	99.0
340.5	100.0
567.5	92.5
681.0	84.0
794.5	74.0
908.0	62.0
1021.5	46.0
1078.0	38.0
1112.0	30.0
1125.0	18.0
1135.0	0
chord = 1135 mm	
x_{offset} = 48 mm	

Enplates Height = 10cm	
x [mm]	y [mm]
0	0
15.5	46.0
31.0	62.5
62.0	84.0
92.5	103.0
123.5	115.5
185.5	135.0
247.0	144.0
370.5	150.0
617.5	139.0
741.0	126.0
864.5	111.0
988.0	93.0
1111.0	70.0
1173.0	57.0
1210.0	45.0
1224.0	27.0
1235.0	0
chord = 1235 mm	
x_{offset} = 100 mm	

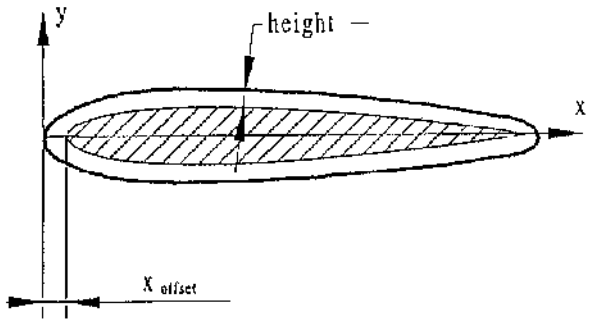

Thickness of Endplates: 4mm

Geometry Data Of Specially Designed Endplates

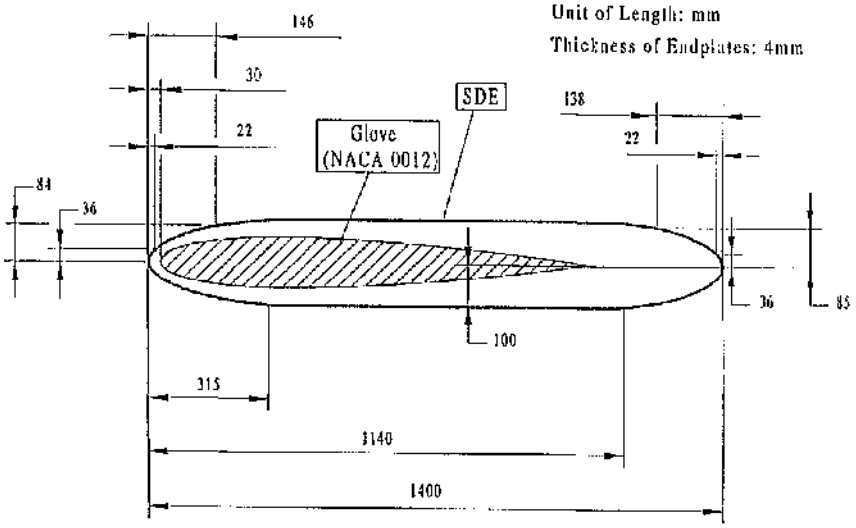

Appendix

E

Radio Control Equipment Data

RADIO CONTROL EQUIPMENT DATA

Receiver R-138DP
Channels : 8
Dimensions : 65X36X21.5 mm
Weight : 40.3 g
Input Voltage : 4.8 - 6.0 V
Current Drain : 12mA at 4.8V

Servo PS3001
Torque : 3 Kgcm
Dimensions : 40.4X19.8X36 mm
Weight : 45.1 g
Input Voltage : 4.8 - 6.0 V
Current Drain : N/A

Hi-Torque Servo PS3032
Torque : 8 Kgcm
Dimensions : 59.2X28.8X49.8 mm
Weight : 103 g
Input Voltage : 4.8 - 6.0 V
Current Drain : 0.9A at 6.0V

Hi-Torque Servo PS3801
Torque : 14 Kgcm
Dimensions : 59.2X28.8X49.8 mm
Weight : 103 g
Input Voltage : 4.8 - 6.0 V
Current Drain : 1.4A at 6.0V

Nickel Metal Hydride Battery
Pt. No. 0-4N2500NMHWF
Capacity : 4.8V 2.5Ah
Charging : 16 hours at 250mA
Max Discharge Rate : 7.5A
Disposal : No special disposal facilities are required
Storage : Recharge after 3 weeks for full capacity

Switch Harness 2 LED Robbe F 1403
Dimensions : 34.5X15.5X15 mm
Weight : ca. 12g
Display Range : 3.5 - 7.0 V
Current Drain : 20mA at 4.8V
Functions : RC receiving ON/OFF switch
Receiver battery voltage monitor
Receiver battery charging via integral charge socket

PUSHROD

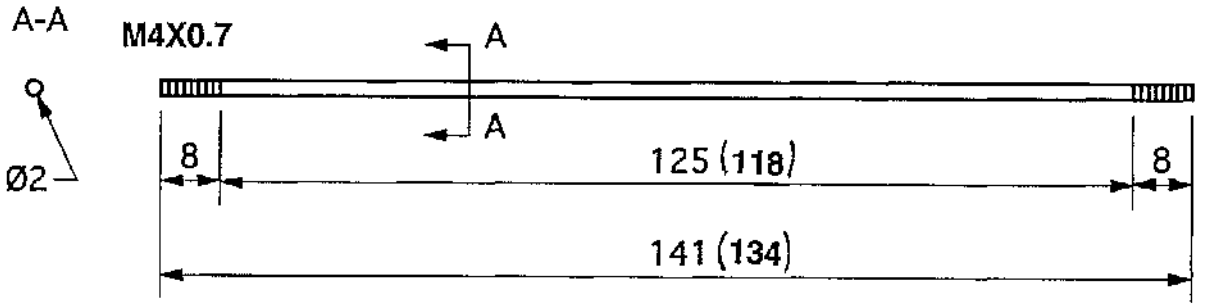

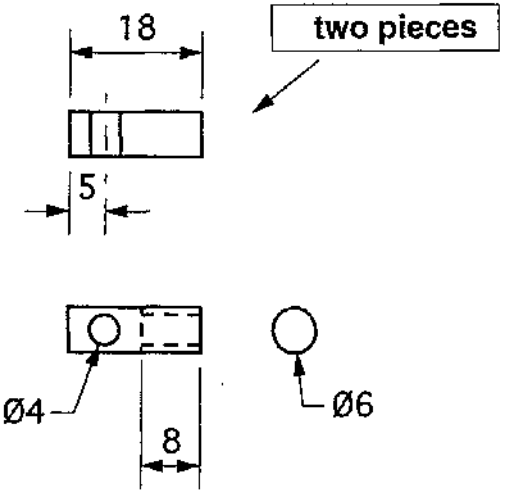

SERVO-HORN

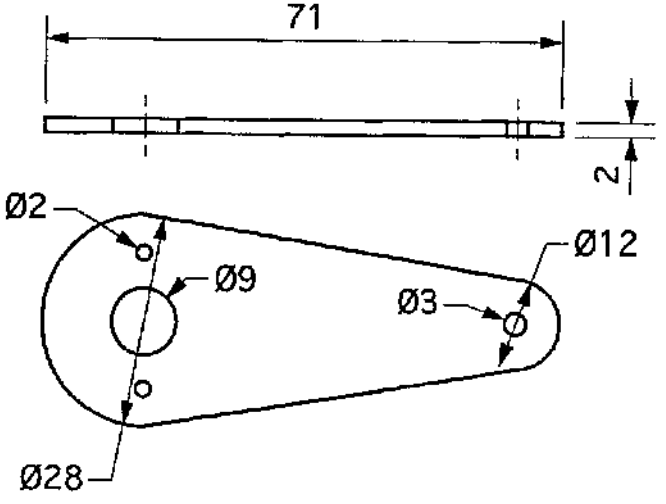

Scale 1:1
Units : mm

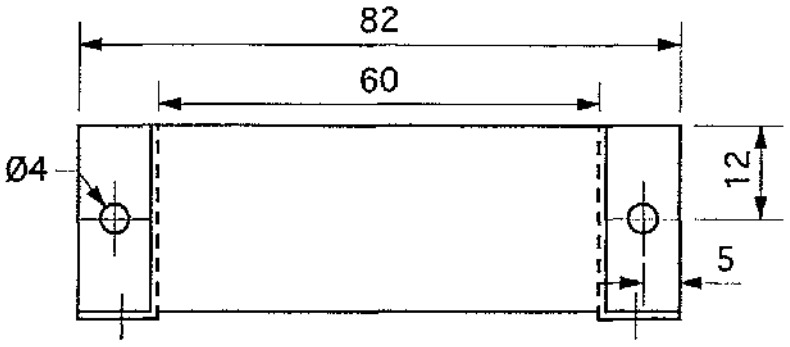

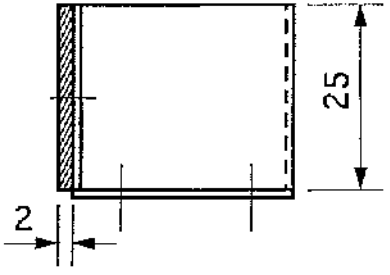

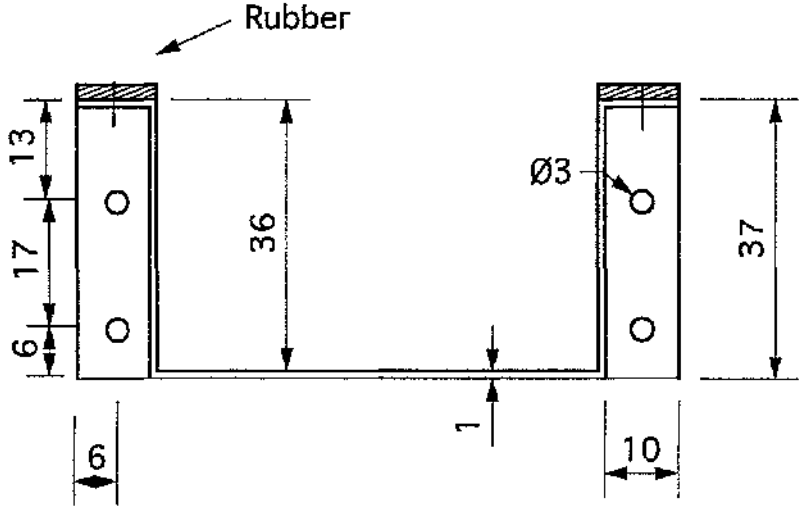

Scale 1:1
Units : mm

SERVO-BRACKET
- Flaps

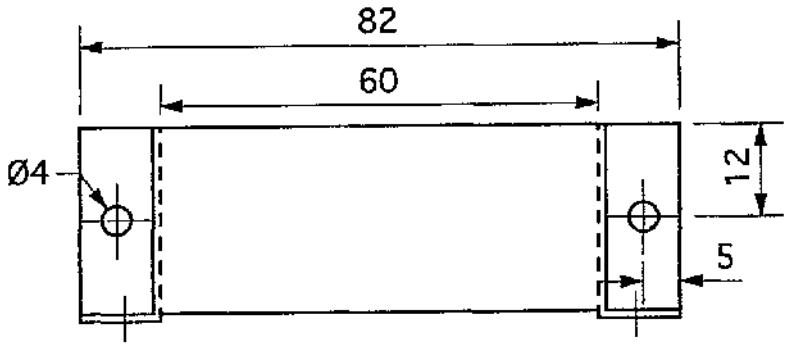

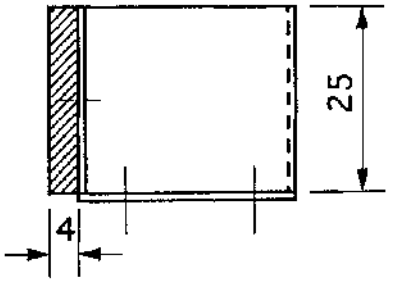

Scale 1:1
Units : mm

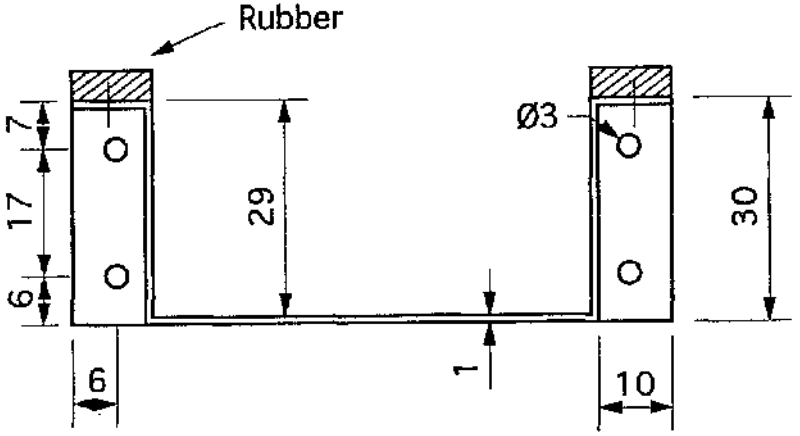

SERVO-BRACKET
- **Elevator**
- **Rudder**
- **Aileron**

SERVO-BRACKET

Scale 1:1
Units : mm

Bracket for servo S3001 : 40.4*19.8*36

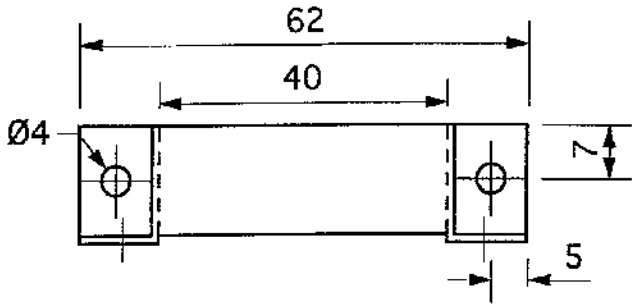

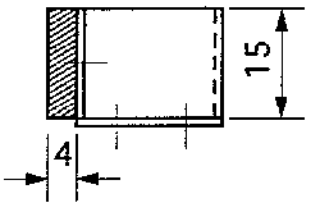

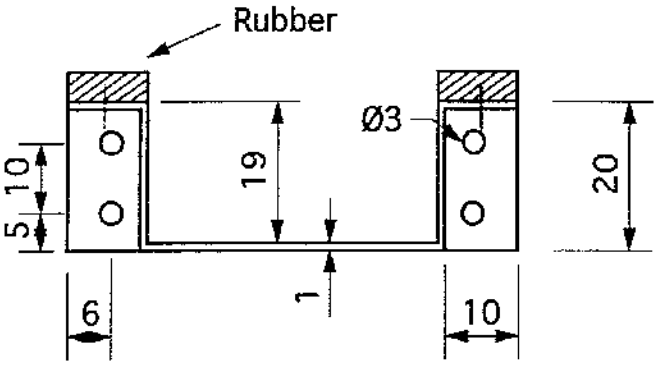

Servo-bracket of the engine

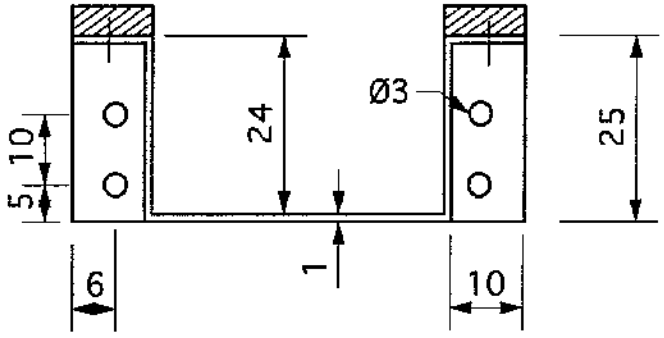

Appendix

F

HINGEMOMENTS CALCULATIONS

3.2.1 HINGE MOMENTS CALCULATIONS

The methods used apply only in the linear range of the control surface deflection (less than twenty degrees) and in the linear range of the angle of attack (less than twelve degrees). As a consequence, methods apply as long as the airflow over the surface is attached. No effect of horns, gap, internal balance plates has been taken into account during the calculations. Calculations were performed following guidelines in Ref.17 and at the approach speed because it is customary for design purpose to assume that maximum control surface deflections occur at that airspeed. Please consult the above reference for the nomenclature used in this section, too. The Reynolds number will be calculated at $V_{app} = 1.2V_S$, although VLA 75 prescribes $V_{app} = 1.3V_S$, but the latter is regarded too high for an RPV. This will also take into account the fact that the stalling speed will be estimated using SOJKA $C_{L_{max}} = 1.21$ from Ref.7 and Condor wing area, giving :

$$V_S = \sqrt{\frac{2W}{\rho_0 S C_{L_{max}}}} = \sqrt{\frac{2(145)(9.80665)}{(1.225)(4.124)(1.21)}} = 21.6 \text{ m/s}$$

The maximum lift coefficient is certainly higher than estimated owing to the higher wing area of the Condor provided by its wing extensions and therefore the actual stall speed is likely to be lower than calculated. It is then :

$$V_{app} = 1.2(21.6) = 25.9 \text{ m/s}$$

3.2.2 CALCULATION OF RUDDER HINGE MOMENT

It is assumed that the sideslip angle β is zero. The hinge moment coefficient is :

$$C_H = C_{H_\delta}\delta_r + C_{H_\beta}\beta + C_{H_0}$$

The tail fin profile is the NACA 0010, which is symmetric, therefore C_{H_0} is zero and $\tan(\phi/2) = t/c = 0.10$

The above 3-D value must be calculated from 2-D values. Following steps are described in detail in Ref.17.

Calculation of C_{H_β}

Calculation of 2-D value

Step 1

In this section in order to calculate the Reynolds number we will use the vertical tail mean aerodynamic chord, according to Ref.17 fig.10.64 p.469 :

$$R_N = \frac{\rho_0 V_{app} c}{\mu_0} = \frac{(1.225)(25.9)(0.38)}{1.7894 \cdot 10^{-5}} = 6.73 \cdot 10^5$$

which from Ref.17 fig.10.64a p.469 gives :

$$\frac{c_{l_\beta}}{(c_{l_\beta})_{theory}} = 0.79$$

as the closest value for R_N is 1e6.

Step 2 - calculation of c'_{h_β}

From Ref.17 fig.10.63a and fig.10.63b p.468 we have :

$$\frac{c_f}{c} = \frac{127mm}{380mm} = 0.33 \Rightarrow \frac{c'_{h_\beta}}{(c_{h_\beta})_{theory}} = 0.5$$

$$(c_{h_\beta})_{theory} = -0.60 rad^{-1} \Rightarrow c'_{h_\beta} = \frac{c'_{h_\beta}}{(c_{h_\beta})_{theory}} (c_{h_\beta})_{theory} = (0.5)(-0.60) = -0.3 rad^{-1} =$$

$$= -0.0052 \deg^{-1}$$

Step 3

Skipped because $\tan(\phi/2) = t/c$

Step 4 - calculation of $(c_{h_\beta})_{bal}$

From the vertical tail geometry it is :

$c_b = 30mm \qquad c_f = 127mm \qquad t_c/2 = 24mm$

hence the balance ratio will be :

$$\text{BAL. RATIO} = \sqrt{\left(\frac{c_b}{c_f}\right)^2 \left(\frac{t_c/2}{c_f}\right)^2} = \sqrt{\left(\frac{30}{127}\right)^2 \left(\frac{24}{127}\right)^2} = 0.14$$

In fig.10.65a p.471 of Ref.17 the closest profile is the NACA 0009 and the rudder nose is assumed to be ROUND, which yields

$$\frac{(c_{h_\beta})_{bal}}{c'_{h_\beta}} = 0.92 \Rightarrow (c_{h_\beta})_{bal} = c'_{h_\beta} \frac{(c_{h_\beta})_{bal}}{c'_{h_\beta}} = (-0.0052)(0.92) = -0.00478 \deg^{-1}$$

Step 5 - calculation of final 2-D value

The compressibility effect is here considered, which in turn depends on the Mach number. At ISA conditions the speed of the sound will be

$t_0 = 15^\circ C \Rightarrow T_0 = 273 + 15 = 288^\circ K$

$\gamma = 1.4$ as the fluid is air

$R = 287 J / Kg^\circ K$

$a = \sqrt{\gamma R T_0} = 340 \text{ m/s}$

and hence the Mach number is

$$M = \frac{V_{app}}{a} = \frac{25.9}{340} = 0.076$$

which yields

$$(c_{h_\beta})_M = \frac{(c_{h_\beta})_{tail}}{\sqrt{1 - M^2}} = -0.00479 \deg^{-1}$$

which differs little from the uncorrected value, owing to the low Mach number.

Calculation of 3-D value

From the vertical tail geometry again we have

AR=1.2 $\quad \Lambda_{c/4} = 0 \Rightarrow \cos(\Lambda_{c/4}) = 1$

and from Ref.17 fig.10.77c p.483 :

$$\frac{c'_f}{c'} = \frac{160mm}{380mm} = 0.42 \qquad \frac{c'_b}{c'_f} = 0.19 \Rightarrow B_2 = 1.16$$

It is also, according to Ref.17eq.10.144 p.482

$K_\beta = 1$

because the rudder covers the whole fin. As a result it is (Ref.17fig.10.77a p.483)

$$AR = 1.2 \Rightarrow \frac{\Delta C_{H_\beta}}{c_{l_\beta} B_2 K_\beta} = 0.022$$

and in addition, from the database in Ref.18 for the NACA 0010 we find

$c_{l_\beta} = 0.1 \deg^{-1}$

and eventually

$\Delta C_{H_\beta} = (0.022)(0.1)(1.16)(1) = 0.0026 \deg^{-1}$

$$C_{H_\beta} = \left(\frac{AR \cos(\Lambda_{c/4})}{AR + 2\cos(\Lambda_{c/4})} \right) (c_{h_\beta})_M + \Delta C_{H_\beta} = \left(\frac{1.2}{1.2 + 2} \right) (-0.00479) + 0.0026 = 0.0008 \deg^{-1}$$

The latter is Ref.17eq.10.142 p.481

Calculation of C_{H_δ}

Calculation of 2-D value

Step 1

This is a repeat of step 1 for calculating C_{H_β}

t/c = 0.10 $\quad R_N = 6.73e5$

hence

$$\frac{c_{l_\alpha}}{(c_{l_\alpha})_{theory}} = 0.79$$

being 10^6 the closest value in fig.10.64a p.469

Step 2 - calculation of c'_{h_δ}

According to Ref.17fig.10.69a and fig.10.69b p.475 is

$$\frac{c_f}{c} = \frac{127mm}{380mm} = 0.33 \Rightarrow \frac{c'_{h_\delta}}{(c'_{h_\delta})_{theory}} = 0.817$$

$$(c_{h_\delta})_{theory} = -0.91 rad^{-1} = -0.0159\,\mathrm{deg}^{-1}$$

hence

$$c'_{h_\delta} = \frac{c'_{h_\delta}}{(c_{h_\delta})_{theory}}(c_{h_\delta})_{theory} = (0.817)(-0.0159) = -0.0130\,\mathrm{deg}^{-1}$$

Step 3

Skipped for the same reason as stated before.

Step 4 - calculation of $(c_{h_\delta})_{bal}$

In fig.10.71 p.477 of Ref.17 the closest profile is the NACA 0009 and the rudder nose is assumed ROUND, which yields, by using the balance ratio previously seen

$$\frac{(c_{h_\delta})_{bal}}{c'_{h_\delta}} = 0.80 \Rightarrow (c_{h_\delta})_{bal} = c'_{h_\delta}\frac{(c_{h_\delta})_{bal}}{c'_{h_\delta}} = (-0.0130)(0.80) = -0.0104\,\mathrm{deg}^{-1}$$

Step 5 - calculation of final 2-D value

We already know what the Mach number is. We have

$$(c_{h_\delta})_M = \frac{(c_{h_\delta})_{bal}}{\sqrt{1-M^2}} = -0.01043\,\mathrm{deg}^{-1}$$

Calculation of 3-D value

From the vertical tail geometry we have

AR=1.2 $\quad \Lambda_{c/4} = 0\,\mathrm{deg} \Rightarrow \cos(\Lambda_{c/4}) = 1 \quad \Lambda_{hl} = 0\,\mathrm{deg} \Rightarrow \cos(\Lambda_{hl}) = 1$

and from Ref.17 fig.10.77c p.483

$$\frac{c'_f}{c'} = \frac{160mm}{380mm} = 0.42 \qquad \frac{c'_b}{c'_f} = 0.19 \Rightarrow B_2 = 1.16$$

and in addition, from Ref.17 fig.8.14 p.228 we find

t/c =0.10 $\quad c_f/c = 0.33 \Rightarrow c_{l_\delta} = 4.67 rad^{-1} = 0.0815 \deg^{-1}$

It is also, according to Ref.17 eq.10.147 p.484

$K_\delta = 1$

because the rudder covers the whole fin. As a result it is (Ref.17 fig.10.78a p.485)

$$AR = 1.2 \Rightarrow \frac{\Delta C_{H_\delta}}{c_{l_\delta} B_2 K_\delta} = 0.044$$

and eventually

$$\Delta C_{H_\delta} = (0.044)(0.0815)(1.16)(1) = 0.00416 \deg^{-1}$$

The 3-D derivative is written as (Ref.17 eq.10.145 p.484)

$$C_{H_\delta} = (c_{h_\delta})_M + \alpha_\delta (c_{h_\beta})_M \frac{2\cos(\Lambda_{c/4})}{AR + 2\cos(\Lambda_{c/4})} + \Delta C_{H_\delta}$$

which in turn gives

$$C_{H_\delta} = (-0.01043) + \alpha_\delta (-0.00479) \frac{2}{1.2+2} + (0.00416) = -0.00627 - 0.00299\alpha_\delta \deg^{-1}$$

In Ref.17 fig.8.17 p.230 α_δ is a function of $c_f / c = 0.4$ and the deflection δ_r :

(deg) δ_r	1-15	16	17	18	19	20
(deg^{-1}) α_δ	0.6	0.598	0.594	0.588	0.584	0.583

The hinge moment coefficient will be

$C_H = C_{H_\beta}\beta + C_{H\delta}\delta_r$ $\quad$ with $0^\circ \le \delta_r \le 20^\circ$ and $\beta = 0 \deg$

whilst the moment will be

$M_H = qS_r c_{f_r} C_H$

with

$S_r = 0.072 m^2 \qquad c_{f_r} = 0.127 m \qquad q = (0.5)\rho_0 V_{app}^2 = 410.9 Pa$

where c_{f_r} is the rudder mean chord computed from the hinge line. Calculations are performed by a Fortran code. The moment is multiplied by 1.25 according to VLA 395(a). The result of the calculations is in Fig.3.3. It is seen that the servo Futaba ps3001 cannot allow a reasonable rudder deflection at the given approach speed (8 degrees of

deflection does not seem adequate), therefore the more powerful Futaba ps3032 should be used, which can cope up to 20 degrees of deflection, according to the plot in Fig.3.3.

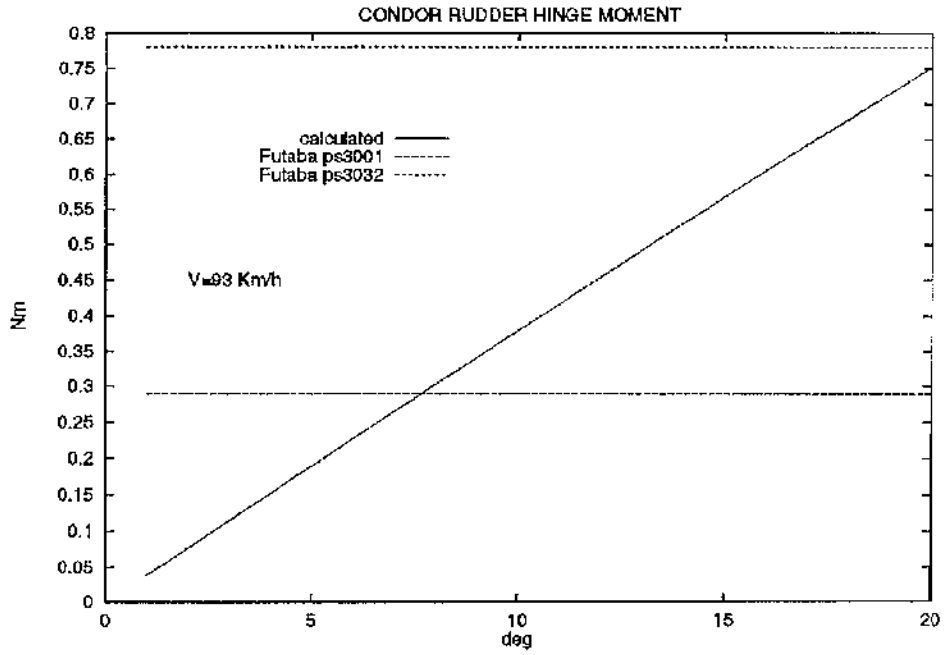

Fig.3.3 Rudder Hingemoment Against Deflection Angle.

3.2.3 CALCULATION OF ELEVATOR HINGE MOMENT

The hinge moment coefficient is

$$C_H = C_{H_\alpha}\alpha + C_{H_\delta}\delta_e + C_{H_0}$$

The horizontal tail profile is again the NACA 0010, which is a symmetric one, thus giving $C_{H_0} = 0$ and again $\tan(\phi/2) = t/c = 0.10$

The above 3-D value must be calculated from 2-D values. Following steps are described in detail in Ref.17.

Calculation of C_{H_α}

Calculation of 2-D value

Step 1

In this section in order to calculate the Reynolds number we shall use the horizontal tail mean aerodynamic chord, according to Ref.17 fig.10.64 p.469 :

$$R_N = \frac{\rho_0 V_{app} c}{\mu_0} = \frac{(1.225)(25.9)(0.448)}{1.7894 \cdot 10^{-5}} = 7.94 \cdot 10^5$$

which from Ref.17 fig.10.64a gives :

$$\frac{c_{l_\alpha}}{(c_{l_\alpha})_{theory}} = 0.79$$

as the closest value for R_N is 10^6.

Step 2 - calculation of c'_{h_α}

From Ref.17 fig.10.63a and fig.10.63b p.468 we have :

$$\frac{c_f}{c} = \frac{148mm}{448mm} = 0.33 \Rightarrow \frac{c'_{h_\alpha}}{(c_{h_\alpha})_{theory}} = 0.5$$

$$(c_{h_\alpha})_{theory} = -0.60 rad^{-1} \Rightarrow c'_{h_\alpha} = \frac{c'_{h_\alpha}}{(c_{h_\alpha})_{theory}} (c_{h_\alpha})_{theory} = (0.5)(-0.60) = -0.3 rad^{-1} =$$

$$= -0.0052 \deg^{-1}$$

Step 3

Skipped because $\tan(\phi/2) = t/c$

Step 4 - calculation of $(c_{h_\alpha})_{bal}$

From the horizontal tail geometry it is :

$c_b = 36mm \quad c_f = 148mm \quad t_c/2 = 16mm$

hence the balance ratio will be :

$$\text{BAL. RATIO} = \sqrt{\left(\frac{c_b}{c_f}\right)^2 \left(\frac{t_c/2}{c_f}\right)^2} = \sqrt{\left(\frac{36}{148}\right)^2 \left(\frac{16}{148}\right)^2} = 0.22$$

In fig.10.65a p.471 of Ref.17 the closest profile is the NACA 0009 and the elevator's nose is assumed to be ROUND, which yields

$$\frac{(c_{h_\alpha})_{bal}}{c'_{h_\alpha}} = 0.73 \Rightarrow (c_{h_\alpha})_{bal} = c'_{h_\alpha} \frac{(c_{h_\alpha})_{bal}}{c'_{h_\alpha}} = (-0.0052)(0.73) = -0.00380 \deg^{-1}$$

Step 5 - calculation of final 2-D value

The Mach number necessary to take into account the compressibility effect has been calculated, thus yielding

$$(c_{h_\alpha})_M = \frac{(c_{h_\alpha})_{bal}}{\sqrt{1-M^2}} = -0.00381 \deg^{-1}$$

which differs little from the uncorrected value, owing to the low Mach number.

Calculation of 3-D value

From the horizontal tail geometry we have

AR=3.18 $\quad \Lambda_{c/4} = 0 \Rightarrow \cos(\Lambda_{c/4}) = 1$

and from Ref.17 fig.10.77c p.483

$$\frac{c'_f}{c'} = \frac{184mm}{448mm} = 0.41 \qquad \frac{c'_b}{c'_f} = \frac{36}{184} = 0.2 \Rightarrow B_2 = 1.14$$

It is also, according to Ref.17 eq.10.144 p.482

$$K_\alpha = 1$$

because the elevator covers the whole horizontal tail. As a result it is (Ref.17 fig.10.77a p.483)

$$AR = 3.18 \Rightarrow \frac{\Delta C_{H_\alpha}}{c_{l_\alpha} B_2 K_\alpha} = 0.013$$

and in addition, from the database in Ref.18 for the NACA 0010 we get

$$c_{l_\alpha} = 0.1 \deg^{-1}$$

and eventually

$$\Delta C_{H_\alpha} = (0.013)(0.1)(1.14)(1) = 0.00148 \deg^{-1}$$

$$C_{H_\alpha} = \left(\frac{AR\cos(\Lambda_{c/4})}{AR + 2\cos(\Lambda_{c/4})}\right)(c_{h_\alpha})_M + \Delta C_{H_\alpha} = \left(\frac{3.18}{3.18+2}\right)(-0.00381) + 0.00148 =$$

$$= 0.000859 \deg^{-1}$$

The latter is Ref.17 eq.10.142 p.481

Calculation of C_{H_δ}

Calculation of 2-D value

Step 1

This is a repeat of step 1 for calculating C_{H_α}

t/c = 0.10 $\qquad R_N = 7.94 \cdot 10^5$

hence

$$\frac{c_{l_\alpha}}{(c_{l_\alpha})_{theory}} = 0.79$$

being 1e6 the closest value for R_N in fig.10.64a p.469

Step 2 - calculation of c'_{h_δ}

According to Ref.17 fig.10.69a and fig.10.69b p.475 it is

$$\frac{c_f}{c} = \frac{148mm}{448mm} = 0.33 \Rightarrow \frac{c'_{h_\delta}}{(c'_{h_\delta})_{theory}} = 0.817$$

$$(c_{h_\delta})_{theory} = -0.91 rad^{-1} = -0.0159 \deg^{-1}$$

hence

$$c'_{h_\delta} = \frac{c'_{h_\delta}}{(c_{h_\delta})_{theory}}(c_{h_\delta})_{theory} = (0.817)(-0.0159) = -0.0130\,\text{deg}^{-1}$$

Step 3

Skipped for the same reason as stated before.

Step 4 - calculation of $(c_{h_\delta})_{bal}$

In fig.10.71 p.477 of Ref.17 the closest profile is the NACA 0009 and the control surface nose is assumed to be ROUND, which yields, by using the balance ratio previously seen :

$$\frac{(c_{h_\delta})_{bal}}{c'_{h_\delta}} = 0.60 \Rightarrow (c_{h_\delta})_{bal} = c'_{h_\delta}\frac{(c_{h_\delta})_{bal}}{c'_{h_\delta}} = (-0.0130)(0.60) = -0.0078\,\text{deg}^{-1}$$

Step 5 - calculation of final 2-D value

We already know what the Mach number is. We have

$$(c_{h_\delta})_M = \frac{(c_{h_\delta})_{bal}}{\sqrt{1-M^2}} = -0.00782\,\text{deg}^{-1}$$

Calculation of 3-D value

From the horizontal tail geometry we have

AR=3.18 $\quad \Lambda_{c/4} = 0\,\text{deg} \Rightarrow \cos(\Lambda_{c/4}) = 1 \quad \Lambda_{hl} = 0\,\text{deg} \Rightarrow \cos(\Lambda_{hl}) = 1$

and from Ref.17fig.10.77c p.483

$$\frac{c'_f}{c'} = \frac{184mm}{448mm} = 0.41 \qquad \frac{c'_b}{c'_f} = 0.20 \Rightarrow B_2 = 1.14$$

and in addition, from Ref.17 fig.8.14 p.228 we find

t/c =0.10 $\quad c_f/c = 0.33 \Rightarrow c_{l_\delta} = 4.67rad^{-1} = 0.0815\,\text{deg}^{-1}$

It is also, according to Ref.17 eq.10.147 p.484

$K_\delta = 1$

because the elevator covers the whole horizontal tail. As a result it is (Ref.17 fig.10.78a p.485)

$$AR = 3.18 \Rightarrow \frac{\Delta C_{H_\delta}}{c_{l_\alpha} B_2 K_\delta} = 0.022$$

and eventually

$$\Delta C_{H_\delta} = (0.022)(0.0815)(1.14)(1) = 0.00204\,\text{deg}^{-1}$$

The 3-D derivative is written as (Ref.17 eq.10.145 p.484)

$$C_{H_\delta} = (c_{h_\delta})_M + \alpha_\delta (c_{h_\delta})_M \frac{2\cos(\Lambda_{c/4})}{AR + 2\cos(\Lambda_{c/4})} + \Delta C_{H_\delta}$$

which in turn gives

$$C_{H_\delta} = (-0.00782) + \alpha_\delta (-0.00381) \frac{2}{3.18+2} + (0.00204) =$$

$$= -0.00578 - 0.001471\alpha_\delta \text{ deg}^{-1}$$

It is noted that α_δ is a function of $c_f / c = 0.4$ (again !) and the deflection δ_e. The same table as in 3.2.2 must be used, as the above chord ratio is unchanged. The hinge moment coefficient will be

$$C_H = C_{H\alpha}\alpha + C_{H\delta}\delta_e \qquad \text{with } 0^\circ \le \delta_e \le 20^\circ \text{ and } \alpha = 12 \text{ deg}$$

whilst the moment will be

$$M_H = qS_e c_{f_e} C_H$$

with

$$S_e = 0.262m^2 \qquad c_{f_e} = 0.148m \qquad q = (0.5)\rho_0 V_{app}^2 = 410.9Pa$$

where c_{f_e} is the elevator mean chord computed from the hinge line. Calculations are performed by a Fortran code. The moment is multiplied by 1.25 according to VI.A 395(a). The result of the calculations is in Fig.3.4. It is seen that the servo Futaba ps3032 cannot allow a reasonable elevator deflection at the given approach speed (14 degrees of deflection does not seem adequate), therefore the more powerful Futaba ps3801 should be used, which can cope up to 20 degrees of deflection, according to the plot in Fig.3.4. The elevator is equipped with two servos type ps3801, although the torque of only one servo has been considered. Two servos provide added safety as one will still be active if one of them fails, assuming common-mode failure is not possible.

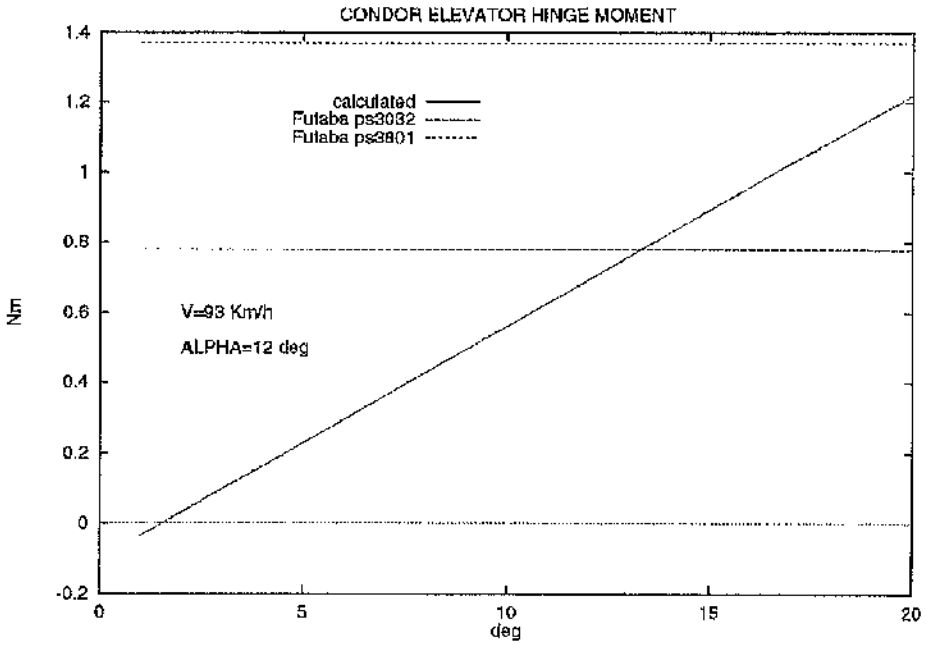

Fig.3.4 Elevator Hingemoment Against Deflection Angle.

3.2.4 CALCULATION OF INNER AILERON HINGE MOMENT

The hinge moment coefficient is

$$C_H = C_{H_a}\alpha + C_{H_\delta}\delta_a + C_{H_0}$$

The wing profile is the non-symmetrical NACA 2415, thus giving $C_{H_0} \neq 0$. This derivative should be determined from experimental data. However, we have to neglect it because this data is not available. It is also $\tan(\phi/2) = t/c = 0.15$. The above 3-D value must be calculated from 2-D values. Following steps are described in detail in Ref.17.

Calculation of C_{H_α}

Calculation of 2-D value

Step 1

In this section in order to calculate the Reynolds number we will use the chord of the wing area whose planform is rectangular (which the inner aileron belongs to). It is, according to Ref.17 fig.10.64 p.469 :

$$R_N = \frac{\rho_0 V_{app} c}{\mu_0} = \frac{(1.225)(25.9)(0.700)}{1.7894 \cdot 10^{-5}} = 1.24 \cdot 10^6$$

which from Ref.17 fig.10.64a gives :

$$\frac{c_{l_\alpha}}{(c_{l_\alpha})_{theory}} = 0.74$$

as the closest value for R_N is 10^6.

Step 2 - calculation of c'_{h_α}

From Ref.17 fig.10.63a and fig.10.63b p.468 we have :

$$\frac{c_f}{c} = \frac{106mm}{700mm} = 0.15 \Rightarrow \frac{c'_{h_\alpha}}{(c_{h_\alpha})_{theory}} = 0.11$$

$$(c_{h_\alpha})_{theory} = -0.30 rad^{-1}$$

$$\Rightarrow c'_{h_\alpha} = \frac{c'_{h_\alpha}}{(c_{h_\alpha})_{theory}} (c_{h_\alpha})_{theory} = (0.11)(-0.30) = -0.033 rad^{-1} = -0.000576 \deg^{-1}$$

Step 3

Skipped because $\tan(\phi/2) = t/c$

Step 4 - calculation of $(c_{h_\alpha})_{bal}$

From the Condor wing geometry it is :

$c_b = 27mm \qquad c_f = 106mm \qquad t_c/2 = 17mm$

hence the balance ratio will be :

$$\text{BAL. RATIO} = \sqrt{\left(\frac{c_b}{c_f}\right)^2 \left(\frac{t_{c/2}}{c_f}\right)^2} = \sqrt{\left(\frac{27}{106}\right)^2 \left(\frac{17}{106}\right)^2} = 0.20$$

In fig.10.65a p.471 of Ref.17 the closest profile is the NACA 0015 and the aileron's nose is assumed to be ROUND, which yields

$$\frac{(c_{h_\alpha})_{bal}}{c'_{h_\alpha}} = 0.80 \Rightarrow (c_{h_\alpha})_{bal} = c'_{h_\alpha} \frac{(c_{h_\alpha})_{bal}}{c'_{h_\alpha}} = (-0.00058)(0.80) = -0.000464 \deg^{-1}$$

Step 5 - calculation of final 2-D value

The Mach number necessary to take into account the compressibility effect has been calculated, thus yielding

$$(c_{h_\alpha})_M = \frac{(c_{h_\alpha})_{bal}}{\sqrt{1-M^2}} = -0.000465 \deg^{-1}$$

which differs little from the uncorrected value, owing to the low Mach number.

Calculation of 3-D value

From the Condor wing geometry we have

AR=8.5 $\qquad \Lambda_{c/4} = 0 \Rightarrow \cos(\Lambda_{c/4}) = 1$

and from Ref.17 fig.10.77c p.483

$$\frac{c'_f}{c'} = \frac{133mm}{700mm} = 0.20 \qquad \frac{c'_b}{c'_f} = \frac{27}{133} = 0.2 \Rightarrow B_2 = 0.84$$

It is now $K_\alpha \neq 1$, since the inner aileron does not cover the entire wing span. From the Condor wing geometry data and according to Ref.17 fig.10.77b it is

$b/2 = 2050 + 915 = 2965mm$

hence

$$\eta_i = \frac{1218}{2965} = 0.4 \qquad \eta_o = \frac{2050}{2965} = 0.7 \Rightarrow (K_\alpha)_{\eta_i} = 1.625 \qquad (K_\alpha)_{\eta_o} = 2.625$$

$$K_\alpha = \frac{(1.625)(1-0.4) - (2.625)(1-0.7)}{0.7-0.4} = 0.625$$

and (Ref.17 fig.10.77a p.483)

$$AR = 8.5 \Rightarrow \frac{\Delta C_{H_\alpha}}{c_{l_\alpha} B_2 K_\alpha} = 0.0039$$

and in addition, from the database in Ref.18 for the NACA 0010 we find

$c_{l_\alpha} = 0.106 \deg^{-1}$

and eventually

$\Delta C_{H_\alpha} = (0.0039)(0.106)(0.84)(0.625) = 0.000217 \deg^{-1}$

$$C_{H_\alpha} = \left(\frac{AR\cos(\Lambda_{c/4})}{AR + 2\cos(\Lambda_{c/4})}\right)(c_{h_\alpha})_M + \Delta C_{H_\alpha} = \left(\frac{8.5}{8.5+2}\right)(-0.000465) + 0.000217 =$$

$= -0.000159 \deg^{-1}$

The latter is Ref.17 eq.10.142 p.481

Calculation of C_{H_δ}

Calculation of 2-D value

Step 1

This is a repeat of step 1 for calculating C_{H_α}

t/c = 0.15 $\qquad R_N = 1.24 \cdot 10^6$

hence

$$\frac{c_{l_\alpha}}{(c_{l_\alpha})_{theory}} = 0.74$$

Step 2 - calculation of c'_{h_δ}

According to Ref.17 fig.10.69a and fig.10.69b p.475 it is

$$\frac{c_f}{c} = \frac{106mm}{700mm} = 0.15 \Rightarrow \frac{c'_{h_\delta}}{(c'_{h_\delta})_{theory}} = 0.794$$

$$(c_{h_\delta})_{theory} = -0.683 rad^{-1} = -0.01192\,\deg^{-1}$$

hence

$$c'_{h_\delta} = \frac{c'_{h_\delta}}{(c_{h_\delta})_{theory}}(c_{h_\delta})_{theory} = (0.794)(-0.01192) = -0.00947\,\deg^{-1}$$

Step 3

Skipped for the same reason as stated before.

Step 4 - calculation of $(c_{h_\delta})_{bal}$

In fig.10.71 p.477 of Ref.17 the closest profile is the NACA 0015 and the aileron's nose is assumed ROUND, which yields, by using the balance ratio previously seen :

$$\frac{(c_{h_\delta})_{bal}}{c'_{h_\delta}} = 0.73 \Rightarrow (c_{h_\delta})_{bal} = c'_{h_\delta}\frac{(c_{h_\delta})_{bal}}{c'_{h_\delta}} = (-0.00947)(0.73) = -0.00691\,\deg^{-1}$$

Step 5 - calculation of final 2-D value

We already know what the Mach number is. We have

$$(c_{h_\delta})_M = \frac{(c_{h_\delta})_{bal}}{\sqrt{1-M^2}} = -0.00693\,\deg^{-1}$$

Calculation of 3-D value

From the Condor wing geometry we have

AR=8.5 $\quad \Lambda_{c/4} = 0\,\deg \Rightarrow \cos(\Lambda_{c/4}) = 1 \quad \Lambda_{hl} = 0\,\deg \Rightarrow \cos(\Lambda_{hl}) = 1$

and from Ref.17 fig.10.77c p.483

$$\frac{c'_f}{c'} = \frac{133mm}{700mm} = 0.20 \qquad \frac{c'_b}{c'_f} = 0.20 \Rightarrow B_2 = 0.84$$

and in addition, from Ref.17 fig.8.14 p.228 we find

t/c =0.15 $\quad c_f/c = 0.15 \Rightarrow c_{l_\delta} = 3.194 rad^{-1} = 0.0557\,\deg^{-1}$

It is now $K_\delta \neq 1$, since the inner aileron does not cover the entire wing span. From the Condor wing geometry data and according to Ref17 fig.10.77b it is

$b/2 = 2050 + 915 = 2965mm$

hence

$$\eta_i = \frac{1218}{2965} = 0.4 \quad \eta_o = \frac{2050}{2965} = 0.7 \Rightarrow (K_\delta)_{\eta_i} = 1.5 \quad (K_\alpha)_{\eta_o} = 2.43$$

$$K_\delta = \frac{(1.5)(1-0.4)-(2.43)(1-0.7)}{0.7-0.4} = 0.57$$

As a result it is (Ref.17 fig.10.78a p.485)

$$AR = 8.5 \Rightarrow \frac{\Delta C_{H_\delta}}{c_{t_\delta} B_2 K_\delta} = 0.00857$$

and eventually

$$\Delta C_{H_\delta} = (0.00857)(0.0557)(0.84)(0.57) = 0.00023\,\text{deg}^{-1}$$

The 3-D derivative is written as (Ref.17eq.10.145 p.484)

$$C_{H_\delta} = (c_{h_\delta})_M + \alpha_\delta (c_{h_\alpha})_M \frac{2\cos(\Lambda_{c/4})}{AR + 2\cos(\Lambda_{c/4})} + \Delta C_{H_\delta}$$

which in turn gives

$$C_{H_\delta} = (-0.00693) + \alpha_\delta (-0.000465)\ \frac{2}{8.5+2} \div (0.00023) =$$

$$= -0.00670 - 0.0000886\alpha_\delta\ \text{deg}^{-1}$$

In Ref.17 fig.8.17 p.230 α_δ is a function of $c_f / c = 133/700 = 0.2$ and the deflection δ_a :

(deg) δ_a	1-5	6-10	11-15	16	17	18	19	20
(deg^{-1}) α_δ	0.45	0.44	0.439	0.436	0.432	0.429	0.425	0.422

The hinge moment coefficient will be

$$C_H = C_{H_\alpha}\alpha + C_{H_\delta}\,\delta_a \qquad \text{with } 0^\circ \le \delta_a \le 20^\circ \text{ and } \alpha = 12\,\text{deg}$$

whilst the hinge moment will be

$$M_H = qS_a c_{f_a} C_H$$

with

$$S_a = 0.1107 m^2 \qquad c_{f_a} = 0.106 m \qquad q = (0.5)\rho_0 V_{app}^2 = 410.9\,Pa$$

where c_{f_a} is the aileron mean chord computed from the hinge line. Calculations are performed by a Fortran code. The moment is multiplied by 1.25 according to VLA 395(a). The result of the calculations is in Fig.3.5. It is seen that the servo Futaba ps3032 can cope up to almost 20 degrees of deflection, according to the plot in Fig.3.5. This amount of deflection is regarded as adequate and therefore a more powerful servo is not required in this case.

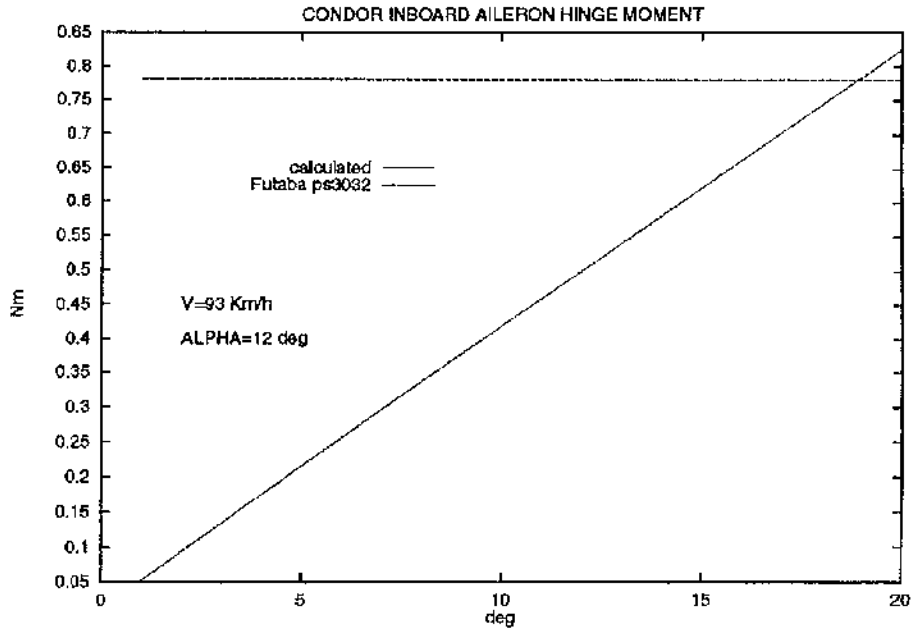

Fig.3.5 Inboard Aileron Hingemoment Against Deflection Angle.

3.2.5 CALCULATION OF OUTER AILERON HINGE MOMENT

The calculation is omitted because of the similarity of the outer and inner aileron's geometry. It is therefore assumed that the same servo Futaba ps3032 may well be adequate for the outer aileron, too.

Appendix

Landing Gear Loading Calculations

This appendix deals with calculations on the Condor landing gear loading. Please refer to sections and figures of Chapter 3 of this thesis where needed.

3.4.1 LOADING

Ground loads (nose wheel type) are calculated according to JAR-VLA requirements (Ref.22). Nose wheel loading calculations were added for completeness.

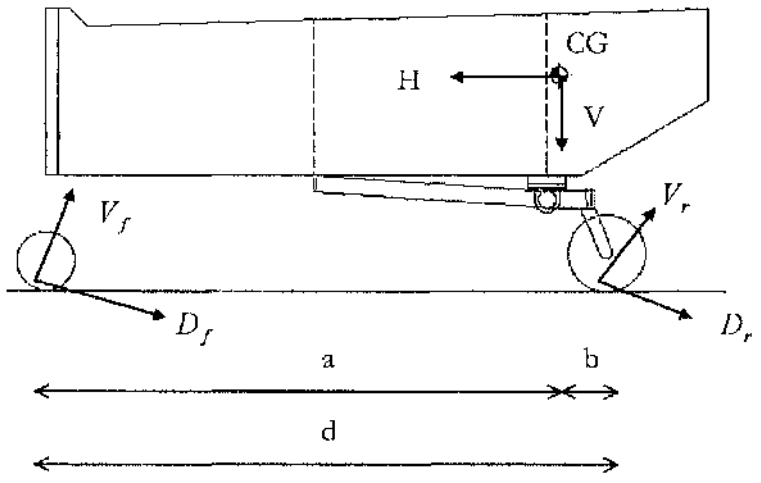

Fig. 3.19 Level Landing Ground Loads.

Level landing - Inclined reactions (VLA 479 (a)(2)(i) and Appendix C of Ref.22)

Weight of the aircraft W=Mg=(145)kg(9.81)m/ s^2
Nose and main wheels contact the ground simultaneously (r is called "L" in Appendix C of Ref.22) :

$$L = 0.667W \Rightarrow r = \frac{L}{W} = 0.667 \text{ (VLA 725 d)}$$

$$n_{min} = n = 2.67 \text{ (limit inertia factor)}$$

Vertical and horizontal component at CG (Fig.3.19) :
$V = nW = 3797\,\text{N}$ H=KnW=949 N [K=0.25]
Vertical and horizontal component at ground :
$V_g = (n - r)W = 2848\,\text{N}$ $H_g = KnW = 949\,\text{N}$
The angle of the resultant force with respect to the vertical is :

$$\tan\beta = \frac{H_g}{V_g} = 0.333 \Rightarrow \beta = 18.4\,\text{deg}$$

From figure at page 1-App C-2 (Ref.22) we have :
$a' = a\cos\beta - h\sin\beta = 1026\,\text{mm}$ $d' = d\cos\beta = 1355\,\text{mm}$
$b' = d' - a' = 329\,\text{mm}$
hence main wheel loads (both wheels) are

$$V_r = V_g\frac{a'}{d'} = 2156\,\text{N} \qquad D_r = H_g\frac{a'}{d'} = 718\,\text{N}$$

Note that this notation refers to loads per wheel in the Excel worksheet. Nose wheel loads :

$$V_f = V_g\frac{b'}{d'} = 346\,\text{N} \qquad D_f = H_f\frac{b'}{d'} = 115\,\text{N}$$

Finally, spin-up loads will be (ACJ-VLA 479 b) at the main wheels axle :
$P_X = -0.5V_r = -1078\,\text{N}$ $P_Z = 0.6V_r = 1294\,\text{N}$
and at the axle nose wheel
$P_X = -0.5V_f = -173\,\text{N}$ $P_Z = 0.6V_f = 208\,\text{N}$
whilst spring-back loads will be at the main wheels axle
$P_X = 0.5V_r = 1078\,\text{N}$ $P_Z = 0.8V_r = 1725\,\text{N}$
and at the nose wheel axle
$P_X = 0.5V_f = 173\,\text{N}$ $P_Z = 0.8V_f = 277\,\text{N}$

Landing with nose wheel clear (VLA 479 (a)(2)(ii))

This can be regarded as a subcase of VLA 479 (a)(2)(i). In fact :
$V_r = V_g = 2848\,\text{N}$ $D_r = H_g = 949\,\text{N}$
Spin-up loads
$P_X = -0.5V_r = -1424\,\text{N}$ $P_Z = 0.6V_r = 1709\,\text{N}$
Spring-back loads
$P_X = 0.5V_r = 1424\,\text{N}$ $P_Z = 0.8V_r = 2278\,\text{N}$

Landing with tail down (VLA 481 (2) and VLA 481 (b))

Load at main wheels (both wheels)
$V_r = (n - r)W = 2848\,\text{N}$

Side load conditions (VLA 485 (a)(b)(c))

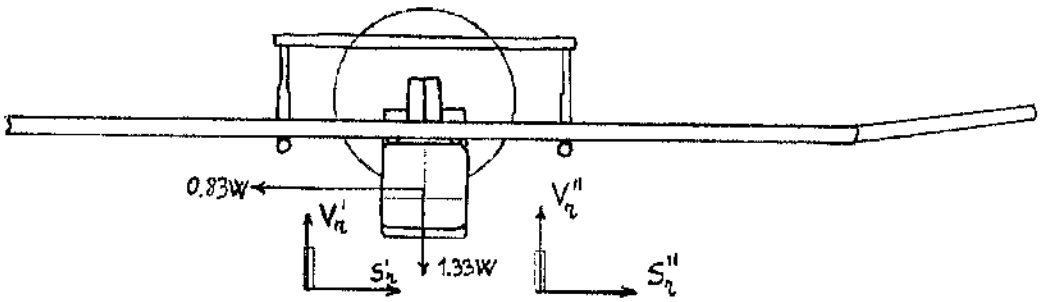

Fig.3.20 Ground Side Loads.

$$V'_r = V''_r = \frac{1.33W}{2} = 1892\,\text{N}$$

while inboard and outboard reactions are, respectively
$S'_r = 0.5W = 711\,\text{N}$ $S''_r = 0.33W = 469\,\text{N}$

Braked roll conditions (VLA 493 (a)(b)(c)

This case is added for completeness since no brakes are expected on the landing gear. Calculations assume that brakes act on the main gear only (Fig.3.21). Friction drag on the nose wheel is neglected.

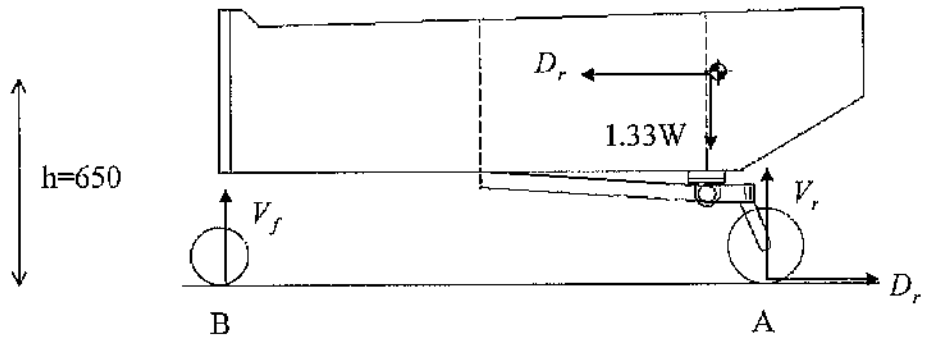

Fig.3.21 Braked Roll Loads.

Calculating moments about "B"

$$V_r = \frac{1.33Wa}{\mu h + d} = 1260\,\text{N} \qquad D_r = \mu V_r = 1008\,\text{N}$$

Calculating moments about "A"

$$V_f = \frac{1.33Wb + D_r h}{d} = 631\,\text{N}$$

3.4.1.1SUPPLEMENTARY CONDITIONS FOR NOSE WHEEL

Conditions for nose wheels (VLA 499 (a)(b)(c))

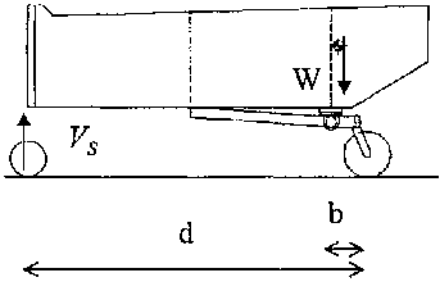

Static load on nose wheel

$$V_S = \frac{Wb}{d} = 129\,\text{N}$$

Aft loads

$$V_f = 2.25V_S = 291\,\text{N} \qquad D_f = 0.8V_f = 233\,\text{N}$$

Forward loads

$$V_f = 2.25V_S = 291\,\text{N} \qquad D_f = 0.4V_f = 117\,\text{N}$$

Side loads

$$V_f = 2.25V_S = 291\,\text{N} \qquad D_f = 0.7V_f = 204\,\text{N}$$

Estimation of the nose wheel static turning moment is necessary to size the servomotor which will be devoted to nose leg steering. Ref.34 (p.39) suggests a method employed in the following. Static torque can be written as

$$M_S = C_M V_S$$

where C_M is a function of the tire contact lenght "g". From the Appendix C we find the nose wheel outside diameter

$D_O = 6$ in = 0.15 m

The loaded radius can be estimated as

loaded radius = 39 % D_O = 0.059 m d = $D_O/2$ - 0.059 = 0.016 m

$$a = 2\sqrt{d(D_O - d)} = 0.0926\,\text{m} \qquad g \cong 0.85a = 0.079\,\text{m} = 3\,\text{in}$$

Eventually we find (Ref.24, p.41, Fig.4-30)

$C_M = 0.0039\,\text{m} \Rightarrow M_S = (0.0039)(129) = 0.5\,\text{Nm}$

The servo Futaba ps3032 capable of a 0.79 Nm max torque seems to be adequate for the nose wheel steering. Note that in Tab.3.3 the static load on tire V_S is different from the value used here and calculated in section 3.4.1.1; however, the value in Tab.3.3 is lower, thus still validating the result of these calculations. Moreover, notation for wheel loads has been unified, hence in Tab.3.3 loads P_X, P_Z are indicated as D_r, V_r respectively, or D_f, V_f respectively. This notation will be used in the following, too.

h (mm) =	550		W (kg) =	145			
a (mm) =	1298		r =	0.667			
b (mm) =	105		n =	2.67			
d (mm) =	1403		K =	0.25			
a' (mm) =	1057.535		beta (deg)=	18.43065	←) Angle of inclined reactions (VLA 479 a. 2. i.)		
d' (mm) =	1331.035		Vs (N) =	106.4192	←) Static Load on nose wheel		
g (m/s2)=	9,80665		Safety factor	1.5			
Ref. Section	VLA 479 (a)(2)(i)	VLA 479 (a)(2)(ii)	VLA 481 (a)(2) & (b)	VLA 485	VLA 499 (a)	VLA 499 (b)	VLA 499 (c)
Case	Inclined Reactions	Nose Wheel Clear	Tail Down Landing	Side Loads	Aft Loads *	Forward Loads *	Side Loads
V	5694.966	5694.966	5694.966	2836.818	2132.946	2132.946	2132.946
H	1423.741	1423.741	0	1770.345	0	0	0
Vr	1697.211	2136.145	2136.145	1418.409	0	0	0
Dr	-565.5960	-711.8708	0	0	0	0	0
S'r	0	0	0	1066.473	0	0	0
S''r	0	0	0	703.8723	0	0	0
Vf	438.9339	0	0	0	359.1650	359.1650	359.1650
Df	-146.2747	0	0	0	-287.3320	143.6660	0
Sf	0	0	0	0	0	0	251.4155
Cases from ACI-VLA 479 (a)(b)							
Rif. Section	VLA 479 (a)(2)(i)	VLA 479 (a)(2)(ii)					
Case	Spin Up *	Spin Up *					
Vr	1018.327	1281.687					
Dr	-848.6059	-1068.072					
Vf	263.3603	0					
Df	219.4669	0					
Case	Spring Back *	Spring Back *					
Vr	1357.769	1708.916					
Dr	848.6059	1068.072					
Vf	351.1471	0					
Df	-219.4669	0					
NOTES :							
* = Loads at axle							
Positive vertical forces are upwards.			Positive horizontal forces are aft.			Forces are calculated per wheel.	

Tab.3.3 Calculation of ground ultimate loads.

3.4.2 SUPPORT REACTION CALCULATION

In order to calculate the support reactions we must apply on the structure the loads calculated in section 3.4.1, multiplied by a safety factor of 1.5 to get the ultimate loads. From this point and onwards we use the most severe cases listed in Tab.3.3.

The first loading case on the structure (Fig.3.22) to be analyzed is VLA 479 (a)(2)(ii).

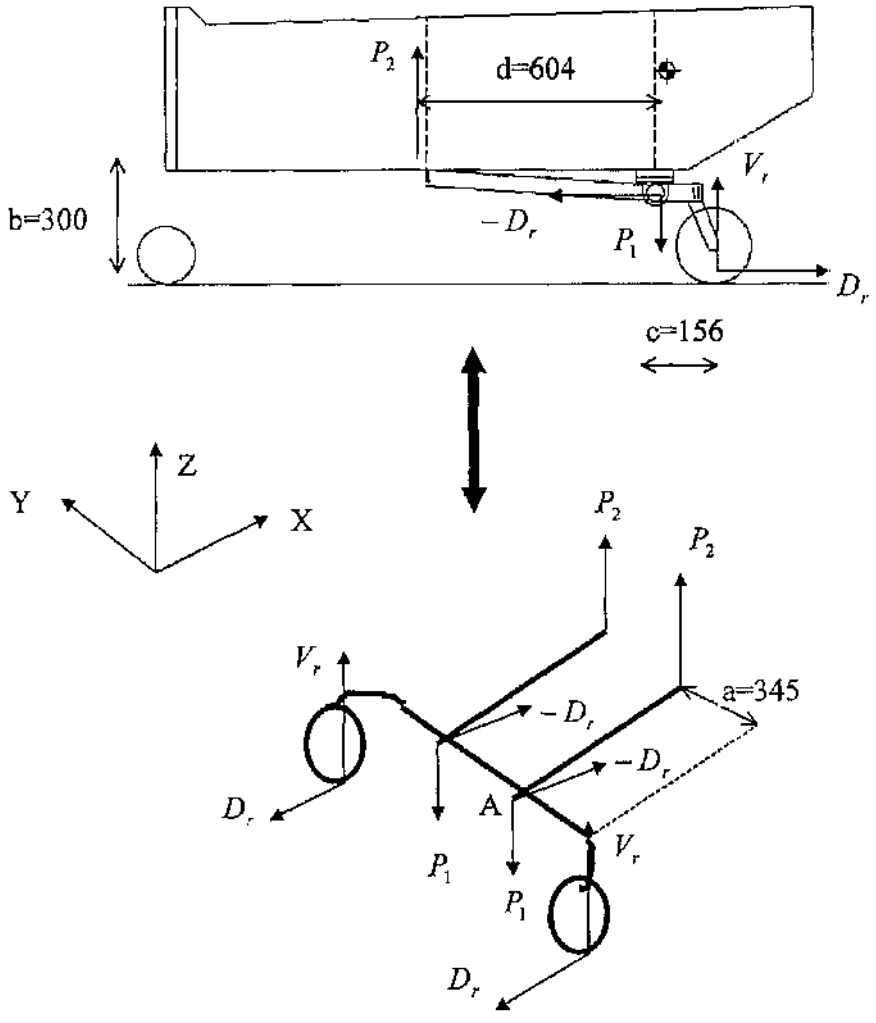

Fig.3.22 Schematic of Main Landing Gear Structure.

Calculating moments about an axis passing through "A" and parallel to the y-axis:

$$P_2 = \frac{(300)(712) + (156)(2136)}{604} = 905\,\text{N}$$

while from the equilibrium of forces :

$$P_1 = -905 - 2136 = -3042\,\text{N}$$

Spring-back loads are applied at the wheel axle, thus giving

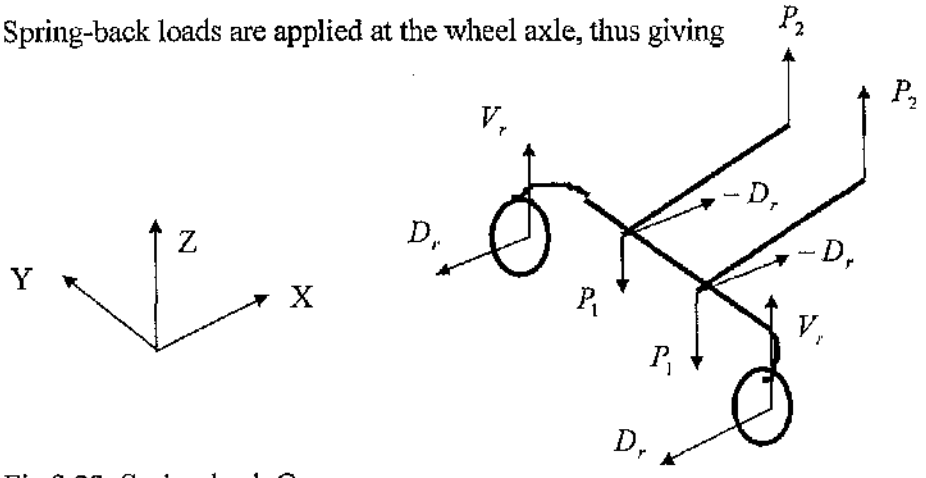

Fig.3.23 Spring-back Case.

$$P_2 = \frac{(200)(1068) + (156)(1709)}{604} = 795\,\text{N}$$

$$P_1 = -1709 - 795 = -2504\,\text{N}$$

Spin-up loads are also applied at the wheel axle, thus giving

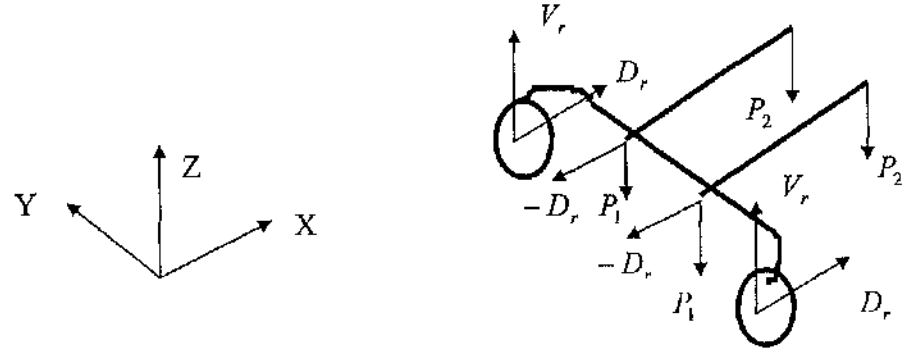

Fig.3.24 Spin-up Case.

$$P_2 = \frac{(156)(1282) - (200)(1068)}{604} = -23\,\text{N}$$

$$P_1 = -1282 + 23 = -1259\,\text{N}$$

VLA 485 loading (side load conditions)

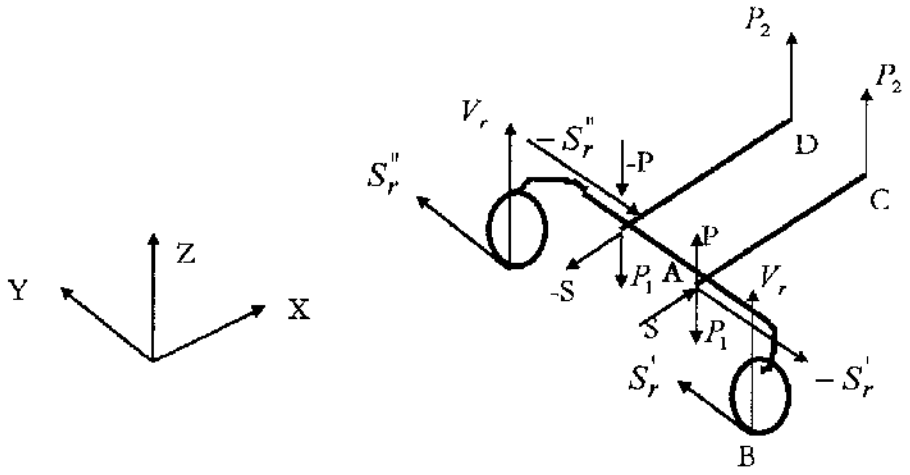

Fig.3.25 Side Load Case.

Note that on points C and D no other reaction than P_2 is considered because otherwise the assembly becomes redundant. Calculating moments about an axis passing through "A" and parallel to the y-axis

$$P_2 = \frac{(1418)(156)}{604} = 366\,\text{N} \qquad P_1 = -1418 - 366 = -1784\,\text{N}$$

$$P = \frac{(300)S''_r + (745)V_r - (400)P_1 + (400)P_2 - (345)V_r + (300)S'_r}{400} = 1328\,\text{N}$$

Calculating moments about an axis passing through "B" and parallel to the z-axis

$$(345)S - (156)S'_r - (745)S - (156)S''_r = 0 \Rightarrow S = \frac{(156)(1066) + (156)(704)}{400} = 690\,\text{N}$$

therefore the total vertical reactions on point A and its symmetric one are, respectively

$$P'_1 = -1784 + 1328 = -456\,\text{N} \qquad P''_1 = -1784 - 1328 = -3112\,\text{N}$$

Final design values taken from the Excel worksheet are listed below

Ref. Section	VLA 479 (a)(2)(ii)	VLA 479 (a)(2)(ii)	VLA 479 (a)(2)(ii)	VLA 485
Case	Nose wheel clear	Spin up	Spring back	Side loads
V_r	2136	1282	1709	1418
D_r	-712	-1068	1068	
S'_r				1066
S''_r				704
P_2	772	21	647	317
P_1	-2908	-1260	-2536	-1735
S				597
P				1106

Tab.3.4 Calculation of Support Reactions.

3.4.3 CALCULATION OF MOMENTS AT INTERFACE FUSELAGE/LEG

According to the proposed design (Fig.3.18) the main gear torque tube would be attached to the bottom fuselage at the existing landing skid hinge attachment points. Loads applied at the landing gear wheels will generate there maximum bending moments about the x and z axis. There is also a torsion moment about the y axis. These moments will be calculated in reference to the loading cases in Tab.3.3 and to the moment arms shown in Fig.3.22.

Case VLA 479 (a)(2)(i) - Nose wheel clear (Fig.3.22)

$$M_X = (0.345)V_r = 737\,\text{Nm}$$
$$M_Z = (0.345)D_r = 246\,\text{Nm}$$
$$M_Y = (0.156)V_r + (0.300)D_r = 547\,\text{Nm}$$

Moments from the spring-back loads (Fig.3.23)

$$M_X = (0.345)V_r = 590\,\text{Nm}$$
$$M_Z = (0.345)D_r = -368\,\text{Nm}$$
$$M_Y = (0.156)V_r + (0.200)D_r = 480\,\text{Nm}$$

Moments from the spin-up loads (Fig.3.24)

$$M_X = (0.345)V_r = 442\,\text{Nm}$$
$$M_Z = (0.345)D_r = 368\,\text{Nm}$$
$$M_Y = (0.156)V_r - (0.200)D_r = -14\,\text{Nm}$$

Case VLA 485 (a) - Side conditions (Fig.3.25)

$$M_X = (0.345)V_r - (0.300)S'_r = 169\,\text{Nm}$$
$$M_Z = (0.156)S'_r = 166\,\text{Nm}$$
$$M_Y = (0.156)V_r = 221\,\text{Nm}$$

Case VLA 485 (b) - Side conditions (Fig.3.25)

$$M_X = (0.345)V_r + (0.300)S''_r = 700\,\text{Nm}$$
$$M_Z = (0.156)S''_r = 110\,\text{Nm}$$
$$M_Y = (0.156)V_r = 221\,\text{Nm}$$

Final design values taken from the Excel worksheet are shown in the table below. Moment arms of Fig.3.22 have been changed during optimization.

	a (mm) =	275			
	b (mm) =	250			
	c (mm) =	135			
	bw (mm) =	150			
	d (mm) =	604			
Applied Loads	Spin-Up *	Spring Back *	Nose Wheel Clear	Side Loads	Side Loads
Dr Drag (N)	1068.072	-1068.072	711.8708	0	0
Sr Side (N)	0	0	0	1066.473	703.8723
Vr Vertical (N)	1281.687	1708.916	2136.145	1418.409	1418.409
Mx (BM1) (Nm)	352.4640	469.9520	587.4400	123.4442	566.0306
My (Leg Torsion) (Nm)	12.81687	390.9146	466.3473	191.4852	191.4852
Mz (BM2) (Nm)	293.7200	-293.7200	195.7644	143.9738	95.02276
NOTES :					
* = Loads at axle					
Dr = +ve forward					
Sr = +ve to outboard					
Vr = +ve up					

Tab.3.5 Ultimate Loads at Interface fuselage/leg (cases from VLA 479 a.2.ii and 485).